Inflight performance of the PILOT experiment

Gabriel Foënard

THÈSE

En vue de l'obtention du

DOCTORAT DE L'UNIVERSITÉ DE TOULOUSE

Délivré par : *l'Université Toulouse 3 Paul Sabatier (UT3 Paul Sabatier)*

Présentée et soutenue le *27/03/2018* **par :**

Gabriel FOENARD

Inflight performance of the PILOT experiment.

JURY

Premier MEMBRE	Peter VONBALLMOOS	Examinateur
Second MEMBRE	Giancarlo DE GASPERIS	Rapporteur
Troisième MEMBRE	Kazuhito DOBASHI	Rapporteur
Quatrième MEMBRE	Ken GANGA	Rapporteur
Cinquième MEMBRE	Francoise DOUCHIN	Examinateur
Sixième MEMBRE	Yuying LONGVAL	Examinateur
Septième MEMBRE	Jean-Philippe BERNARD	Directeur de these
Huitième MEMBRE	Ludovic MONTIER	Directeur de these

École doctorale et spécialité :
SDU2E : Astrophysique, Sciences de l'Espace, Planétologie

Unité de Recherche :
Institut de Recherche en Astrophysique et Planétologie (UMR 5277)

Directeur(s) de Thèse :
Jean-Philippe BERNARD et *Ludovic MONTIER*

Rapporteurs :
Giancarlo DE GASPERIS, *Kazuhito DOBASHI* et *Ken GANGA*

Contents

Résumé

PILOT, pour Polarized instrument for Long Wavelength Observation od the Tenuous interstellar medium, est une expérience d'astrophysique embarquée sous ballon stratosphérique dont l'objectif principal est la mesure de l'émission polarisée de la lumière par les poussières du milieu interstellaire. Cette expérience permettra la cartographie du champ magnétique galactique à une résolution de l'ordre de la minute d'arc à une longueur d'onde de 240 µm (1.2 THz).
La détection de la polarisation est réalisée à l'aide d'un polariseur placé à 45^o dans le faisceau, le décomposant en deux composantes polarisées orthogonales chacune détectées par quatre matrices de 256 bolomètres, et d'une lame demi-onde rotative.
Les observations de PILOT s'inscrivent en complément des observations effectuées à l'aide du satellite Planck, avec une meilleure résolution angulaire, et en complément des observations en polarisation menées au sol avec des instruments comme NIKA2 installé sur le télescope de 30m de l'IRAM.
Cette thèse se divise en trois parties, la première étant consacrée à la présentation du contexte scientifique qui entoure l'instrument ainsi qu'à la présentation de l'instrument et des deux campagnes de vol ayant eu lieu à Timmins au Canada et Alice Spring en Australie. La deuxième partie se focalise sur les performances en vol de PILOT et la troisième partie présente le pipeline mis en place pour le traitement des données ainsi que les premières cartes en polarisation obtenues.

Abstract

PILOT, for Polarized instrument for Long Wavelength Observation of the Tenuous interstellar medium) is a stratospheric balloon astrophysics experiment whose main objective is the measurement of the polarized emission of light by the dust of the interstellar medium. This experiment will allow the mapping of the galactic magnetic field to a resolution of the order of one arcmin at a wavelength of 240 µm (1.2 THz).
The polarization detection is carried out using a polarizer placed at 45^o in the beam, decomposing it into two orthogonal polarized components each detected by four matrices of 256 bolometers, and a half-wave plate.
The PILOT observations are in addition to the observations made using the Planck satellite, with better angular resolution, and in addition to polarization observations conducted on the ground with instruments such as NIKA2 installed on the IRAM 30m telescope.
This thesis is divided into three parts, the first being devoted to the presentation of the scientific context surrounding the instrument as well as to the presentation of the instrument and the two flying campaigns that took place in Timmins in Canada and Alice Spring in Australia. The second part focuses on the inflight performance of PILOT and the third part presents the pipeline set up for data processing and the first polarization maps obtained.

Introduction générale

Le domaine de l'infrarouge couvre la gamme de longueurs d'ondes comprises entre 0.75 et 200 micromètres. Au sein de ce domaine, nous pouvons distinguer l'infrarouge proche qui s'étend de 0.75 à 5 micromètres, l'infrarouge moyen allant de 5 à 25 micromètres et l'infrarouge lointain de 25 à 200 micromètres. A l'infrarouge, on peut associer le domaine submillimétrique s'étendant de 200 à 1000 micromètres.
Suite au développement des détecteurs thermophiles, l'astronomie infrarouge a connu une forte expansion car elle permet l'observation des objets froids de l'univers tels que les grains de poussière du milieu interstellaire.
L'étude du spectre d'émission des poussières a permis de déduire l'existence de trois familles de grains qui se distinguent de par leur taille. Parmi les grains de poussière, il y a donc les très petits grains ayant une taille allant de 1 à 20 nm composés de graphite, les gros grains d'une taille moyenne de 200 nm constitués de graphite et silicate enrobés de glace et les grains de taille moléculaire constitués de quelques dizaines d'atomes de carbone et d'hydrogène. Dans l'infrarouge et le submillimétrique, l'émission thermique des gros grains est modélisée à l'aide d'un spectre de corps noir modifié avec un pic d'émission se situant autour de 140 µm et une température d'équilibre de 18 K.
A la fin des années 40, la dépendance entre le rougissement stellaire et l'émission polarisée des poussières a permis de mettre en évidence leur forme allongée et leur alignement dans une direction imposée par le champ magnétique galactique. Le petit axe des grains de poussière est aligné parallèlement aux lignes de champs magnétiques. Les processus physiques responsables de cet alignement sont toujours sujets à débats. Le rayonnement d'un grain se produisant préférentiellement selon son grand axe, son émission est polarisée perpendiculairement aux lignes de champs magnétiques. A l'inverse, l'absorption de lumière par un grain se faisant préférentiellement selon son petit axe, une lumière non polarisée provenant de l'arrière-plan d'un nuage de poussières serait observée polarisée parallèlement aux lignes de champs magnétiques.

Bien que ne représentant que 1% de la masse du milieu interstellaire, les poussières du milieu interstellaire sont des composantes clé dans de nombreux processus astrophysiques galactiques. Elles sont en revanche un obstacle à l'observation de phénomènes plus lointains tels que la polarisation du fond diffus cosmologique (CMB).
En effet, le rayonnement électromagnétique du CMB, issu d'une époque appelée "époque de dernière diffusion" 380 000 ans après le Big Bang, est polarisé. La polarisation du CMB peut être décomposée en deux composantes distinctes, appelées modes E et B. Les modes B, produits par une hypothétique phase d'inflation aux premiers instants après le Big Bang, n'ont à ce jour pas encore été observés car très faibles. La poussière représente un avant-plan à l'observation du fond diffus cosmologique qu'il est nécessaire de contraindre au maximum si nous souhaitons être en mesure d'observer les modes B de polarisation, et contraidre ainsi les modèles d'inflation.
La difficulté majeure liée à l'observation en infrarouge et le submillimètre est lié à l'atmosphère terrestre. En effet, l'infrarouge fait partie des longueurs d'ondes absorbées par celle-ci ; les observations au sol sont donc essentiellement limitées à l'émission lumineuse dans les régions de formation d'étoiles. Pour s'affranchir de cette contrainte il est donc nécessaire de passer par des télescopes spatiaux ou des télescopes embarqués sous ballons stratosphériques.
La mission PILOT est une expérience astrophysique embarquée sous ballon stratosphérique dont l'objectif est l'étude de l'émission polarisée des grains de poussière du milieu interstellaire. PILOT permettra notamment la cartographie des lignes de champs magnétiques galactiques avec une résolution de l'ordre de la minute d'arc. Pour atteindre les objectifs scientifiques et satisfaire les besoins en sensibilité, il est critique de comprendre et contrôler la qualité de l'optique et les performances en polarisation de l'instrument PILOT. Ces performances doivent être caractérisées sur la totalité du champ de vue instantané (FOV) de $0,8^o \times 1^o$, en tenant compte de la présence éventuelle de grandes variations thermiques de la structure mécanique pendant le vol, et des déformées sous gravité du aux changements d'élévation de l'instrument.
Mes recherches de doctorat ont porté sur l'évaluation des performances de l'instrument lors de deux vols qui ont eu lieu à Timmins au Canada et Alice Springs en Australie ainsi que sur le traitement et l'analyse des données scientifiques.
Ce manuscrit est subdivisé en trois parties.
La première partie, composée de deux chapitres, est consacrée à l'exposition du contexte scientifique qui entoure la mission et à une présentation détaillée de l'expérience.
Dans le premier chapitre je présente le domaine de l'astronomie infrarouge

et submillimétrique. J'expose également les propriétés des poussières du milieu interstellaire et leur interaction avec le champ magnétique galactique. J'explique quel est leur rôle dans le traitement des données cosmologiques et tout particulièrement dans le cadre de la mesure des modes B de polarisation.
Le deuxième chapitre donne un aperçu de la mission PILOT et détaille les observations effectuées avec l'instrument lors des lancements à Timmins au Canada et à Alice Springs en Australie. J'évoque notamment les problèmes rencontrés à la suite du premier vol et quelles ont été les actions menées entre les deux missions pour améliorer l'instrument.
Le seconde partie du manuscrit présente les performances en vol de l'instrument au cours du vol 1 et du vol 2.
Le chapitre 3 est donc consacré à l'étude des constantes de temps des détecteurs et des méthodes utilisées pour les estimer et corriger les données de leurs effets.
Le chapitre 4 s'attarde sur le calcul des coordonnées observées par chaque bolomètre. J'explique les méthodes qui nous ont permis d'estimer et de corriger les variations de pointages liées aux déformations thermiques de l'instrument et aux effets de gravité dus aux changements d'élévation de l'instrument.
Le chapitre 5 est consacré à l'étude du bruit. Je présente les différents types de bruits liés aux systèmes bolométriques qui peuvent affecter les mesures. Je montrerai quels sont les niveaux de bruits observés au cours du vol et j'étudierai la distribution spatiale et temporelle de ce bruit.
Le chapitre 6 développe l'étude du background et des réponses mesurées sur les détecteurs. Ces mesures en vol sont comparées avec les mesures effectuées lors des tests au sol.
Le chapitre 7, dernier chapitre de la deuxième partie expose l'étude des performances optiques de l'instrument lors du vol. Ces performances seront comparées aux mesures effectuées au sol ainsi qu'aux simulations effectuées pour vérifier ces mesures. Les effets de la constante de temps sur la détermination de la PSF sont abordés au cours de ce chapitre.
La dernière partie est réservée, quant à elle, aux différentes méthodes nous permettant de construire des cartes PILOT.
Je souligne, dans le chapitre 9, le lien entre les paramètres de polarisation I,Q,U et la mesure effectuée avec l'instrument et l'influence des différents éléments optiques sur la mesure de polarisation.
Enfin, le chapitre 10 est l'occasion de présenter le pipeline de traitement des données mis en place pour PILOT ainsi que les premières cartes de polarisation obtenues à l'aide des mesures effectuées par l'instrument.

General introduction

The infrared range covers the wavelength range between 0.75 and 200 micrometers. Within this area, we can distinguish near-infrared that ranges from 0.75 to 5 micrometers, mid-infrared from 5 to 25 micrometers and far-infrared from 25 to 200 micrometers.With infrared, we can associate the submillimetric domain extending from 200 to 1000 micrometers.
Following the development of thermophilic detectors, infrared astronomy has expanded considerably because it allows the observation of cold objects in the universe such as the dust grains of the interstellar medium.
The study of the emission spectrum of dust made it possible to deduce the existence of three families of grains which are distinguished by their size. Among the dust grains, there are therefore the very small grains having a size ranging from 1 to 20 nm composed of graphite, the large grains of an average size of 200 nm made of graphite and silicates coated with ice and the grains of molecular size consisting of a few tens of carbon atoms and hydrogen. In the infrared and submillimeter, the thermal emission of large grains is modeled using a modified blackbody spectrum with an emission peak around 140 µm and an equilibrium temperature of 18 K.
At the end of the 1940s, the dependence between stellar reddening and polarized emission of dust made it possible to highlight their elongated shape and their alignment in a direction imposed by the galactic magnetic field. The small axis of the dust grains is aligned parallel to the magnetic field lines. The physical processes responsible for this alignment are still subject to debate. The radiation of a grain occurring preferentially along its major axis, its emission is polarized parallel to the lines of magnetic fields. Conversely, the light absorption by a grain being preferably along its minor axis, unpolarized light from the background of a dust cloud would be observed polarized perpendicular to the magnetic field lines.
While accounting for only 1 % of the mass of the interstellar medium, dust of the interstellar medium are key components in many astrophysical galactic process. On the other hand, they are an obstacle to the observation of distant phenomena such as the polarization of the cosmic microwave back-

ground (CMB).
Indeed, this electromagnetic radiation of the CMB, dating to the epoch of recombination 380 000 years after the big bang, is polarized. The polarization of the CMB can be decomposed into two distinct components, called E and B modes. The B modes, produced by a hypothetical phase of inflation in the first moments after the Big Bang, have not yet been observed. A B-mode detection will pose strong constraints on inflationary model and the B-mode quest is now an active and challenging tak of the CMB community. Dust represents a foreground to the observation of the cosmic microwave background that is necessary to constrain to the maximum if we want to be able to observe polarization B modes.
The major difficulty in infrared observation and the submillimeter is related to the Earth's atmosphere. Indeed, infrared is one of the wavelengths absorbed by it, ground observations are essentially limited to light emission in star formation regions. To overcome this constraint, it is necessary to go through space telescopes or telescopes embedded under stratospheric balloons.
The PILOT mission is a stratospheric balloon astrophysical experiment whose objective is the study of the polarized emission of the dust grains of the interstellar medium. PILOT will map galactic magnetic field lines with a resolution of the order of one arcminute. To achieve the scientific objectives and meet the sensitivity requirements, it is critical to understand and control the quality of the optics and polarization performances of PILOT. These performances must be characterized over the whole instantaneous field of view (FOV) of $0.8^o \times 1^o$, taking into account the possible presence of large thermal variations of the mechanical structure during flight , and deformed under gravity due to changes in elevation of the instrument.
My doctoral research focused on instrument performance evaluation during the two flights that took place in Timmins, Canada and Alice Springs, Australia, as well as the processing and analysis of scientific data. This manuscript is subdivided into three parts.
The first part, consisting of two chapters, is dedicated to the scientific context surrounding the mission and to a detailed presentation of the experience. In the first chapter I present the infrared and submillimetric astronomy. I also expose the properties of interstellar dust and their interaction with the galactic magnetic field. I will explain their role in the processing of cosmological data and especially in the measurement of B modes.
The second chapter provides an overview of the PILOT mission and details the observations made with the instrument during launches in Timmins, Canada and Alice Springs, Australia. I explain in particular the problems encountered following the first flight and what were the actions carried out

between the two missions to improve the instrument.
The second part of the manuscript presents inflight performances of the instrument during flight 1 and flight 2.
Chapter 3 is devoted to the study of detectors time constants and the methods used to estimate and correct the data of their effects.
Chapter 4 focuses on the calculation of the coordinates observed by each bolometer. I will talk about the methods that allowed us to estimate and correct the variations of pointing related to the thermal deformations of the instrument and the effects of gravity due to the elevation changes of the instrument.
Chapter 5 is devoted to the study of noise. I present the different types of noise related to bolometric systems that can affect measurements. I will show the noise levels observed during the flight and I will talk about the spatial and temporal distribution of this noise.
Chapter 6 is devoted to the study of background and measured response on detectors. These in-flight measurements are compared with the measurements made during the ground tests.
Chapter 7, last chapter of the second part is devoted to the study of optical performance of the instrument during flight. These performances will be compared with ground measurements as well as simulations performed to verify these measurements. The effects of the time constant on the determination of the PSF are discussed in this chapter.
The last part is devoted to different methods allowing us to build PILOT maps.
I present in Chapter 9 the connection between the polarization parameters I, Q, U and the measurement made with the instrument and the influence of the different optical elements on the polarization measurement.
Finally, Chapter 10 is an opportunity to present the data processing pipeline put in place for PILOT as well as the first polarization maps obtained using measurements made by the instrument.

Part I

Scientific context and PILOT instrument

Chapter 1

Scientific Context

1.1 Infrared astronomy and polarization of light

Infrared radiation was discovered by the astronomer William Herschel in 1800, when he observed a warm-up of a thermometer while moving along a spectrum well beyond red wavelenght range. It was an area neglected by astronomers until the development of the first thermophilic detectors in the 1960s.
The infrared domain ranges from 0.75 µm to 200 µm. It is divided into three subdivisions:

- The near infrared from 0.75 µm to 5 µm
- The mid-infrared from 5 µm to 25 µm
- The far infrared from 25 µm to 200 µm

At the infrared, astronomers generally associate the submillimeter domain which ranges from 200 µm to 1000 µm. Infrared radiation in astronomy allows us to observe the emission from mainly cold objects such as dust grains and the young objects of the Universe. Most of the radiation emitted in the infrared is absorbed by water molecules and carbon dioxide present in the Earth's atmosphere. It is therefore necessary, except for a few frequency bands such as the 2.2 µm band (observed by Neugebauer and Leighton 1969), to carry out observations at high altitude when it is needed to observe in the infrared range. The stratospheric balloon is an option that has been exploited, allowing the instruments to be raised to an altitude sufficient to

overcome atmospheric effects at certain wavelengths.

One of the first ballon-borne experiments was led by the Johns Hopkins University who launched a balloon to 26.5 km altitude. The scientific instrument consisted of a telescope 30 cm in diameter and a spectrometer. It had been used for the first time as part of the 1959 Moore-Ross manned flight then modified to make the system unmanned. The purpose of this mission was to measure the emission of Venus at 1.3 µm (Bottema et al. 1964). This mission was followed by the Stratoscope II mission which observed the emission between 0.81 and 3.05 µm of Jupiter, the Moon and many stars in 1963 (Woolf et al. 1964). The first FIR balloon-borne astronomical observation was carried out in 1969 to study the emission at 100 µm from the Galactic Center region (Hoffmann and Frederick 1969). The PAHs (Polycyclic aromatic hydrocarbons) were studied by the AROME balloon mission during three flights in 1987, 1988 and 1992 (Giard 1988) who boarded an instrument specifically designed for the detection of near infrared emission bands ($\lambda = 3$–$12\mu m$) from extended sources of low surface brightness with an angular resolution of 0.5^o. Dust emission from the interstellar medium was subsequently studied with balloon missions such as PRONAOS (PROgramme National d'Observations Submillimétriques, Ristorcelli 1995, Bernard et al. 1999, Stepnik et al. 2003), launched in 1994, 1996 and 1999. It consisted of a 2 meters diameter telescope, and four detectors that were bolometers cooled to 300 mK. Observing in four photometric band centered at 200 µm, 260 µm, 360 µm and 583 µm, with a resolution of 2.0' , 2.0', 2.5' and 3.5', respectively.

At the same time, infrared exploration was complemented by satellite missions such as IRAS (Infrared Astronomical Satellite, Neugebauer et al. 1984) in 1983 which performed an all-sky survey in four photometric bands (12, 25, 60 and 100 µm). The discoveries of IRAS include the discovery of a dusty disk around Vega, the first observations of cirrus clouds and the first images of the Galactic center, impossible to observe in the visible range because of the considerable absorption of the interstellar medium. IRAS was later followed by the COBE satellite (Cosmic Background Explorer, Hauser and Dwek 2001), which was launched in 1989 and by the ISO satellite (Infrared Space Observatory, Kessler et al. 1996) in 1995. COBE was equipped with DIRBE (Diffuse Infrared Background Experiment), FIRAS (Far Infrared Absolute Spectrophotometer) and DMR (Differential Microwave Radiometers) instruments designed to study the cosmic diffuse background. DMR allowed, in particular, to map the anisotropies of the cosmic background radiations, FIRAS showed a perfect fit of the CMB and the theoretical curve for a black body at a temperature of 2.7 K and thanks to the DIRBE data it was

possible to conclude that grains of asteroidal origin populate the interplanetary dust bands and the smooth interplanetary dust cloud. ISO operated at wavelengths between 2.5 and 240μm and consisted of a cryostat containing superfluid helium to cool a Richtey-Chrétien type telescope and scientific instruments at a temperature of 2-8 K. By observing the Coma cluster, ISO revealed for the first time the presence of dust in regions between galaxies. This observation implies that the Universe is less transparent than expected.

In 2009, as part of its "Horizon 2000" program, the European Space Agency placed in orbit (at L2 Lagrange points) two telescopes: Herschel (Pilbratt et al. 2010) and Planck (Tauber et al. 2010). Both missions were designed to be complementary. Herschel is an observatory responsible for mapping specific regions of the sky to a resolution of a few arcseconds (18 arcsec on the 250μm band). Its objective was the study, in the far infrared and sub-mm wavelength range (at 55 and 672 μm), of the formation of stars, the birth of primitive galaxies, the evolution of galaxies and the study of the interstellar medium. Planck is an all-sky survey mission whose purpose was to map the temperature variations of the cosmic microwave background (see section 1.2), the study of the interstellar medium, the study of galaxy clusters and the verification of hypotheses related to the Big Bang Theory. For this purpose it was equipped with a primary mirror of 1.5 m diameter and 54 detectors covering 9 frequency bands from 30 to 857 GHz. Planck mapped the sky at a resolution of 5 arcmin. Some of the results of this mission will be briefly described throughout this chapter and will be briefly summarized in section 1.4.

1.1.1 Thermal emission

When an electron is excited by electromagnetic radiation, it passes from a fundamental energy level to an excited energy level. The spontaneous desexcitation that occurs later so that the electron regains its fundamental energy level is accompanied by a monochromatic radiation of energy $h\nu$ where h is the Planck constant and ν is the frequency of the emitted radiation. This is at the origin of the emission spectral lines characteristic of chemical species. The black body is an ideal object that would perfectly absorb the electromagnetic energy it receives, without reflecting or transmitting it. Under the effect of thermal agitation, the black body emits electromagnetic radiation. At thermal equilibrium, emission and absorption are balanced and the radiation actually emitted depends only on the temperature. At thermal equilibrium, the spectral energy luminance of the thermal radiation of the black body will be defined according to its thermodynamic temperature by

means of the following law:

$$B_\lambda = \frac{2hc^2}{\lambda^5} \frac{1}{e^{hc/\lambda k_B T} - 1}, \tag{1.1}$$

Where h is the Planck constant, k_B the Boltzmann constant, c the speed of the light and λ the wavelength.
From this law it is possible to deduce two other laws:

- Wien's law of displacement according to which the black body emission peaks at a wavelength inversely proportional to the temperature. The wavelength corresponding to the peak of light emission of the black body is expressed $\lambda_{max} = b/T$ where λ_{max} is expressed in meter, T in Kelvin and b is a constant equal to $2.898e^{-3}K.m$.
- The law of Stefan-Boltzmann states that the radiant exitance of a black body in watts per square meter is related to its temperature T expressed in Kelvin by the relation:
$$P = \sigma T^4, \tag{1.2}$$
where σ is the Stefan-Boltzmann constant which is about $5.67\text{x}10^{-8}\text{W}\cdot\text{m}^{-2}\cdot\text{K}^{-4}$.

According to the previously stated laws, the cold objects of the Universe are observable in the fields of infrared, submillimeter and radio waves.

1.1.2 Polarization of an electromagnetic wave

An electromagnetic wave is polarized when the evolution of its electric field in time is not random. The most general state of polarization is the state of elliptical polarization, for which the projections of the electric field on two axes x and y orthogonal to the direction of propagation z (see figure 1.1) can be written as follows:

$$E_x(t) = A_x(t)e^{i\omega t} \tag{1.3}$$

$$E_y(t) = A_y(t)e^{i(\omega t+\phi)}. \tag{1.4}$$

If ω is constant, which is the case for a monochromatic wave, as well as the amplitudes A and the phase ϕ, we observe a "naturally" polarized wave. If $\phi = 0$, the wave is linearly polarized. If $\phi = \frac{\pi}{2}$ and $A_x = A_y$, the wave is circularly polarized. We can also define the right and left polarizations if we take ϕ between 0 and 2 π, depending on whether the phase is positive or

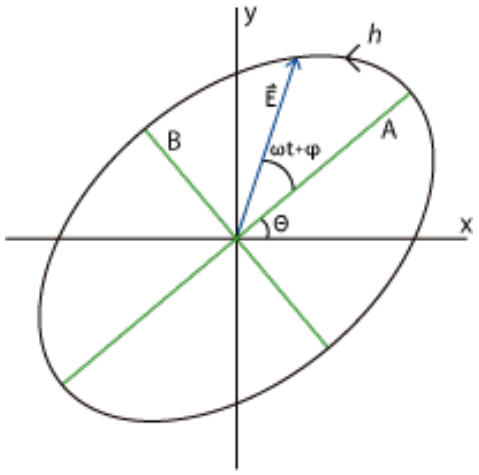

Figure 1.1: Representation of the polarization ellipse.

negative. Knowing the state of polarization of a radiation is equivalent to determining the different parameters of the equations 1.3 and 1.4.
To describe the state of polarization of light we use a notation introduced by Gabriel Stokes: the vector of Stokes. The stokes parameters as defined herein are given in a reference plane $(\vec{x}, \vec{y})$ orthogonal to the propagation direction $\vec{z}$ of the wave. The intensity of a wave is given by:

$$I =< |E_x^2| > + < |E_y^2| >= I_x + I_y \tag{1.5}$$

‘

Linear polarization is described by the elements Q and U defined as follows:

$$Q = I_x - I_y \tag{1.6}$$

$$U = I_x^{45} - I_y^{45} \tag{1.7}$$

‘

The exponent 45 in the equation 1.7 means that we place ourselves in a base oriented at 45^o with respect to x. U is the equivalent of Q in this base. If Q is positive, then the major axis of the ellipse is rather along the x axis. On the contrary, if it is negative, it is rather along the y axis (see figure 1.2). Since Q alone is not sufficient to describe the state of polarization (several

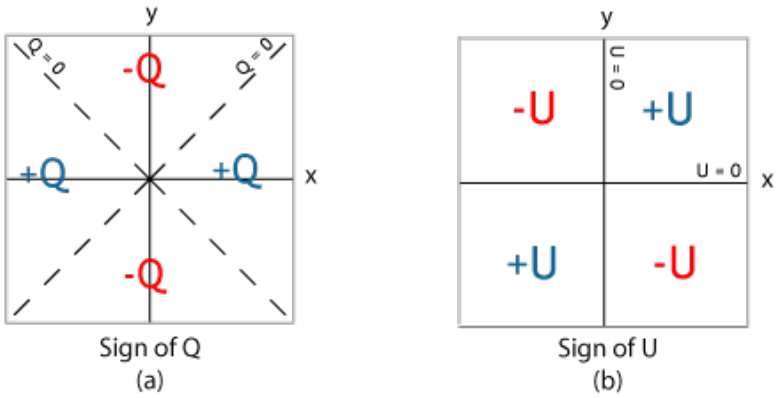

Figure 1.2: Sign of the parameters Q and U according to the orientation of the ellipse in the plane $(\vec{x}, \vec{y})$. Credit: Dan Moulton

ellipses may have the same Q parameter), the observable U must be used. All of these three parameters make it possible to locate the ellipse in the plane $(\vec{x}, \vec{y})$.

A fourth element has been introduced by Stokes:

$$V = 2 \cdot A_x \cdot A_y \cdot \sin \phi \tag{1.8}$$

‘

It allows us to fully characterize the state of polarization by adding the knowledge of the sign of the phase. However this sign is not accessible by photometry measurements.

We define the polarisation fraction p by the following equation:

$$p = \frac{\sqrt{Q^2 + U^2 + V^2}}{I}. \tag{1.9}$$

If the wave is completely polarized, we have the following relation:

$$I^2 = Q^2 + U^2 + V^2 \tag{1.10}$$

In the case of linear polarization, we define the polarization fraction, the polarisation angle and the polarized intensity as follows:

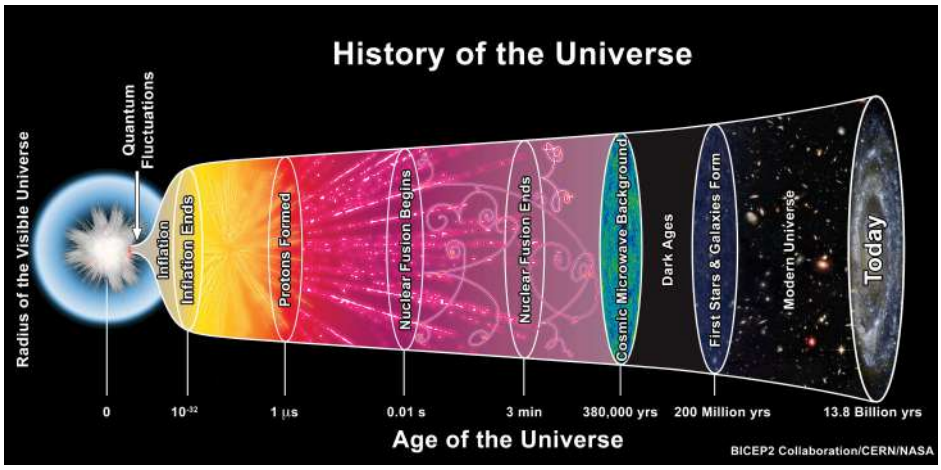

Figure 1.3: Schematic representation of the Big Bang Theory. Crédit : Bicep2 Collaboration/CERN/NASA

$$p_l = \frac{\sqrt{Q^2 + U^2}}{I}, \tag{1.11}$$

$$\psi = 0.5 \cdot \arctan(U, Q), \tag{1.12}$$

$$P = p_l I = \sqrt{Q^2 + U^2}. \tag{1.13}$$

1.2 Cosmic Microwave Background (CMB)

1.2.1 The Big Bang

The Big Bang is the cosmological model used to describe the evolution of the Universe proposed in 1927 by Georges Lemaitre. Ironically called Big Bang by Fred Hoyle, this model was validated by serendipitous observation of the cosmic microwave background by Penzias and Wilson (1965).

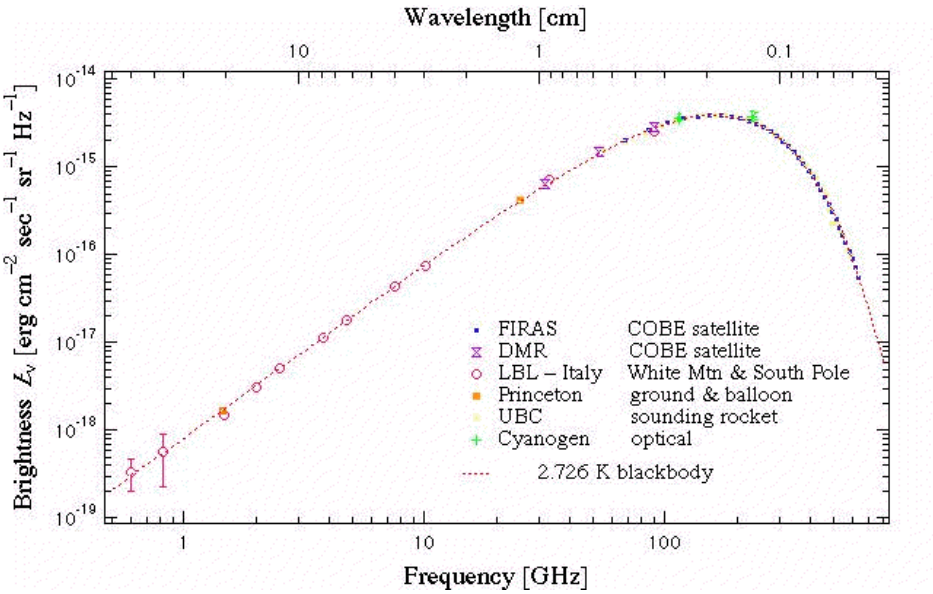

Figure 1.4: Spectrum measured by the FIRAS and DMR instruments, adjusted by the spectrum of a black body at 2.73 K. Credit : CMB Astrophysics Research Program

According to the model, the primordial Universe, extremely dense and warm, was in a state of thermal equilibrium. Its temperature was then higher than the ionization temperature of the hydrogen. The photons were continuously interacting with the material and their mean free paths was then very short. Following an extremely rapid expansion period called inflation, the Universe then cooled, its density decreased and the interactions of the photons with the particles have become rarer (this is the decoupling of the radiation). The photons could then spread freely and the Universe became transparent about 380,000 years after the big bang. It is this first light of the Universe that we call the Cosmic Microwave Background (CMB). The CMB is observed today as a modified black body radiation at a temperature $T = 2.7255 \pm 0.0006$ K and with an emission peak at 150 GHz, i.e., 3 mm (see figure 1.4) .

The CMB is isotropic but exhibits inhomogeneities. Indeed, when the CMB is observed with great accuracy, temperature variations of an order of magnitude of a few μK appear. The size of these anisotropies has many things to teach us concerning for example the curvature of the Universe or the ratio between visible mass and black energy. These information are encoded ih the power spectum of the CMB. Any point in the CMB is identified by a

longitude θ and a latitude φ. The temperature difference of one point relative to the mean temperature of the CMB is noted $\frac{\Delta T(\theta,\varphi)}{T_{avg}}$. These temperature variations of the cosmic diffuse background are the consequence of the density fluctuations of the primordial Universe. A photon from a dense region will lose a fraction of its energy to fight against gravity and will reach us colder. On the contrary, a photon from a less dense region will reach us warmer. The density fluctuations result, for their part, from the superposition of accoustic waves propagating in the primordial fluid. These acoustic waves propagate in the primordial plasma, overlap and evolve gradually. The sum of all these waves gives zones of overdensity and zones of under-density. Large clusters of material produce long wavelength acoustic waves and small clusters of material produce short wavelength acoustic waves propagating through the Universe at the time of the recombination. The signal resulting of all these components can be decomposed into spherical harmonics as follows:

$$\frac{\Delta T(\theta,\varphi)}{T_{avg}} = \sum_{l=1}^{+\infty} \sum_{m=-l}^{+l} (a_{lm} Y_{lm}(\theta,\varphi)) \tag{1.14}$$

where l and m are integer indices, Y_{lm} is the Legendre's associated function and a_{lm} are the generalized Fourier coefficients. Spherical harmonics constitute a set of normed functions, orthogonal to each other. The orthonormalization relation of Y_{lm} is expressed as follows:

$$\int_{4\pi} Y^*_{lm} Y_{l'm'} d\Omega = \delta_{ll'}\delta_{mm'}, \tag{1.15}$$

where $\delta_{ll'}$ and $\delta_{mm'}$ are dirac functions The equation 1.14 multiplied by Y^*_{lm} and integrated over the whole solid angle gives:

$$a_{lm} = \int_{4\pi} \frac{\Delta T(\theta,\varphi)}{T_{avg}} Y^*_{lm}(\theta,\varphi) d\Omega \tag{1.16}$$

a_{lm} contain all the information relating to temperature fluctuations. The angular power spectrum $\{C_l\}_{l=1,\infty}$ is then defined by:

$$\langle a_{lm} a^*_{l'm'} \rangle = C_l \delta_{ll'} \delta_{mm'} \tag{1.17}$$

where the delta functions arise from isotropy. In the case where the a_{lm} are Gaussian, this spectrum contains all the statistical information. We are limited on the number of independent m-modes we can measure. There are

only $(2l+1)$ of these for each multipole. We can write the following expression for the power spectrum:

$$C_l = \frac{1}{2l+1} \sum_{m=-l}^{+l} \left\langle |a_{lm}|^2 \right\rangle \tag{1.18}$$

Plotting C_l (or sometimes $D_l = \frac{l(l+1)C_l}{2\pi}$) as a function of l makes it possible to analyze the amplitudes of each spherical harmonics as a function of their spatial frequency. Figure 1.5 shows a power spectrum of typical CMB temperature anisotropies as measured by Planck in 2013. The "low l part" (before the first peak) corresponds to disturbances larger than the horizon (limit of the observable universe) at the moment of decoupling. The different peaks are respectively at the fundamental frequency for the first peak and the harmonics for the following. The fundamental frequency corresponds to an over-density whose extension was maximum at the time of the Big-Bang, and which compressed before the decoupling. The analysis of this first peak gives us information on the curvature of the Universe. The amplitude decrease that can be observed after the third peak (ℓ greater than 1500) is due to the fact that the recombination process is not instantaneous giving a "thickness" to the last diffusion surface. By observing it we integrate on the line of sight all the contributions of this thickness. This erases small-scale fluctuations. These small fluctuations in the density of the primordial Universe are necessary to trigger a mechanism called instability of Jeans. Discovered by James Jeans in 1902, Jeans instability, or gravitational instability, occurs when the gravitational attraction caused by an overdensity of a medium becomes greater than the internal pressure forces that tend to relax this overdensity. This mechanism is at the origin of the formation of stars (called population III or popIII) and galaxies later in the Universe (about 200 million years after the Big Bang). Between the emission of the cosmic diffuse background (recombination) and the ignition of the first generation of stars, there was a period during which no astrophysical process produced electromagnetic radiation. This period is called "Dark Ages".

1.2.2 Polarization of the CMB

The CMB is also polarized. This polarized signal is about 10 times lower than the total signal emitted by the CMB. The patterns observed in the polarization map of the cosmic diffuse background can be decomposed into two classes, called E modes ("electric" modes, see figure 1.6) and B modes ("magnetic" modes). This denomination has nothing to do with the elec-

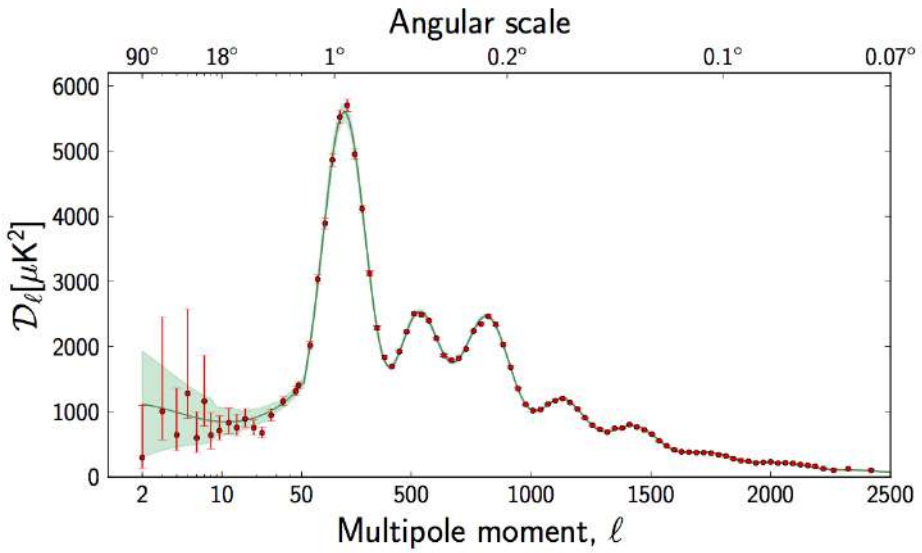

Figure 1.5: Temperature fluctuations in the Cosmic Microwave Background detected by Planck at different angular scales on the sky. The multipolar moments are represented on the x-axis and their intensity on the y-axis. Figure from Planck Collaboration. XV. et al. (2014)

tric and magnetic fields of an electromagnetic wave, but essentially aims to say that the polarization field can be decomposed into a curl-free part (the "electrical" mode), and a divergent-free part (the "magnetic" mode). Linear polarization of a radiation can be seen as a field of arrowless vectors. When this field is purely radial or orthoradial, it corresponds to modes E. When, on the contrary, it has a swirling form locally, we are in the presence of B modes (see figure 1.6).
The E and B modes have distinct origins. Indeed, according to the theory of cosmological perturbations, the E modes of polarization would originate in the passage of density waves generated very early in the history of the Universe. The study of the E modes of polarization of the CMB allows a better understanding of the movements of matter related to the variations of density at the moment of the decoupling.
On the other hand, only the passage of primordial gravitational waves is able to generate both E and B modes. The polarization B is expected to be considerably lower than the polarization E, itself already difficult to be detected.

Polarization B modes have not been detected yet. The team in charge of the BICEP2 instrument, claimed in 2014 to have observed these modes

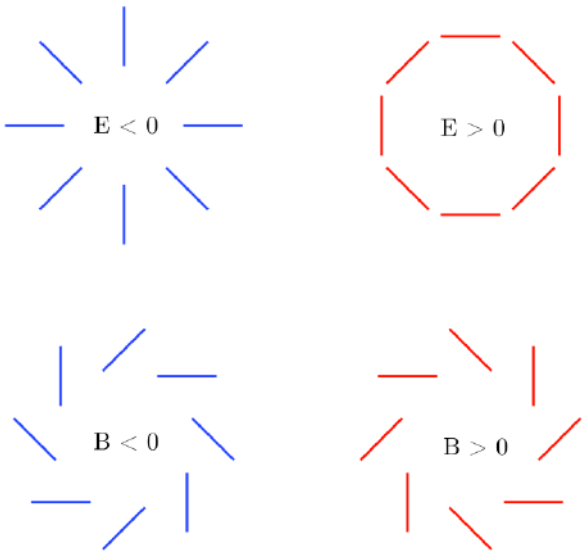

Figure 1.6: Top: E modes of radial symmetry polarizations. Bottom: B modes of polarization. Figure extracted from Krauss et al. (2010)

(see figure 1.7 from BICEP2 Collaboration et al. (2014)). A joint study by the Planck and BICEP2/Keck collaborations (Ade et al. 2015) subsequently established that, the signal observed by BICEP2 was compatible with the contamination signal from Galactic Dust as observed by Planck.

1.2.3 Observational bias

As it can be seen, with the difficulties encountered by the BICEP2 team in highlighting B modes, an increased knowledge of the contaminants of this signal is essential. Indeed, other sources of radiation in the millimetric and submillimetric are grafted to the fossil radiation in this wavelength. These sources constitute what are called the cosmological foregrounds. The main sources of emission are (see fig. 1.8):

- The synchrotron emission, a non-thermal radiation, produced by charged relativistic particles in helical motion around the galactic magnetic field lines. These particles emit a radiation whose frequency is proportional to the square of the intensity of the magnetic field along which they move.
- The bremsstrahlung, or free-free radiation which corresponds to the

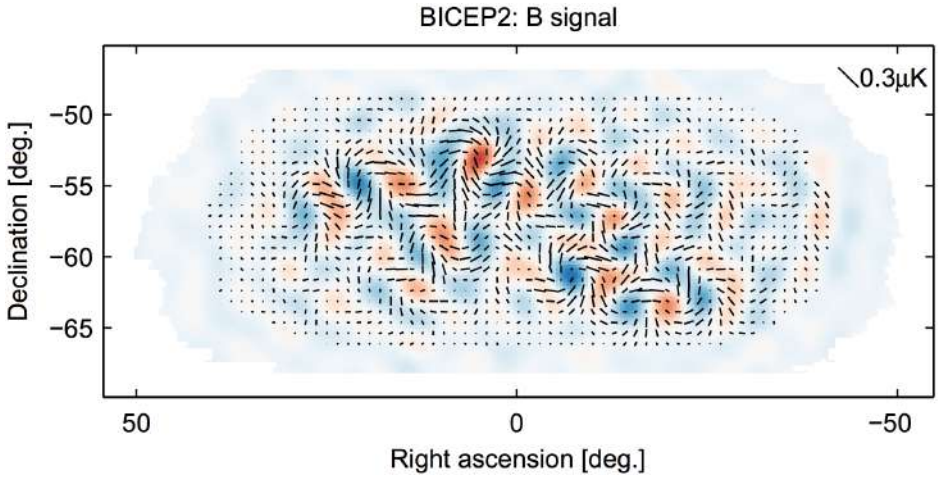

Figure 1.7: *B*-modes map of the polarization in the Cosmic Microwave Background from BICEP2. Colours show the overall brightness, while the black lines show the direction and intensity of the polarization. Figure 1.7 from BICEP2 Collaboration et al. (2014)

braking radiation of the charged particles interacting with other charged particles. This radiation occurs in ionized media such as hydrogen clouds.

- Spinning dust emission or anomalous microwave emission (AME). This emission comes from the rapid rotation of small dust grains with a permanent electric dipole. This emission is predicted to peak arround 30 GHz. This emission probably originates from molecules called polycyclic aromatic hydrocarbon.

- The emission of dust from the interstellar medium.

The bremsstrahlung radiation and the spinning dust emission contribute significantly to total intensity but are thought to be unpolarized or only weakly polarized. The emission of dust and the synchrotron emission contribute significantly to both intensity and polarization. While the synchrotron and free-free emission dominate the CMB spectrum up to 20 GHz, dust from the interstellar medium is the most emissive foreground at the frequencies at which the CMB is most intense, at 150 GHz.

Knowledge of the emission polarized by the dust of the interstellar medium is therefore essential for the processing of cosmological data.

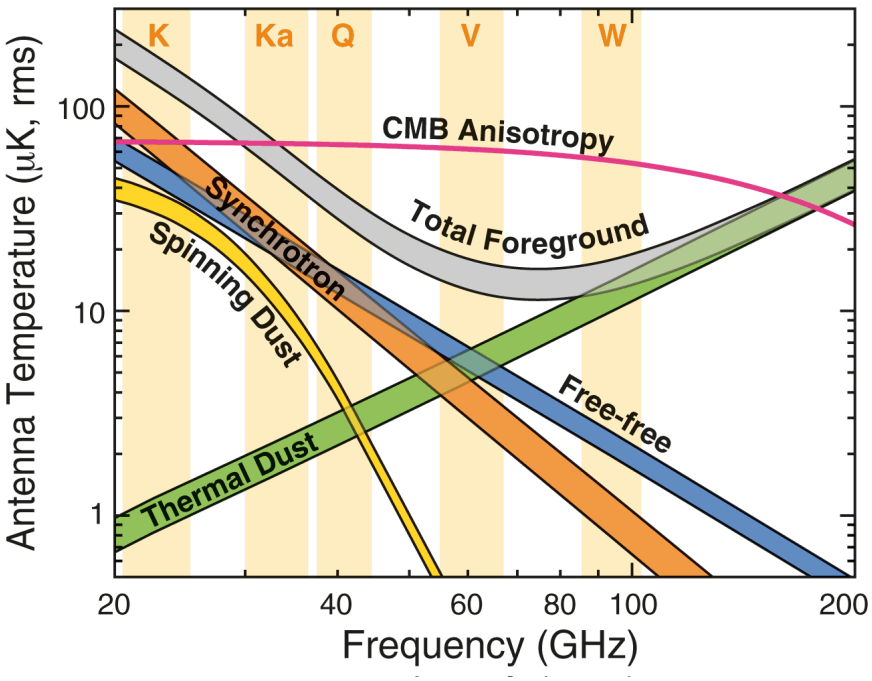

Figure 1.8: Spectra of CMB and foreground anisotropy. The foreground anisotropy results are averages over the three foreground models (Bennett et al. 2013)

Phases	State of matter	Density (atoms/cm^{-3})	Temperature (K)
Molecular clouds	molecular	$> 10^3$	10-20
Cold Neutral Medium	atomic	50	80-100
Warm Neutral Medium	atomic	0.5	8.10^3
Warm Ionized Medium	ionized	1	$10^3 - 10^4$
HII Regions	ionized	$10^2 - 10^4$	8.10^3
Hot Ionized Medium	Ionized	0.006	10^6

Table 1.1: Components of the interstellar medium

1.3 The interstellar medium

The interstellar medium (ISM) is the material that, in a galaxy, fills the space between stars and blends into the surrounding intergalactic environment. Its density is of the order of a few particles per cm^3. Despite this, the interstellar medium in our Galaxy accounts for about 10% of its total mass. The matter of the interstellar medium is in two forms:

- Gas, of which 89% is hydrogen, 9% helium and 2% heavy elements (carbon, oxygen, nitrogen, etc.).
- Dust, which represents 1% of the total mass of the ISM.

It is present in all spiral galaxies, barred spiral, irregular and almost non-existent in elliptical and lenticular galaxies. The interstellar medium bathes in a field of radiation produced by the stars present in the galaxies. The interstellar medium is composed of several phases that are distinguished by their temperature, their density and the state of matter. The different components of the ISM are presented in table 1.1.

1.3.1 The Galactic magnetic field

The presence of an interstellar Galactic magnetic field was postulated for the first time in 1937 by Hannes Alfvén and then by Enrico Fermi in 1949. Its presence was later confirmed by the observation in 1949 of the linear polarization of light emitted by nearby stars and the observation of synchrotron emission in the Milky Way in 1950. The intensity of the Galactic magnetic field is of the order of a few micro-gauss (about 10,000 times weaker than

the Earth's magnetic field). It plays an important role in many astrophysical processes. For example, the magnetic field opposes the gravitational force to explain the thickness of the Galactic disk. It is also essential in the stellar formation process, initially limiting the collapse of the molecular clouds by opposing the gravitation and then allowing the continuation of the collapse process by allowing to evacuate kinetic momentum to the outside of the stellar system. Finally, during magnetic reconnection and ambipolar diffusion processes, a large amount of energy is dissipated mainly in thermal form which constitutes an important source of heating of the ISM. The Galactic magnetic field is generated and driven by a Galactic dynamo operating throughout the entire volume of the Galaxy under the combined action of its rotation and the turbulent movements generated by the explosion of supernovae.

1.3.2 Interstellar dust

By crossing the clouds of the interstellar medium, the light emitted by the stars is attenuated. It is called the "extinction" which is due to the absorption and the diffusion, by the dust grains, of the radiation. Figure 1.9 shows the normalized interstellar extinction curves from the far-IR through the UV. This curve provides a basis for making hypotheses about the characteristics of the interstellar medium grains. Based on these observations, we suppose that dust of the interstellar medium can be classified into three main families:

- The very small grains whose sizes vary between 0.4 nm and 1.2 nm. Responsible for the characteristics of the extinction curve in the far-UV
- Big grains with an average size of 100 nm composed of ice-coated graphites and silicates. These grains are mainly responsible for the extinction in visible and infrared and partially responsible for the extinction in near UV.
- PAHs (Polycyclic Aromatic Hydrocarbons), molecules consisting of a few tens of carbon and hydrogen atoms organized in aromatic cycles. The presence of these explain the UV bump around 217.5 nm.

The constituents of dust (silicate and graphite) are produced by stars. The stars form in the interstellar medium by gravitational collapse of cold and dense cores (or clouds). Most of the life of a star happens on the main sequence defined by the Hertzsprung-Russell diagram relating the mass of a

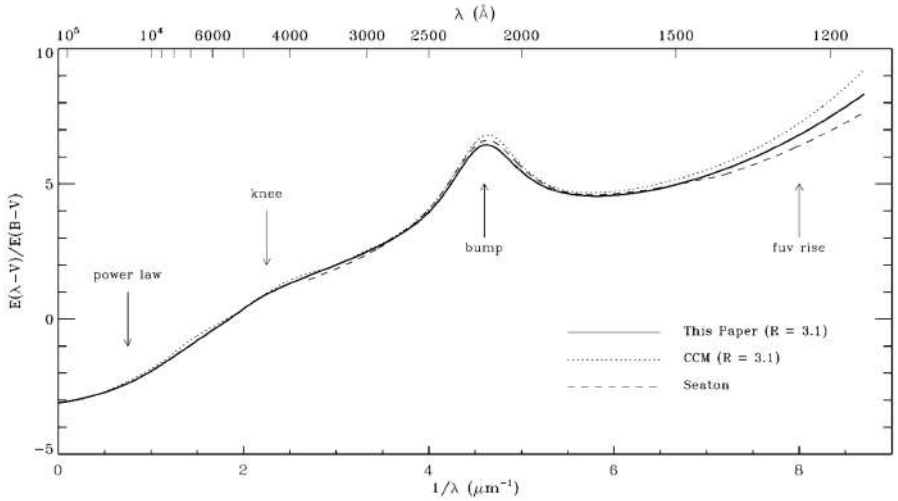

Figure 1.9: Normalized interstellar extinction curves from the far-IR through the UV. Figure from Fitzpatrick (1999).

star on the one hand, the radius and luminosity of this star on the other. The density of the surrounding environment of stars is large enough to allow the formation of more complex molecules and for the formation of dust. At the end of their life, when they emerge from the main sequence, the stars eject matter in the form of stellar winds or supernova explosion for the most massive ones. This material is the main constituent elements of the dust of the interstellar medium. These dust grains will then mix, with the gas present in the MIS, to form an interstellar cloud which, by collapse, will again permit the formation of a star. These stages constitute what is called the cycle of matter or dust cycle in the interstellar medium (see figure 1.10).

In the Milky Way, dust is distributed mainly in the galactic plane with a higher concentration around the central nucleus. When moving away from the plane, the dust density becomes much lower (see figure 1.11).

1.3.3 Thermal emission of dust

Despite their low abundance, dust grains account for 30% of the energy emission of the galaxy in the submillimetric range. The dust grains are heated by the ambient radiation from the stars of the Galaxy. The large grains at thermal equilibrium re-emit the absorbed energy in the form of a continuous radiation according to a modified black body law (NB: $\epsilon(\lambda)B_\lambda(T)$, where $\epsilon(\lambda)$ is the grain emissivity). For large grains of dust, their maximum emission

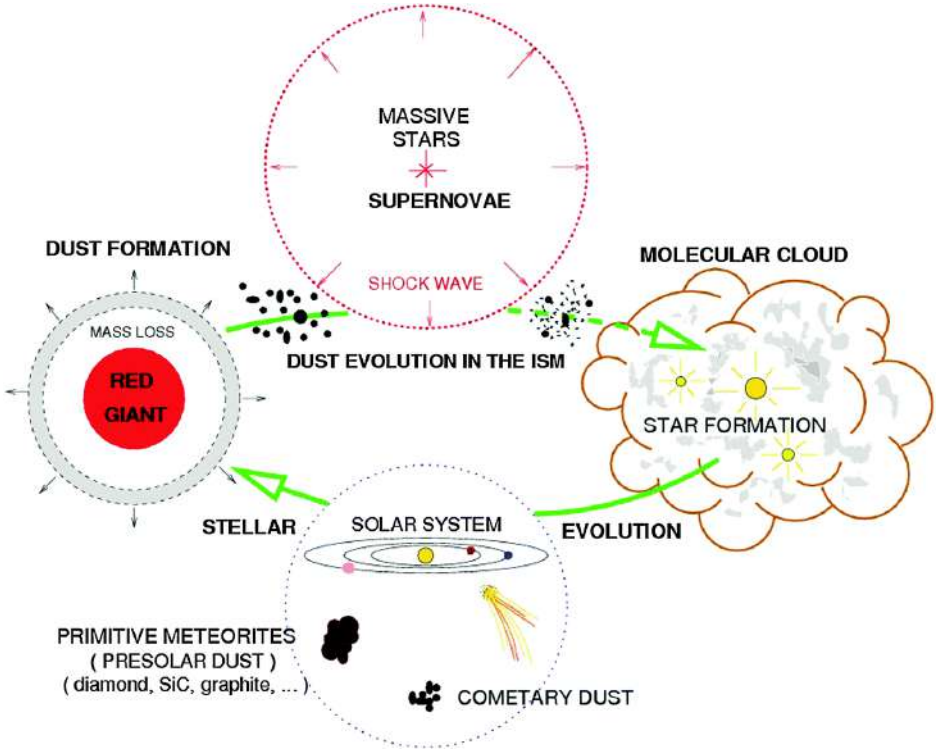

Figure 1.10: Schematic representation of the dust cycle. Figure from Jones and Spitzer (1967).

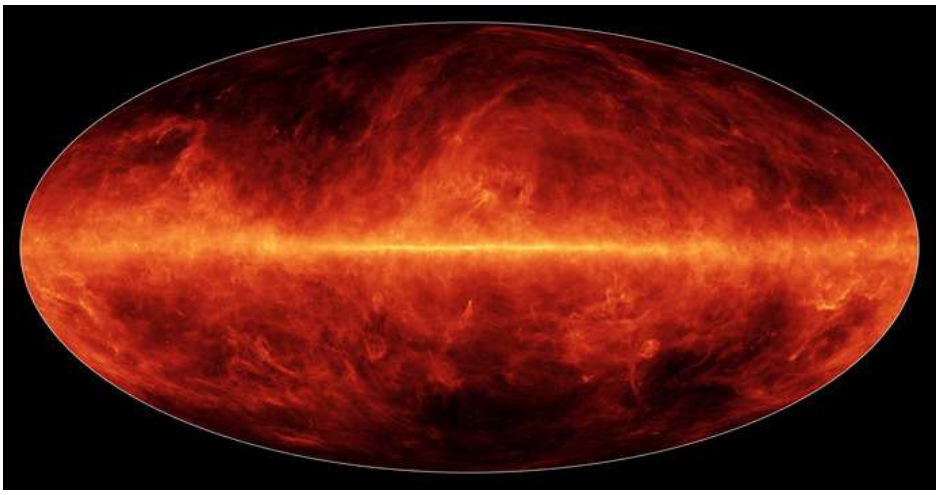

Figure 1.11: Thermal emission of dust particles strewn throughout the galaxy. Image from the European Space Agency's Planck mission.

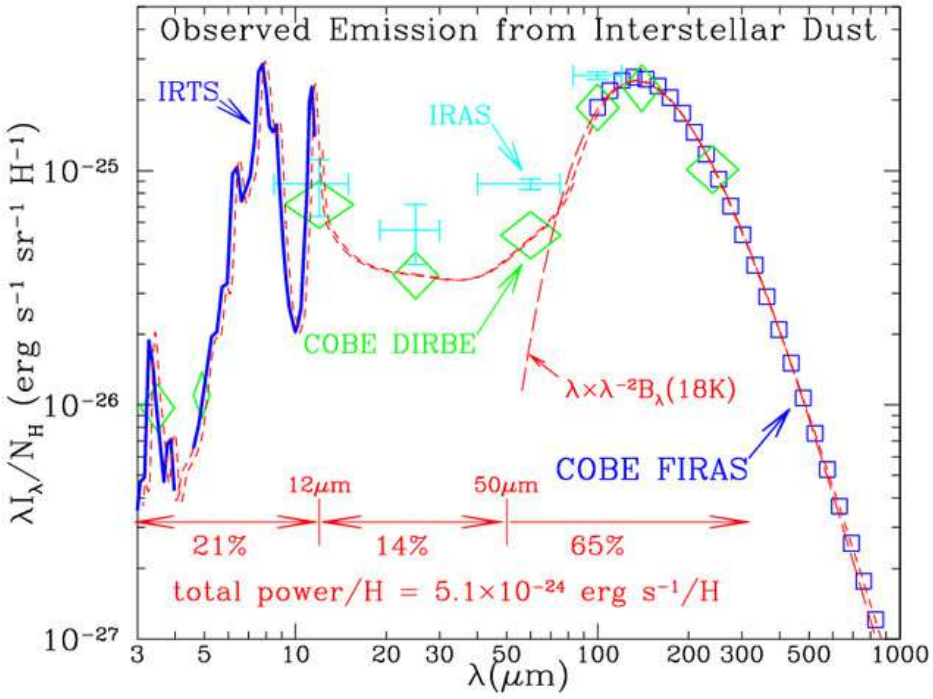

Figure 1.12: Average emission spectrum of the diffuse interstellar medium of the Milky Way, data obtained by the COBE, IRTS and IRAS satellite. The spectrum of the big grains is adjusted by a modified blackbody law, with β = 2 and T = 18 K. Figure taken from Draine (2003).

wavelength is 140 µm at a temperature of 18 K. Figure 1.12 represents the average emission spectrum of the diffuse interstellar medium of the Milky Way as measured by IRAS, IRTS and COBE satellites. As for extinction, this emission curve can be explained by the presence of at least three types of grains. Approximately 65% of the total grain emission is provided by the big grains. The emission below 50 µm is explained by the grains smaller than 15 nm and the PAHs are responsible for the emission observed between 3 and 12 µm. The emission between 12 and 50 µm would be linked to the UV bump and therefore to very small grains.

1.3.4 Polarized emission and extinction of galactic dust

At the end of the 1940s, the first observations of the polarization of the stellar radiation by the dust grains were carried out (Hiltner 1949, Hall 1949). A dependence between stellar reddening and polarized emission has been

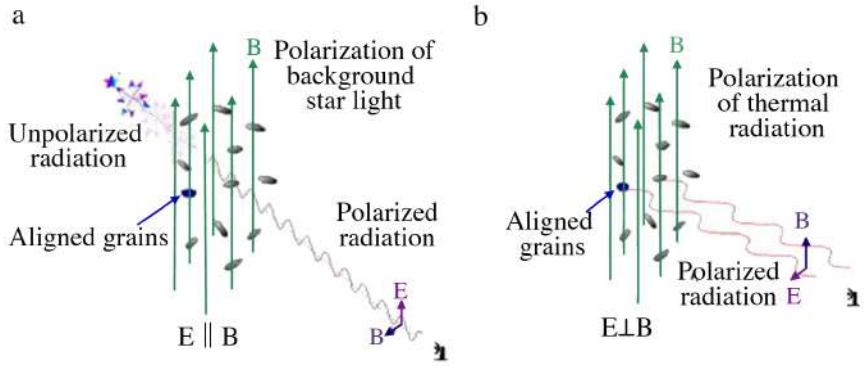

Figure 1.13: (a) Polarization of the background induced by dust extinction when the light passes through the aligned grains to the magnetic field lines. The direction of polarization is parallel to the direction of the magnetic field lines. (b) Polarization of light in emission. Figure from Lazarian (2007)

demonstrated. It as been deduced that the grains have an elongated shape and that they are aligned in a direction imposed by the Galactic magnetic field. Even extremely very weak, the Galactic magnetic field interacts with the interstellar medium and particularly with dust grains. Indeed, the minor axis of the grains tends to align parallel to the direction of the magnetic field lines B (see figure 1.13). The physical process behind this alignment remains open to debate. One of the explanations has been proposed by Davis and Greenstein (1951). It relies on paramagnetic dissipation of energy in rotating grains and spinning up by collisions with the gas to align grains with the magnetic field. Another explanation would be that a grain tends to tumble due to a systematic gas flow and aligns its spin axis orthogonal to the flow. This was suggested by Gold (1952).
The grains preferentially absorb the component of the incident electric field parallel to their major axis. Accordingly, the extinction polarization direction is parallel to the magnetic field lines. Similarly, since the emission is more intense along the major axis of the grains, the direction of emission polarization is orthogonal to the magnetic field lines.

Thus, the polarization maps observed allow us to study the geometry of the Galactic magnetic field projected on the plane of the sky and this despite a lack of information about the physics of the grains and of the alignment process.

The polarized emission of dust is also dependent on the wavelength. Few informations are available about the polarization in emission. Some studies

tend to show strong variations in polarization fraction with wavelength, with a minimal fraction around 350 µm (Vaillancourt et al. 2008). These variations, which were measured by different instruments on multiple objects, were however not confirmed by the Planck all-sky study. Planck observed only a slight decrease in the polarization fraction with an increase in the wavelength beyond 850 µm. The question of variations of the polarization fraction as a function of the wavelength is still subject to debate. The data provided by instruments measuring dust polarized emission at different wavelength will be crucial to answer this. This knowledge is in particular essential in the context of foreground separation and the design of future instruments.

1.4 Observations of polarized emission from dust

The first observation of the dust polarized emission at 850 μm (353 GHz) over a large fraction of the Galactic plane was made by the Archeops balloon mission (Benoit et al. 2004). These measurements indicated high polarization levels (up to 15%) in the diffuse ISM. In continuity with Archeops, the Planck satellite, launched in 2009, has produced the first all-sky map of the polarized emission from dust at sub-mm wavelenghts (Planck Collaboration. XI. et al. 2014). This survey was an immense step forward in sensitivity, coverage and statistics on the main polarization parameters. Planck provided new insight into the structure of the galactic magnetic field and dust properties. It also provided the first statistical characterization of the main foreground to CMB. I will try to summarize here some important results provided by the mission.

The link between the hydrogen column density (denoted N_H) and the polarization fraction p_l has been studied (Planck Collaboration Int. XX. et al. 2015). It shows that the maximum value of p_l is high (around 20%) and that it has been observed in regions with a moderate column density (less than $2 \cdot 10^{21} cm^{-2}$). In addition, a statistical analysis has shown that p is decreasing with N_H above $10^{21}\mathrm{cm}^{-2}$, and is anti-correlated with the angle dispersion function characterizing the spatial structure of the polarisation angle. The polarization angle is ordered over extended areas that are separated by structures where the sky polarisation changes abruptly. Comparison of this observation with magnetohydrodynamic simulations tends to attribute these scatter of p to fluctuations in the orientation of the magnetic field lines along the line of sight.

The study of the role of the magnetic field in the formation of interstellar medium structures has also been studied (Planck Collaboration Int. XXX et al. 2016). The Planck intensity map shows elongated structures (filaments or ridges) also visible on the polarization maps. These structures seem preferentially aligned with the magnetic field especially. Toward denser regions, the relative orientation changes progressively from parallel in areas with lowest hydrogen column density to perpendicular in areas with highest hydrogen column density. Simulations show that such a change could be related to the degree of magnetisation of the cloud, particularly when magnetic energy is in equipartition with turbulent energy (Hennebelle 2013, Soler et al. 2013, Chen et al. 2016).

As previously explained, polarized dust emission from the ISM represents the main foreground of CMB polarization measurements above 100 GHz. The polarized dust angular power spectra C_l^{BB} et C_l^{EE} were measured by Planck on all multipoles ℓ between 40 and 600 far away from the Galactic plane (Planck Collaboration Int. XXX et al. 2016). The polarization power spectra of the dust are well described by power laws in multipole, $C_l \propto l^\alpha$ with $\alpha = -2.42 \pm 0.02$ for both EE and BB spectra. The data has also shown that there is no region of the sky for which CMB B-mode polarization measurements can be made without having to previously remove the polarized dust emission.

1.5 PILOT scientific objectives

PILOT (for Polarized Instrument for the Long-wavelength Observation of the tenuous ISM) is an astrophysical experiment designed to measure the polarized emission of light by interstellar medium dust in the far infrared (FIR). The band used for observations with PILOT is centered around 240 µm. The experiment is designed to fly under a stratospheric balloon at an altitude of 40 km, in the stratosphere. This allows us to limit the absorption and the thermal noise produced by the atmosphere. The PILOT experiment is embarked under a stratospheric balloon, with a volume of approximately 800 000 m^3 to reach this altitude during flights. Figure 1.14 shows a view of the PILOT gondola under the Australian sky during the second campain in Alice Springs. The scientific objectives of the mission are multiple. One of the objectives is to use the polarized emission of the dust grains of the interstellar medium to map the direction and intensity of the magnetic field of our Galaxy. These measurements will also lead to a better understanding of the magnetic properties of the grains of the interstellar medium. The PILOT

Figure 1.14: PILOT Gondola under the Australian sky during the second campaign in Alice Springs.

measurements are complementary to those carried out by the Planck satellite. They are made at a wavelength closer to the maximum light emission of the interstellar dust. This allows us to obtain more flux. This also has the advantage of providing a better angular resolution for a given mirror size, the angular resolution of an instrument being proportional to the ratio of the observed wavelength to the mirror diameter ($\theta = 1.22 * \lambda/D$). The other major objective of the mission is to use dust-polarized emission measurements on diffuse regions of the sky with unprecedented sensitivity. PILOT will play a crucial role in the preparation of missions for measuring the polarization of the cosmic diffuse background to help in the characterisation of the foreground polarisation. The PILOT data will help us to constrain the variations of polarization fraction as a function of wavelength in the infrared range which is an important aspect of extrapolating dust polarization data obtained at high frequencies to CMB wavelengths.

Chapter 2

PILOT instrument

2.1 Description of the instrument

The PILOT instrument is described in details in Bernard et al. (2016). Here I only include a short description.

2.1.1 The gondola

The terrestrial atmosphere being opaque to the wavelengths observed by PILOT, it is necessary to get rid of this constraint. The experiment is thus carried in a gondola under a balloon with a volume of $800000m^3$ at an altitude of about 40 km (see figure 2.1). Mapping the sky can be accomplished by rotating the gondola around its azimuthal axis with constant or variable elevation. The elevation of the gondola can vary between 20^o and 60^o. The attitude of the instrument and its direction of pointing are reconstructed a posteriori using information provided by the stellar sensor ESTADIUS. Scan speed in azimuth is determined to be a compromise between two constraints. First, we need to map large fields and reduce instrumental drifts. Secondly, we need to distinguish source detections from parasitic signals and to respect the constraint imposed by response of the bolometers and the gondola. The balloon, the flight chain and the gondola (including thermal protection and stellar sensor) are developed by CNES. The total weight of the gondola is about 1100kg.

2.1.2 Optics

PILOT is a Gregorian-type telescope with an 800 mm diameter off-axis primary mirror (visible in figure 2.2). The angular resolution of the instrument is about 2 arcminutes is a compromise between the need to map large fields of

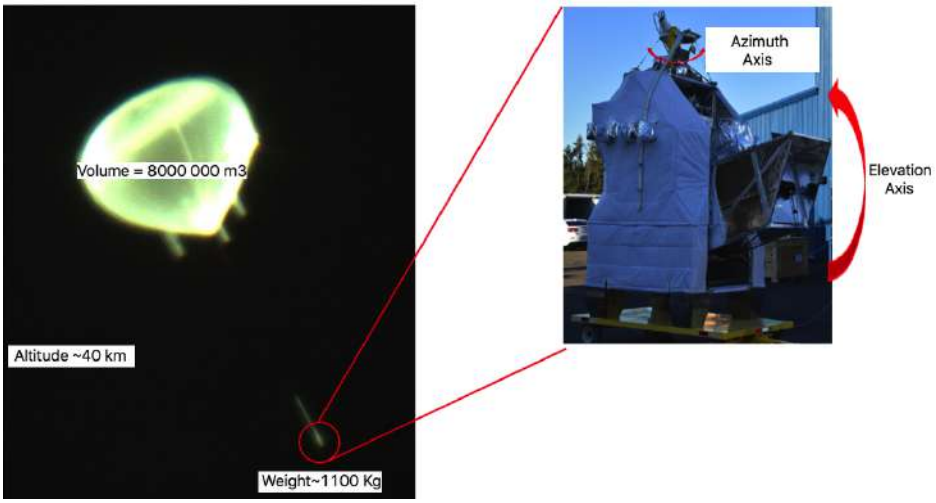

Figure 2.1: Views of the PILOT experience. Left: the stratospheric balloon in flight above Timmins in September 2015. Right: the gondola on the way to the tarmac.

the sky and the maximum size imposed by the weight limits of the gondola. The field of view of PILOT is 1^o x 0.76^o. The equivalent focal length is 1790 mm. The focal/diameter ratio of the instrument is f/2.6. The instrument is composed of an off-axis parabolic primary mirror (M1) and an ellipsoidal secondary mirror (M2) made of aluminum. Details of the characterization and performances of M1 are given in Engel (2012) and Engel et al. (2013).

The image of the sky is focused on the detector using two lenses acting like a telecentric lens. Telecentric lens allows to limit the effects of parallax in the image in perspective. A Lyot stop is placed between these two lenses. The polarization measurement is carried out using the rotation of a half-wave plate (HWP) placed near the Lyot stop and a polarizer placed in front of the detectors. The polarizer is inclined by 45^o in order to reflect a polarization component on one focal called the reflection, or REFLEX, focal plane and to transmit the other component on one focal plane called the transmission, or TRANS, focal plane. Only the mirror M1 is at room temperature. The rest of the optics is located inside the cryostat and is cooled to a temperature of about 2K. Figure 2.3 is schematic diagram of the PILOT optics located inside the cryostat.

Figure 2.2: A picture of the PILOT primary mirror M1 attached to its interface plate in the PILOT instrument structure. The mirror is made of Aluminum.

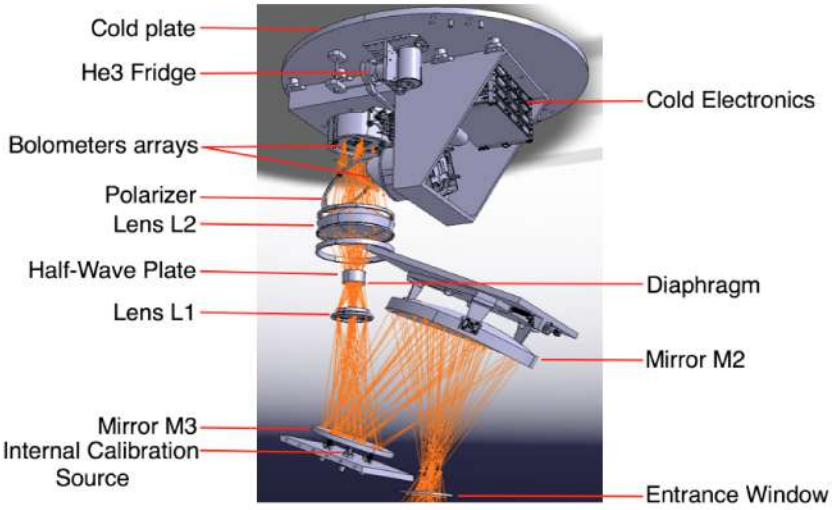

Figure 2.3: Schematic diagram of the PILOT optics

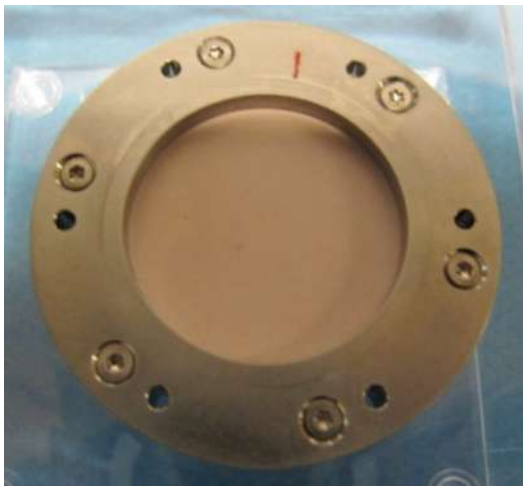

Figure 2.4: Picture of the Half-wave plate

2.1.3 The Half Wave Plate

The half-wave plate (HWP, see figure 2.4) is designed from a birefringent material that introduces a phase shift between the two orthogonal components of the incident radiation. The polarizer which is located between the half-wave plate and the detectors then separates the incident beam into two other linearly polarized beams enabling us to measure the polarization parameters when measurements from more than two different HWP angles are combined. PILOT observations are made at a fixed HWP position for a complete portion of the sky and then a rotation of the HWP is performed and the same portion of the sky is observed again.

2.1.4 Detectors

PILOT is equipped with bolometer arrays developed by CEA/LETI for the PACs instrument onboard the Herschel satellite (see figure 2.6). Their principle is to convert the energy incident on the detector into internal energy of the absorber that composes it. The increase in the temperature of the absorber modifies the electrical resistance of the bolometer. A voltage source and a load resistor connected in series with the bolometer are used to convert this resistance variation into a variation of the electrical potential (see figure 2.5) . The PILOT detectors are divided into 8 arrays of 16x16 active detectors. The readout is multiplexed in time so that 16 pixels are read by the same amplifier. The arrays are connected two by two to the same buffer responsible for the multiplexing and the amplification of the signal. The arrays

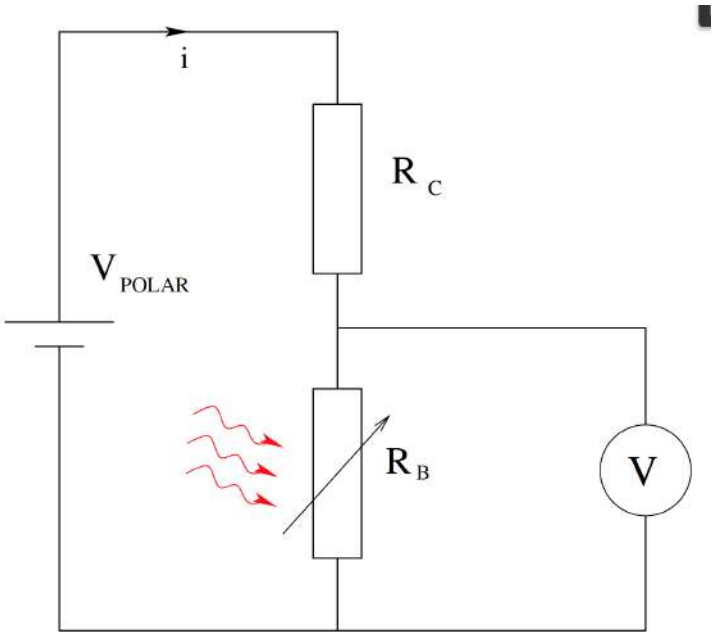

Figure 2.5: Electrical mounting, i.e. a voltage divider bridge, typically used to measure the signal across the thermistor. V_{polar} is the voltage source, R_C the load resistor and R_B the bolometer. Changes in the electric potential is measured across V. Figure from Billot (2007)

5 and 6 are therefore connected to the same buffer, as are the arrays 1-2, 3-4 and 7-8. The instrument is made up of 2048 active detectors in total. They are cooled to a temperature of 300mK. To achieve such a temperature, the detectors are placed in a cryostat fed by Helium 3. Originally intended to observe using two frequency bands at 240 and 550 µm, the entire focal plane has been configured to operate at 240µm on the two scientific flights of PILOT to optimize the observation time on this frequency band. To avoid holes in missing columns and to attenuate inter-pixel response variation effects, the focal plane arrays are oriented such that they scan the sky with an angle of 45^o between the edge of the array and the scan direction. Each bolometer is 750 microns wide, which corresponds to a size of 1.425 arcminutes on the sky. The Noise Equivalent Power (NEP) of each bolometer is a few $10^{-16}W/\sqrt{Hz}$, including noise from the readout electronics. The readout speed of this type of detector is much slower than for individual bolometers. The sampling frequency of the bolometers is 40 Hz. Details about the detectors can be found in Simoens et al. (2004).

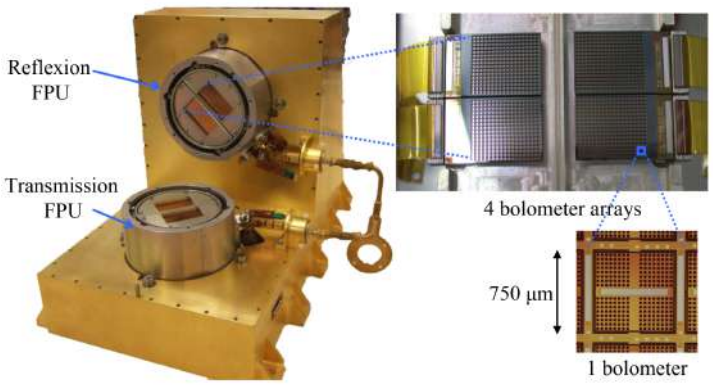

Figure 2.6: Image of the transmission and reflection focal plane units as implemented in the cryostat. The zooms show the details of ne focal plane and of one bolometer pixel.

2.1.5 The cryostat

All optical elements of PILOT, except the primary mirror, are placed in a cryostat in order to reduce the instrumental background radiation on the detectors. The cryostat consists of multiple thermal shields arranged on several layers. The different layers are cooled using helium 3 injected into the cryostat via the transfer tube. The helium is stored in a reservoir located in the upper part of the cryostat. The external shell and the thermal shields reach an equilibrium temperature of 300 K for the external part and then respectively 150 K, 80 K, 30 K and 3 K. The coldest parts of the cryostat are cooled to 4.2 K at atmospheric pressure on the ground and 2.3 K at ceiling altitude(at 40 km) when the pressure of the helium bath is lowered to 4 hPa through pumping towards the stratosphere. The detectors are cooled down to 0.3 K using a closed-cycle Helium 3 fridge mounted on the cold plate (Torre and Chanin (1985)). The incoming beam from the primary mirror of the telescope enters from the bottom of the cryostat. A schematic view of the cryostat is visible in figure 2.7. The cryostat was developed at La Sapienza University in Rome under the supervision of the IAS.

2.1.6 Filters

Entrance Window

The incoming beam from the primary mirror of the telescope enters the cryostat through a window which sustains the vacuum inside and a variable

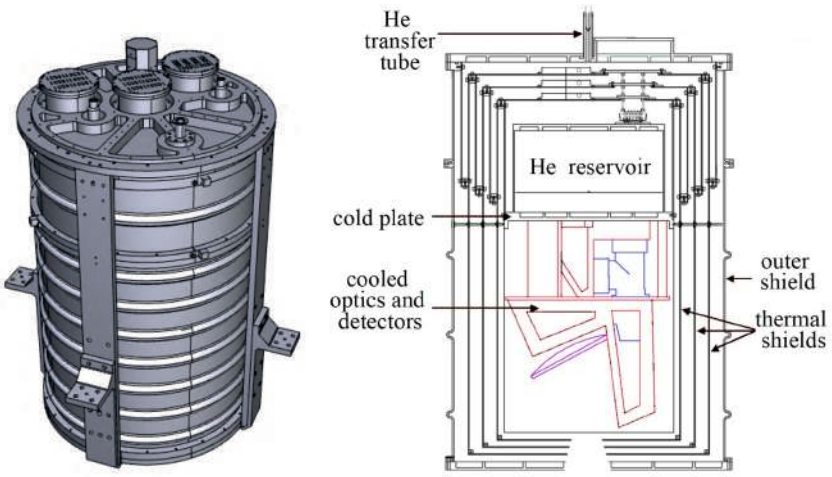

Figure 2.7: Left: Schematic view of the cryostat. Right: A cross section of the cryostat.The cryostat consists of multiple thermal shields arranged on several layers. The different layers are cooled using helium 3 injected into the cryostat via the transfer tube. The helium is stored in a reservoir located in the upper part of the cryostat. The detectors are cooled down to 0.3 K using a closed-cycle Helium 3 fridge mounted on the cold plate. The incoming beam from the primary mirror of the telescope enters from the bottom of the cryostat.

Table 2.1: PILOT Filter spreadsheet

Filter Name	Material	Temperature (K)	Reference	Thickness (mm)
Common Filters				
Flight Window	PP[1]	300		0.15-0.16
Ground Test Window	UHMWPE[2]	300		4
Therm 1	PP	300	C8-C12	5 mm ring section
Therm 2	PP	150	C8-C12	5 mm ring section
65 cm^{-1} LPE[3]	PP	80	W1360	0.32
Therm 3	PP	30	C12-C16	5 mm ring section
60 cm^{-1} LPE	PP	3	W1359+ARC[4]	0.47
80 cm^{-1} LPE	PP	3	W1337	0.25
HWP	Sapphire	3		8 mm ring section
Polarizer	Mylar	3	filter 1796	10 mm ring section
240 μm Band Filters				
36 cm^{-1} HPE[5]	PP	0.3	W1356, W1506[6]	0.21
48 cm^{-1} LPE	PP	0.3	W1336, W875[6]	0.32
58 cm^{-1} LPE	PP	0.3	W1375, W1371[6]	0.25
550 μm Band Filters				
15.2 cm^{-1} HPE	PP	0.3	W984	0.56
21.2 cm^{-1} LPE	PP	0.3	W1376	0.98
25 cm^{-1} LPE	PP	0.3	W892	0.65

[1] Polypropylene [2] Ultra High Molecular Weight Polyethylene [3] low pass edge (LPE) [4] 6 μm Low-density polyethylene anti reflective coating for both side [5] high pass edge (HPE) [6] for Array 3 and 4

pressure outside. The pressure outside the cryostat was 1024 hPa during ground tests conducted in 2014 and 2016 at the IAS (Institut d'Astrophysique Spatiale, Paris sud) and $\sim$ 4 hPa at 40 km altitude during flights. The entrance window is made of polypropylene. The choice of this material is due to its low emissivity and good transmission in the spectral bands of PILOT. A heating system can be mounted around it in order to avoid the formation of ice on the entrance window during ascent of the PILOT instrument. The details of the entrance window parameters are given in table 2.1

Thermal Filters

A set of thermal filters are mounted on the thermal shields just behind the entrance window, allowing to minimize thermal loading on the inner screens of the cryostat, and to minimize thermal loading on the detectors via re-radiation. The thermal and spectral filters are based on the metal mesh interference filter technology (Ade et al. 2006). Most of them are made of multi-layer metallic grids spaced by a dielectric layer. They are designed to

have a low emissivity. The dimensions and temperature of the filters are given in table 2.1

Spectral Filters

A set of low-pass (LPE) and high pass edge (HPE) filters are used to define the bandpasses of the two photometric PILOT channels. Some of the LPE filters are common to both the 240 µm and the 550 µm bands and are located before the HWP on the 3 K shield. The rest of the LPE and HPE filters are located between the polarizer and the detectors. The material, dimensions and temperature of the cut-off filters are given in Table 2.1. All filters were developed by Cardiff university, Great Britain.

2.1.7 Internal Calibration Source (ICS)

An internal calibration source (ICS), placed behind the mirror M3 (see figure 2.8), is used to allow an intercalibration of the bolometers in the most precise way possible to facilitate the reconstruction of the polarization measurements. The source used is the spare model of the SPIRE instrument on the Herschel satellite. The ICS was used during each scene to calibrate the detector response variations. The ICS is controlled in current with a square modulation and a maximum current of 2 mA. The voltage and current are measured continuously in order to trace the variations of the electric power dissipated in the source independently of the changes of its impedance related to the variations of temperatures. The ICS was developed by the University of Cardiff, Great Britain.

2.1.8 House-Keeping Electronics

A dedicated electronics (UGTI, for "Unité de gestion des données Techniques de l'Instrument") is used for a variety of house-keeping tasks. In particular, the UGTI monitors cryogenic temperatures in the range 2-77K inside the cryostat, and ambient temperatures for the rest of the instrument. The UGTI is also used to regulate the intensity of the current inside the ICS calibration source, to operate cryogenic valves that open and close the cryostat helium tank, and to operate heaters on the outer shell of the cryostat and in the helium tank.

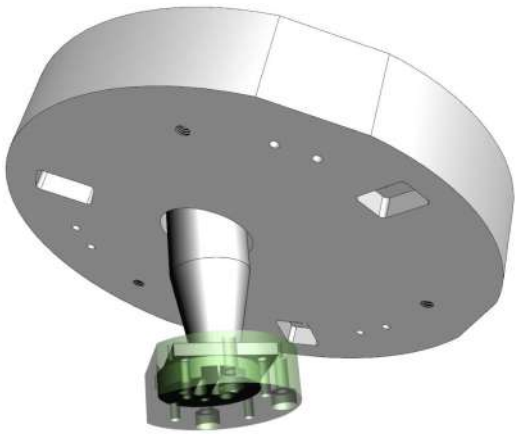

Figure 2.8: Schematic view of the PILOT Internal Calibration Source (ICS) as implemented behind the M3 flat miror. The ICS is the puck-shaped part in green. The conical portion is present for collimating the radiation from the ICS

2.1.9 Stellar Sensor

PILOT has a stellar sensor called Estadius developed by CNES. It is equipped with a gyroscopic optic fiber, a 16 megapixel CCD camera and a large aperture lens with a focal length of 135mm. The field of view of the stellar sensor is 10^ox15^o. The system provides accurate star position measurements due to the small angular size of each pixel, and is able to detect stars against a bright sky background. It allows us a reconstruction of the pointing in the order of 1 arcsec in translation and 6 arcsec in rotation at 1σ. Estadius demonstrates good autonomy through the use of automatic constellation recognition. A schematic view of Estadius is visible in figure 2.9. A complete description of the stellar sensor is presented in Montel (2015).

2.2 Polarization measurement with PILOT

The signal measured on the sky by the instrument is defined according to the Stokes parameters as follows:

$$m = \frac{1}{2}\left[R_{xy}T_{xy} \cdot [I \pm Q\cos(4\omega + 2\varphi) \pm U\sin(4\omega + 2\varphi)] + O_{xy}\right] \qquad (2.1)$$

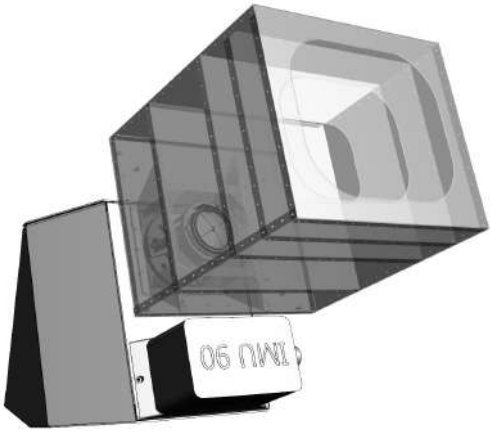

Figure 2.9: Schematic view of the Estadius stellar sensor. The cubic part is the stellar sensor baffle.

with I the total intensity, R_{xy} the detector response, T_{xy} is the optics transmission. The $\pm$ sign is positive $(+)$ for the TRANS arrays and negative $(-)$ for the REFLEX arrays. The additional term O_{xy} is to account for an arbitrary electrical or signal offset. ω and φ are respectively the Half-Wave plate angle and the parallactic angle defined as described in chapter 8. The calculations linking the Stokes parameters to the measurement carried out by PILOT are detailed in chapter 8.

The measurement of the polarization state is carried out using the half-wave plate and the fixed grid polarizer (see figure 2.10). They make it possible to modify the state of polarization of the incident beam and to separate it into two beams of orthogonal polarization state. In the context of PILOT observations, the half-wave plate remains in a fixed position during the same observation, in contrast to other systems where the HWP rotates continuously during an observation. Each observation must be carried out at minimum with two different HWP positions in order to optimally reconstruct the Stokes parameters I, Q, U allowing us to describe the polarization state of a wave (see chapter 8). When an object is observed with a certain position of the half wave plate, we call this observation a "scene". A scene can be subdivided into different sequences:

- SLEW: the slews correspond to the passage between the end of a scene and the start of the next scene. Slews are performed simultaneously in azimuth and elevation. HWP position changes occur at the end of the

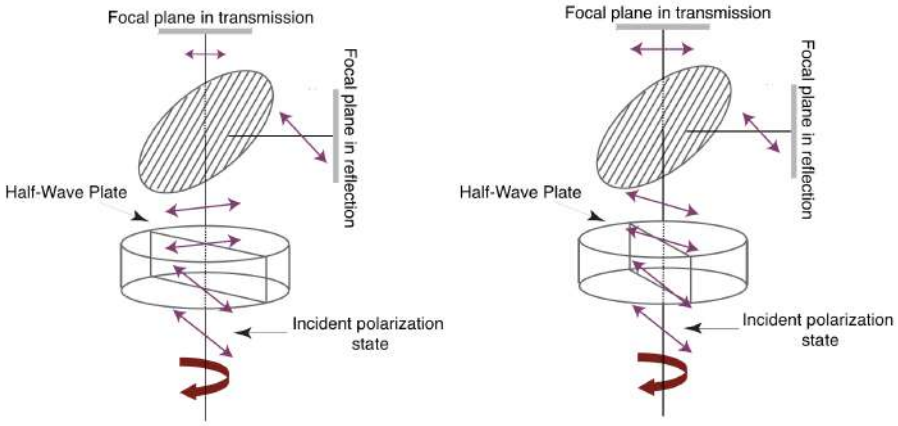

Figure 2.10: Schematic representation of the measuring principle of the PILOT instrument, based on the rotation of the Half-Wave Plate and the selection of two orthogonal states by the fixed grid polarizer. Figure adapted from Engel (2012)

slew sequence at the beginning of each scene

- SCAN: scans correspond to a sweep of a portion of a scene (at constant or variable elevation. see section 2.4.1.2 and 2.4.2.3).

- CALIB: these sequences correspond to the time when the internal calibration source is functioning. These sequences are performed between two scans.

- CHAZEL: This corresponds to relative displacements of the pointed load in azimuth and elevation. These are the transition movements from one scan to another.

Figure 2.11 show a shematic view of the decompoition of an observation with scans at constant elevation and calibration sequences at the end of each scans.

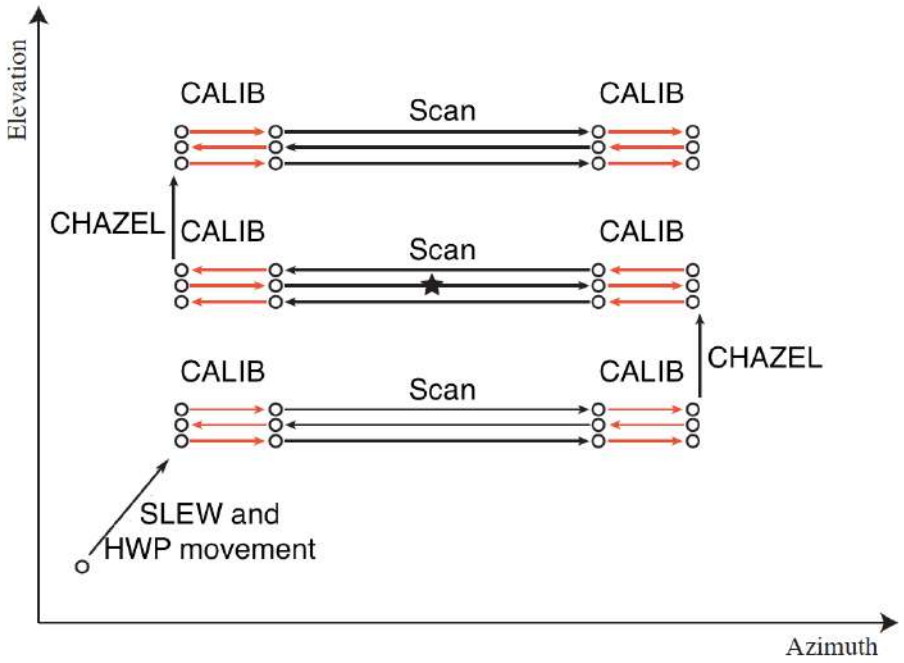

Figure 2.11: Schematic view of the decomposition of an observation sequence in individual gondola sequences. SLEW: passage between the end of a scene and the start of the next scene. SCAN: scans of a portion of a scene. CALIB: calibrations using the ICS. CHAZEL: relative displacements of the pointed load in azimuth and elevation.

2.3 PILOT data format

2.3.1 Pilot Instrument MOdel (PIMO)

We developped an instrumental model implemented in IDL initializing a global variable containing the PIMO (Pilot Instrument MOdel) information. The data in PIMO comes from both computer modeling of the instrument, ground calibration data and flight calibration data. This model contains information used to describe the instrument and how it affects astrophysical data. The instrument model contains, among others, the following information :

- Position in the focal plane of each detector relative to the focal plane center (the Focal Plane Geometry).
- Properties of each bolometers (electronic channel, time constants, response, cross-polarization coefficient, polarization rotation angle, normalized flat-field value...)
- Photometric Information : these informations allows us to compute the thermal emission of the instrument and how light propagates from any optical element to any other optical element in the instrument (filter transmissions, temperatures, solid angles).
- Offset of the Stellar Sensor with respect to the focal plane reference position.
- Payload caracteristics, such as slew and scan velocity profiles, payload trajectory.

The PIMO sofware generates an IDL structure which is defined as a global variable so that it can be used by any component of the scientific ground segment.

2.3.2 Data File Format

The data is saved in several ways. On board, they are saved on a flash storage memory in the RAW format to prevent data loss in case various telemetry problems appear.
On the ground the data are received by telemetry and are recorded in a RAW format. They are also saved in a FITS format which correspond to

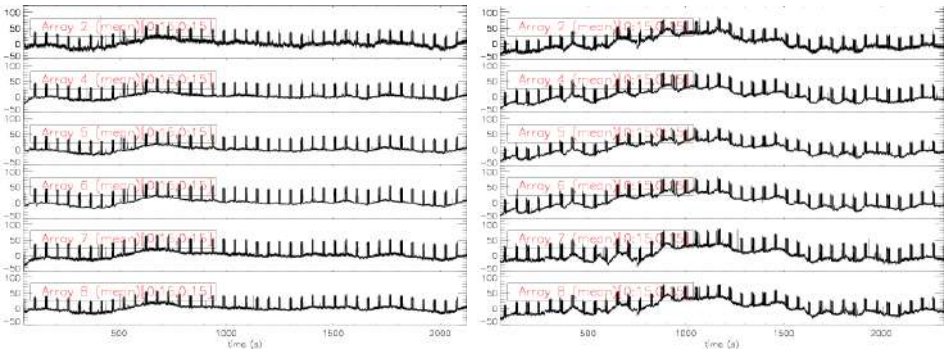

Figure 2.12: Exemple of array averaged timelines obtained on Orion during the first flight. Since matrices 1 and 3 are not functional, they have not been shown here. The top timeline corresponds to the average of the timelines of the pixels in array 2. From top to bottom we have the matrix 2 then 4, 5, 6, 7 and 8. Timelines are represented in ADU (analog digital unit) as a function of time. Left: Observation on orion during the night. Right: Observation on orion during the day. On both plots, the observed peaks of signal corresponds to the ICS calibration sequences. The signal variations common between arrays observed during the day are induced by the external straylight.

the raw file of the telemetry and on which different transfer functions have been applied. The FITS files can be easily accessed through a set of IDL subroutines which stores the requested data (scientific and house-keeping) in memory, allowing access to the data from any subroutine without data duplication.

As previously mentioned, the PILOT data is sampled at 40 Hz. These data are recorded under the form of timelines, also called TOIs (Time Ordered Information). For the data, we therefore have a file per bolometer array containing 16x16 TOIs. An exemple of TOI can be seen on figure 2.12. The observed peaks of signal corresponds to the ICS calibration sequences on which we shall return later in this section (see 2.4).

All the data provided by the HK electronics is stored in the same way as the individual data of the bolometers. This allows us to access different information such as the temperature of the primary mirror hexapods, the different temperatures inside the cryostat and the intensity values injected into the ICS

2.4 PILOT flights

The PILOT mission was the subject of two launches, one in the northern emisphere and the other in the southern emisphere. A third launch, in the northern emisphere again, is currently under preparation.
The first flight of the mission took place in Timmins on September 21, 2015. The balloon was launched from the city's airport. The launch was carried out as part of a launch campaign led by CNES and in collaboration with the Canadian Space Agency (CSA). This campaign allowed the launch of 4 experiments including PILOT.
The second flight was conducted from the southern hemisphere in the town of Alice Springs in the northern territories of Australia. This launch was also carried out as part of a launch campaign led by CNES, and enabled the launch of the CLIMAT, CARMEN and PILOT experiments. The launch from the southern hemisphere was the occasion to make observations of objects which are observable only from these latitudes. I will come back to these observations later in this section.
In this section I will discuss in detail the characteristics of each flight, in particular the trajectories followed by the balloons, the observations that have been made and the scanning strategy used. I would also present the solutions implemented for the second flight to the dysfunctions observed during the tests on the ground and on Flight#1

2.4.1 First Flight

2.4.1.1 Flight and trajectory

The balloon trajectory is measured in real time using a using multiple GPS systems. One of them is embedded in the flight chain, and another is located in the instrument. The data used to plot the figure 2.13 comes from the GPS system located in the instrument. It took 2.5 hours for the balloon to reach an altitude of 38 km. The altitude of the balloon remained relatively stable, varying between 38 and 39 km for more than 18 hours. The total duration of the flight was 24 hours allowing to obtain about 15 hours of scientific data. Approximately 4 hours were used for the configuration of the detectors, the cycling of the fridge and the slew between each scenes.

2.4.1.2 Flight plan and scanning strategy

The scanning strategy defined for this first flight was to scan the sky at constant elevation with several HWP positions and then to return later to

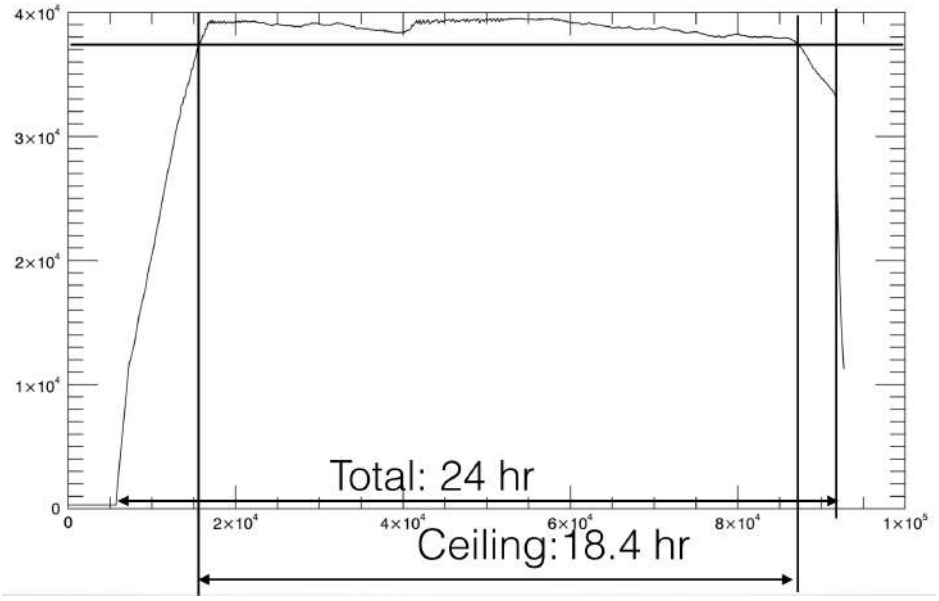

Figure 2.13: Variations in altitude of the experiment during Flight#1

that same source again using HWP positions optimized to make coverage homogeneous. The sequences of observations were defined by parameters such as scanning amplitude, number of scans, scanning speed, magnitude of elevation change steps, half-wave plate position, frequency and duration of the calibration sequences. These parameters have been set in order to guarantee a sufficient signal-to-noise ratio for each source.

The flight plan was built using mission-specific software that takes into account various observational constraints such as source visibility, minimum angular distance from the sun, and elevation limits due to the presence of the Earth on one side and the balloon on the other. The expected performance of the instrument were also taken into account when establishing the flight plan, including the need to observe the same source at different angles of the half-wave plate and a sufficient number of observations with a different scan angle to allow efficient suppression of the 1/f noise and a good reconstruction of the polarization (see chapter 8).

Estimates of sensitivities were calculated as described in Bernard et al. (2016). Some parameters needed in the sensitivity calculations could not be determined during the ground calibration. These include the absolute value of the instrument's transmission, reliable prediction of the background intensity falling on the detectors which itself determines the response values.

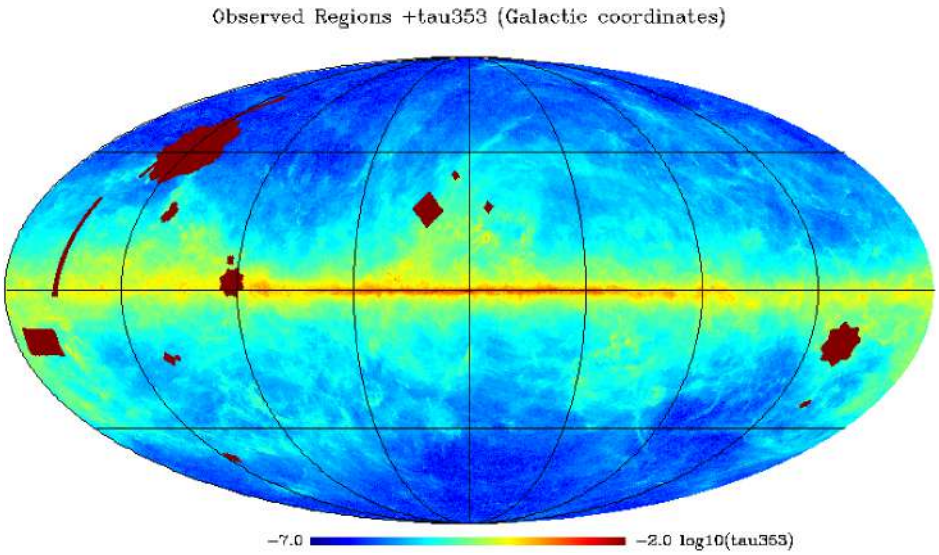

Figure 2.14: Map of all sky τ_{353GHz} from Planck data derived from a modified black body fit of Planck and IRAS at 100µm extracted from Planck Collaboration. XI. et al. (2014). Regions observed by PILOT during flight#1 are overlaid in red.

These parameters can however be measured during the flight.

2.4.1.3 Observations

The observations made during the flight in Timmins are summarized in table 2.2. We collected 5.5 h of observation on star forming regions and 1.4 h on the Andromeda galaxy (M31). 4.6 hours of observations were made on the deep fields, that is on zones farther from the stronger foreground contaminated zones such as the "cosmo field". We also observed for 2.4 h dense and compact region of interstellar clouds where the dust temperature is measured to be around 14K or below. These regions are referred to as "cold cores". These dense cores are interesting because they can eventually collapse under gravity. They represent early stages of the star formation process before or at the beginning of the collapse phase. The regions that were covered during the flight can be also seen in figure 2.14.

2.4.1.4 Dysfunctioning arrays

Figure 2.15 show a map of the bad pixels as determined from flight data. Matrices 1 and 3 did not work during Flight#1 as during most of the ground

Table 2.2: Observations made on Flight#1

Sources	Number of scenes	Observation Time [mn]	Map size [deg x deg]	Scene depth [Degˆ2/h]	Total depth [Degˆ2/h]
Taurus	6	117	12 x 8	331	57
Orion	4	145.3	10 x 10	191	47.8
Aquila Rift	2	46	8 x 8	188	94
Cygnus OB7	2	21	7 x 7	333	166.5
L1642	4	44	2 x 2	38	9.5
G93	6	61	2 x 2	38	6.3
L183	4	41	2 x 2	38	9.5
M31	8	84	3 x 3	49	6.1
Polaris	10	160	5 x 5	123	12.3
Cosmo field	3.5	116	16 x 16	562	160
Uranus	3	31	3 x 2	57	19
Saturn	2	12	2 x 2	68	34
SkyDip	2	10			

tests. Array 5, which showed intermittent behaviour during ground tests was fully functional during the flight. As a consequence, the whole flight was performed with 6 operational arrays out of 8. For operational arrays, the figure shows the location of pixels with anomalies, as flagged through inspection of flight data. The fraction of operational pixels over the six functional arrays was 83%. The pixels at the edge of the dies (in orange in the figure) are indicated as bad pixels because they show anomalies on the polarization measurement. (see chapter 6)

2.4.1.5 External straylight

After inspection of the instrument at the end of the flight, it appeared that the baffle of the instrument had deteriorated during the day part of the flight (see 2.16). This was confirmed by the viewing of the video recorded during the flight using a camera placed on the gondola. This degradation was caused by a defect in the thermal insulation of the baffle which caused it to overheat. This caused the baffle to open which produced additional straylight which impacted about 14% of the scientific data, mostly those taken when pointing close to the sun. A large fraction of this signal can be removed as a common mode through data analysis and map-making but this signal is likely te be polarized. On Figure 2.12, we can directly observe the effects of baffle degradation by comparing night (on the left) and day (on the right) data on Orion observations.

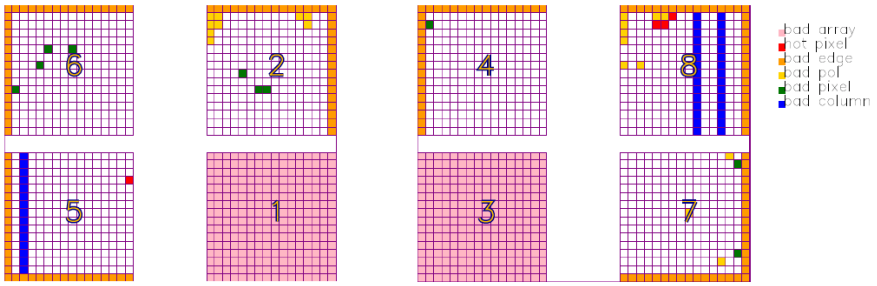

Figure 2.15: map of the bad pixels as determined from flight data. Six out of eight arrays (arrays 2, 4, 5, 6, 7, and 8) were fully functional and operated appropriately: The figure shows the location of pixels with anomalies: bad isolated pixels (green), bad columns (in blue), hot pixels (red) bad edges (orange), bad arrays (pink). The rate of working pixels is 83% on the six arrays

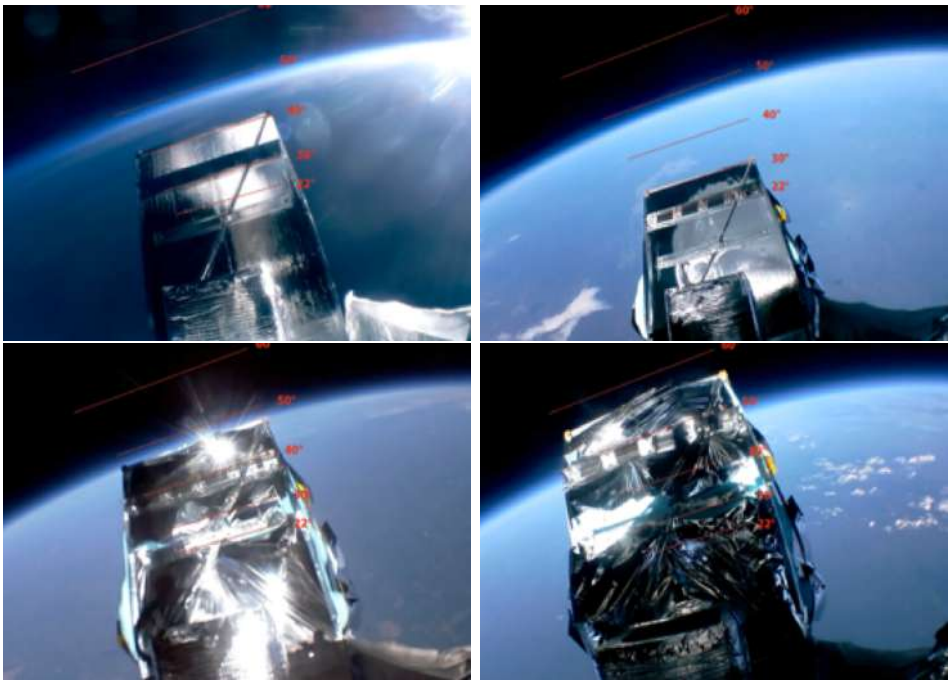

Figure 2.16: Degradation of the baffle from the begining of the day (top left) to the end of the day (bottom right) during Flight#1

2.4.2 Second Flight

The second flight was conducted from the southern hemisphere in the town of Alice Springs in the northern territories of Australia. This launch was also carried out as part of a launch campaign led by CNES, and enabled the launch of the CLIMAT, CARMEN and PILOT experiments. The launch from the southern hemisphere was the occasion to make observations of objects which are observable only from these latitudes. I will come back to these observations later in this section.

2.4.2.1 Improvements for Flight#2

Between the first and second flights, improvements have been made to the instrument:

- A repair attempt was performed on the arrays 1 and 3. As a result, only arrays 1 and 5 were dysfunctional during ground tests. However, during the second flight, the array 3 has become inoperative again. We therefore only worked with arrays 2,4,6,7 and 8. The origin of these disconnections is under investigation for flight 3
- Autonomy tests were carried out with a bolometer temperature of 300 mK (i.e. 20 mK below the temperature reached during Flight#1). These tests were conclusive, the autonomy of the cryostat having been established at 33.5h.
- The size of the field stop has been increased to avoid edge effects on the polarization (see chapter 6)
- Baffle insulation has been modified. No deterioration was observed during Flight#2 and the data did not appear to be impacted by straylight.
- The scanning strategy has been changed (see section 2.4.2.3)
- The flight time has been extended by about 60% in particular thanks to a better autonomy of the cryostat.

2.4.2.2 Flight and trajectory

The flight lasted approximately 33 hours during which 24 hours of observations were obtained. The launch took place at about 6:30 AM from Alice

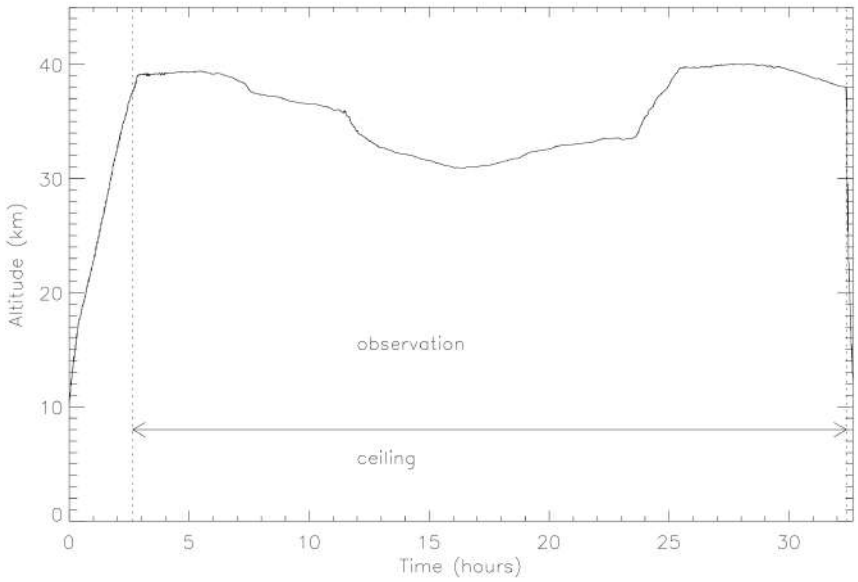

Figure 2.17: Variations in altitude of the experiment during Flight#2

Springs Airport. Balloon altitude changes throughout Flight#2 are visible in the figure 2.17. The balloon reached its ceiling altitude after about 2 hours. As the second flight was longer than the first flight, there was a day-night transition and a night-day transition during the flight. During the day-night transition, the temperature decreases, the gas in the balloon cools down and thus the altitude of the balloon decreases. The instrument descended to an altitude of 31 km during the night. A higher altitude could not be maintained by getting rid of all the ballast since it had to be preserved for the end of mission.

2.4.2.3 Flight plan and Scanning strategy

An improved version of the software used for the first flight was used to develop the flight plan followed during this mission. The main difference resides in the scan strategy used during the flight. Indeed, contrary to flight one, the scans were not carried out at constant elevation but with variable elevation for the majority of the sources observed. This new strategy has two main benefits:

- It makes it possible to determine throughout a scene the variations of response which can be measured on the residual atmosphere signal.

Table 2.3: Observations made on Flight#2

Sources	Number of scenes	Observation Time [mn]	Map size [deg x deg]	Scene depth [Degˆ2/h]	Total depth [Degˆ2/h]
L30	8	72	5 x 5	187	21
L0	4	32	2 x 5	75	18.8
LMCridge	16	134.4	3.5 x 1	15.7	1.6
LMCridgeBIG	19	232.5	4.0 x 2	39.2	2.0
Orion	6	140.8	5 x 10	127.8	21.3
BICEP	14	290.1	30 x 12	253.1	74.5
Rho-oph	11	268.8	9 x 4	88.4	8.0
Musca	14	185.6	2 x 3	27.0	1.9
Jupiter	5	27.7	3 x 2	65.0	13.0
Saturn	3	23.5	5 x 3.4	130.2	43.0
Skydip	8	21.3	1 x 32		

This makes it possible to reduce the time spent on the calibration of the detectors

- By scanning at variable angles with respect to the horizon, it is possible to obtain different scan directions on the sky without having to wait for the sky to rotate. The data was acquired in order to obtain sufficient redundancy of the signal on the detectors. The previous scan strategy (scan performed at constant elevation) presented the risk of observing a source at the beginning of the flight and not being able to re-observe it later with a different scan angle, preventing optimal data reconstruction.

2.4.2.4 Observations

The observations made during the flight in Alice Springs are summarized in table 2.3. Orion is the only object of Flight#1 to have been re-observed during Flight#2. A large integration time has been allocated to the large Magellanic cloud (LMC) which is only observable from the southern hemisphere. Measurements have been made in the BICEP2 field to help characterize the spectral energy distribution of dust polarization in a faint region of the sky where measurments at other wavelength are available. The regions that were covered during the flight can be also seen in the figure 2.18.

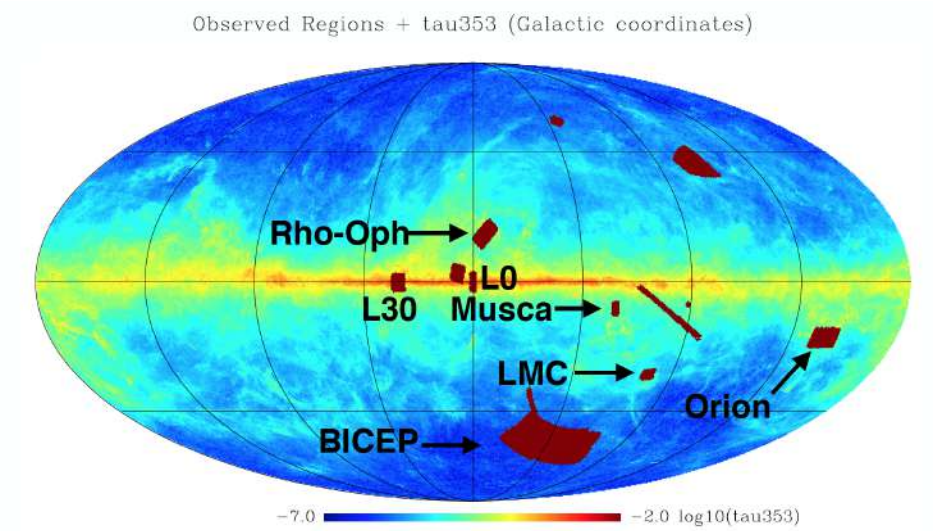

Figure 2.18: Map of all sky τ_{353GHz} from Planck data derived from a modified black body fit of Planck and IRAS at 100µm extracted from Planck Collaboration. XI. et al. (2014). Regions observed by PILOT during flight#2 are overlaid in red.

Part II

Inflight performances PILOT

Chapter 3

Time constants

The latency time, or response time, of a system is the time offset between a command and the execution thereof. This phenomenon is inherent in any system, be it mechanical, electronic or thermal and depends on its physical properties. The bolometers that equip PILOT have their own response time which it is important to constrain in order to reconstruct the observed data correctly. In this work, when we talk about time constant, we actually refer to the thermal time constant of the detectors. This time constant is related to two parameters:

- The thermal conductance $G = \frac{P}{\Delta T}$ $(W.K^{-1})$. It's the thermal link between the absorber and the bolometer thermostat (see figure 3.1).
- The heat capacity of the thermometer C $(J.K^{-1})$

Using the energy conservation, we can write:

$$C\frac{d\Delta T}{dt} + G\Delta T = Q \tag{3.1}$$

where $\Delta T = T - T_0$, and Q is the heat flow. For a constant Q, a constant temperature $\Delta T = \frac{Q}{G}$ is reached so that $\frac{d\Delta T}{dt} = 0$. If the power flow is stopped after some time, we can write:

$$\Delta T = \frac{Q}{G}e^{-\frac{t}{\tau}} \tag{3.2}$$

where $\tau = \frac{C}{G}$ is the thermal time constant of a detector.

In order to measure it we have to submit the detectors to a sudden variation of illumination to measure the time necessary for them to attain their

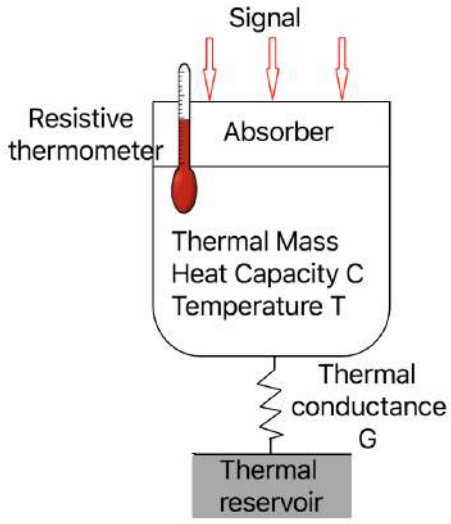

Figure 3.1: Conceptual schematic of a bolometer. Power, P, from an incident signal is absorbed by the bolometer and heats up a thermal mass with heat capacity C, and temperature T. The thermal mass is connected to a reservoir of constant temperature through a link with thermal conductance G. The temperature increase is $\Delta T = P/G$. The change in temperature is read out with a resistive thermometer. The intrinsic thermal time constant is $\tau = C/G$. Image credit: D.F. Santavicca.

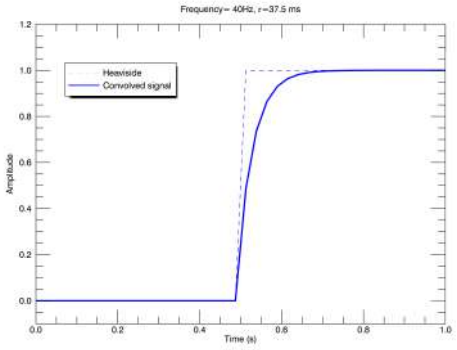

Figure 3.2: Simulation of a Heaviside function sampled at 40 Hz convolved with a function of the form $\exp(-t/\tau)$ with τ= 37.5ms

new state of equilibrium. As shown in figure 3.2 the behavior of a bolometer following this stimulation can then be modeled by the convolution of a Heaviside step function and an exponential function of the form $\exp(-t/\tau)$ where $\tau = 37.5ms$ is the time constant.

By a succession of ignition and extinction of the ICS we should therefore be able to adjust an exponential function on the signal observed by our bolometer and thus derive the time constant of our detectors. In order to determine these time constants, we have relied on the tests carried out during two ground tests in 2014 and 2016 at the IAS, as well as on the calibration measurements made during the acquisition of the data during the flights in Timmins and Alice Springs in 2015 and 2017. However, the measurement of time constants is disturbed by different effects such as the ICS time constant or data-reading time delay that I present in the following sections. It is important to consider these effects in order to obtain the best possible estimate of the detector's time constants.

3.1 Data-reading time delay

The detectors are organized in 8 arrays of 16 by 16 pixels. For each array, the reading is performed simultaneously for all the pixels of the same line. A first line is then read by the electronics, then a second line and so on until the 16th line. However, the data are assigned the same time by the readout electronics while, in reality, a sample has elapsed between reading the first and the last lines. As a consequence, each line of pixels is read with an offset of one-sixteenth of the samples with respect to the line which precedes it. It

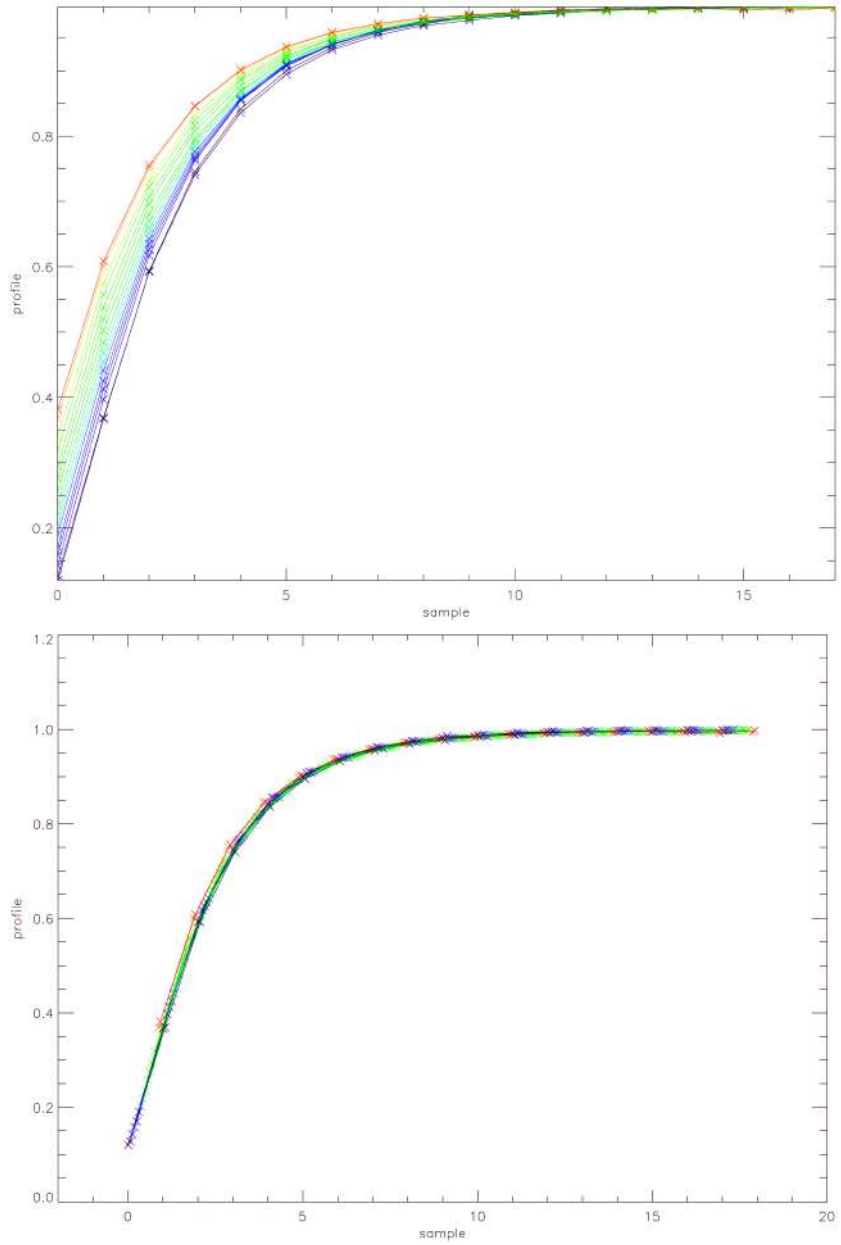

Figure 3.3: Average profile of 16 pixels in a line for array 4. Each profile in the plot correspond to a line of pixels in the array. Top: Not corrected from time delay. Bottom: Corrected for the data-reading time delay using the first pixel line as a reference.

is therefore necessary to take this shift into account in the calculation of the time constants since it can induce an error of the order of a sample in their determination. The top panel of figure 3.3 shows the ICS climbs averaged over the 16 pixels of each row for the array 4. Each of the different colored ascents represents a row of the array. On the bottom panel, we see the effect of a correction of this offset by an offset of 1/16 samples on each of these ascent. We see very clearly the time offset in the reading of each line of pixels. Figure 3.4 shows the distribution in the focal plane of the order in which the pixel lines are read. The four arrays shown on the left (resp. right) belong to the TRANS (resp. REFLEX) focal planes, such that arrays 6 and 4 (or 2 and 8) are optical conjugates. In this representation, elevation increases towards the top-left and cross-elevation increases towards the top-right corner of each focal plane. The same convention and array numbering is used for all figures of this manuscript. The values are shown in sample number. The pixel line for which the value is zero is the reference line used for timing the data and was set by checking how data are stored in telemetry packets. The timing accuracy is of the order of a few picoseconds. This offset is important as it must be used to correct time before computing pointing on the sky of each detector from the stellar sensor information (see chapter 4). As PILOT is scanning the sky up to $1^o/sec$, this offset can produce pointing differences as large as 1.5 arcmin.

3.2 Time constant of the ICS

As outlined in section 2.1.7, PILOT is equipped with the spare model of PCAL internal calibration source. This calibration source does not allow a clear transition between extinction and ignition because it has its own response time. In the case of ICS decays, the measure of the time constant that we perform here is the convolution product of the ICS and bolometer transfer functions (which we will designate by f_{bolo} and f_{ics} , respectively, hereafter). Both functions being of the form $\exp -\frac{t}{\tau}$ with τ the time constant of the considered system. The convolution of the two functionsf_{bolo} and f_{ics} is written:

$$(f_{bolo} * f_{ics})(x) = \int_{-\infty}^{+\infty} f_{bolo}(x-t) f_{ics}(t) dt = \int_{-\infty}^{+\infty} f_{bolo}(t) f_{ics}(x-t) dt \quad (3.3)$$

This formula is a generalization of the idea of moving average. If the two functions f_{bolo} and f_{ics} are integrable, then the Fourier transform of the convolution product is obtained by multiplying the Fourier transforms of the two functions:

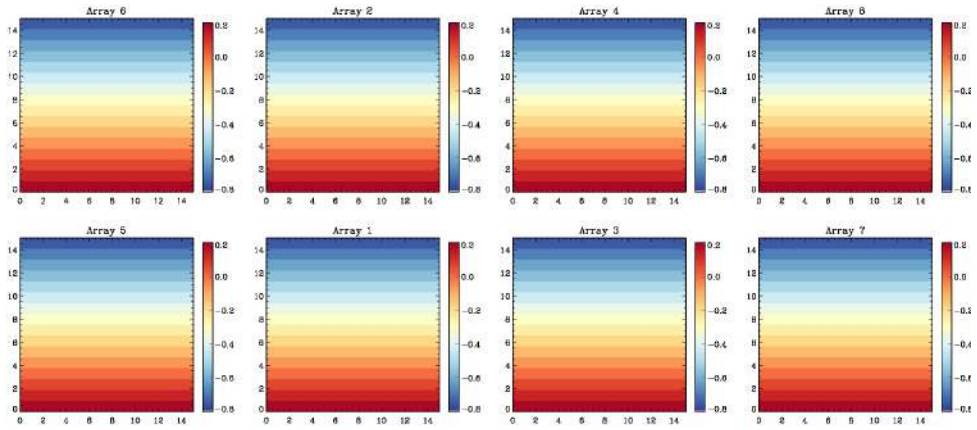

Figure 3.4: Value of the observed reading offset of the full focal plane.The four arrays shown on the left (resp. right) belong to the TRANS (resp. REFLEX) focal planes, such that arrays 6 and 4 (or 2 and 8) are optical conjugates. In this representation, elevation increases towards the top-left and cross-elevation increases towards the top-right corner of each focal plane. The same convention and array numbering is used for all figures of the thesis.

$$F(f_{bolo} * f_{ics}) = F(f_{bolo})F(f_{ics}) \tag{3.4}$$

Knowing the values of the time constants of the ICS, we can remove its effects on the data. The deconvolution of the signal is performed in the frequency domain using the Fast Fourier Transform (FFT). The signal of the bolometers (f_{bolo}) is the inverse FFT (noted F^{-1}) of the ratio of the Fourier transform of the data (f_{data}) and of the ICS transfer function (f_{ics}):

$$f_{bolo} = F^{-1}\left(\frac{F(f_{data})}{F(f_{ics})}\right). \tag{3.5}$$

However, we must be careful when deconvolving two functions via the Fourier transform because a problem may arise if the spectrum of the kernel has zero or small values.

A first estimate of ICS time constant is provided by Hargrave et al. (2003) for a source similar to that embedded on PILOT. In figure 3.5 it can be seen that the downward time constants of the ICS are significantly shorter (right figure) than for the upward time constants (Left figure). It is therefore important to take this into account when deconvolving the ICS time constant measurement signal. As a consequence, the case of the upward and downward time constants must be treated separately in order to deconvolve the signal.

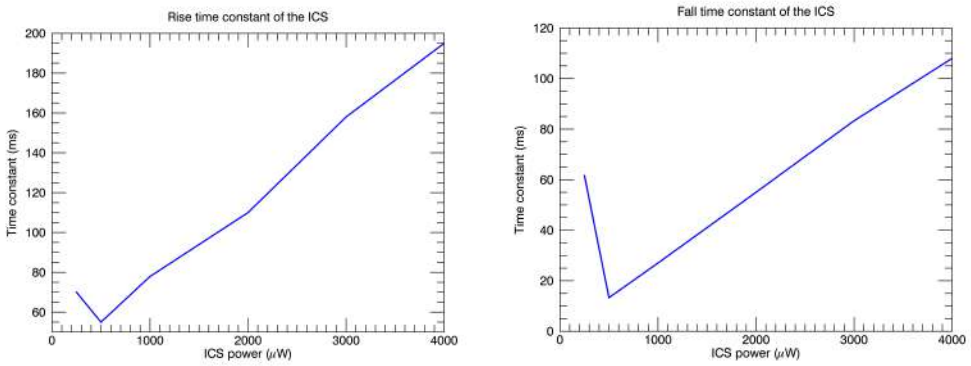

Figure 3.5: Left: Upward time constant of the PILOT ICS as a function of the power dissipated in the ICS. Right: Downward time constant of the ICS as a function of the power dissipated in the ICS. Extracted from Hargrave et al. (2003).

3.3 ICS ground tests

A preliminary estimate of the time constants of the bolometers has been obtained using the data taken during the PILOT photometric tests which took place at IAS in 2014. A complete description of the end-to-end and photometric tests performed on PILOT is available in Misawa et al. (2016). The data shown in this section were obtained with an Ecossorb plate placed in front of the cryostat window in order to have a 300 K background on all the detectors. Table 3.1 shows the upward array averaged time constants obtained during these tests before and after deconvolution of the ICS time constant taken from figure 3.5. The values given here are in sample number and must be multiplied by the sampling frequency to obtain values in seconds. We can see that the effect of the time constant of the ICS is important on the determination of the time constant of the bolometers passing from an average total time constant of more than 2 samples to a bolometer time constant of about 1.5 samples for the array 2. We can also see that arrays 5 and 6 are much slower than the other arrays with expected time constants between 2.5 and 3 samples. This behavior is not explained to date and is still under study. Overall, we will see throughout this manuscript that the array 6 shows a different behavior from the other arrays. It acts as if the TRANS focal plane was colder. However, if these observations were due to the temperature of the focal plane, we would observe a similar behavior for the array 2. The two arrays being located on the focal plane in transmission,

Arrays	1	2	3	4	5	6	7	8	Trans	Reflex
Time constant before correction	-	2.32	-	2.46	3.17	3.87	2.27	2.47	3.12	2.40
Time constant after correction	-	1.52	-	1.71	2.41	3.06	1.43	1.61	2.33	1.58

Table 3.1: Array-averaged values of the time constants obtained during the IAS tests before and after correcting timelines for the ICS time constants and reading time delay. Values are in sample number. Arrays 1 and 3 were not operationals during these tests.

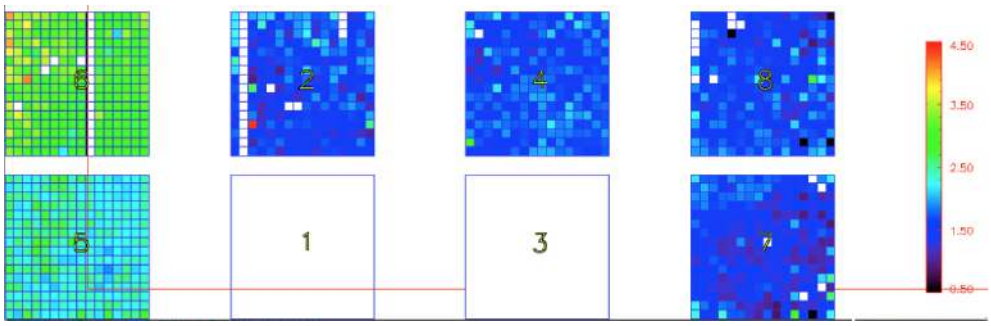

Figure 3.6: Image of the bolometers time constant obtained during IAS tests after correcting timelines for the ICS time constants and data-reading time delay. Values are in sample number. Arrays 1 and 3 were not operational during these tests.

the latter is therefore slower than the focal plane in reflection. The values of the time constants obtained for each pixel are shown in figure 3.6.

3.4 Glitches in-flight measurments.

The determination of time constants is possible using a method that does not require the use of the ICS. Indeed, when a charged particle interacts with the detectors, this causes a fast variation of signal. This is called a glitch. Following the fast energy deposition and the related increase in temperature, the bolometer relaxes to its equilibrium temperature with a certain time constant, which is in principle the same as for fast variations of the luminous signal. Following the detection of a glitch, we therefore observe an exponential decay of the signal. When the energy of the particle is released within the detector, the temperature of the pixel then relaxes in a characteristic time τ

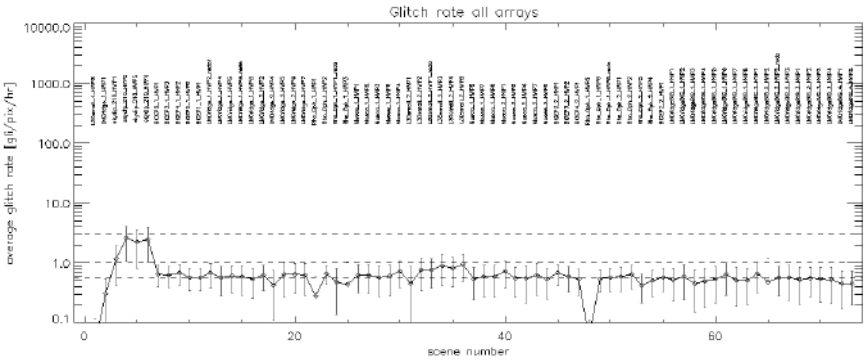

Figure 3.7: Evolution of the glitches rate averaged over the whole focal plane during Flight#2, for positive glitches intensity > 150 ADU. Error bars show uncertainties assuming Poissonian distribution.

which is actually the time constant of the detector. A study of glitches was conducted by Alexandra Lacourt during an internship in the summer of 2016 and 2017.

3.4.1 Glitches detection method.

In order to detect the glitches, we used a method based on a local estimation of the noise on the timelines by defining a sliding window on the timelines. Prior to detection, all timelines were flattened by removing the atmospheric correlation, flattening the ICS sequences with a mask, and flattening the signal from the strong sources by subtracting an average timeline from the observed signal derived from an intensity map of the instrument. Figure 3.7 shows the evolution of the glitch-rate averaged over the whole focal plane during Flight#2, for positive glitches intensity > 150 ADU. The average glitch-rate over all arrays above 150 ADU is 0.68 gli/pix/hr. Scenes with fake glitches (like sources detected as glitches) are identified by computing for each scene the fraction of glitches whith an intensity lower than 30% of the intensity measured in the data. Scenes where this fraction is below 60% are removed from the analysis. This scene selection removes most scenes at the very beginning of the flight, a well as scenes on bright objects where fake glitches are common, due to the presence of bright sources (SATURN, JUPITER, L0 and Orion).

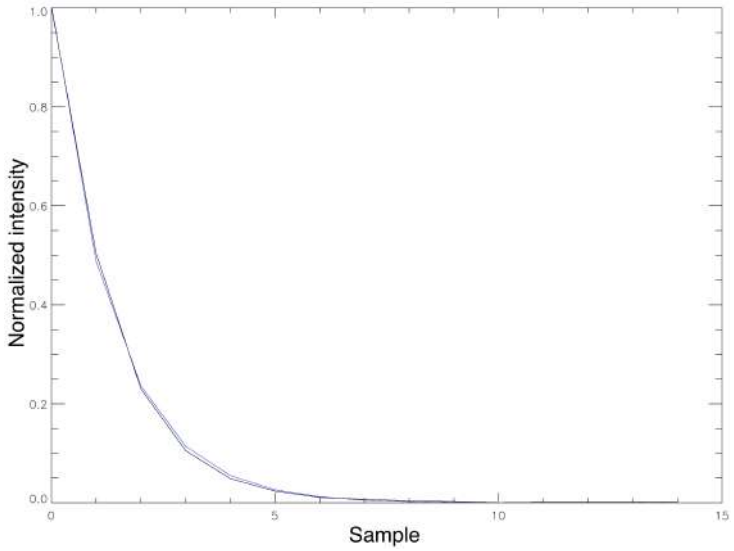

Figure 3.8: Black curve: Profile measured by averaging the measured values of 15 samples after detection of a glitch. Blue curve: fitted profile with the time constant as a free parameter.

3.4.2 Time constant measurement.

We measure the time constant using glitches, which we designate τ_{gli}, for each bolometer by averaging the measurements performed on 15 samples following the glitch detection. Only glitches with an amplitude greater than 200 ADU have been selected for this analysis due to noise fluctuations. An example of a measured profile is shown in figure 3.8. The profile shown here is obtained by averaging measurements on the glitch for all the detectors of the array 6 during an observation in the BICEP zone. The black curve is the measured curve and the blue curve is the fitted exponential curve having as parameter the time constant.

The time constant values obtained for Flight#2 over the whole focal plane are shown in figure 3.9. As we can see in table 3.2 the time constants are arround 0.7 ± 0.13 sample (17.5 ± 3.25 ms). The values measured on the array 6 remain higher than for the other arrays and are of the order of 1.5 samples. In theory this measurement allows us to directly access the measurement of the time constant of the bolometers compared to the ICS measurment which are affected by the ICS time constant. However uncertainty of calculation on the time constant remains important because of the low statistics of glitches. In addition, the detection of a glitch is dated according to the sample for which we measure the maximum detection, this creates an uncertainty of

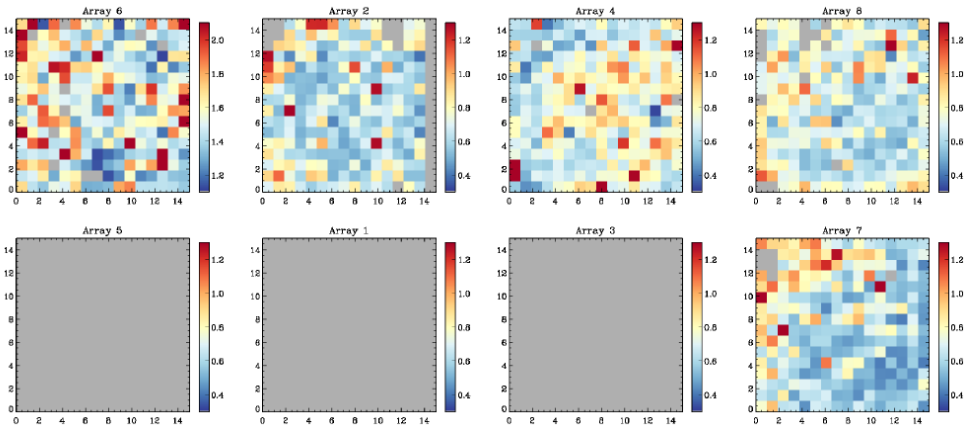

Figure 3.9: Image of the bolometers time constant measured by averaging profiles of each glitch detected on each pixel during Flight#2. Values are in sample number. Arrays 1, 3 and 5 were not operational during these tests.

the order of a sample on the dating of this detection. The time constant measured on the glitches can therefore be over or underestimated, leading to a wide dispersion of the estimates

3.5 ICS in-flight measurments

Since there are uncertainties concerning the measurement of the time constant on the glitches and of the time constant of the ICS, we have implemented a method to determine with the best possible accuracy the bolometer time constants combining both measurments. We first measure the time constant using glitches as explained in the previous section. In a second step, we measure the time constant τ_{ics} of the ICS using calibration sequences. We stack all decays of the signal following the extinction of the ICS and compute the corresponding average ICS downward profile viewed by each pixel. We then deconvolve this profile in Fourier space, using the transfer function $e^{-t/\tau}$, with $\tau = \tau_{gli}$. We then average this profiles over pixels and fit the average profile with an exponential funtion and derive a value of τ_{ics}. Before deconvolution, the signal had been corrected for atmospheric effects and sensor response to avoid biasing the estimate of the time constants. Data have also been corrected for the data-reading time delay. We derive a value of 0.41 ± 0.09 samples (10.25 ± 2.20 ms). This has to be compared to the value of 9.23 ms provided by Hargrave et al. (2006) for a device similar to the ICS onboard. In the last step, we determine the final values of τ_{det}. We

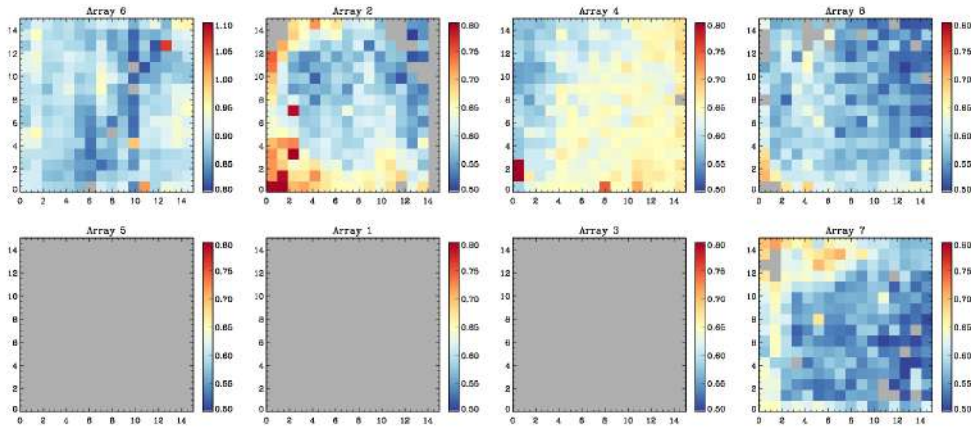

Figure 3.10: Image of the bolometers time constant measured by averaging profiles of each calibration performed during Flight#2 after correcting timelines for the ICS time constants and data-reading time delay. Values are in sample number. Arrays 1, 3 and 5 were not operational during these tests. Note that the colour range of array 6 is different than for the other arrays

proceed in the same way as for the measurement of τ_{ics}, except that we use here the above value of τ_{ics} as parameter for the deconvolution kernel and fit the downard profile of each pixel in order to derive the values of τ_{det} for each pixel. The average values are presented in table 3.2. The measured values are of the order of 0.63 ± 0.04 samples (15.75 ± 1 ms). On average, array 6 is slower than other arrays, with an average τ_{det} of 23 ± 0.75 ms (0.92 ± 0.03 samples). The focal plane distribution of τ_{det} is visible on figure 3.10.

	TRANS			REFLEX				ALL
Array	2	6	Avg	7	4	8	Avg	Avg
τ_{gli}	0.61 ± 0.13	1.51 ± 0.11	1.06 ± 0.12	0.69 ± 0.14	0.74 ± 0.13	0.68 ± 0.12	0.70 ± 0.13	0.85 ± 0.13
τ_{det}	0.62 ± 0.05	0.92 ± 0.03	0.77 ± 0.04	0.64 ± 0.05	0.66 ± 0.03	0.62 ± 0.03	0.64 ± 0.04	0.69 ± 0.04

Table 3.2: Array-averaged values of glitches, ICS and bolometers time constant

Chapter 4

Pointing reconstruction

Accurate instrument pointing is necessary for the reconstruction of the polarized data. The reconstruction of the data from observations made at individual analysis angles of the HWP requires an accuracy of about 5" in translation and 15" in field of view rotation. This requirement was set at the begining of the project, based on simulations of the instrument performances on a realistic sky (see Bernard et al. (2007)). Comparable requirements with respect to the beam size were obtained for similar experiments such as Ebex (see Reichborn-Kjennerud et al. (2010)).Since the PILOT observation strategy involves fast wide-field scanning, the pointing system must also remain accurate for angular scan speeds up to a few degrees per second during day and night. Only a system based on a daytime star sensor coupled to an accurate gyrometer is able to fulfil both these requirements.

4.1 Stellar sensor

As exposed in section 2.1.9, PILOT is equipped with the ESTADIUS stellar sensor designed by CNES. With its optical fiber gyrometer and its wide-field stellar sensor, ESTADIUS is able to provide accurate star position measurements thanks to the small angular size of each pixels of its camera. The stellar sensor is able to detect stars even in the presence of a bright background. ESTADIUS is able to work at altitude as low as 25 km even with unstable flight conditions. It provides pointing reconstruction with an accuracy of 1 arcsec in translation and 6 arcsec in rotation at 4 Hz and demonstrates good autonomy through the use of automatic constellation recognition. It remains accurate at scanning angular speeds up to a few degrees per second. ESTADIUS is also robust against straylight due to a high performance baffle (visible on picture 4.1). Note that for PILOT, we require only a posteriori

accuracy. The a priori requirement is much lower than the a posteriori one, typically 15 arcmin.

4.2 Focal plane geometry

The focal plane geometry is defined as the relative position of each bolometer relative to the focal plane center. The parameters defining the focal plane geometry are contained in a text file loaded in PIMO. The file contains for each of arrays, their average offset value in elevation and cross-elevation, the average size in cross-elevation and elevation of the bolometers of the same array and the angle of rotation of each array with respect to the cross-elevation axis.

4.3 Sky Coordinates Calculations

4.3.1 Coordinate systems

There are different kinds of coordinate systems used in astronomy. The most common coordinate systems are the Horizontal, the Equatorial, and the Galactic coordinates system. These systems use a coordinate grid projected onto the celestial sphere, analogous to geographic coordinate systems used on the Earth's surface. They differ in the choice of reference plane, which divides the sky into two hemispheres along a great circle. Each system is named according to its reference plane. The poles are located at $\pm 90^o$ from the fundamental plane. The primary direction is the starting point of the longitudinal coordinates. The origin is the zero distance point, the "center of the celestial sphere". Table 4.1 lists the common coordinate systems in use by the astronomical community. A schematic view of the three coordinate systems is shown in figure 4.2.

4.3.2 Euler angles

Euler angles are used to determine the rotation of a body in a coordinate system. They can be defined as three rotations relative to the three main axes. An exemple can be seen on figure 4.3. On this figure the three euler angles are noted α, β, γ. The rotation shown here is composed of three rotations. The first around the z axis, the second around the y_1 axis, and the third around the z' axis. this specific rotation can be refered as a 323-Euler rotation or ZYZ-Euler rotation.

Figure 4.1: Picture of PILOT during the health tests of the stellar sensor in Alice Springs, in April 2017. The black part over the baffle opening of the PILOT mirror is the baffle of the ESTADIUS stellar sensor

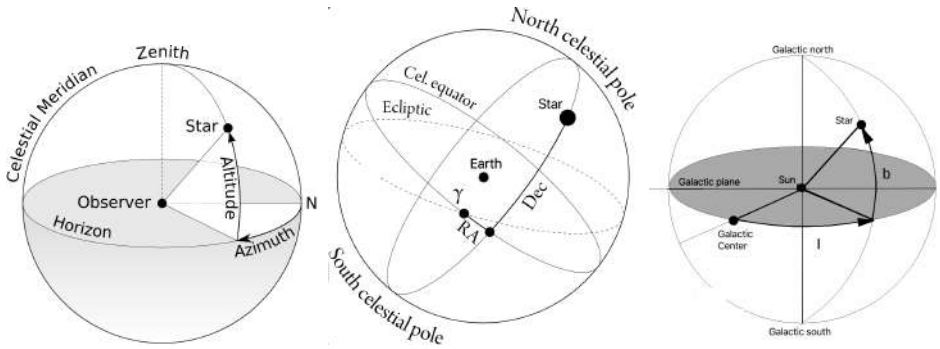

Figure 4.2: Schematic representation of the different coordinate systems. Left: The horizontal coordinate system. The observer is the central point. The angle of elevation (or altitude) is the vertical angle between the horizon of the place where the observer is located and the target object. The azimuth is determined by the angle between the cardinal north and the projection of the direction of the object observed on the horizontal plane. Middle: The equatorial coordinate system. The earth is the central point. The declination is the vertical angle between the celestial equator(projection of the terrestrial equator on the celestial sphere) and the target object. The right ascension is determined by the angle between the vernal point (Noted γ) and the projection of the direction of the object observed on the celestial equator. The vernal point is defined by the position of the Sun on the celestial sphere at the time of the spring equinox in the Northern Hemisphere. The ecliptic is the circular path on the celestial sphere that the Sun appears to follow over the course of a year. Right: The galactic coordinate system. The sun is the central point. The galactic latitude is the vertical angle between the galactic plane and the target object. The right ascension is determined by the angle between the galactic center and the projection of the direction of the object observed on the galactic plane.

Coordinate system	Center point	Fundamental plane (0^o Latitude)	Poles	Latitude	Longitude	Primary direction (0^o longitude)
Horizontal	observer	horizon	zenith /nadir	elevation (el)	azimuth (az)	North point of horizon
Equatorial	Earth center	celestial equator	celestial poles	declination (δ)	right ascension (α)	vernal equinox
Galactic	Sun center	galactic plane	galactic poles	galactic latitude (b)	galactic longitude (l)	galactic center

Table 4.1: Common coordinate systems in use by the astronomical community. The celestial equator is the projection of the terrestrial equator on the celestial sphere. The vernal point is defined by the position of the Sun on the celestial sphere at the time of the spring equinox in the Northern Hemisphere. The ecliptic is the circular path on the celestial sphere that the Sun appears to follow over the course of a year.

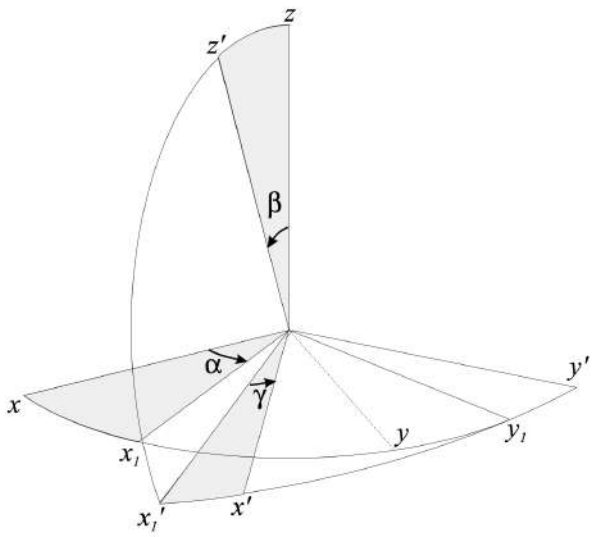

Figure 4.3: Euler angle definition (α,β,γ). Figure from Olsen et al. (2003)

In a 3-dimensional Euclidean space, the following rotational matrices correspond respectively to rotations about the x, y and z axes:

$$R_x(\theta) = \begin{pmatrix} 1 & 0 & 0 \\ \cos\theta & -\sin\theta & 0 \\ \sin\theta & \cos\theta & 0 \end{pmatrix} \tag{4.1}$$

$$R_y(\theta) = \begin{pmatrix} \cos\theta & 0 & \sin\theta \\ 0 & 1 & 0 \\ -\sin\theta & 0 & \cos\theta \end{pmatrix} \tag{4.2}$$

$$R_z(\theta) = \begin{pmatrix} \cos\theta & -\sin\theta & 0 \\ \sin\theta & \cos\theta & 0 \\ 0 & 0 & 1 \end{pmatrix} \tag{4.3}$$

In the case of the transformation presented in figure 4.3, the transition matrix of the coordinates in the reference frame $(O_{x'y'z'})$ to the reference frame (O_{xyz}) is expressed:

$$\big[A\big] = \begin{pmatrix} \cos\alpha & -\sin\alpha & 0 \\ \sin\alpha & \cos\alpha & 0 \\ 0 & 0 & 1 \end{pmatrix} \begin{pmatrix} \cos\beta & 0 & \sin\beta \\ 0 & 1 & 0 \\ -\sin\beta & 0 & \cos\beta \end{pmatrix} \begin{pmatrix} \cos\gamma & -\sin\gamma & 0 \\ \sin\gamma & \cos\gamma & 0 \\ 0 & 0 & 1 \end{pmatrix} \tag{4.4}$$

$$\big[A\big] = \begin{pmatrix} \cos\alpha\cos\beta\cos\gamma - \sin\alpha\sin\gamma & -\cos\alpha\cos\beta\sin\gamma - \sin\alpha\cos\gamma & \cos\alpha\sin\beta \\ \sin\alpha\cos\beta\cos\gamma + \cos\alpha\sin\gamma & -\sin\alpha\cos\beta\sin\gamma + \cos\alpha\cos\gamma & \sin\alpha\sin\beta \\ -\sin\beta\cos\gamma & \sin\beta\sin\gamma & \cos\beta \end{pmatrix} \tag{4.5}$$

4.3.3 Quaternions

The stellar sensor is providing sky coordinates under the form of quaternions. Quaternions are the extension of the complex numbers to four dimensions. A quaternion is written as:

$$q = iq_0 + jq_1 + kq_2 + q_3 \tag{4.6}$$

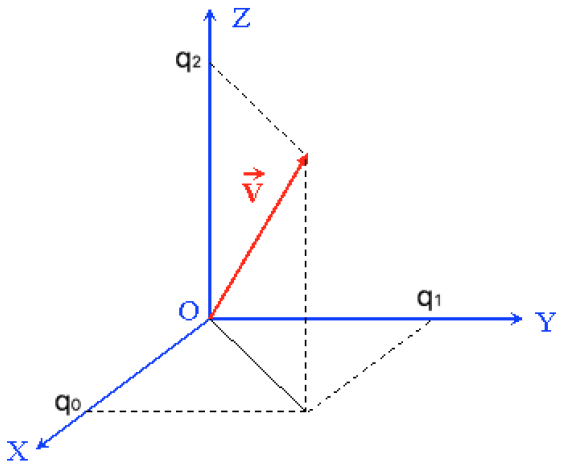

Figure 4.4: Spatial representation of quaternions.

where q_0, q_1, q_2 and q_3 are real numbers. i, j, k are imaginary coefficients for which the following rules of multiplication apply:

$$i^2 = j^2 = k^2 = -1, \tag{4.7}$$

$$j.k = -k.j = i, \tag{4.8}$$

$$k.i = -i.k = j, \tag{4.9}$$

$$i.j = -j.i = k. \tag{4.10}$$

Note that the multiplication of quaternions does not commute. Quaternions of the form given by equation 4.6 are compounds of a scalar part q_3 and a vector part $\vec{v} = (iq_0, jq_1, kq_2)$ (see figure 4.4). Note here that the quaternions are noted on the basis of the IDL convention, that is to say with the three vector terms first followed by the scalar term. ESTADIUS quaternions are given in the CNES convention with the scalar term first.

A quaternion is called unit quaternion when its norm is equal to 1:

$$|q| = q_0^2 + q_1^2 + q_2^2 + q_3^2 = 1 \tag{4.11}$$

The product of quaternions $q_a = (q_{a0}, q_{a1}, q_{a2}, q_{a3})$ and $q_b = (q_{b0}, q_{b1}, q_{b2}, q_{b3})$ is given by:

$$q_a q_b = \begin{pmatrix} q_{a0} \cdot q_{b3} + q_{a1} \cdot q_{b2} - q_{a2} \cdot q_{b1} + q_{a3} \cdot q_{b0} \\ -q_{a0} \cdot q_{b2} + q_{a1} \cdot q_{b3} + q_{a2} \cdot q_{b0} + q_{a3} \cdot q_{b1} \\ q_{a0} \cdot q_{b1} - q_{a1} \cdot q_{b0} + q_{a2} \cdot q_{b3} + q_{a3} \cdot q_{b2} \\ -q_{a0} \cdot q_{b0} - q_{a1} \cdot q_{b1} - q_{a2} \cdot q_{b2} + q_{a3} \cdot q_{b3} \end{pmatrix} \tag{4.12}$$

The orthogonal matrix corresponding to a rotation by means of the unit quaternion $q = iq_0 + jq_1 + kq_2 + q_3$ is given by the expression:

$$R = \begin{pmatrix} q_0^2 - q_1^2 - q_2^2 + q_3^2 & 2 \cdot (q_0 \cdot q_1 - q_2 \cdot q_3) & 2 \cdot (q_0 \cdot q_2 + q_1 \cdot q_3) \\ 2 \cdot (q_0 \cdot q_1 + q_2 \cdot q_3) & -q_0^2 + q_1^2 - q_2^2 + q_3^2 & 2 \cdot (q_1 \cdot q_2 - q_0 \cdot q_3) \\ 2 \cdot (q_0 \cdot q_2 - q_1 \cdot q_3) & 2 \cdot (q_1 \cdot q_2 + q_0 \cdot q_3) & -q_0^2 - q_1^2 + q_2^2 + q_3^2) \end{pmatrix} \tag{4.13}$$

4.3.4 From Euler Angles to quaternions.

We can associate a quaternion q with a rotation around an axis by the following expression:

$$q = \begin{pmatrix} V_0 \sin \frac{\theta}{2} \\ V_1 \sin \frac{\theta}{2} \\ V_2 \sin \frac{\theta}{2} \\ \cos \frac{\theta}{2} \end{pmatrix} \tag{4.14}$$

where θ is a simple rotation angle (the value in radians of the angle of rotation α, β or γ) and V_0, V_1, V_2 are the "direction cosines" locating the axis of rotation. For example, if we return to the case presented in figure 4.3 of a 323-Euler rotation, the representation in quaternion of the rotation is expressed as follows:

$$q = \begin{pmatrix} 0 \\ 0 \\ \sin \frac{\alpha}{2} \\ \cos \frac{\alpha}{2} \end{pmatrix} \begin{pmatrix} 0 \\ \sin \frac{\beta}{2} \\ 0 \\ \cos \frac{\beta}{2} \end{pmatrix} \begin{pmatrix} 0 \\ 0 \\ \sin \frac{\gamma}{2} \\ \cos \frac{\gamma}{2} \end{pmatrix} \tag{4.15}$$

$$q = \begin{pmatrix} -\sin\frac{\alpha}{2}\sin\frac{\beta}{2}\cos\frac{\gamma}{2} + \cos\frac{\alpha}{2}\sin\frac{\beta}{2}\sin\frac{\gamma}{2} \\ \sin\frac{\alpha}{2}\sin\frac{\beta}{2}\sin\frac{\gamma}{2} + \cos\frac{\alpha}{2}\sin\frac{\beta}{2}\cos\frac{\gamma}{2} \\ \sin\frac{\alpha}{2}\cos\frac{\beta}{2}\sin\frac{\gamma}{2} + \cos\frac{\alpha}{2}\cos\frac{\beta}{2}\sin\frac{\gamma}{2} \\ -\sin\frac{\alpha}{2}\cos\frac{\beta}{2}\sin\frac{\gamma}{2} + \cos\frac{\alpha}{2}\cos\frac{\beta}{2}\cos\frac{\gamma}{2} \end{pmatrix}. \tag{4.16}$$

4.3.5 Coordinates calculations

ESTADIUS uses the convention that the attitude of the stellar sensor is regulated by 3 rotations first along the roll axis, second arround the delta axis and last around the roll axis. It's a 323-Euler rotation. The ESTADIUS quaternions are thus linked to the equatorial coordinates (α_{ss},δ_{ss}) of its pointing direction through the following expression:

$$q = \begin{pmatrix} -\sin\frac{\alpha_{ss}-\pi}{2}\sin\frac{\delta_{ss}-\frac{\pi}{2}}{2}\cos\frac{\theta_{ss}}{2} + \cos\frac{\alpha_{ss}-\pi}{2}\sin\frac{\delta_{ss}-\frac{\pi}{2}}{2}\sin\frac{\theta_{ss}}{2} \\ \sin\frac{\alpha_{ss}-\pi}{2}\sin\frac{\delta_{ss}-\frac{\pi}{2}}{2}\sin\frac{\theta_{ss}}{2} + \cos\frac{\alpha_{ss}-\pi}{2}\sin\frac{\delta_{ss}-\frac{\pi}{2}}{2}\cos\frac{\theta_{ss}}{2} \\ \sin\frac{\alpha_{ss}-\pi}{2}\cos\frac{\delta_{ss}-\frac{\pi}{2}}{2}\sin\frac{\theta_{ss}}{2} + \cos\frac{\alpha_{ss}-\pi}{2}\cos\frac{\delta_{ss}-\frac{\pi}{2}}{2}\sin\frac{\theta_{ss}}{2} \\ -\sin\frac{\alpha_{ss}-\pi}{2}\cos\frac{\delta_{ss}-\frac{\pi}{2}}{2}\sin\frac{\theta_{ss}}{2} + \cos\frac{\alpha_{ss}-\pi}{2}\cos\frac{\delta_{ss}-\frac{\pi}{2}}{2}\cos\frac{\theta_{ss}}{2} \end{pmatrix} \tag{4.17}$$

Since ESTADIUS quaternions are sampled at 4Hz we need, before carrying out any operation, to interpolate them at the bolometers sampling frequency. We note Q_o the quaternion containing the information of the offsets between the stellar sensor and the optical axis of the instrument (or center of the focal plane). Similarly, let us note Q_b the quaternion derived from the geometry of the focal plane and giving the relative position of each bolometer with respect to the center of the focal plane. A first measurement of the geometry of the focal plane was determined during the IAS tests and will be further improved using the measurements made during the flights. This focal plane geometry is contained in a structure called PIMO (see section 2.3.1). Finally, Q_e is the quaternion provided by the stellar sensor. To obtain the observed coordinates for each bolometer we proceed as follows:

- We perform a first rotation by multiplying the ESTADIUS quaternion Q_e by Q_o. This rotation results in a quaternion which we will denote by Q_{fpc} for focal plane center. From this point it is possible to extract the pointing angles (α_{fpc}, δ_{fpc} and θ_{fpc}) of the center of the optical axis of the instrument.

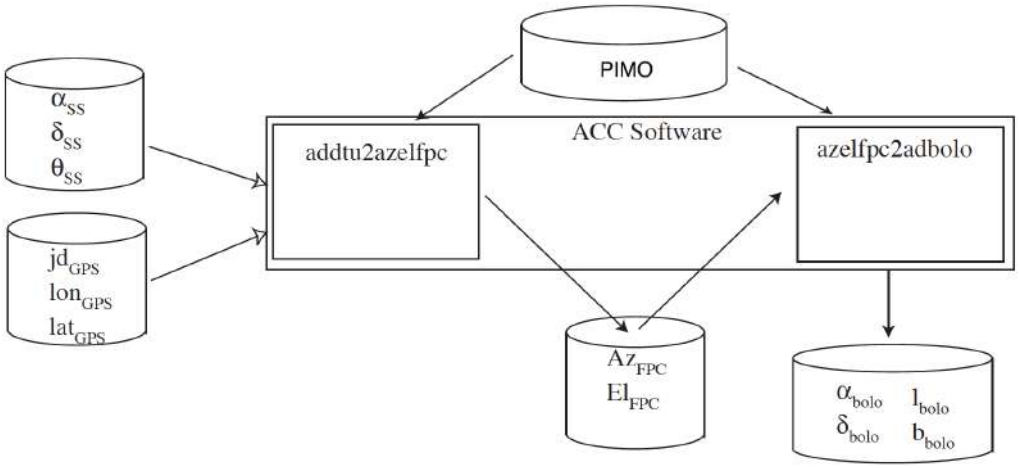

Figure 4.5: Schematic view of the coordinates calculation. α_{bolo}, δ_{bolo}, are equatorial coordinates and l_{bolo} and b_{bolo} are galactic coordinates. PIMO is a structure containing the focal plane geometry information (see section 2.3.1)

- We then perform a second rotation by multiplying Q_{fpc} by Q_b
- The Euler angles (α_{bolo}, δ_{bolo} and θ_{bolo}) of each bolometers are then extracted from the rotation matrix associated with the final quaternion.

Equatorial coordinates (α_{bolo}, δ_{bolo}) can be subsequently converted to Horizontal coordinates(az_{bolo}, el_{bolo}) or to Galactic coordinates (l_{bolo}, b_{bolo}). Coordinates are computed for each bolometers. A schematic view of coordinates calculation can be seen in figure 4.5.

4.4 Issues in pointing reconstruction

Two main factors may be responsible for errors in pointing reconstruction:

- The determination of the focal plane geometry,
- the determination of the offset between the stellar sensor and the instrument.

Since the stellar sensor is only roughly aligned with the optical axis of the instrument (see figure 4.1), there is an offset between the direction observed

by the sensor and that observed by PILOT. This must be determined with each new assembling of the gondola. Due to the thermoelastic and gravity deformations of the instrument, a drift of this offset is possible during the flight. Several methods that I will detail here have been developped in order to best constrain these drifts. The geometry of the focal plane was measured during the ground tests in 2014 using an external artificial point source projected on the focal plane. The offsets between each array can also be measured by applying the reconstruction methods described below, individually for each array. The determination of these drifts is not possible for certain observations of PILOT, so it is necessary to construct a pointing model of the instrument allowing to interpolate corrections. This pointing model can be constrained by correlating the observed drifts with physical parameters such as the elevation of the gondola and different temperatures of the instrument (see section 4.8).

4.5 Compact sources method

To determine the offset between the ESTADIUS and the PILOT optical axes, we construct a map of the observed source and then make a Gaussian fit on this source. The maximum value of this Gaussian fit is considered to be the observed position of the source. This position is then compared with the theoretical position of the source at the time of observation provided either by the ephemerides of the Institute of Celestial Mechanics and Calculation of Ephemerides (IMCCE) or by the Jet Propulsion Laboratory (JPL) if it is a planet or by the positions observed with others Instruments in the case of fixed sources. Figure 4.6 shows the different positions expected and observed for Saturn during one of the observations of Flight#1 in images using the focal planes in transmission and reflection. As the JPL DE405 ephemeris that we used was created in 1997 and that the ephemeral IMCCE INPOP was established in 2014, the expected position of the planet varies by a few arcseconds. The calculation of the offset in this case was made from the coordinates of the IMCCE. This method is quite simple, but can only be applied to bright sources such as the planets or the strongest sources, in Orion for example. For the first flight, the number of sources to which we could apply it was quite small. So we could not build a pointing model.

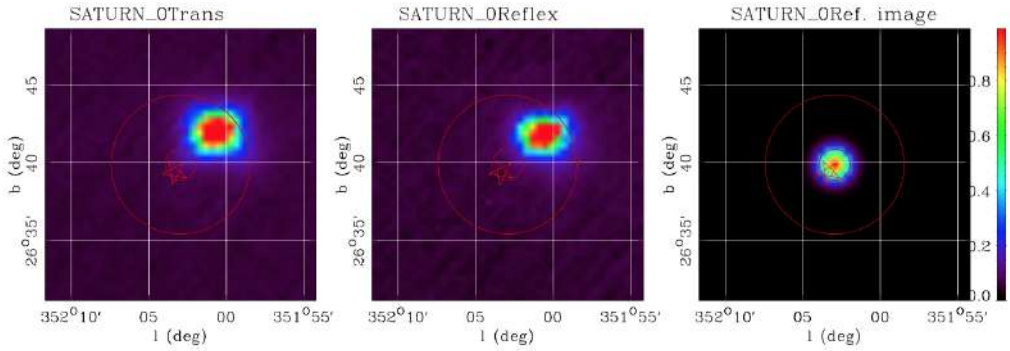

Figure 4.6: From left to right: Saturn observed on the matrices in transmission, reflection, and simulated by a gaussian at its theoretical position. The red star indicates the expected position of the planet provided by the JPL ephemerides. The red circles are centered on the coordinates provided by the IMCCE. The radius of the large circle is 2 arcminutes.

4.6 Maximum correlation method

During the flights we observed many objects that had been observed with the Herschel satellite mission. The latter has made numerous observations in intensity at wavelengths between 55 and 672 µm with a pointing accuracy of 0.81" (see Improvement et al. (2012)). To constrain the offsets we used the observations made with the SPIRE instrument on board Herschell at 250 µm, because the wavelength is close to that used by PILOT. Herschel maps were smoothed to 2 arcminutes while keeping the initial pixel size of the maps to preserve pointing accuracy bellow the resolution of 2'. The PILOT and Herschel maps have been projected around bright compact sources to avoid the biases induced by the absence of data on one or the other map. This is also to not be influenced by the data at the edge of the maps. We then perform a correlation between the two maps by shifting one of them pixel by pixel. If needed, this method can also be used on planets using a simulated map of the point source instead of the Herschel map. Figure 4.7 show an example of the application of this method on one of the visible sources in Orion.

a. 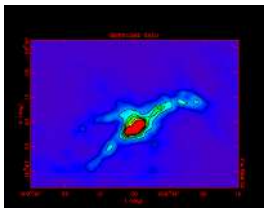 b. 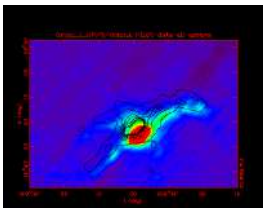 c. 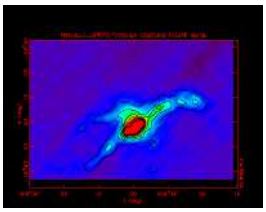

Figure 4.7: From left to right: a. Zoom on a bright region of Orion observed with Herschel smoothed to PILOT resolution. b. Zoom on the same region observed with PILOT before correction of the ESTADIUS offset. c. Zoom on the same region observed with PILOT after correction of the ESTADIUS offset based on the maximum correlation method. For each image, the black outlines correspond to the intensity contours on the Herschel map.

4.7 The barycentric method

This method is similar to that described in 4.5 except that this calculation is not based on the expected position of the source on a map but on its expected position on the focal plane. To do this, the calculation is done in six steps. We first calculate the inertial coordinates of a known source (a planet for example) using:

$$U_i = \begin{pmatrix} \cos(\alpha_{th})\cos(\delta_{th}) \\ \sin(\alpha_{th})\cos(\delta_{th}) \\ \sin(\delta_{th}), \end{pmatrix} \tag{4.18}$$

where α_{th} and δ_{th} are the equatorial coordinates provide by the IMCCE ephemeris.

By applying a rotation of this vector with the quaternions provided by ESTADIUS (q_0,q_1,q_2,q_3), we determine the normalized steering vector from the instrument to the planet, called U_s as:

$$U_s = \begin{pmatrix} q_0^2 - q_1^2 - q_2^2 + q_3^2 & 2\cdot(q_0\cdot q_1 - q_2\cdot q_3) & 2\cdot(q_0\cdot q_2 + q_1\cdot q_3) \\ 2\cdot(q_0\cdot q_1 + q_2\cdot q_3) & -q_0^2 + q_1^2 - q_2^2 + q_3^2 & 2\cdot(q_1\cdot q_2 - q_0\cdot q_3) \\ 2\cdot(q_0\cdot q_2 - q_1\cdot q_3) & 2\cdot(q_1\cdot q_2 + q_0\cdot q_3) & -q_0^2 - q_1^2 + q_2^2 + q_3^2) \end{pmatrix} U_i. \tag{4.19}$$

We then deduce from the vector U_s the position $p(x, y)$ of the source on the focal plane. The value of this position is given in units of pixels.

From this position, we define a submatrix of pixels for which we will calculate the barycentre defined as follows:

$$\vec{p_{mes}}(x,y) = \frac{\sum V_{ij}\vec{p}_{ij}(x,y)}{\sum V_{ij}}, \tag{4.20}$$

with $\vec{p_{mes}}(x,y)$ the measured position of the source, $\vec{p}_{ij}(x,y)$ the position of the pixel ij, and V_{ij} the signal measured for the pixel ij.
Finally we calculate the difference between the theoretical position of the source $\vec{p_{ij}}(x,y)$ and the observed coordinates determined by the calculation of the barycentre $\vec{p_{mes}}(x,y)$. This method has some advantages. Indeed, contrary to the methods applied so far, the barycentric method allows us to access the variations of pointing throughout the same scene. On the data of the first flight for which we have few bright compact sources, this method can provides to us the necessary tool to understand the observed fast variations in pointing. This method can also be used to reconstruct a geometry of the focal plane with an accuracy of a few arcseconds, at the level of the ESTADIUS accuracy.

4.8 Preliminary pointing model

Using the methods described above, it was possible to determine a preliminary ad.hoc model of the pointing variations throughout the second flight. To establish this model, the coordinates were calculated using fixed values of the pointing offsets determined on the first observation of Saturn. The model was established using a linear regression between the measured offsets and the temperatures of the hexapods of the mirror as well as the elevation of the gondola at the time of the observation, as follows:

$$\text{offset} = \sum_i (A_i \cdot Th_i) + a \cdot El_g^2 + b \cdot El_g + c, \tag{4.21}$$

where Th_i is the hexapod temperature of leg i in degree Celsius, El_g is the pointing elevation in degree of the focal plane center and offset is the pointing offset derived using the maximum correlation method for scenes with sufficient strong compact sources. The same model was constrained on cross-elevation and elevation offsets. The derived parameters A_i, a, b, c are given by table 4.2

On figure 4.9 we can see the offset values measured before and after correcting pointing. The set of coordinates observed by the bolometers obtained by correcting pointing with this model will be referred to as "V1 Coordinates" later. Overall, we can see that the coordinates are quite well corrected, with offsets values sometimes passing from more than 5 arcmin to less than 1 arcmin (at $t \simeq 28h$). However, at the beginning of the flight, we observe a larger

Name	Cross-Elevation	Elevation	Sigma
Th_1[řC]	-0.2130	-0.1717	0.0192
Th_2[řC]	-0.3335	-0.7085	0.0375
Th_3[řC]	2.8039	5.6983	0.3027
Th_4[řC]	-2.7150	-6.0179	0.3054
Th_5[řC]	0.5069	1.9908	0.0560
Th_6[řC]	-0.0171	-0.7765	0.0169
a [deg]	0.0014	-0.0021	0.0002
b [deg]	-0.0856	0.1136	0.0124
c	1.6384	-6.4779	0.0000

Table 4.2: Table of parameters used for the pointing model

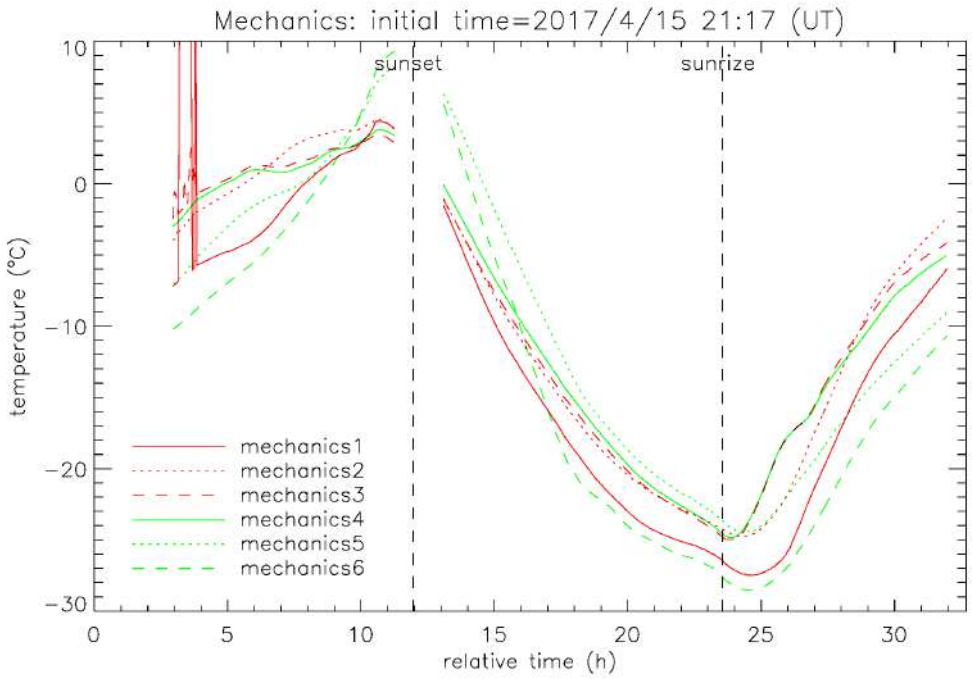

Figure 4.8: Hexapods temperatures during Flight#2 as a function of time.

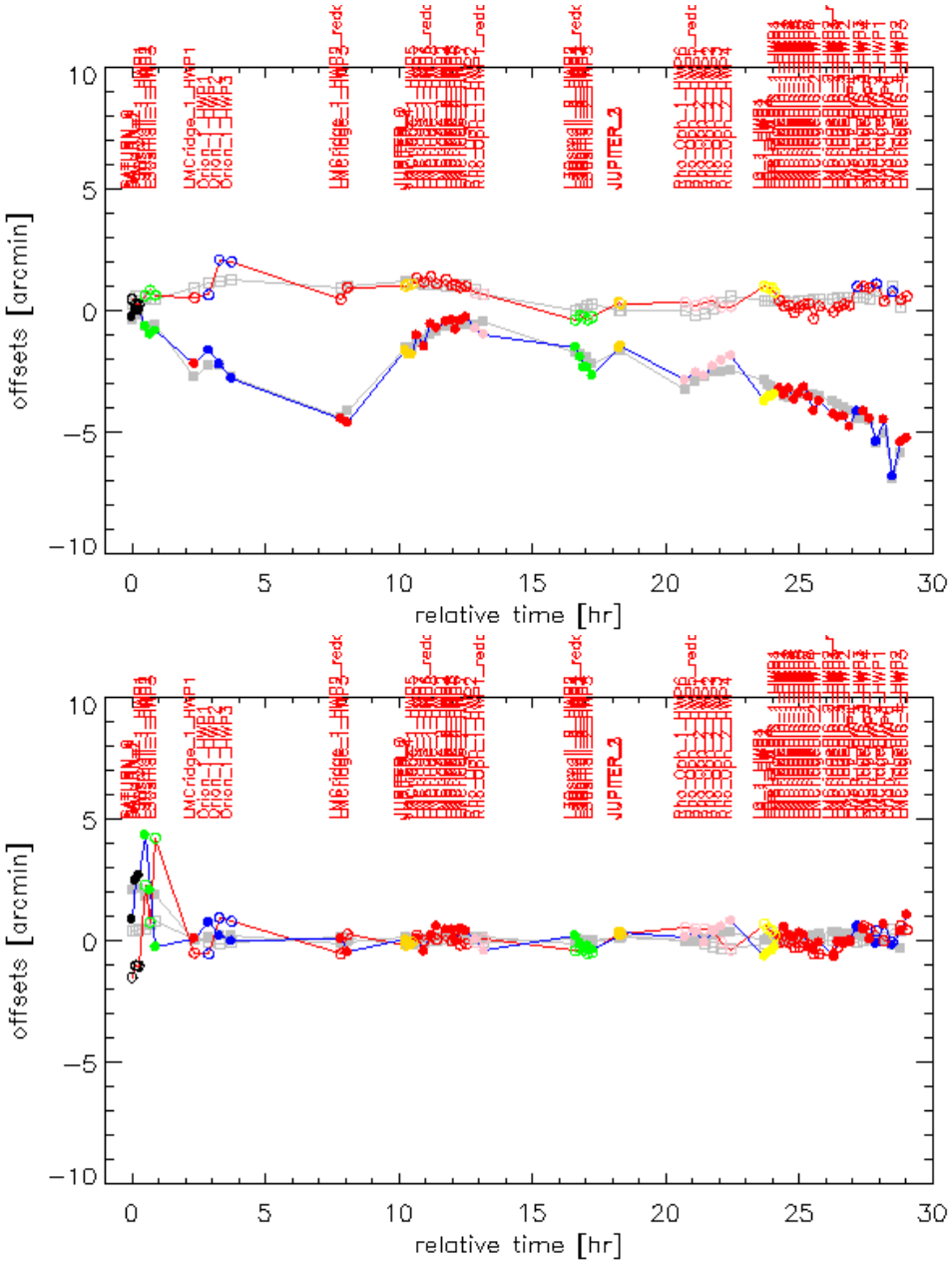

Figure 4.9: Top: Averaged cross-elevation and elevation offsets measured during Flight#2 before applying the model correction. Bottom: Same but after application of the pointing model correction. The red curves correspond to the cross-elevation offset and blue curves to the elevation offsets. The gray curves show the prediction of the current pointing model described in eqs. 4.21 and tab 4.2.

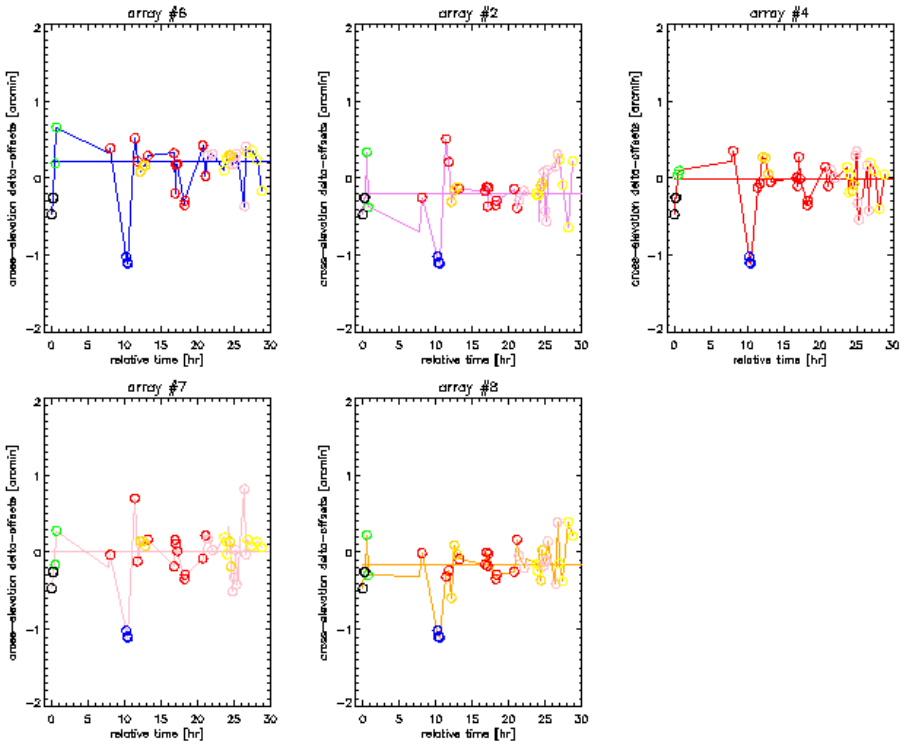

Figure 4.10: Cross-elevation offsets derived for each array. The horizontal line shows the average of the above, excluding data with differences higher than 2 arcminutes

residual offset (of the order of 5 arcmin). This difference corresponds to the time when the hexapod temperature measurments are erratic, in particular for the hexapod "mechanics 1" (see figure 4.8). We thus removed erratics measurments on the hexapod before establishing the pointing model.
We also computed the equation independently for each array of the focal plane in order to check the precision of the geometry of the focal plane that have been determined during ground tests. Figures 4.10 and 4.11 show respectively the Cross-elevation and elevation offsets derived for each array. The horizontal line shows the average of the above, excluding data with differences higher than 2 arcminutes. If we remove differences greater than 2 arcmin, which are probably due to a poor correlation with Herschel maps, we observe small systematic differences. These are probably due to uncertainty in the method. We have therefore also corrected the focal plane geometry by taking account of these offsets of each individual array.

The quality of the correction on the reconstruction of the coordinates is

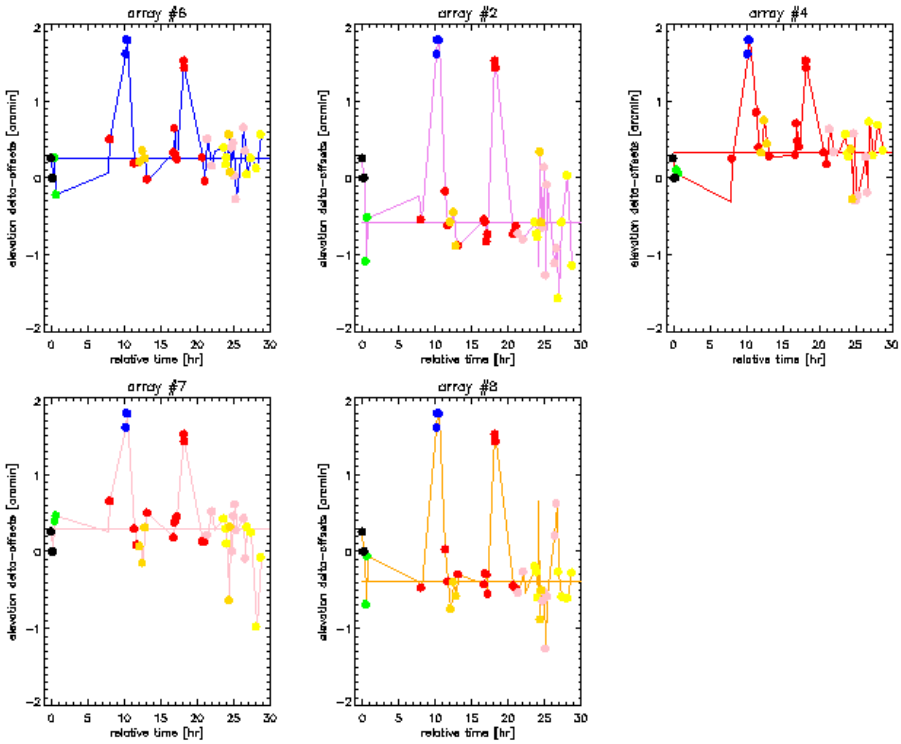

Figure 4.11: Elevation offsets derived for each array. The horizontal line shows the average of the above, excluding data with differences higher than 2 arcminutes.

Version	Focal Plane Geometry version	Initial cross-elevation offset	Initial elevation offset	Initial rotation offset	Correction of the reading time delay	Correction applied to the initial offset
V0	2013_5pos	-0.07888	1.1877	0	No	None
V1	2017_v1	-0.07888	1.1877	0	No	Offset corrected using the pointing model
V2	2017_v1	-0.07888	1.1877	0	No	Offset adjusted using offset measured on bright sources in a scene
V2.1	2017_v1	-0.07888	1.1877	0	Yes	Offset adjusted using offset measured on bright sources in a scene

Table 4.3: Summary of the different versions of coordinates (see text).

dependent on the number of sources that are available with sufficient signal to noise ratio in the maps of individual observations. This reconstruction can be improved with the destriped data that can be provided by destriping tools (see chapter 8). They will allow us to use weaker sources and thus improve correlation with Herschel maps.

4.9 Coordinates versions

As part of the data processing of the instrument, several sets of coordinates have been created by applying a different correction on the ESTADIUS offsets, geometry of the focal plane or by correcting them for the readout time delay described in section 3.1. A summary of the different versions of coordinates is given in table 4.3. The focal plane geometry version 2013_5pos, was measured during ground tests. The focal plane geometry version 2017_v1 corresponds to version 2013_5pos corrected using offsets measured on each array during the second pilot flight. The initial offsets in cross-elevation, elevation and rotation correspond to the values of offsets measured during Flight#2 on the first observation of Saturn. These values are entered in the PIMO structure and serve as a reference for the correction of residual offsets. The coordinate set used as reference in the construction of the PILOT maps are the coordinates v2. They have the advantage of using the real offsets calculated on the sources of each scene and thus to be more precise than the coordinates computed from the current pointing model. However V2 coordinates cannot be calculated on scenes without visible sources.

Chapter 5

Noise properties

The sensitivity of a detector is one of the most important parameters for defining the overall performance of the instrument. It determines the integration time required for the observation of a source at a given signal to noise ratio (SNR). The sensitivity of a bolometer is expressed in terms of noise-equivalent power (NEP). The NEP is defined as the signal power that gives a signal-to-noise ratio of one in a one Hertz output bandwidth. In this section, we present the different sources of noise encountered in bolometric systems and the noise measurements made during the two flights of the instrument as well as the measurements obtained during the ground tests.

5.1 Noise sources

5.1.1 Photon noise

The photon noise originates from fluctuations in the detection of the photon flux. It comes from the corpuscular nature of the incident radiation. It can not be deleted, but it can be reduced by a longer integration time. In infrared, one of the contributions to the incident flux is the own emission of the telescope. Similarly, the atmosphere contributes to this flux. These two contributions are not negligible and must be taken into account in the quantification of the photon noise. Since the photons are bosons, the use of the Bose-Einstein statistics allows us to recover the expression of the NEP photon noise. The number of photons transmitted by the optical system and absorbed by the bolometer is given by:

$$n = \frac{\eta_{\mathrm{det}} \epsilon(\nu) \tau_{\mathrm{r}}(\nu)}{e^{\frac{h\nu}{k_{\mathrm{B}}T}} - 1}, \tag{5.1}$$

where η_{det} is the detector efficiency, $\epsilon(\nu)$ the emissivity of a gray body at the emission frequency ν of the photon and $\tau_{\mathrm{r}}(\nu)$ the transmission of the instrument; k_{B} is the Boltzmann's constant and h is the Planck constant; T is the temperature of the gray body.

For bosons, the mean of the square of the fluctuations δn of the number of particules n in the mode considered can be expressed as:

$$(\delta n)^2 = n \cdot (n+1). \tag{5.2}$$

The expression of the NEP_{photon} is obtained integrating the equation 5.2 having previously multiplied it by the amount $S\Omega$, the solid angle subtended by one bolometer. The density of states of the mode considered $2h\nu^3/c^2$ and the energy of the photon $h\nu$ must also be taken into account. A factor 2 must also be applied to take into account the 2 possible states of polarization. NEP_{photon} is therefore expressed:

$$NEP^2_{\mathrm{photon}} = 4\frac{h^2}{c^2}(S\Omega)^2 \int_0^{+\infty} \nu^4 (\delta n)^2 d\nu. \tag{5.3}$$

5.1.2 Thermal noise

A phonon denotes a quantum of vibrational energy in a crystalline solid. Thermal noise, or phonon noise, is related to the fluctuation of the number of phonons transiting via the thermal conductance G between the absorber and the thermal reservoir (see figure 3.1). The quadratic mean of these energy fluctuations is given by:

$$(\Delta E)^2 = k_{\mathrm{B}} T^2 C, \tag{5.4}$$

where C is the heat capacity of the body constituted by the absorber and the thermometer; T is the temperature of the cryostat. These energy fluctuations are translatable into temperature fluctuations:

$$(\Delta T)^2 = \frac{k_B T^2}{C} \tag{5.5}$$

Then in fluctuations of power in the detector:

$$NEP^2_{phonon} = \frac{(\Delta T)^2}{B} G^2 = 4k_{\mathrm{B}} T G. \tag{5.6}$$

where B is the bandwidth related to the time constant ($B = 1/4\tau$). This noise is independent of the frequency and can be considerably reduced when the detector is cooled to very low temperature. In the equations presented above, it is assumed that the bolometer is at the temperature of the cryostat. In reality, the bolometer being exposed to radiation, the temperature of the absorber rises with respect to that of the cryostat. Thermal conductance is therefore higher. Considering this and the expression of NEP given above, the contribution of phonon noise can be over-estimated by about 30% according to Mather (1982).

5.1.3 Johnson-Nyquist noise

Johnson-Nyquist noise is a noise generated in an electrical resistance in thermal equilibrium by thermal agitation of electrons. The thermal noise across a resistor is expressed by the Nyquist relation:

$$(\Delta V)^2 = 4k_{\mathrm{B}} T R, \tag{5.7}$$

where R is the value of the resistance. For a bolometric bridge (see figure 2.5), the resistance to be considered is the equivalent resistance that is expressed:

$$R = \frac{R_B R_C}{R_B + R_C}, \tag{5.8}$$

where R_C is the load resistor and R_B the bolometer.

5.1.4 Flicker noise

Flicker noise, also called $1/f$ noise is part of so-called "pink" sounds with a power curve in $1/f$. In the frequency domain, the origin of this noise depends on the intrinsic properties of the material used and is expressed by a slow drift of the signal which emerges in an excess of noise at low frequencies in

the spectral density of noise. The term "$1/f$ noise" is used as opposed to white noise. It is actually a decreasing noise in $1/f^{\alpha}$ where f is the frequency and α is a coefficient, between 0.8 and 1.3, determined empirically. $1/f$ noise is present in almost all systems and its mechanisms are complicated. It is generally considered that the noise in $1/f$ is related to the fluctuations of the resistance in a resistive device since it appears only during the passage of a current, but its origin is still subject to debate.

5.1.5 Readout noise

The electrical signal supplied by the bolometric bridge is read by a readout electronics. This electronics generates a noise that contributes to the total noise of the detector.

5.1.6 Environmental noise

5.1.6.1 Microphony

Microphony is generated by the mechanical vibration of electrical conductors. When two close wires move relative to one another, variations in electrical capacitance appear and change into voltage or current fluctuations. To limit the problems of microphony, it is necessary to reduce as much as possible the length of the cables and to make sure that they are correctly fixed to the structure of the instrument.

5.1.6.2 Stability of the cryogenic bath

In the cryostat, the temperature of the cryogenic bath fluctuates, which can result in low frequency drifts of the signal. The noise generated by these fluctuations is strongly correlated between detectors.

5.1.6.3 Electromagnetic disturbances

The system is sensitive to electromagnetic disturbances of the environment. These sources of noise can be reduced by magnetic and electrical shielding of the wires connecting the bolometers to the pre-amplifiers.

5.2 Ground calibrations

The noise level of the instrument was first evaluated during the two test sessions in 2012 and 2013 at the IAS. The tests were performed using PILOT's

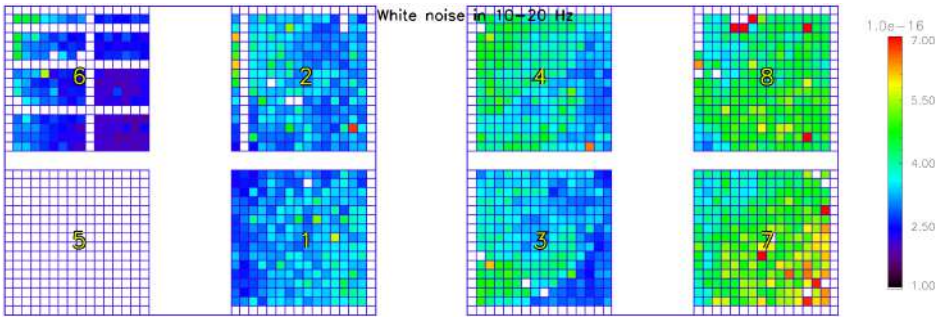

Figure 5.1: Focal plane map of the average white noise in $W/\sqrt{Hz}$ between 10 to 20 Hz. Figure from Misawa (2016)

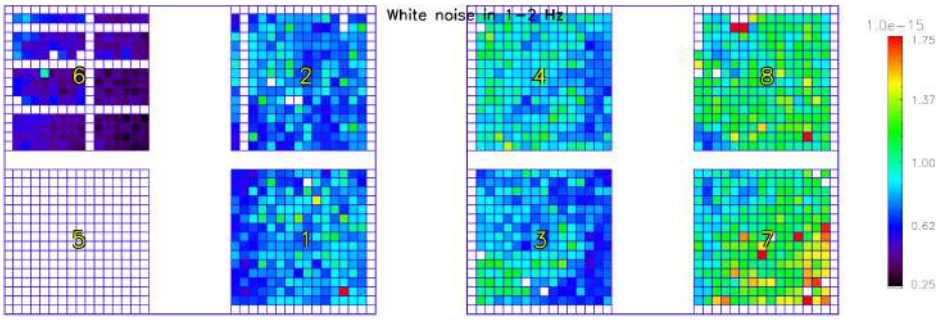

Figure 5.2: Focal plane map of the average 1/f noise in $W/\sqrt{Hz}$ between 1 and 2 Hz. Figure from Misawa (2016)

complete electronics to record the HK and scientific data (see Misawa et al. (2015) for a more complete description of the tests).

Focal plane maps of the average noise level estimated in the frequency range 10 to 20 Hz (white noise regime) and 1 to 2 Hz (part of the flicker noise) measured during ground tests are shown in figures 5.1 and 5.2, respectively. The corresponding values are visible in table 5.1. The array averaged values of the NEP between 10 and 20 Hz, which we refer to as the "white noise level", are of the order of $3.8 \times 10^{-16} W/\sqrt{Hz}$. The white noise level appears to be lower on the TRANS arrays than on the REFLEX arrays. This difference in the measurement of white noise is explained by the difference in temperature between the two focal planes (the REFLEX focal plane temperature was approximately 4 mK higher).

Table 5.1: Array statistics of the NEP in $W/\sqrt{Hz}$ between 10 and 20 Hz. Table from Misawa (2016)

ARRAY	MIN ($W/\sqrt{Hz}$)	MAX ($W/\sqrt{Hz}$)	AVG ($W/\sqrt{Hz}$)	MED ($W/\sqrt{Hz}$)	STDEV ($W/\sqrt{Hz}$)
1	$2.366\,10^{-16}$	$5.628\,10^{-16}$	$3.306\,10^{-16}$	$3.292\,10^{-16}$	$4.607\,10^{-17}$
2	$2.373\,10^{-16}$	$6.774\,10^{-16}$	$3.419\,10^{-16}$	$3.292\,10^{-16}$	$5.907\,10^{-17}$
6	$1.804\,10^{-16}$	$5.525\,10^{-16}$	$2.661\,10^{-16}$	$2.523\,10^{-16}$	$6.380\,10^{-17}$
T_Average	$2.181\,10^{-16}$	$5.976\,10^{-16}$	$3.129\,10^{-16}$	$3.036\,10^{-16}$	$5.631\,10^{-17}$
3	$2.495\,10^{-16}$	$6.150\,10^{-16}$	$3.561\,10^{-16}$	$3.494\,10^{-16}$	$5.743\,10^{-17}$
7	$3.314\,10^{-16}$	$7.559\,10^{-16}$	$4.851\,10^{-16}$	$4.770\,10^{-16}$	$7.516\,10^{-17}$
4	$2.721\,10^{-16}$	$6.446\,10^{-16}$	$3.908\,10^{-16}$	$3.926\,10^{-16}$	$5.474\,10^{-17}$
8	$2.948\,10^{-16}$	$3.810\,10^{-15}$	$4.760\,10^{-16}$	$4.519\,10^{-16}$	$2.511\,10^{-16}$
R_Average	$2.870\,10^{-16}$	$1.456\,10^{-15}$	$4.270\,10^{-16}$	$4.177\,10^{-16}$	$1.096\,10^{-16}$
Average	$2.574\,10^{-16}$	$1.088\,10^{-15}$	$3.781\,10^{-16}$	$3.688\,10^{-16}$	$8.676\,10^{-17}$

5.3 Calculation of noise levels and power spectra

We compute the noise power spectra during Flight#1 and Flight#2 for each detector and during each observation scan. The data are first corrected for the response time variations (see sections 6.2 and 9.2.4) and converted to watts using the detector-averaged ground calibration value of $2.116\text{x}10^{10}$ V/W derived from ground calibrations of the detectors alone in front of an absolute black body. As explained in section 2.2, PILOT flights are divided into scenes that correspond to the observation of an object at a given HWP position. Each scene is divided into scans. Scans are performed at constant elevation for Flight#1 (see section 2.4.1.2) and at variable elevation for most of the scenes in Flight#2 (see section 2.4.2.3). The calibrated timelines are corrected for the atmospheric signal to first order , by removing their linear correlation with observation elevation as calculated over each observation, taking into account only scan data (i.e., excluding time samples associated to the calibrations, slews, etc... see section 9.2.3). Given the noise levels, we can assume that, after the atmospheric signal removal, the individual detector timelines are dominated by instrumental noise. We compute the mean timeline among valid pixels of each array and scale it by the square root of the number of valid detectors in each array to keep a single-detector

ARRAY	MIN [10^{-16} W/$\sqrt{\text{Hz}}$]	MAX [10^{-15} W/$\sqrt{\text{Hz}}$]	AVG [10^{-16} W/$\sqrt{\text{Hz}}$]	MED [10^{-16} W/$\sqrt{\text{Hz}}$]	STDEV [10^{-16} W/$\sqrt{\text{Hz}}$]
2	5.212	1.631	7.888	7.795	1.377
5	3.143	0.7879	4.592	4.412	0.8447
6	2.436	3.031	3.381	3.108	2.058
T_Average	3.597	1.82	5.287	5.105	1.427
4	4.065	0.9802	5.550	5.450	0.7443
7	5.040	1.277	7.130	6.922	1.121
8	4.711	1.086	6.563	6.393	1.019
R_Average	4.605	1.114	6.415	6.255	0.9614
Average	4.101	1.466	5.851	5.679	2.388

Table 5.2: Array statistics of the NEP of one scan during the night of Flight#1 in W/$\sqrt{\text{Hz}}$ between 10 and 20 Hz.

normalization. The array-averaged power spectra $P_{m,s}(\nu)$ are computed for each detector array m and each scan s from these array-averaged timelines, in $W/\sqrt{Hz}$, in the range of frequencies $\nu \in [0.02, 20]$ Hz.
To assess the high-frequency noise level statistics during Flight#2, we repeat the initial steps presented above but instead of averaging the signal among the detectors for each array, we compute the noise power spectra $P_{i,s}(\nu)$ for each detector i and each scan s. For each detector, we compute the flight-averaged spectrum $P_i(\nu)$ as the median over all the scans. The high frequency noise levels are then taken to be the mean value of $P_i(\nu)$ in the range $\nu \in [0.02, 20]$ Hz.

5.4 Noise levels and spatial distribution

Table 5.2 and 5.3 shows the array statistics of the NEP of one scan during the night of flight#1 and flight#2 for each array in W/$\sqrt{\text{Hz}}$ between 10 and 20 Hz. As we can see on these tables, the average noise levels between 10 and 20 Hz that we measured were of the order of $10^{-16}W/\sqrt{Hz}$. This is similar to the value obtained during the ground tests.

Figure 5.3 show the focal plane map of the average white noise between 10 to 20 Hz measured during Flight#1. Overall, the values measured for this flight are of the same order as those observed on the ground. The map shows that the arrays 5 and 6 have a noise level very much lower than the other arrays. We also observed the same behavior during ground tests. Since the detectors of the matrix assemblies are manufactured in the same way, the only possible explanation for this spatial distribution of noise comes from the

ARRAY	MIN $[10^{-16}$ W/$\sqrt{\text{Hz}}]$	MAX $[10^{-15}$ W/$\sqrt{\text{Hz}}]$	AVG $[10^{-16}$ W/$\sqrt{\text{Hz}}]$	MED $[10^{-16}$ W/$\sqrt{\text{Hz}}]$	STDEV $[10^{-16}$ W/$\sqrt{\text{Hz}}]$
2	2.852	9.075	5.955	5.034	6.971
6	1.161	2.092	2.178	1.918	1.367
T_Average	2.006	5.584	4.066	3.476	4.169
7	3.419	8.083	6.598	6.287	4.994
4	2.722	2.111	4.665	4.586	1.354
8	3.144	6.936	5.578	5.196	4.364
R_Average	3.095	5.710	5.614	5.356	3.571
Average	2.659	5.659	4.995	4.604	3.810

Table 5.3: Array statistics of the NEP of one scan during the night of Flight#2 in W/$\sqrt{\text{Hz}}$ between 10 and 20 Hz.

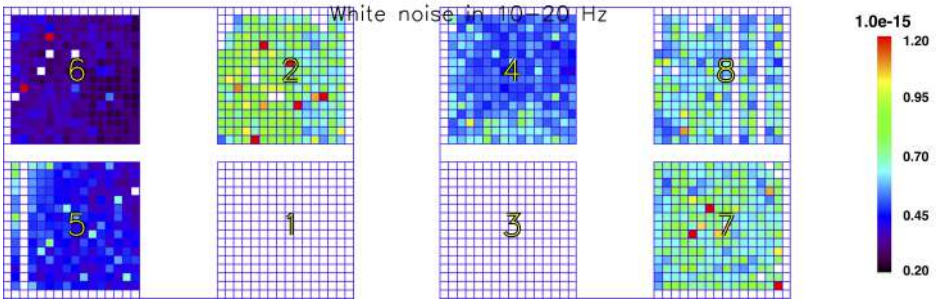

Figure 5.3: Focal plane map of the average white noise in W/$\sqrt{\text{Hz}}$ between 10 to 20 Hz measured during Flight#1.

way in which the arrays are connected. Indeed arrays 5 and 6 are connected to the same buffer unit (see section 2.1.4). This observed noise difference for the matrix pair 5-6 is therefore probably related to specific characteristics of the buffer unit to which they are connected. This is still under investigation and knowing the origin will help us to improve the noise characteristics of other arrays in the future.

5.5 Noise power spectra

Figure 5.4 shows the time-frequency behaviour of the total array-averaged signal for each array during Flight#1. We expect a contribution from photon noise (see section 5.1.1 and Lamarre (1986)) and flicker noise. We can see on this figure the increase of the 1/f noise at low frequencies. This is consistent with expectations from ground calibrations. The frequency range of individ-

ual power spectra is different for individual observations, as the scans have different lenght for each observation. This is the reason why we observe empty regions at low frequencies in the plots. The temporal variations observed at low frequencies mainly during the day are probably due to variations of the external straylight which was caused by a failure of the baffle during this flight (see section 2.4.1.5). Figure 5.5 shows the time-frequency behaviour of the total array-averaged signal for each array during Flight#2. This figure is equivalent to figure 5.4 but for the second flight. We also notice a growth in 1/f noise when the frequency decreases. Unlike Flight#1, the baffle was not degraded during Flight#2. However, for some scenes we still see variations at low frequencies. These are actually related to the method we used to decorrelate the atmospheric effects. Indeed, we perform this decorrelation scan by scan by computing the best fit linear correlation between the signal and elevation. "Scan by scan" method works very well when we scanned the sky at variable elevation. This is much less effective for scans with constant elevation because of the small variations in elevation during these scans that do not allow us to obtain a good correlation with the atmospheric signal. This was the case for scenes on planets (Jupiter, Saturn). For these scenes we have to perform the calculation of the linear fit over the whole scene. We thus obtain a better decorrelation of the atmospheric effects.

5.6 Half-pixel difference noise power spectra

Figures 5.6 and 5.7 show the power spectra computed for the difference between 2 random halves of the pixels for the first and the second flight respectively. Signal variations which are common to all bolometers of a given array are removed. We observe a significant decrease of the low frequency noise and an attenuation of the temporal variations observed in figure 5.4. Other variations are due to the residual atmospheric emission and external straylight from the degrading baffle in Flight#1. The average power spectrum on the total signal shows a raise with decreasing frequency with a slope of about -1 (i.e., noise $\propto 1/f^1$), while the uncorrelated noise raises more slowly, with noise $1/f^{0.65}$. This last behaviour is consistent with what was observed during ground tests with noise $1/f^{0.6}$.

Figure 5.8 shows the uncorrelated noise power spectra for each array averaged over the whole Flight#1 and rescaled for the fact that only half the pixels are considered, compared to the noise power spectra of each array as observed during ground calibration. It can be seen that, at intermediate frequencies, the noise observed during flight matches precisely the expected noise level. For all arrays, with the exception of arrays 5 and 6, the noise level

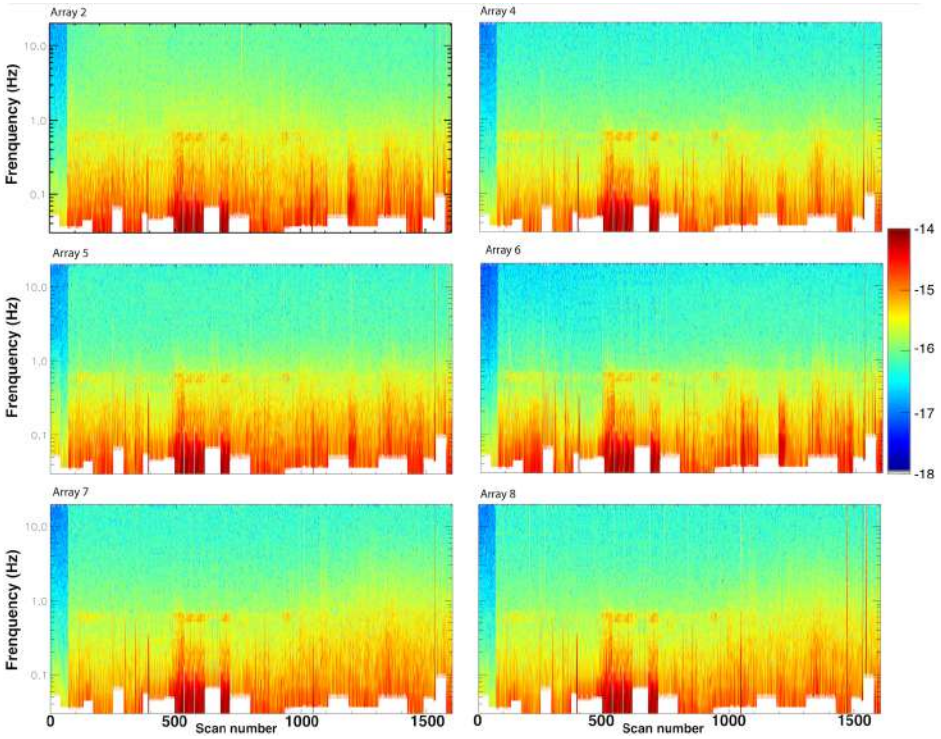

Figure 5.4: Time-frequency behaviour of the total array-averaged signal for each array during the first flight. Individual noise power spectra are computed for the array-average total signal for each individual observing scan.

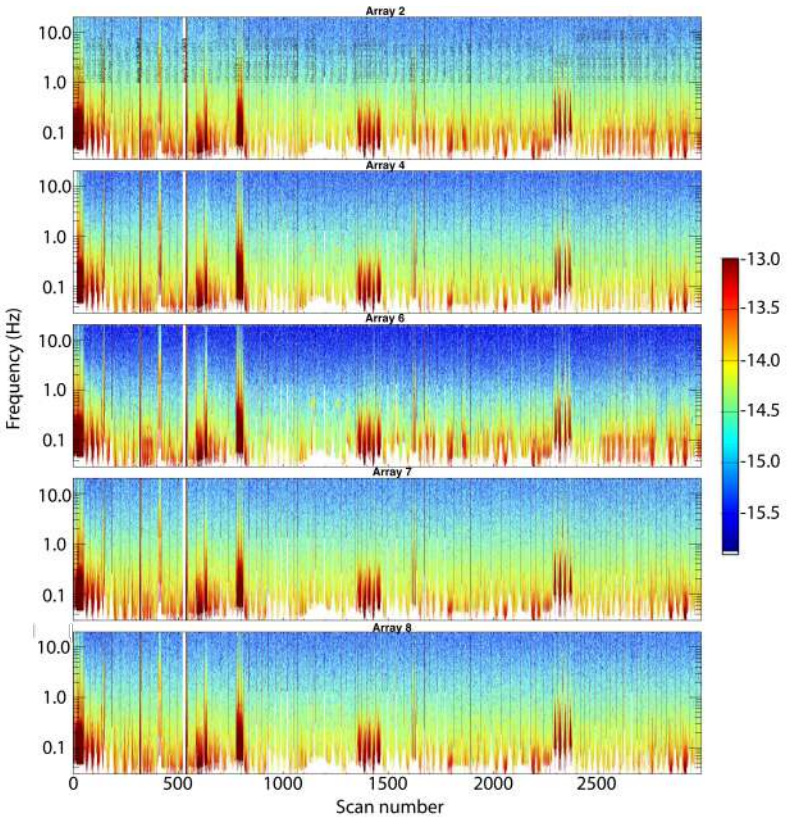

Figure 5.5: Time-frequency behaviour of the total array-averaged signal for each array during the second flight. Individual noise power spectra are computed for the array-average total signal for each individual observing scan.

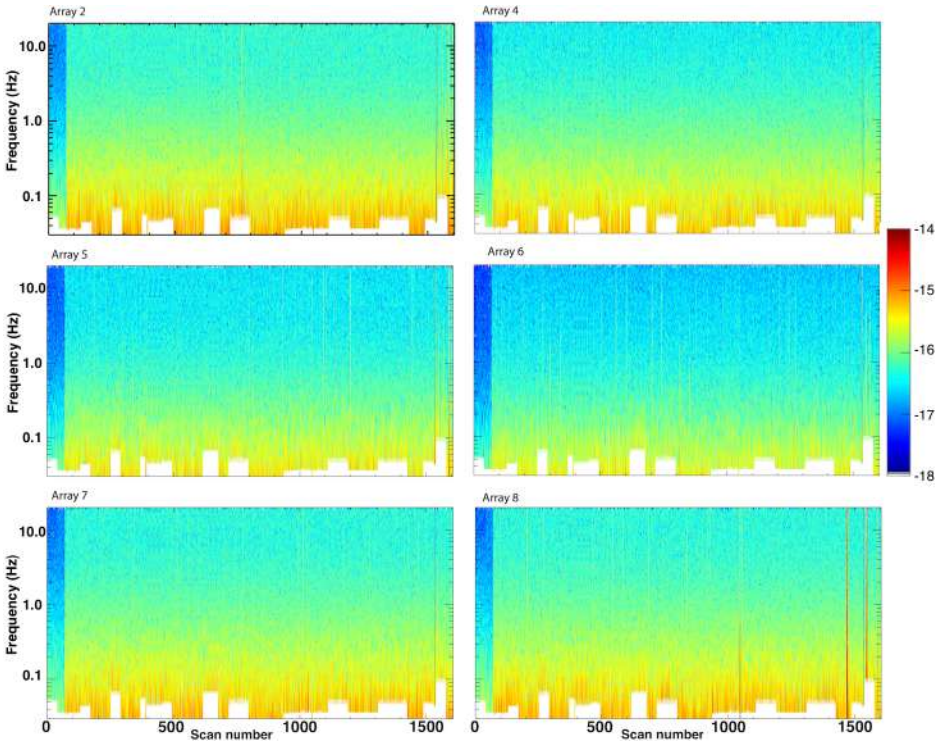

Figure 5.6: Time-frequency behaviour of the total array-averaged signal for each array during the first flight with individual noise power spectra computed for the average difference between half of the pixels of each array, thus removing common mode signal.

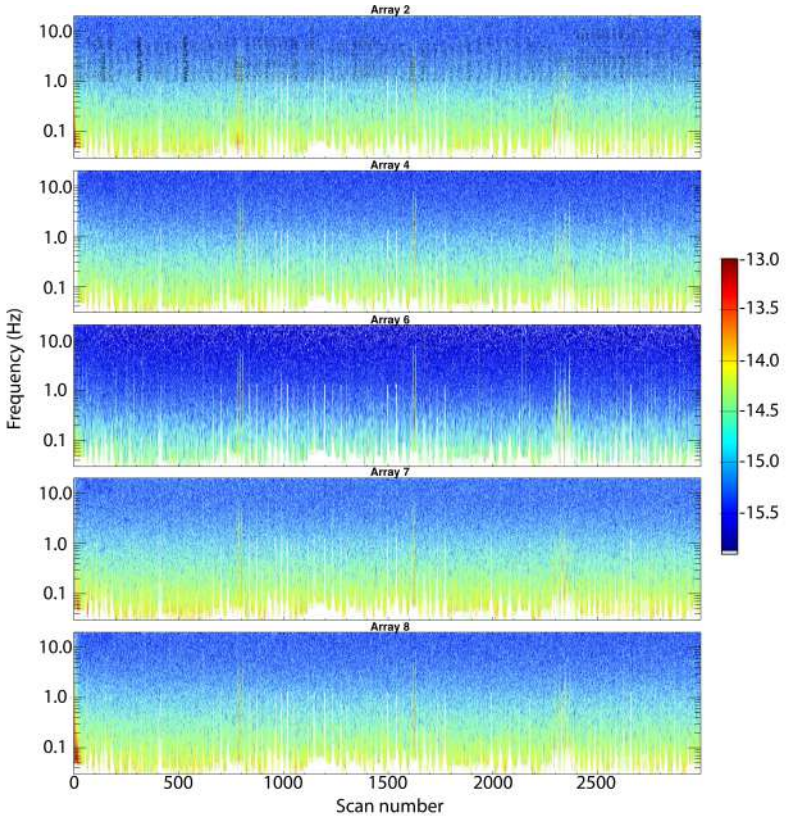

Figure 5.7: Time-frequency behaviour of the total array-averaged signal for each array during the second flight with individual noise power spectra computed for the average difference between half of the pixels of each array, thus removing common mode signal.

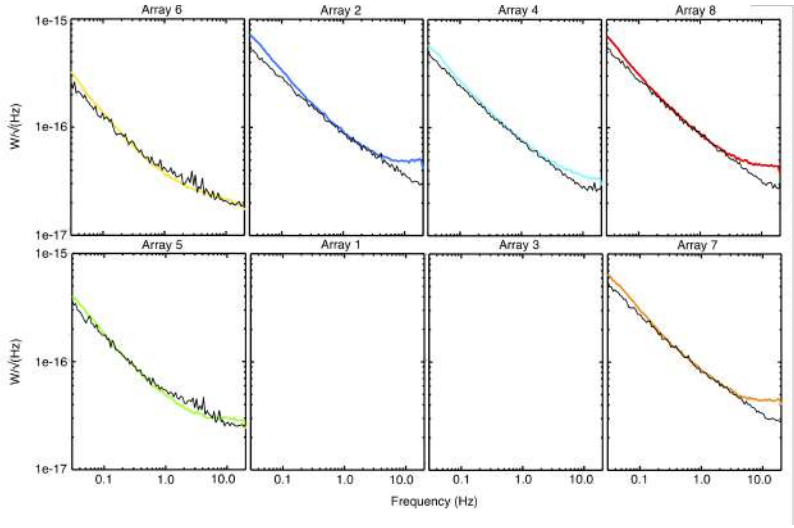

Figure 5.8: Plots of the array-averaged uncorrelated noise power spectra averaged over the whole Flight#1 (black curves) compared to noise power spectra measured during ground calibration (colored curves). The different panels correspond to the average for each array.

at high frequencies appear to be higher than the level observed during ground calibrations (up to a factor of the order of 1.5). The first explanation for this observation would be to impute it to the photon noise. But in this case we would expect the increase to be most prominent for arrays 5 and 6 which have the lowest noise levels, and this is not what is observed. Similarly, we would expect the high frequency noise excess to be stronger in outer regions of the focal plane, where the background is higher (see chapter 6), and again, a similar analysis carried for the central and the outer regions of the focal plane did not show such a difference.

5.7 Temperature fluctuations at 300 mK

Figure 5.9 shows the average signal as a function of time on array 6 and the corresponding signal power spectrum measured on a Musca scene. This scene is particularly short and contains only one scan because it was canceled because of losses in telemetry. In this figure we can see fluctuations of the signal "in teeth" appearing on the data for about 6 minutes. The frequencies marked in the signal power spectrum with the vertical red line are harmonics of $\nu_0 = 0.046$ Hz, corresponding to 21.74 sec. Figure 5.9 also shows the

evolution of the 300 mK shield temperature during the Musca scene. It is clear that the observed signal fluctuations on array 6 are related to fluctuations in temperature fluctuations measured on the shield at 300 mK. This fluctuations behaviour can be seen only on the arrays of the TRANS focal plane (array 2 and 6) but not on the REFLEX focal plane (array 1, 7 and 8). It also appears on other scenes of the flight. The fact tha dents appear at a fixed frequency of 0.046 Hz (20 sec) and harmonics, could indicate an electronics origin. Dents being due to straylight from an external source can probably be excluded, since the sun was set during this scene. Dents can be identified in the difference beetween TRANS and REFLEX arrays and can be corrected in the data.

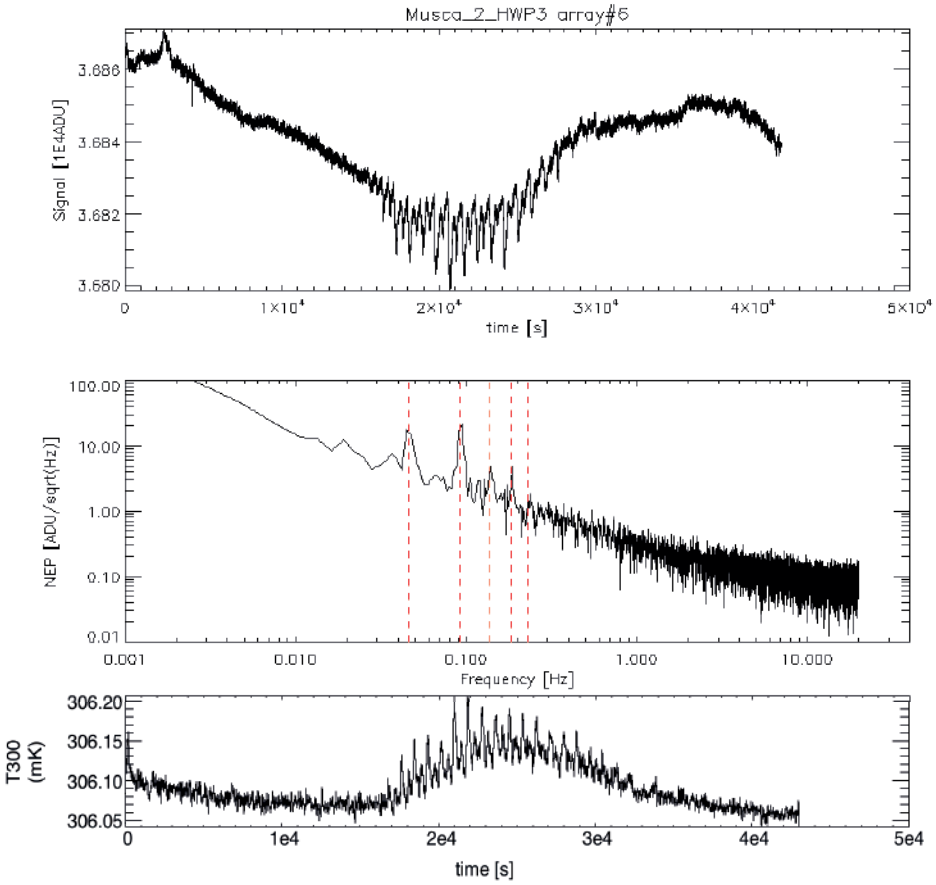

Figure 5.9: Top: Average signal as a function of time on array 6 measured on a Musca scene. Middle: corresponding signal power spectrum. The frequencies marked in the signal power spectrum with the vertical red line are harmonics of $\nu_0 = 0.046$ Hz, corresponding to 21.74 sec. Bottom: Evolution of the 300 mK shield temperature during the Musca scene

Chapter 6

Response and Background of the detectors

6.1 Background

The background signal in the bolometers originates from the thermal emissions from optical elements of the instrument. It is reduced by placing the optics inside the cryostat. Fluctuations in this background have direct impact on the stability of the instrument. The response variations of the bolometers are dependent on background variations, so it is necessary to constrain it as precisely as possible to better understand the response variation. We derived the background level in flight using a specific technique which combines electrical measurements performed during the flight and the results of ground tests carried on the PILOT focal planes. Those tests were performed in front of a controlled background using eccosorb at room temperature (300 K) and cooled down in a Liquid Helium bath (77 K). In both cases, in order to avoid absorption by the atmosphere, the space between the entrance window of the cryostat and the eccosorb was flushed with dry Nitrogen vapor. These measurements were used to establish the relation between the output voltage on the bolometer (a voltage called V_{ptmil} measured at the midpoint of the bolometric bridge for each pixel (see figure 6.1) and the intensity of the optical background incident on the detectors.

6.1.1 Backgroung level

6.1.1.1 Ground test measurements

Figure 6.2 shows the ICS intensity and the signal of one bolometer during the test session. The initial plateau of the signal corresponds to measurements of

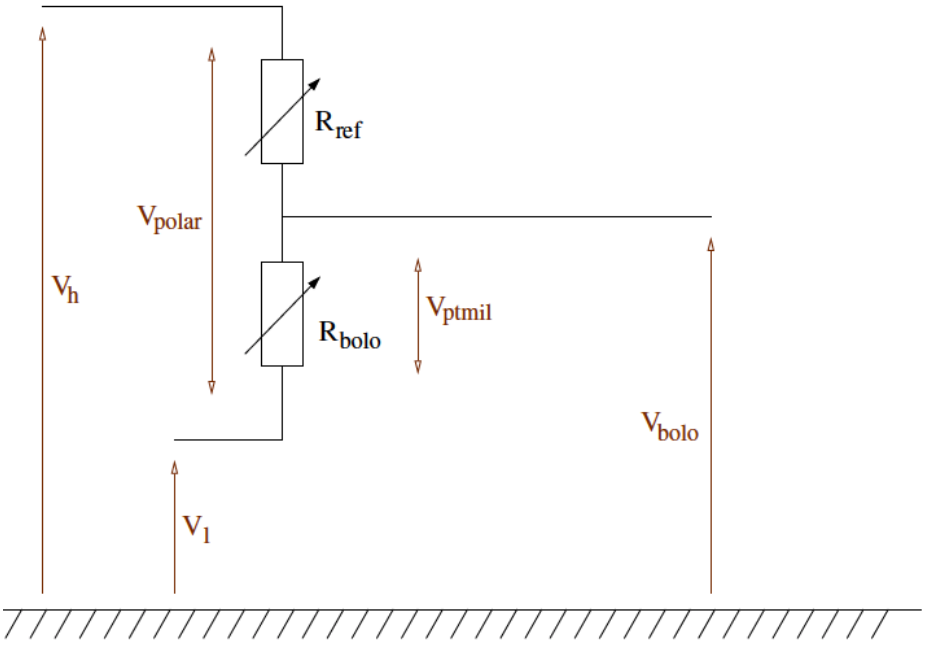

Figure 6.1: Simplified diagram of a bolometric bridge. V_{polar} is the voltage source, R_{ref} the load resistor and R_{bolo} the bolometer. Changes in the electric potential is measured across V_{ptmil}. Figure from Billot (2007)

the 300 K background. The sharp decrease of the signal corresponds to the inclusion of the 77 K liquid nitrogen (LN) bath in front of the cryostat. The following steady rise is caused by the build up of water ice forming on the entrance window of the cryostat. The sharp rise corresponds to the removal of the LN bath. Figure 6.3 shows the background image after division by the response when a 300 K eccosorb layer is placed in front of the photometer (we refer to this as 'the 300 K background'). The background values in the focal plane follows a distribution raising by about a factor of two from the center to the corners of the focal plane, a distribution that is attributed to the absorption in a lens located just in front of the focal plane in the cryostat (Misawa 2016).

6.1.1.2 Inflight measurements

Figure 6.4 and 6.5 show an example of the background image obtained during the Flight#1 and Flight#2 using this technique. Variations in the background level were measured throughout the whole flight. Typically, background values measured are between 13 to 16 pW/pixel. This is higher than the values predicted by the instrument's photometric model (which was about 8 pW). The values measured during the ground calibration in front of the 300 K eccosorb layer with an optical attenuator inserted in the cryostat gave values of about 7 pW. The background distribution in the focal plane follows a similar distribution as observed during ground calibrations, with values raising by about a factor of two from the center to the corners of the focal plane. This distribution is explained by the absorption in the lens located just in front of the focal plane. Figure 6.6 shows the evolution of the array-averaged background level during the first flight. We can see variations due to the emission of the residual atmosphere (background values are higher when observed at lower elevation) and variations due to the polarization of the instrumental background (see 6.1.2).

6.1.2 Background polarization

6.1.2.1 Ground test measurments

During the ground tests, measurements of the signal as a function of the HWP position were made (see Misawa 2016). Figure 6.7 shows the histogram of the polarization angle ψ (left panel) and polarization fraction p (right panel) during IAS tests. The black, red and blue lines show the curves for all pixels and the TRANS and REFLEX pixels, respectively. The polarization fraction measured is between 0% and 10% and the polarization angle is between 20

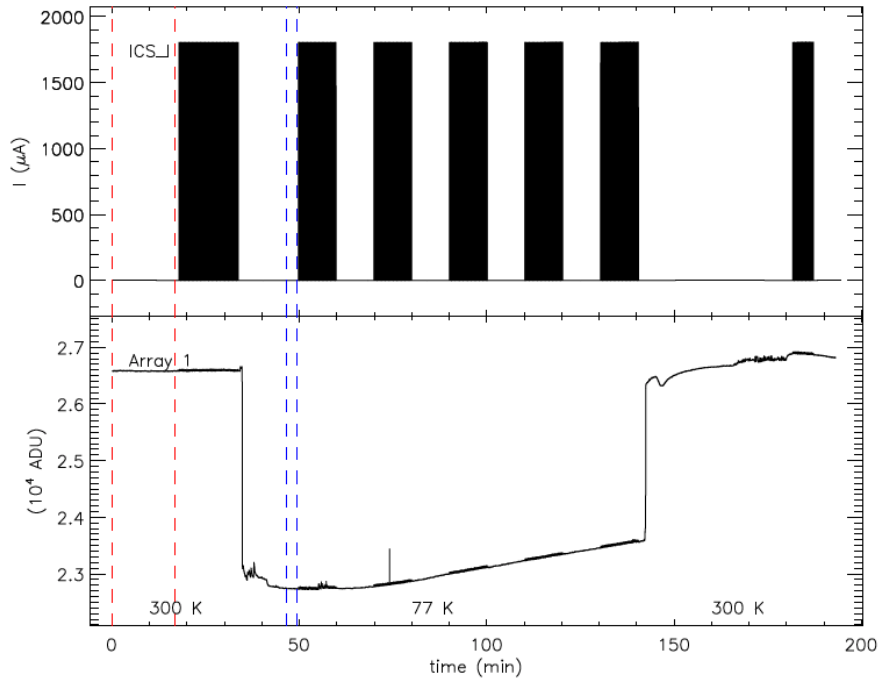

Figure 6.2: Top: ICS current; Bottom : median signal of Array 1 during the 300 K and 77 K background measurements. The first part of the plot is for the 300 K reference background measurement followed by an ICS measurement. The drop corresponds to the installation of the 77 K LN (liquid nitrogen) tank in front of the photometer. The following steady rise corresponds to the increased transmission due to frost depositing on the entrance window. The sharp rise corresponds to the removal of the LN tank. The 300 K background data is used between two red lines and the 77 K background data is used between two blue lines.

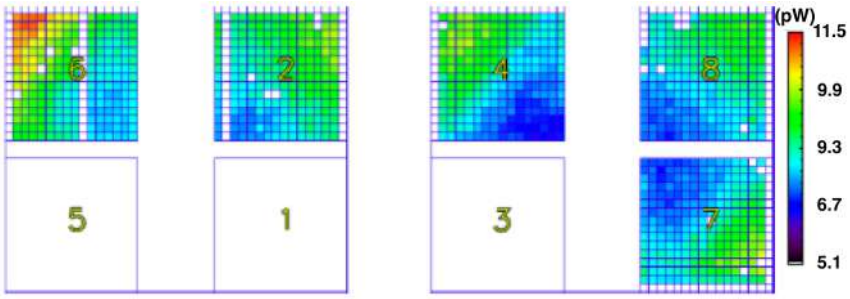

Figure 6.3: Image of the signal on the focal plane during measurements with the eccosorb at 300 K in front of the cryostat. The measured signal has been divided by the detector responses measured by CEA. Background values measured are around 7 pW/pixel.

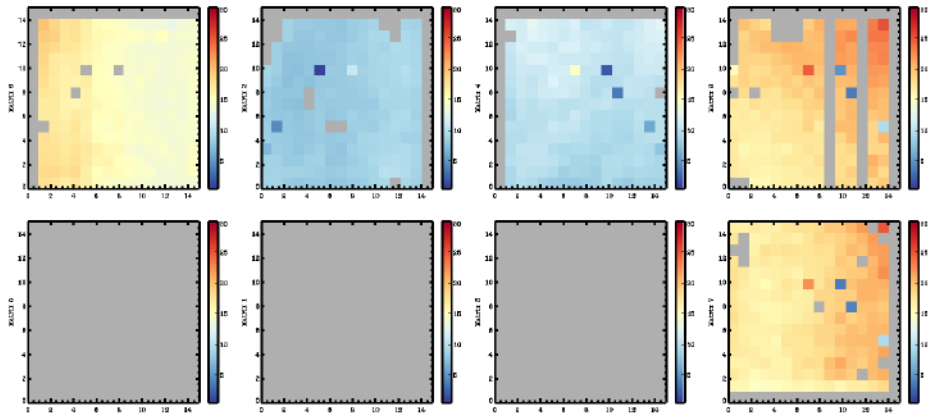

Figure 6.4: Focal plane image of the background as derived in Flight#1 for one observing session obtained during night observations. The background distribution in the focal plane follows a similar distribution as observed during ground calibrations, with values raising from the center to the corners of the focal plane. Background values measured are between 13 to 16 pW/pixel.

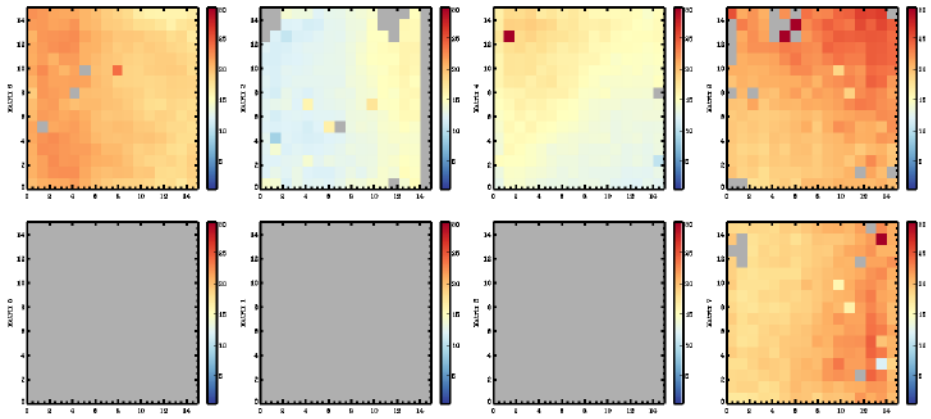

Figure 6.5: Focal plane image of the background level as derived in Flight#2 for one observing session obtained during night observations. The background distribution in the focal plane follows a similar distribution as observed during ground calibrations, with values raising from the center to the corners of the focal plane. Background values measured are between 13 to 16 pW/pixel.

and 5 degrees. The origin of this polarization is uncertain, but may come from the optics of the instrument (in particular the transmission of lens L2).

6.1.2.2 In-flight measurements

Figure 6.8 shows variations of the signal observed on each array as a function of HWP positions during an observation where observing coordinates were essentially constant and the HWP was rotated. We can clearly see on this plot the square modulation due to the ICS signal was turned on during this observation. The signal seems to adopt a sinusoidal shape in phase opposition between the arrays in transmission and in reflection. We used this data to derive the polarization properties of the background. Figure 6.9 shows polarisations angles distributed between 80^o and 100^o from the vertical direction, corresponding to a horizontal polarization. The polarization direction seems to be constant over the focal plane. The polarization fraction is between 4% and 10%. This shows that, as we observed during ground calibrations, the instrumental background is polarized. In flight the fraction of polarization is similar to that observed on the ground, but not the direction of polarization. This difference observed on the polarization direction between ground tests and flights can be attributed to a different origin of the background in the two situations. During the ground measurements, the background is

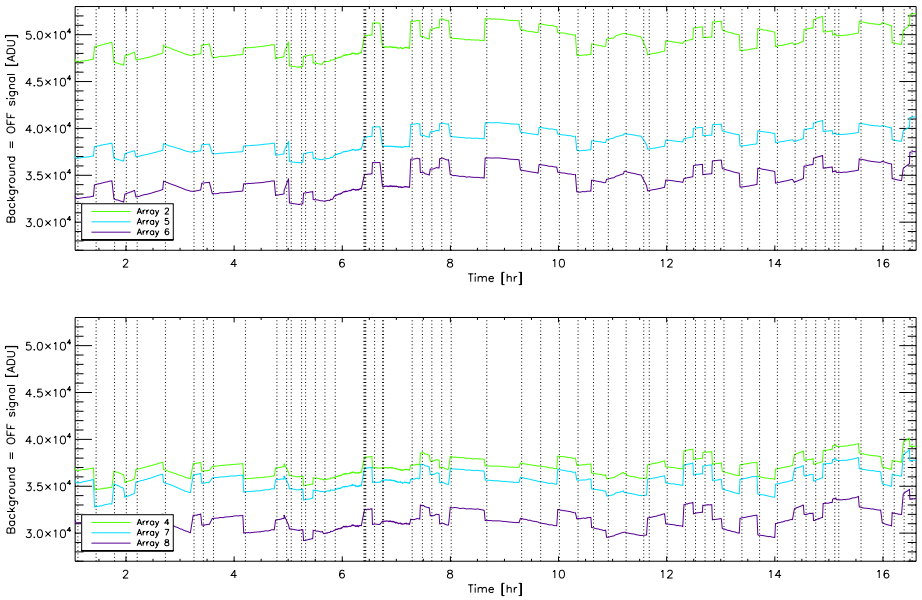

Figure 6.6: Variation of the array-averaged background level on the TRANS (top) and REFLEX (bottom) focal plane arrays during the first flight. Colours indicate different arrays. The vertical dashed lines indicate boundaries between different observations. The variations are mostly due to changes in HWP positions and elevation of of observations between different observations.

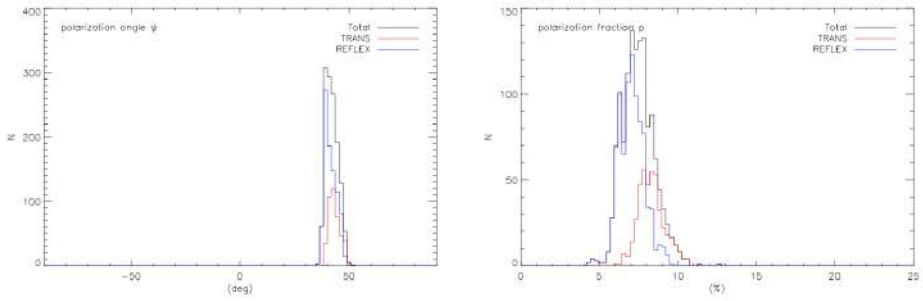

Figure 6.7: Histogram of the polarization angle ψ (left) and polarization fraction p (right) during IAS tests. The black, red and blue lines shows the curves for all pixels and the TRANS and REFLEX pixels respectively.

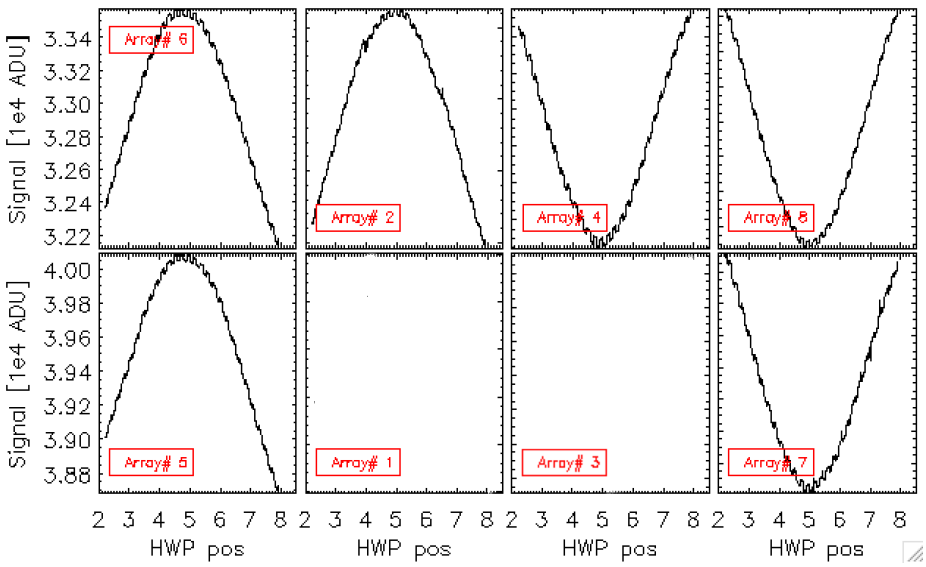

Figure 6.8: Variation of the background signal as a function of the HWP for all arrays during one observation of the first flight. The square modulation of the ICS signal is visible on all arrays. The sine curve with opposite phase on the TRANS and REFLEX arrays is due to the polarization of the instrumental background emission.

dominated by the room atmosphere in the few first centimeters in front of the entrance window of the cryostat. The fact that the angles are strongly rotated indicates that polarization probably arises from propagation of the unpolarized background through the instrument, with a differential rotation depending on origin of the instrumental background.

The background polarization study on Flight#1 was repeated during Flight#2 using a scene specifically designed for this measurement. During this scene, the half wave plate was moved successively from position 1 to position 8 and then from position 8 to position 1. Variations of the signal observed on each array as a function of HWP positions are shown in figure 6.10. The signal amplitude varies by about $2 \cdot 10^3$ ADU, which is equivalent to 0.5 pW (i.e., 6% of the expected background at 8 pW). The maximum (on TRANS array) / minimum (on REFLEX arrays) of the signal is around HWP position 5, which corresponds to the fast axis of the HWP being roughly vertical in the instrument restframe. Given the orientation of the polarizer in the instrument, this implies a polarization direction roughly horizontal.

Figures 6.11 and 6.12 shows variations of the signal observed on each pix-

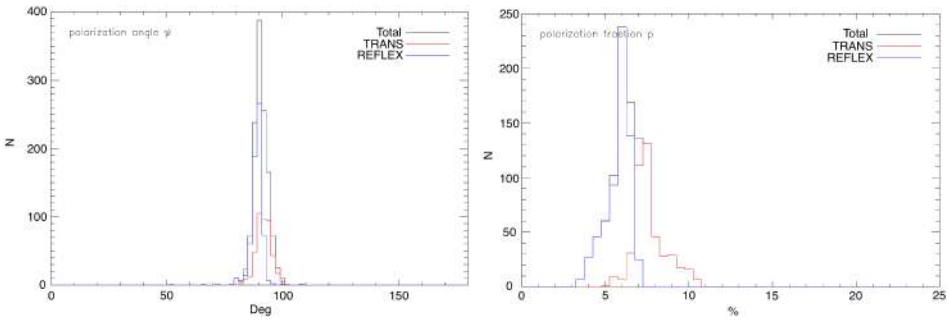

Figure 6.9: Histogram of the polarization angle ψ (left) and polarization fraction p (right) during Flight#1. The black, red and blue lines shows the curves for all pixels and the TRANS and REFLEX pixels, respectively.

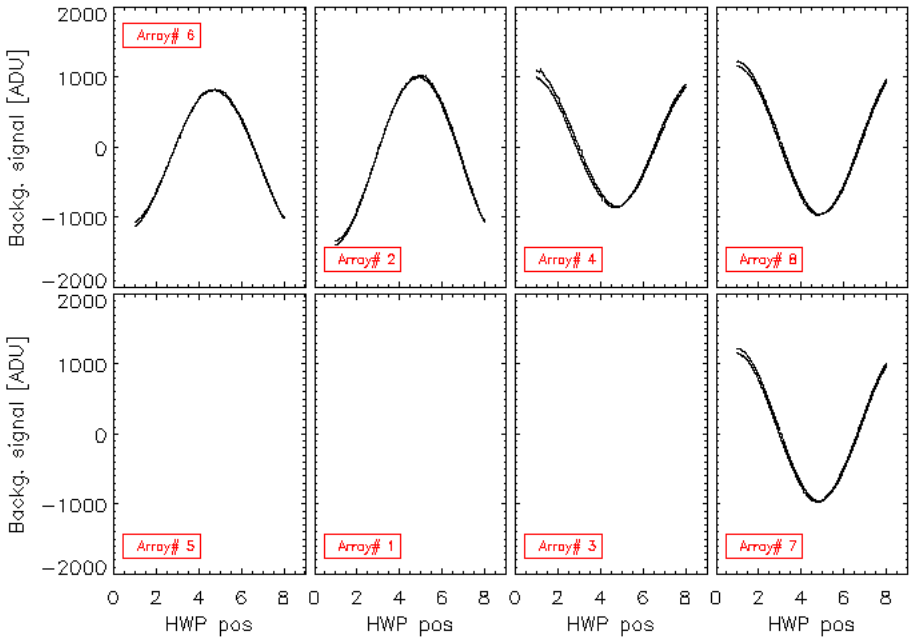

Figure 6.10: Variation of the background signal as a function of the HWP for all arrays during one observation of the second flight. The sine curve with opposite phase on the TRANS and REFLEX arrays is due to the polarization of the instrumental background emission.

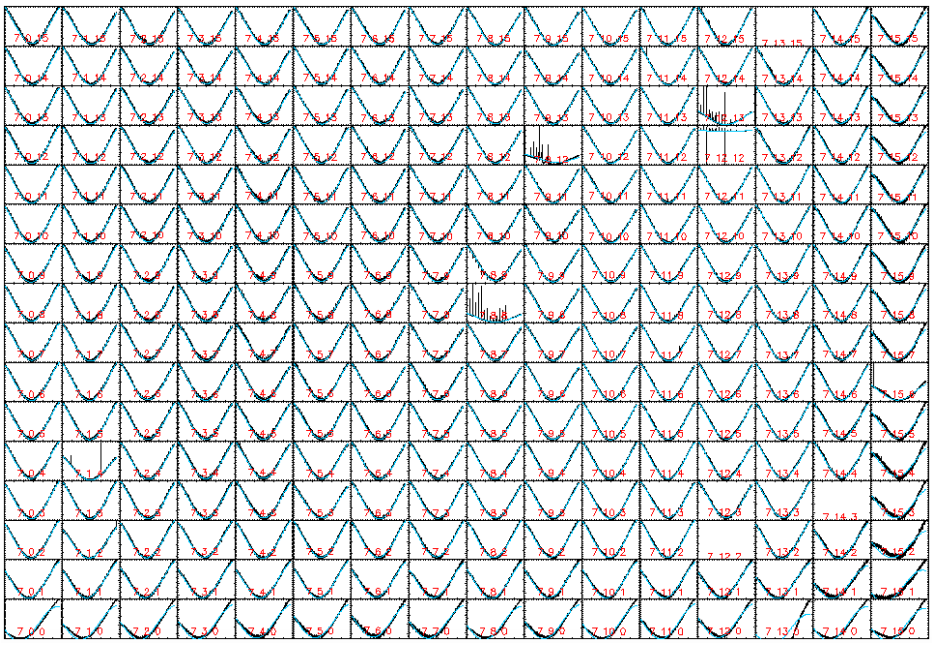

Figure 6.11: Variation of the background signal as a function of the HWP for all pixels of array 7 during one observation flight#1.

els for array 7 as a function of HWP positions for flights 1 and 2, respectively. These signal variations were fitted by the following equation (see chapter 8):

$$S_{T/R} = \frac{1}{2}(I \pm Q\cos 4\omega \pm U \sin 4\omega), \tag{6.1}$$

were ω is the angle of the fast axis of the HWP with respect to the scan direction; I,Q,U are the fitted Stokes parameters in the instrument reference frame. The minus sign is used for the focal plane in transmission and the plus sign for the focal plane in reflection.

The adjusted curves are shown in blue in the figures 6.11 and 6.12. We can see that for the first flight, pixels along the edges of the focal plane shows unexpected polarization curves that cannot be fitted with the equation 6.1. This was already seen in ground calibrations, and was due to reflection by the image field stop. As shown in figure 6.12, the increase in the size of the field stop between the two flights has been effective since the polarization curves at the edge of the arrays now shows a behavior similar to that observed for the rest of the pixels of the array. This study was also used to determine the bad pixels for each array. Thus pixels are defined as bad pixels when showing abnormal polarization curves.

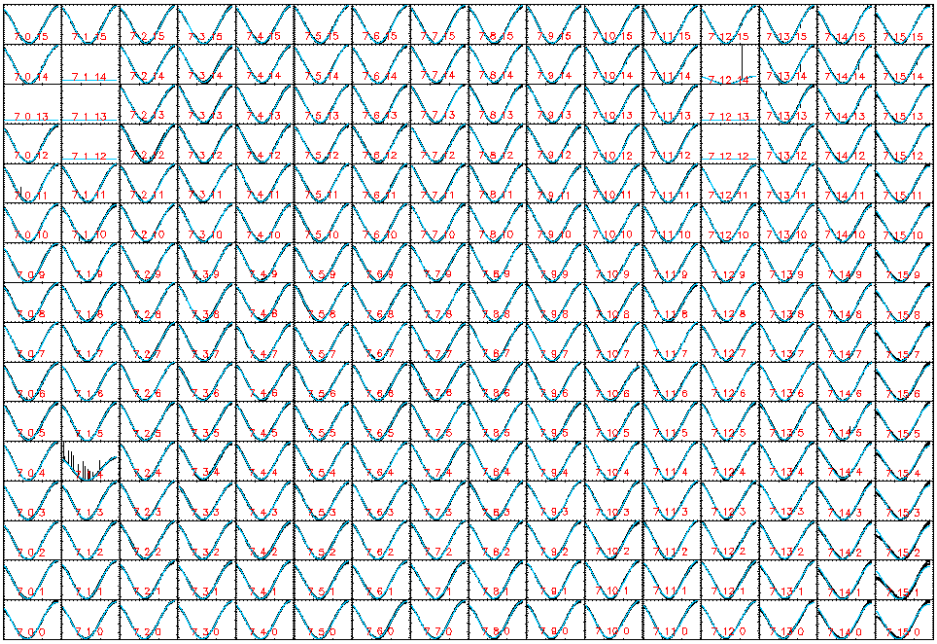

Figure 6.12: Same as figure 6.11 for Flight#2.

6.2 Responses

The response of the bolometers is obtained by dividing the amplitude of the electric signal Δsignal by the amplitude of the flux modulation Δflux that generated this Δsignal:

$$R_{ICS} = \frac{\Delta\text{signal}}{\Delta\text{flux}}, \tag{6.2}$$

The detector signal is measured by averaging the signal when the ICS is ON and when the ICS is OFF. In order to remove transient signal between ONs and OFFs, several data samples are ignored at the beginning and end of each ON and OFF sequence. Ground calibration tests have shown that the ICS flux is directly proportional to the power dissipated in the ICS. The response of the bolometer is thus expressed in the following way:

$$R_{ICS} = \frac{\Delta signal}{\Delta P_{ICS}} \tag{6.3}$$

with:

$$P_{ICS} = U_{ICS} \cdot I_{ICS}, \tag{6.4}$$

where U_{ICS} is the electrical voltage applied to the ICS and I_{ICS} is the current in the ICS. The reference value of the electrical voltage for normalization is 0.54 V corresponding to an ICS resistance of 300Ω and an ICS current reference value of 1.8 mA. The values of I_{ICS} and U_{ICS} are measured throughout the flight. When the current applied to the ICS is greater than 2 mA, the measurement of U_{ics} and I_{ics} are saturated. The saturated voltage measurement is a constant value set at Vsat = 0.56084837 V. The saturated current measurement is a function of the commanded current. The measures are therefore corrected in the context of the study of the responses. This response is expressed in ADU (Analog digital unit) per Watt and converts to volts per watts using the gain value applied during the measurement. We call "ICS Image" the 16x16x8 maps of ICS signal variations on the focal plane.

6.2.1 Temporal variations

To constrain variations in response in flight data, we used the calibration sequences taken during each scene. ICS ON-OFF sequences are corrected for amplitude drift by applying a low-pass filter, defined when ICS is OFF, to all ICS data. The signal variations due to the elevation change in the ICS sequences are removed from the data by using the ICS off sequences. This protocol allows us to remove effects that can bias ICS ON-OFF measurements and that are not due to actual variations in detector response.

Figure 6.13 shows the array-averaged detector response to the ICS throughout the PILOT Flight#1. Arrays on the TRANS focal plane are shown in the top panel, and arrays on the REFLEX focal plane are shown in the bottom panel. The absolute values of R_{ICS} during flight are lower than the values that were observed during the ground tests. This is probably due to a higher background level on the detectors during this flight. We can see clear temporal variations in the response throughout the flight. We also clearly see offsets between different arrays. The most abrupt changes in response are visibly correlated with elevation changes or HWP position changes. The peak-to-peak variation is 30 to 40% for arrays on both focal planes. It can also be noted that the variations of responses for the arrays of the same focal plane are correlated. At boundaries, arrays on the TRANS focal plane often shows the opposite behaviour to arrays on the REFLEX focal plane. At the change near t=4.25 hr, for example, the array-average detector response to the ICS decreases for arrays 2, 5 and 6, but increases by a similar magnitude for arrays 4, 7 and 8. This behaviour suggests that some of the detector response variations are due to changes in the background level, itself induced by the polarization of the background. Figure 6.14 is similar to 6.13 but applied to Flight#2. As before, we can note variations over time of the re-

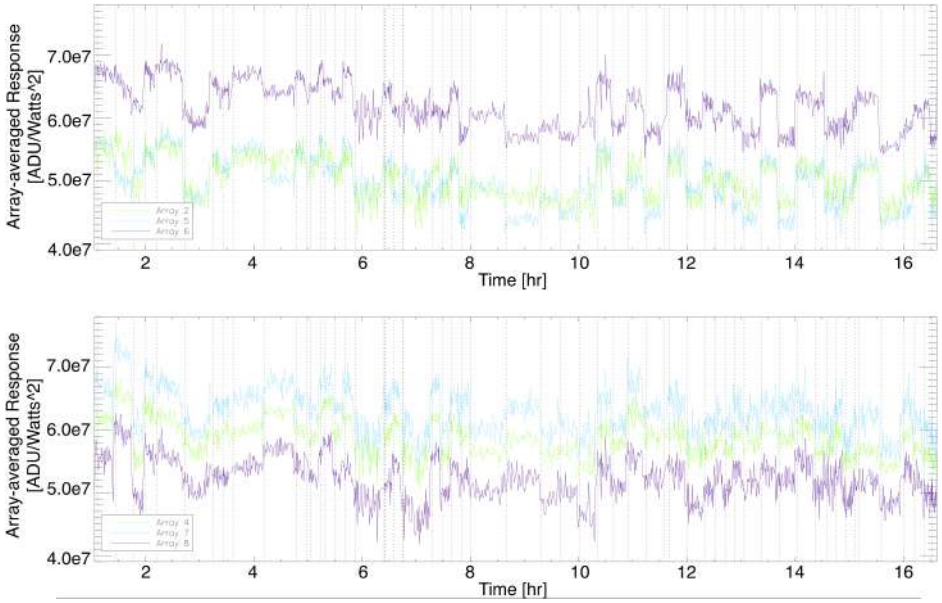

Figure 6.13: Variation of the array-averaged detector response to the ICS for arrays on the TRANS (top) and REFLEX (bottom) focal planes during the first flight. Colours indicate different arrays. The vertical dashed lines indicate boundaries between different observing

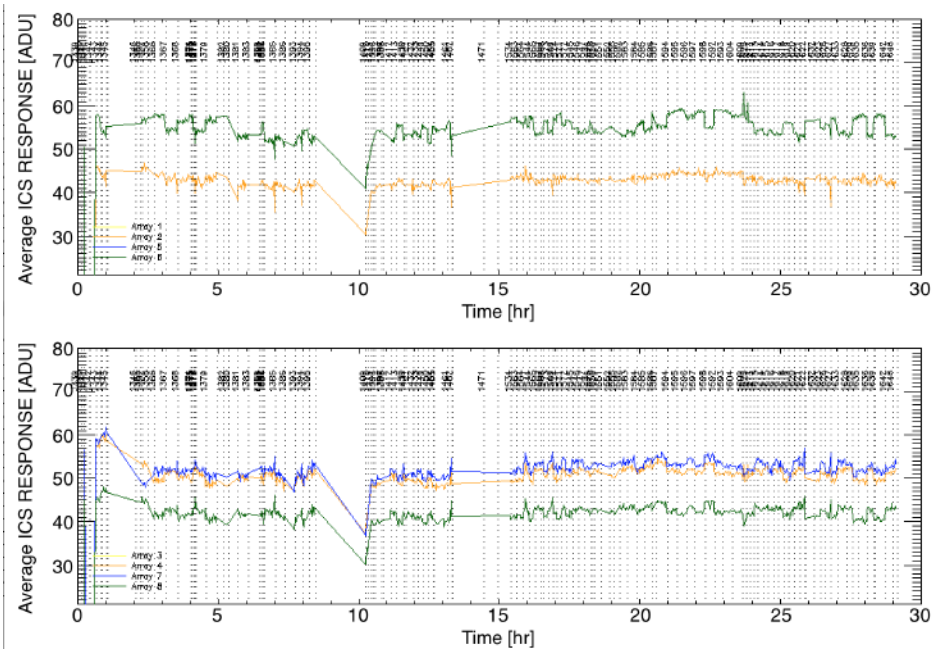

Figure 6.14: Variation of the array-averaged detector response to the ICS for arrays on the TRANS (top) and REFLEX (bottom) focal planes during the second flight. Colours indicate different arrays. The vertical dashed lines indicate boundaries between different observing

sponse related to the elevation of the gondola and changes in position of the HWP. We noted for the first flight that the variations of response between the TRANS and REFLEX array were clearly correlated. When we look at t = 26 h for example, this correlation still seems to be present between the array 6 and the arrays 4, 7 and 8 but does not appear when we look at the array 2. This is probably due to the fact that the array 2 present the worst response.

Figure 6.15 shows the array-averaged response normalized by the averaged TRANS and REFLEX responses. As expected, the variations associated with changes in HWP position disappear. In general, we observe that array 6 has the best response while the arrays 8 and 2 which present the worst response. Array 6 is 25% more responsive than arrays 2 and 8. The variations in the array-averaged responses over time is between 3 and 4%. We observe a degraded response at around t=10h on all arrays, that returns to normal values a few minutes later. This is due to the increase in temperature of the focal plane after the cycling of the 300 mK fridge during flight.

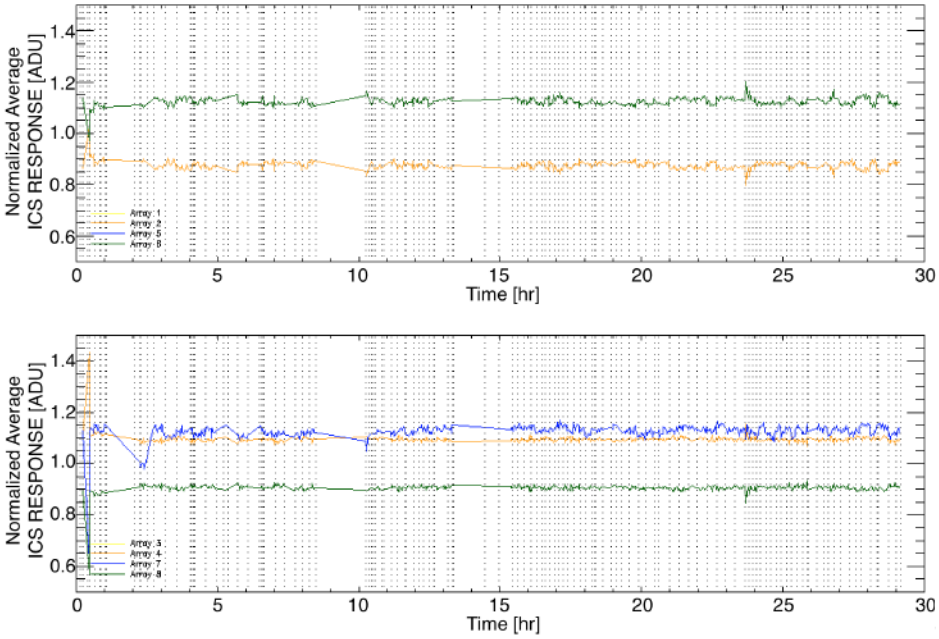

Figure 6.15: Variation of the array-averaged detector response to the ICS for arrays on the TRANS (top) and REFLEX (bottom) focal planes during the second flight normalized by the averaged Trans and Reflex response for arrays 2,6 and 4,7,8, respectively. Colours indicate different arrays. The vertical dashed lines indicate boundaries between different observing

6.2.2 Response Variations with Background

We investigated the link between the response variations and the background in two ways. In figure 6.6, showing variations in background level as a function of time, high frequency fluctuations of the background level within individual observing sequences are not observed. At boundaries, the background level shows abrupt changes, qualitatively similar to what is observed for the detector responses in Fig. 6.13. A visual comparison between figure 6.6 and 6.13 suggests that the average reponse of an array increases when the average background decreases.

The data in Fig. 6.13 shows considerable scatter for each array. We have started to explore whether there are additional parameters that influence the detector response during flight. Although variations of the focal plane temperature (300 mK stage) were small ($\sim 1\%$) during flight, our analysis of the ground test calibration data indicated that the detector response decreases strongly with focal plane temperature.

In figure 6.16, we shows the relative variation in the array-averaged detector response as a function of the array-average background (y-axis) and focal plane temperature (x-axis) for each array. The values are normalized by the median response for each array throughout the whole flight, and the limits of the rainbow colour scale are set such that a 15% increase of the response appears blue, and a 15% decrease of the response appears red. The main trend that we observe is the variation of the detector response with background that we described above, which is evident in Figure 8 as a gradual change in colour from blue to red with increasing background. When the background increases by 1 pW, this leads to a response variation between 12 and 25%. This variation is dependent on the position of the half wave plate. However, a temperature dependence of the ICS response does not seem obvious.

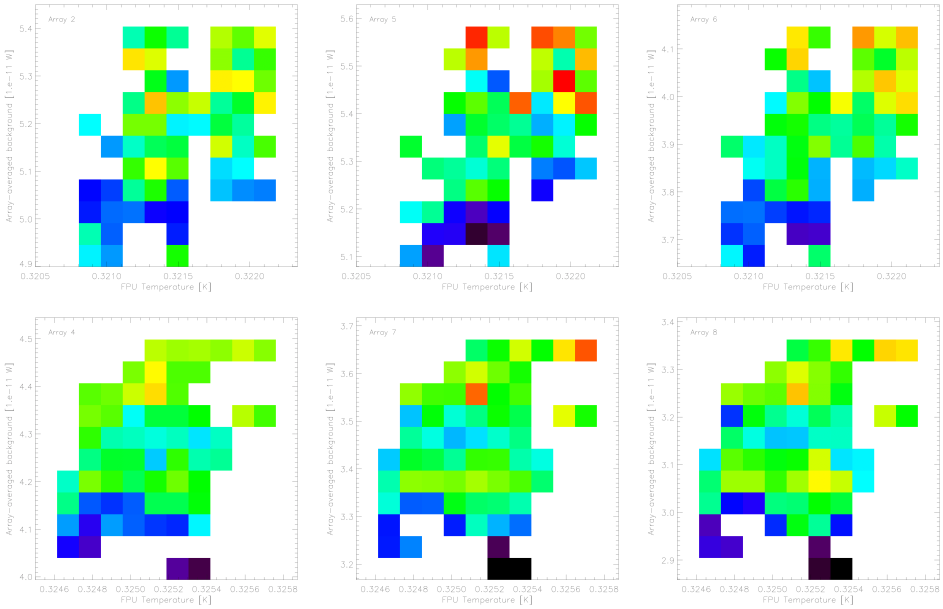

Figure 6.16: Relative variations of the array-averaged detector response as a function of the array-averaged background level (y-axis) and focal plane temperature (x-axis) on each array. The top row shows arrays on the TRANS focal plane, and the bottom row shows arrays on the REFLEX focal plane. The values for each array are normalized by the median response for that array throughout the flight. The measurements are presented using a rainbow colour stretch, such that blue represents a 15% increase of the response, red represents a 15% decrease of the response, and green represents a negligible response variation relative to the average value.

Chapter 7

Optical quality

The point spread function (PSF) is a mathematical function describing the response of an imaging system to a point source. It is also referred as the optical impulse response, the PSF being the impulse response of a focused optical system. When the imaging system is considered linear and invariant, the effect of the PSF is described by a convolution operation on the actual data. In the case of diffraction-limited telescopes, the PSF is dominated by the configuration of the aperture and it is key to many aspects of astrophysical observations. An error in the estimate of the PSF would lead to errors in the calibration and the interpretation of the observations. In addition, images taken by different telescopes have different resolutions. The comparison between each of these images requires the application of a procedure that uses a convolution kernel based on the knowledge of the instrumental PSF. It is also needed to control the image quality across the extent of the focal plane ($0.8^o \times 1^o$)

7.1 Ground tests

The PSF of the instrument was estimated during the ground end-to-end tests at IRAP, before the first flight, using a 1 meter diameter collimator. We used a microscanning technique that consists in moving a point source in the focal plane of the collimator at the focus over a few pixels of the arrays with steps values of arround 1/10th of a pixels. The images corresponding to each step position are constructed by averaging individual frames when the source was on, and subtracting the corresponding frames when the source was off. Individual images are then shifted by the known displacement of the source at the focus of the collimator, brought back to array pixel space through the focal plane geometry. The individual shifted images are then co-added to

produce the final microscan PSF map. Figure 7.1 shows the measured and simulated PSF obtained from these measurements and the profiles of these PSF. The FWHM of the measured PSF during this test is around 2' (1.44 pixels).

7.2 In-flight PSF

In order to determine the in-flight PSF, observations were made during Flights#1 and #2 on Jupiter, Saturn and Uranus, assimilated as point sources at the PILOT angular resolution. High resolution maps of the planet at 0.1' sampling were calculated for each array and for each scan. The parameters of the PSF were derived using an elliptic Gaussian fit. Figure 7.2 shows the images of Jupiter obtained for each array during Flight#2. These images have dimensions of $\sim 20'$x$20'$ were constructed with a pixel size of 0.1'. Note that they were constructed from the data that have been corrected for the responses as described in section 9.2. In these first estimates, the data have not been corrected for systematic effects that could affect the shape of the PSF such as time constant. The PSF shows no particular elongation along the scan direction, which indicates that smearing effects along the scan direction due to, for instance, the time constant of the bolometers, has a limited impact on their shape. However, the PSF images are boxy, which is likely due to the convolution of the optical PSF with a square pixel (see section 7.3).

Table 7.1: Array statistics of the PSF FWHM (arcmin).

ARRAY	MIN	MAX	AVG	MED	STDEV
2	2.49	2.49	2.49	2.49	0.00
6	2.26	2.45	2.35	2.37	0.07
TRANS	2.26	2.49	2.37	2.37	0.08
7	2.12	2.58	2.41	2.48	0.16
4	2.08	2.60	2.40	2.50	0.17
8	2.36	2.58	2.45	2.41	0.10
REFLEX	2.08	2.60	2.42	2.46	0.15
ALL ARRRAYS	2.08	2.60	2.40	2.41	0.13

Figure 7.3 shows the FWHM values obtained for the major axis and the minor axis of the PSF. The average and median values for each array as well

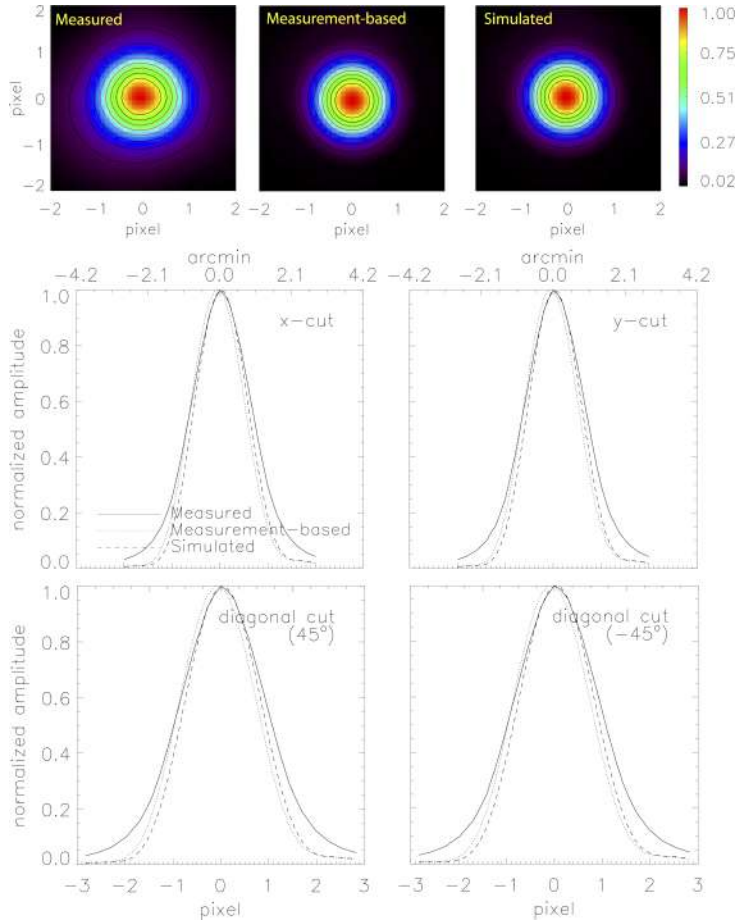

Figure 7.1: Top: images of the PSF measured at the best focus position (left), simulated PSF based on measured micro-scanning position (middle), and the simulated single PSF (right). The measured PSF is obtained from a micro-scanning pattern around pixel (3, 7) of array 6. The simulated single PSF corresponds to the beam at measured position. The amplitude is normalized to the peak intensity. The dimension of the images is 4x4 pixels corresponding to 5.6'x5.6' . The contour levels are in steps of 0.1 between 0.1 and 1.0. Middle and Bottom: profiles of the measured PSF (solid line), the simulated PSF (dashed line) and the measurement-based simulated PSF (dotted line) along the pixel axis and along axis rotated at 45^o and -45^o. Figure from Misawa et al. (2016)

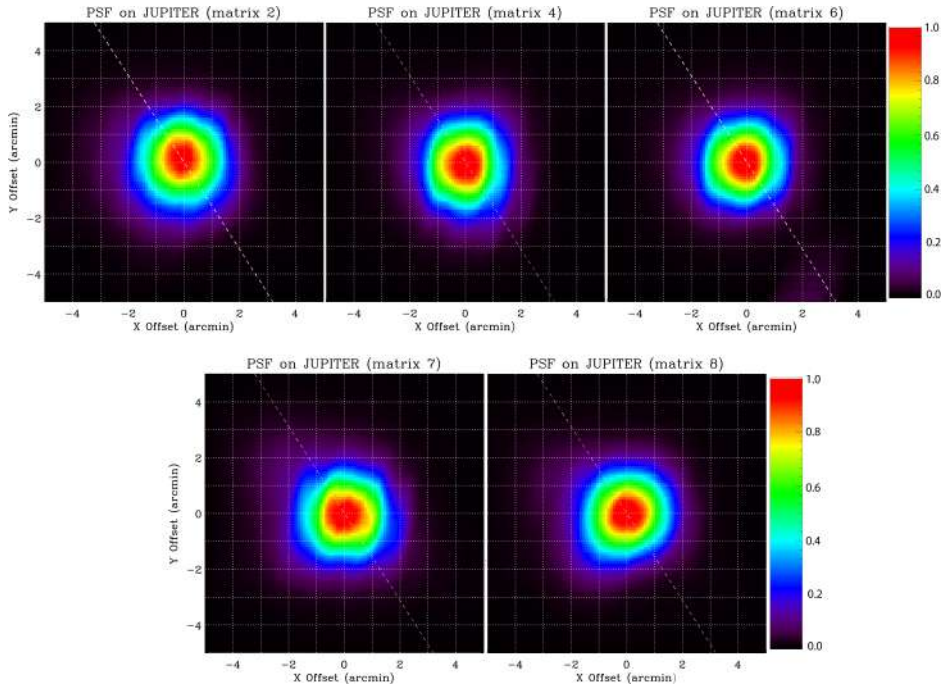

Figure 7.2: Images of Jupiter obtained during FLIGHT#2 with each array of the focal plane, during one of the two observing sequences of the planet. The scan direction is shown by the dashed white line.

Table 7.2: Array statistics of the PSF FWHM (arcmin) measured on data corrected from time constant.

ARRAY	MIN	MAX	AVG	MED	STDEV
2	2.45	2.58	2.53	2.54	0.05
6	2.05	2.34	2.21	2.27	0.09
TRANS	2.05	2.58	2.31	2.28	0.17
7	2.25	2.55	2.42	2.44	0.10
4	2.03	2.54	2.36	2.43	0.16
8	2.34	2.58	2.44	2.51	0.10
REFLEX	2.03	2.58	2.41	2.43	0.13
ALL ARRRAYS	2.03	2.58	2.37	2.40	0.15

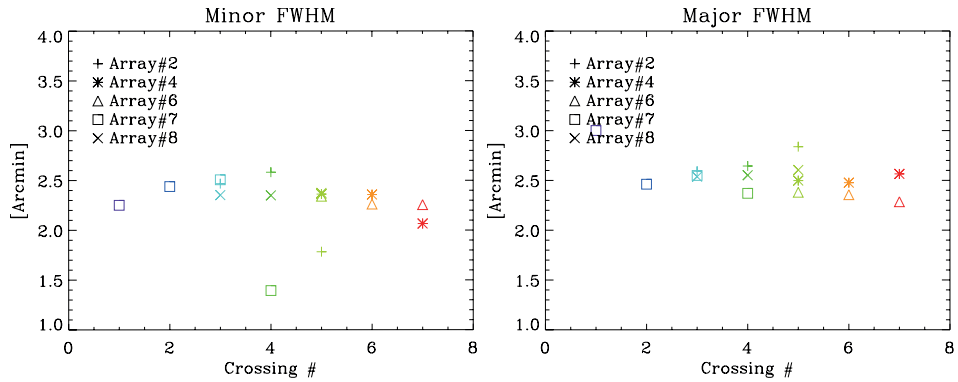

Figure 7.3: Minor axis (left) and major axis (right) of the PSF obtained on Jupiter during the second flight.

as the rms are given in table 7.1. We derive an average FWHM of the PSFs around 2.40' with small relative variations between the arrays ($\sigma = 0.13'$). Table 7.2 is the same as table 7.1, but values are derived from data corrected from the time constant measured on the ICS sequences. As expected, the derived averaged value, FWHM = 2.37', is slightly lower than previously but this diffence is small. Taking into account that the apparent size of Jupiter during the observations was 44.2 arcseconds (0.7367 arcminutes), we derive, after deconvolution, the average FWHM of the PSF $\approx 2.25'$.

Furthermore, Jupiter imaging can be used to check the pointing accuracy. Thus, figure 7.4 shows the difference between the measured position on the sky of the maximum value of the PSF and the expected value of Jupiter po-

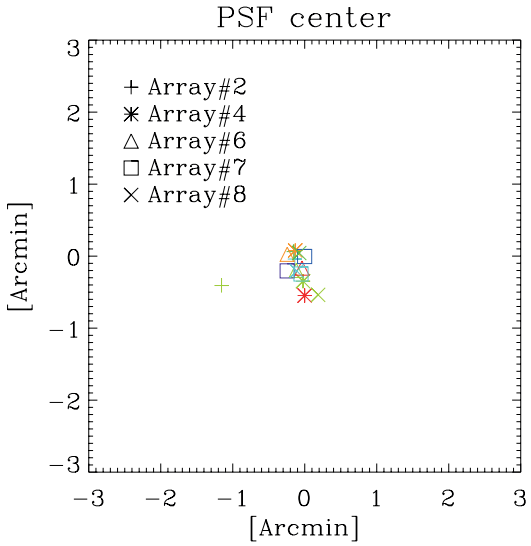

Figure 7.4: PSF center position obtained on Jupiter during the second flight.

sition as defined by the ephemeris. This offset is $\leq 1'$. Without correction of the geometry of the focal plane, we should observe larger differences between arrays. This validates the corrections made on the pointing described in chapter 4. However, between each scans we observe a slight drift of this offset showing the need to refine the study on the offset estadius at the scale of the scan or the scale of the sample (via the barycentric method. See chapter 4)

7.3 Simulated PSF

To understand the origin of the "box effect" which may be induced by the convolution of the PSF and the size of the bolometers pixels, we performed simulations generating timelines at the sampling frequency of PILOT. I have proceeded in two steps. We first generate a Gaussian function of the following form:

$$f(x,y) = A \exp -(\frac{x-x_0}{2\sigma_x^2} + \frac{y-y_0}{2\sigma_y^2}), \tag{7.1}$$

where x_0 and y_0 are the coordinates of the maximum value of the source. They were calulated from the theoretical position of Jupiter, at the time of the observation, provided by the ephemeris; σ_x and σ_y define the standard deviation along x and y (the FWHM is equal to 1.4'). Then the value of

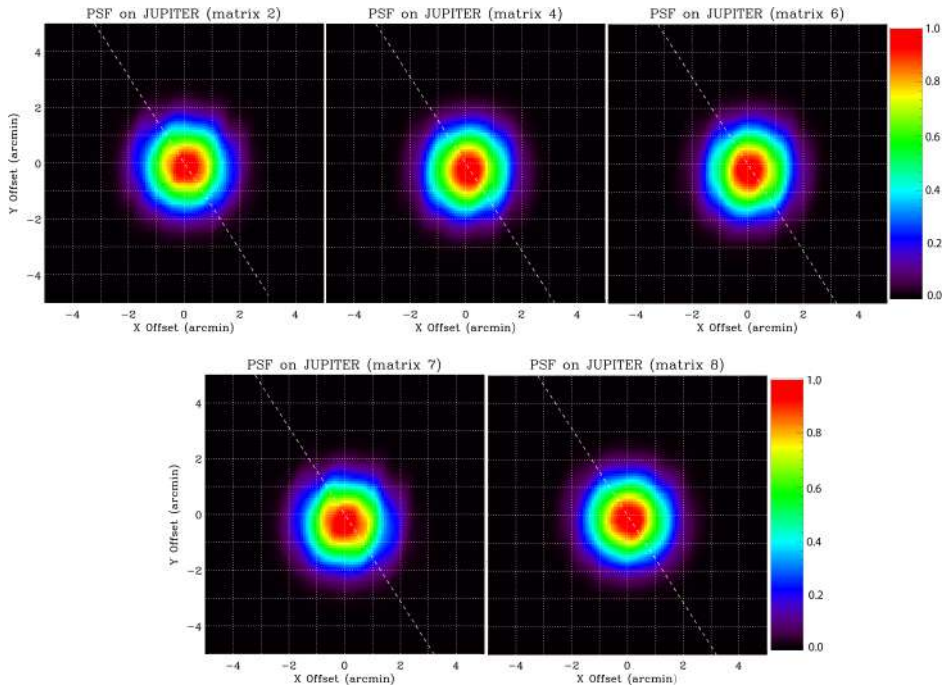

Figure 7.5: Simulation of Jupiter obtained for each array across the focal plane, based on the two observing sequences of the planet during Flight#2. The scan direction is shown by the dashed white line.

each sample of a timeline is calculated as the integral of this function on a square with a side of 1.4' (which corresponds to the solid angle of a pixel) taking into account the distance between the bolometer and the center of the previously generated Gaussian PSF. The resulting maps are shown in Figure 7.5. The simulated PSF also shows the observed "box effect" on the flight data. Similarly, the orientation of the box effect confirms the hypothesis that they result from the convolution of the optical PSF with a square pixel.

Figure 7.6 shows the minor and major axis of the PSF as computed on the simulations. The two figures at the top show the values obtained for simulations on which we apply the time constants measured on the bolometers during the second flight of the mission. The values in figure 7.6 on the bottom are obtained on the same simulation which we corrected for the previously applied time constant with the same method as for the flight data (see section 9.2). This process seems to correct the variations in the value of the PSF observed between the different crossings of the source on the detectors and it also seems to slightly correct the small differences observed between the major axis and the minor axis of the PSF. The effect on the PSF image

remains low compared to the size of the PSF (few arcsec). The average and median values for each array as well as the rms are given in table 7.3. The average value on all the crossings and all the arrays is $2.31 \pm 0.07'$, which is consistent with the measured values in flight.

Table 7.3: Array statistics of the simulated PSF FWHM (arcmin) using a Gaussian function approximation (FWHM= 1.4').

ARRAY	MIN	MAX	AVG	MED	STDEV
2	2.22	2.35	2.29	2.29	0.04
6	2.23	2.40	2.32	2.37	0.08
TRANS	2.22	2.40	2.31	2.31	0.06
7	2.09	2.35	2.29	2.33	0.10
4	2.23	2.39	2.32	2.37	0.07
8	2.28	2.43	2.32	2.31	0.05
REFLEX	2.09	2.43	2.31	2.32	0.08
ALL ARRRAYS	2.09	2.43	2.31	2.32	0.07

On figure 7.7 we show the circular average profile of the PSF measured on the array 6. The black curve in solid line corresponds to measurements from the observations on Jupiter during Flight#2. The dashed blue curve is derived from a timeline simulation using the PSF from the modelling of the optical system with the optical simulation program Zemax (Engel 2012). The dash-dotted red curve is obtained from the simulation using a PSF approximated with a Gaussian function. At half height, differences between the measured profile data and the measured profiles of the simulations are quite low. A slightly larger difference, however, is visible in the "wings" of the PSF between the data and the simulation. This difference was similarly observed during ground tests as can be seen in Figure 7.1

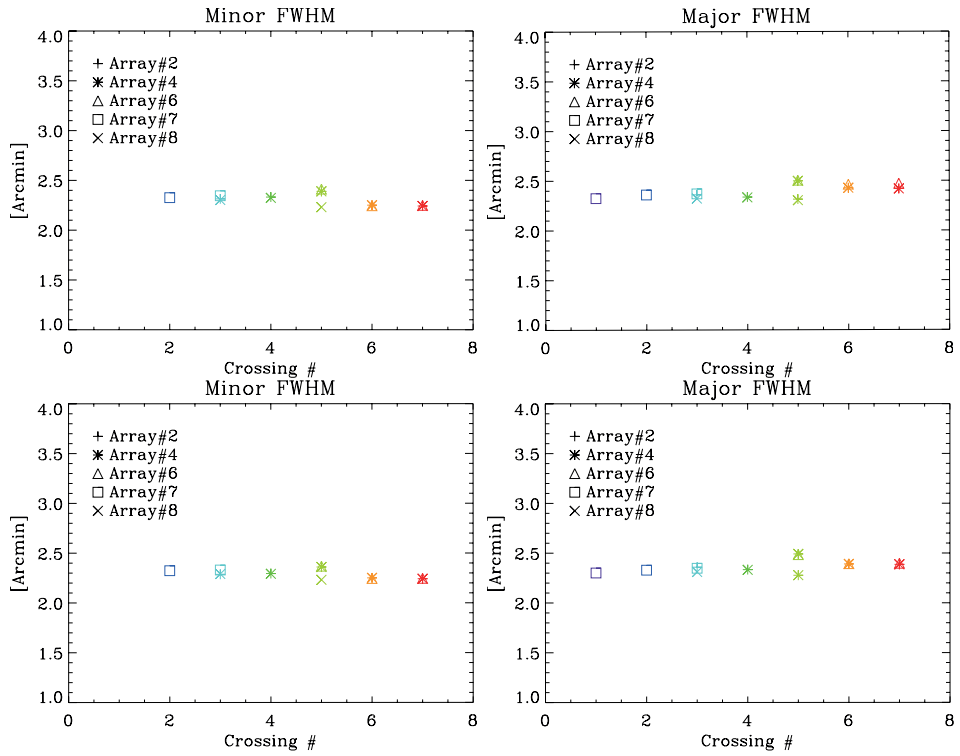

Figure 7.6: Top: Minor axis (left) and major axis (right) of the PSF derived from simulations including a time constant applied by Fast Fourier Transform. Bottom: Minor axis (left) and major axis (right) of the PSF obtained on simulations including a time constant applied by Fast Fourier Transform and then removed by discrete deconvolution.

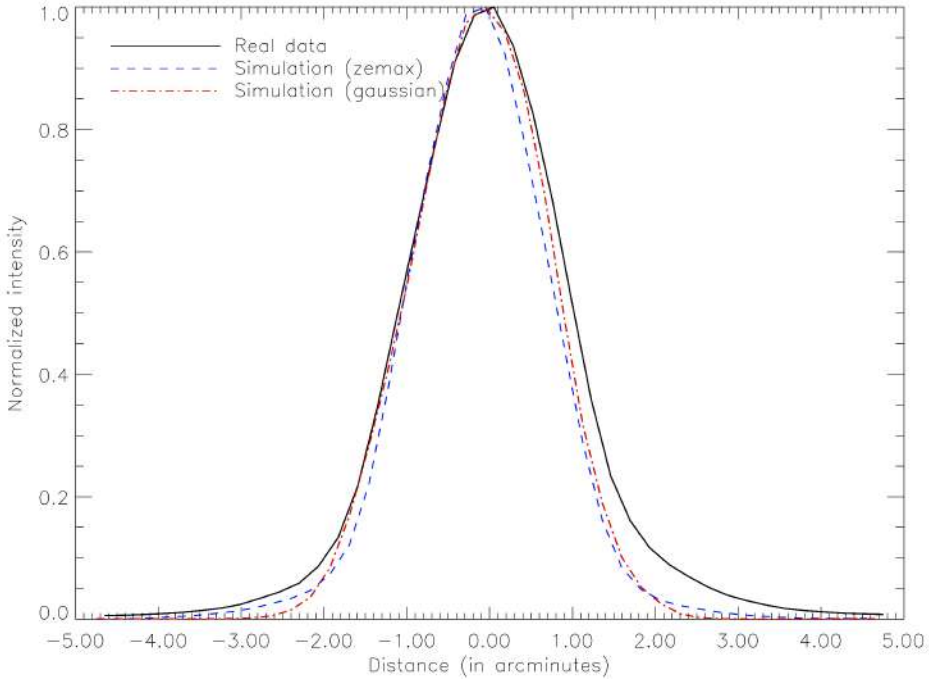

Figure 7.7: Circular average profile of the PSF measured on the array 6. The black curve in solid line corresponds to measurements from the observations on Jupiter during Flight#2. The dashed blue curve is derived from a timeline simulation using the PSF from the modelling of the optical system with Zemax (Engel 2012). The dash-dotted red curve is obtained from the simulation using a PSF approximated with a Gaussian function.

Part III

Map making

Chapter 8

Polarisation measurement

In this chapter I will introduce the formalism of polarization measurements with PILOT. I will make here the links between the Stokes parameters exposed in section 1.1.2 and the measurement carried out with the instrument.

8.1 Stokes parameters

As introduced in section 1.1.2, the Stokes vector is composed of the four followings elements:

$$I =< |E_x^2| > + < |E_y^2| >= I_x + I_y, \tag{8.1}$$

$$Q = I_x - I_y, \tag{8.2}$$

$$U = I_x^{45} - I_y^{45}, \tag{8.3}$$

$$V = 2 * A_x * A_y * \sin\phi, \tag{8.4}$$

with $E_x(t) = A_x(t)e^{i\omega t}$ and $E_y(t) = A_y(t)e^{i(\omega t+\phi)}$.
The polarisation fraction p is defined by the following equation:

$$p = \frac{\sqrt{Q^2 + U^2}}{I} \tag{8.5}$$

The general relation of transformation of the Stokes parameters in a base (a,b) whose axis a makes the angle alpha with respect to the x-axis of the original base is the following (see figure 8.1):

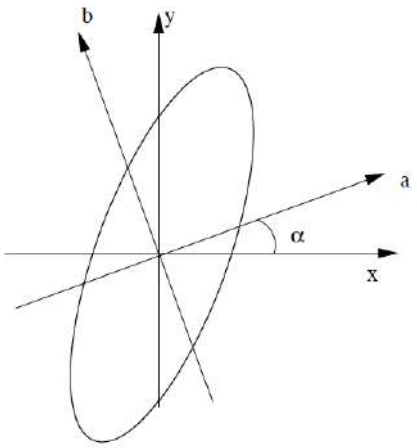

Figure 8.1: Relative orientation convention of the bases (x,y) and (a,b) in which we seek the Stokes parameters of the polarization ellipse represented here

$$\begin{pmatrix} I \\ Q \\ U \end{pmatrix}_{a,b} = \begin{pmatrix} 1 & 0 & 0 \\ 0 & \cos 2\alpha & \sin 2\alpha \\ 0 & -\sin 2\alpha & \cos 2\alpha \end{pmatrix} \begin{pmatrix} I \\ Q \\ U \end{pmatrix}_{x,y} = R_\alpha \begin{pmatrix} I \\ Q \\ U \end{pmatrix}_{x,y} . \tag{8.6}$$

The equation 8.6 provides the determination of the orientation of the ellipse. If the latter makes an angle ψ with respect to the x-axis of reference, the application of the relation 8.6 for the angle -ψ leads to:

$$Q_{x,y} = pI \cos 2\psi, \tag{8.7}$$

$$U_{x,y} = pI \sin 2\psi, \tag{8.8}$$

We therefore can express the polarization direction as follows:

$$\psi = 0.5 \times \arctan(U_{x,y}, Q_{x,y}), \tag{8.9}$$

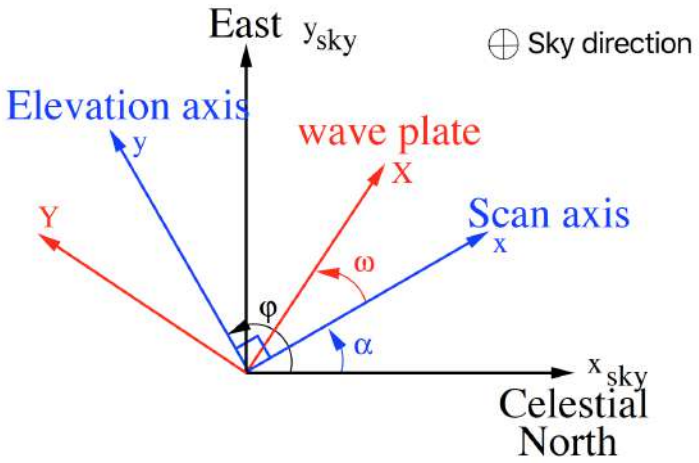

Figure 8.2: Definition of the angles involved in the determination of Stokes parameters. All angles are defined in algebraic value and are positively oriented in the the trigonometric direction defined in the figure, in accordance with the conventions.

8.2 Angles definition

Figure 8.2 is a schematic representation of the angles that we use to define polarisation of PILOT. The Stokes parameters of the sky are defined with respect to x_{sky} and y_{sky}, x_{sky} being oriented to the celestial north pole.

The privileged direction X of the Half-Wave Plate makes the angle ω with respect to x in the reference frame of the focal plane. On PILOT this angle can vary on 8 different positions, separated by 11.25^o, ranging from 0^o to 78^o.

The angle φ is the parallactic angle, defined at a point in the sky as the angle between the direction to the North Celestial Pole and to the zenith. It is measured from North through East. It is calculated from the equatorial coordinates using convention J2000 or by using the local convention.

8.3 Mueller matrices

The matrix formalism used to describe an electromagnetic wave and its evolution through an optical system is called Jones formalism. Based on this formalism, we can establish the expression of the Mueller matrix acting on the Stokes parameters. The Mueller matrix is obtained from the Jones matrix

by the following equation:

$$M_{kl} = \frac{1}{2}\mathrm{Tr}(\sigma_k J \sigma_l \overline{J}), \tag{8.10}$$

where J and $\overline{J}$ correspond to the matrices of Jones and its conjugate,respectively; and where $\sigma_{k,l}$ are the Pauli matrices given by:

$$\sigma_0 = \begin{pmatrix} 1 & 0 \\ 0 & 1 \end{pmatrix} \ \sigma_1 = \begin{pmatrix} 1 & 0 \\ 0 & -1 \end{pmatrix} \ \sigma_2 = \begin{pmatrix} 0 & -i \\ i & 0 \end{pmatrix} \tag{8.11}$$

The fourth Stokes parameter V being inaccessible for the instruments like PILOT, the Mueller matrix which is in a general case a 4×4 matrix is in our case reduced to a matrix 3×3. In the case of an instrument rotating the polarization without attenuating it by an angle alpha, the Jones matrix is expressed as:

$$J = \begin{pmatrix} \cos\alpha & -\sin\alpha \\ \sin\alpha & \cos\alpha \end{pmatrix} \tag{8.12}$$

This gives us the expression of the following Mueller matrix:

$$M = \begin{pmatrix} 1 & 0 & 0 \\ 0 & \cos 2\alpha & -\sin 2\alpha \\ 0 & \sin 2\alpha & -\cos 2\alpha \end{pmatrix} \tag{8.13}$$

We find here, the expression given by equation 8.6

The Mueller matrix of an imperfect instrument (i.e., it transmits a non-zero component in its orthogonal direction to the Jones matrix) whose direction of co-polarization makes an angle α with the axis x of the laboratory is therefore:

$$M = \begin{pmatrix} K & k\cos 2\alpha & k\sin 2\alpha \\ k\cos 2\alpha & K\cos^2 2\alpha + q\sin^2 2\alpha & (K-q)\cos 2\alpha \sin 2\alpha \\ k\sin 2\alpha & (K-q)\cos 2\alpha \sin 2\alpha & K\sin^2 2\alpha + q\cos^2 2\alpha \end{pmatrix} \tag{8.14}$$

with $K = (\tau_1^2 + \tau_2^2)/2$, $k = (\tau_1^2 - \tau_2^2)/2$ and $q = \tau_1\tau_2$ where τ_1 and τ_2 are two factors reflecting the imperfection of the polarizer.

In the case of an imperfect polarizer perfectly aligned with the x-axis of the laboratory ($\alpha = 0$), the Jones matrix is expressed:

$$\sigma_0 = \begin{pmatrix} \tau_1 & 0 \\ 0 & \tau_2 \end{pmatrix} \tag{8.15}$$

and thus the Mueller matrix:

$$M = \begin{pmatrix} K & k & 0 \\ k & K & 0 \\ 0 & 0 & q \end{pmatrix} \tag{8.16}$$

8.4 Measurement and determination of Stokes parameters

We calculate below the Stokes parameters relative to our detectors. To do this we must determine the effect of each optical element on the propagation of the polarization signal of an electro-magnetic wave. The expression of the Stokes parameters on the polarizer with respect to the Stokes parameters in the base (x, y) of the sky is the following:

$$\begin{pmatrix} I \\ Q \\ U \end{pmatrix}_{x,y} = R_{-\omega} M_{XY} R_{\omega} R_{-\theta} R_{\alpha} \begin{pmatrix} I \\ Q \\ U \end{pmatrix}_{sky} \tag{8.17}$$

with:

- R_α the transformation matrix of Stokes parameters from the base (x, y) of the sky to the instrumental base,
- $R_{-\theta}$ reflecting the rotational action of the polarization induced by the passage of the electromagnetic wave through the mirrors M1 and M2,
- R_ω used to obtain the expression of the Stokes vector in the proper base of the half-wave plate,

- M_{XY} reflecting the effect of the birefringent plate,
- $R_{-\omega}$ applied to re-express the Stokes vectors in the base of the detectors.

If we consider the birefringent plate as perfect, we have:

$$R_{-\omega}M_{XY}R_{\omega} = \begin{pmatrix} 1 & . & . \\ . & \cos 2\omega & -\sin 2\omega \\ . & \sin 2\omega & \cos 2\omega \end{pmatrix} \begin{pmatrix} 1 & . & . \\ . & 1 & . \\ . & . & -1 \end{pmatrix} \begin{pmatrix} 1 & . & . \\ . & \cos 2\omega & \sin 2\omega \\ . & -\sin 2\omega & \cos 2\omega \end{pmatrix} \tag{8.18}$$

leading to:

$$R_{-\omega}M_{XY}R_{\omega} = \begin{pmatrix} 1 & . & . \\ . & \cos 4\omega & \sin 4\omega \\ . & \sin 4\omega & -\cos 4\omega \end{pmatrix} \tag{8.19}$$

and

$$R_{-\theta}R_{\alpha} = \begin{pmatrix} 1 & . & . \\ . & \cos 2(\alpha-\theta) & \sin 2(\alpha-\theta) \\ . & -\sin 2(\alpha-\theta) & \cos 2(\alpha-\theta) \end{pmatrix} \tag{8.20}$$

We can see on the figure 8.2 that $\alpha = \varphi - \pi/2$. We thus come to the following expression:

$$M_{instr}^{perf} = R_{-\omega}M_{XY}R_{\omega}R_{-\theta}R_{\alpha} = \begin{pmatrix} 1 & 0 & 0 \\ 0 & -\cos(4\omega+2\varphi-2\theta) & -\sin(4\omega+2\varphi-2\theta) \\ 0 & -\sin(4\omega+2\varphi-2\theta) & \cos(4\omega+2\varphi-2\theta) \end{pmatrix} \tag{8.21}$$

when $\varphi = 0$, which is the case where the elevation axis is aligned with the celestial north, the x axis of scan corresponds to $-y_{sky}$ and the y-axis has the axis x_{sky}. So we have $(Q,U)_{xy} = -(Q,U)_{sky}$. This justifies the sign before the terms of equation 8.21.

In the PILOT configuration, a detector located in the focal plane in transmission will measure the intensity transmitted by the polarizer and the fixed grid attached to it. It therefore measures:

$$m_T = \begin{pmatrix} 1 \\ 0 \\ 0 \end{pmatrix} M_{g_T} M_{s_T} R_{-\omega} M_{XY} R_{\omega} R_{-\theta} R_{\alpha} \begin{pmatrix} I \\ Q \\ U \end{pmatrix}_{sky}, \tag{8.22}$$

where m_T is the measure in transmission. The polarizer is possibly misaligned by an angle Ψ with respect to x, its Mueller matrix in the instrument frame is therefore:

$$M_{s_T} = \begin{pmatrix} K & k\cos 2\Psi & k\sin 2\Psi \\ k\cos 2\Psi & K\cos^2 2\Psi + q\sin^2 2\Psi & (K-q)\cos 2\Psi \sin 2\Psi \\ k\sin 2\Psi & (K-q)\cos 2\Psi \sin 2\Psi & K\sin^2 2\Psi + q\cos^2 2\Psi \end{pmatrix} \tag{8.23}$$

with $K = (\tau_1^2 + \tau_2^2)/2$, $k = (\tau_1^2 - \tau_2^2)/2$ and $q = \tau_1\tau_2$ where τ_1 and τ_2 are two factors reflecting the imperfection of the polarizer.

The grid attached to the polarizer can also be imperfect. Assuming a perfect alignment of the grid, we have:

$$M_{g_T} = \begin{pmatrix} K_g & k_g & 0 \\ k_g & K_g & 0 \\ 0 & 0 & q_g \end{pmatrix} \tag{8.24}$$

with $K_g = (\tau_{g1}^2 + \tau_{g2}^2)/2$, $k_g = (\tau_{g1}^2 - \tau_{g2}^2)/2$ and $q_g = \tau_{g1}\tau_{g2}$ where τ_{g1} and τ_{g2} are two factors reflecting the imperfection of the grid.

Now assuming that the polarizer and the grid are perfect ($\tau_1 = \tau_{g1} = 1$, $\tau_2 = \tau_{g2} = 0$), we have:

$$M_{g_T} M_{s_T} = \begin{pmatrix} 1/2 & 1/2 & 0 \\ 1/2 & 1/2 & 0 \\ 0 & 0 & 0 \end{pmatrix} \tag{8.25}$$

Finally, the measurement performed in transmission is expressed:

$$m_T = \frac{1}{2}\left[I_{sky_0} - Q_{sky_0}\cos(4\omega + 2\varphi - 2\theta) - U_{sky_0}\sin(4\omega + 2\varphi - 2\theta)\right] \tag{8.26}$$

Similarly for the measurement carried out in reflection ($\tau_2 = \tau_{g2} = 1$, $\tau_1 = \tau_{g1} = 0$):

$$M_{g_R} M_{s_R} = \begin{pmatrix} 1/2 & -1/2 & 0 \\ -1/2 & 1/2 & 0 \\ 0 & 0 & 0 \end{pmatrix} . \tag{8.27}$$

This leads to:

$$m_R = \frac{1}{2}\left[I_{sky_0} + Q_{sky_0} \cos(4\omega + 2\varphi - 2\theta) + U_{sky_0} \sin(4\omega + 2\varphi - 2\theta) \right] . \tag{8.28}$$

The parralactic angle φ varies over time.

In our case, as we have multiple measurements we can generalize this to a matrix system:

$$\mathbf{M} = \mathcal{A}\mathbf{S} + \mathbf{N} \tag{8.29}$$

where $\mathbf{M}$ is a vector of n measures m_i, $\mathbf{N}$ is the noise vector, $\mathbf{S}$ the Stokes vector parameters and $\mathcal{A}$ the pointing matrix. The determination of the Stokes vector is done by minimizing the χ^2 of the system:

$$\chi^2 = (\mathbf{M} - \mathcal{A}\mathbf{S})^T \mathcal{N}^{-1} (\mathbf{M} - \mathcal{A}\mathbf{S}) \tag{8.30}$$

With $\mathcal{N}$ the covariance matrices of the noise. The solution is then:

$$\mathbf{S} = (\mathcal{A}^T \mathcal{N}^{-1} \mathcal{A})^{-1} \mathcal{A}^T \mathcal{N}^{-1} \mathbf{M} \tag{8.31}$$

Chapter 9

Map-Making and preliminary results

In this chapter I present the map-making pipeline currently implemented for PILOT and the premliminary results. This pipeline is based mainly on two map making algorithms, Scanamorphos and ROMA that I introduce in the first section of this chapter. I then expose the operation of data preprocessing pipelines implemented upstream of these algorithms. I also present the data simulation tool that has been put in place to help improve data processing. In the last part I present the preliminary intensity and polarizations maps obtained with the help of the observations carried out during two flights of the mission and I conclude on the work that remains to be done in the data processing.

9.1 Map-making algorithms

9.1.1 Scanamorphos

Scanamorphos is a map-making software developed initially for the processing of Herschel data. It can be applied more widely to other instruments similar to PACS or SPIRE. As Herschel makes observations in intensity only, Scanamorphos initially does not take into account the polarization. The code was adapted by Hélène Roussel to take into account polarization in order to process the data obtained by PILOT and by NIKA2 (New IRAM KID Arrays) installed at the IRAM 30m telescope. A complete description of the algorithm is available in Roussel (2013). Here are the major processing steps performed by the software:

- Calculation of coordinates of the map from the sky coordinates of the provided samples,
- Calculation of high frequency noise level,
- Subtraction of long-timescale drifts (linear baselines substraction),
- Subtraction of short timescale drifts (timescales smaller than scan duration) and glitch masking,
- Projection of signal error, drift and weight maps.

Scanamorphos does not rely on any detector noise description and does not apply any Fourier-space filtering. It uses only the redundancy appearing in the data. This method allows us to register "cleaned timelines" as a product. This help us to test the tool more efficiently and to make a comparison directly on the timelines between the simulated data presented hereafter and the cleaned data provided by Scanamorphos. An example of the Scanamorphos process applied on Herschel data is visible in figure 9.1. The example shown here is from the unpolarized version of Scanamorphos.

9.1.2 ROMA

ROMA (Roma Optimal Map-making Algorithm, De Gasperis et al. 2005) is a map-making algorithm for polarised CMB data-sets. It allows us to product optimal multidetctor maps of CMB total intensity and polarisation. The code was used to analyse the polarised data set from the BOOMERanG experiment (Masi et al. 2002). The algorithm is based on the resolution of the polarization equations through Generalized Least Squares solution.

The combination of sky signal and correlated noise is defined in De Gasperis et al. (2005) by the following equation:

$$D_t = \frac{1}{2} A_{tp}(I_p + Q_p \cos 2\phi_t + U_p sin2\phi_t) + n_t = A_{tp} S_p + n, \qquad (9.1)$$

where A_{tp} is the pointing matrix, S_p is the sky signal, and n the noise. I_p, Q_p, U_p are the Stokes parameters. $\phi_t = 4\omega_t + 2\phi_t$ where ω_t and ϕ_t are respectively the Half-Wave plate angle and the parallactic angle. The standard Generalized Least Square solution is defined as

$$\tilde{S_p} = (A^t N^{-1} A)^{-1} A^t N^{-1} D, \qquad (9.2)$$

where

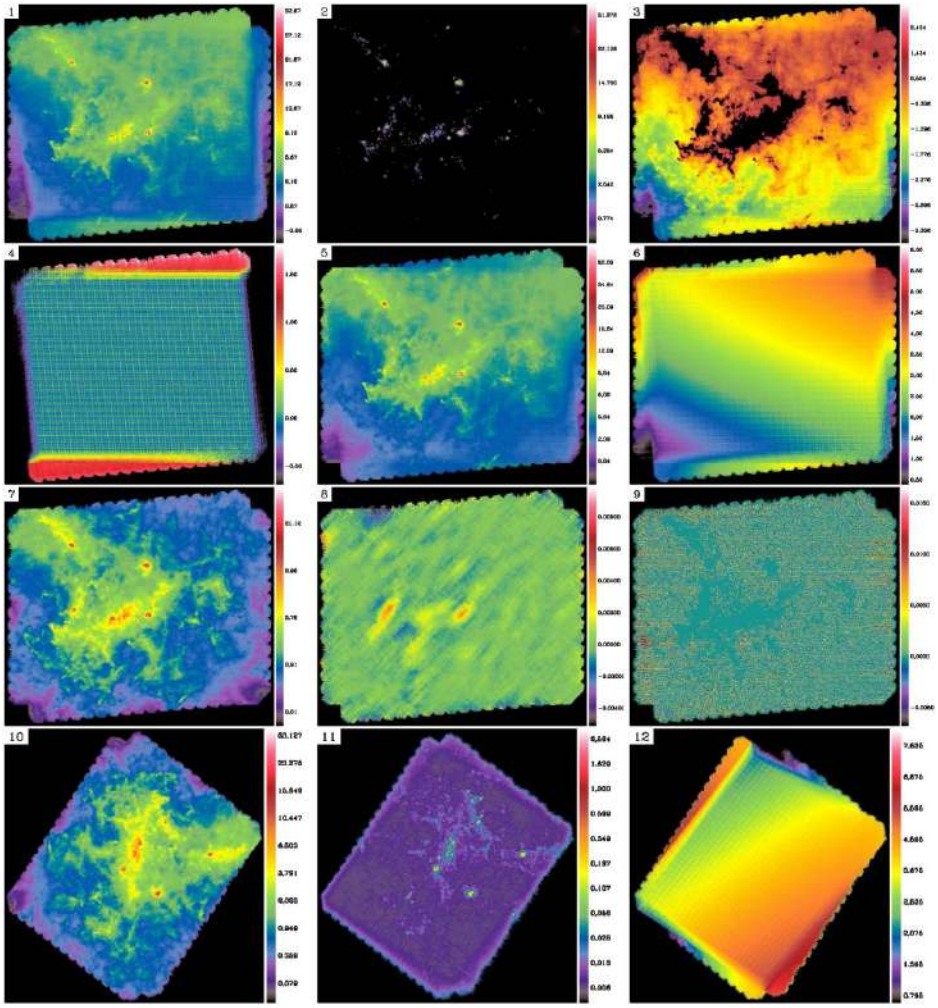

Figure 9.1: The Rosette 250 µm observations made by Herschel. Each image shows the different steps followed by Scanamorphos. (1) raw level-1 data; (2) signal of compact sources interpolated for the computation of high-frequency noise; (3) mask applied for the computation of baselines; (4) simple baselines obtained by zero-order fits; (5) data after subtraction of the simple baselines; (6) residual baselines derived from the redundancy; (7) data after subtraction of the residual baselines; (8) average drift subtracted at the first iteration; (9) individual drifts subtracted at the first iteration for these; (10) final map; (11) error map; (12) total drifts. The final map shows a wealth of filamentary structures at various spatial scales, and compact sources, with no sign of residual striping. The example shown here is from the unpolarized version of Scanamorphos. Roussel (2013)

$$A_{tp} \equiv \frac{1}{2}\begin{pmatrix} A^1_{tp} & cos2\phi_t A^1_{tp} & sin2\phi_t A^1_{tp} \\ \vdots & \vdots & \vdots \\ A^k_{tp} & cos2\phi_t A^k_{tp} & sin2\phi_t A^k_{tp} \end{pmatrix}, \tag{9.3}$$

and

$$N \equiv \langle \mathbf{n}_t \boldsymbol{n}_{t'} \rangle = \begin{pmatrix} n^1_t n^1_{t'} & \cdots & n^1_t n^k_{t'} \\ \vdots & \ddots & \vdots \\ n^k_t n^1_{t'} & \cdots & n^k_t n^k_{t'} \end{pmatrix}. \tag{9.4}$$

Note that in the current status of data processing in PILOT, we are not using all the noise covariance information among detectors in the focal planes. We assume that the matrix N is block-diagonal, with the non-zero blocks $n^i_t n^i_{t'}$ containing the single-detector noise covariance and assuming $n^i_t n^j_{t'} = 0$ if i is not equal to j. The idea is to decompose the product $(A^t N^{-1} A)^{-1}$ to avoid computing and storing the map correlation matrix and to make use of a preconditioned conjugate gradient (PCG) solver. The key assumptions are that

- the beam is axisymmetric, so as to keep the structure of the pointing matrix A_{tp} as simple as possible and
- the noise is stationary and its correlation function decays after a time much shorter than the duration of the timeline being processed.

9.2 Data processing pipeline

The transition from the data measured by PILOT to the polarization maps requires many data preprocessing steps. A data processing pipeline was then established. A schematic view of the data processing pipeline is visible in figure 9.2. The disks represent the data read or generated by the different routines and the rectangle are the data processing routines. The dashed arrows and lines represent processing steps that are added as the iterations proceed. From reading the data, the pipeline is divided into three main branches. The first concerns the calculation of coordinates. These are calculated from the ESTADIUS quaternions and the pointing offsets integrated into the PIMO structure or recalculated from the intensity maps (see chapter 4). The other two branches are each dedicated to the two map-making algorithms presented previously. As the two algorithms work differently, the data provided to each do not go through the same preprocessing steps. The steps common to both algorithms are the correction of time constants and the correction of detector

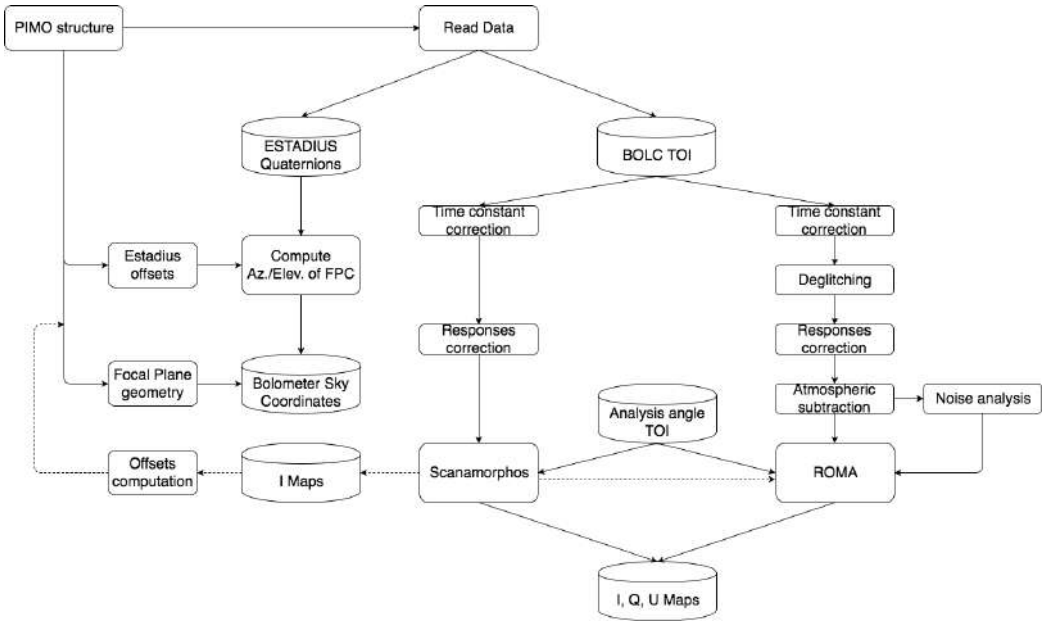

Figure 9.2: Schematic view of the data processing pipeline. The disks represent the data read or generated by the different routines and the rectangle are the data processing routines. The dashed arrows and lines represent processing steps that are added as the iterations proceed.

responses. ROMA, unlike Scanamorphos, does not include deglitching tools and does not correct the effects related to the atmosphere. These steps are therefore included in the preprocessing of the data provided to ROMA. Since the ROMA algorithm is based on noise estimates, it is necessary to provide the noise covariance matrices. This data processing pipeline is iterative, so we can see by the presence of the dashed arrows that the intensity maps provided by Scanamorphos can be reused in order to recalculate the pointing offsets. Similarly scanamorphos being able to produce timelines as outpout, it is possible to inject these in the algorithm of ROMA to exploit the complementary of the methods (see section 9.1). Some preprocessing steps visible on this scheme are described in the following sections.

9.2.1 Time constant deconvolution.

Knowing the time constant of the detectors (see chapter 3), we can correct the data of its effects. Using the fast Fourier transform, we can deconvolve the timelines from the convolution kernel. However, we have to be careful when applying the deconvolution because we have to take into account a

normalization factor. This factor is calculated by generating a timeline for which each sample value is equal to 1. The time constant is applied on this timeline by a convolution product. We then perform a deconvolution of this timeline from the same time constant. The output timeline gives us the values of the normalization factor to be applied for each sample.

Figure 9.3 shows an example of the effect of deconvolution from the time constant. On the top left, we can see the map of Jupiter when no further correction of the time constant has been applied (we will refer to it as Map_{bc}). On the top right, the image of Jupiter has been obtained including a correction from the time constant (we will refer to it as Map_{ac}). Finally, the bottom the figure shows the difference, Map_{diff}, between the two previous maps defined as:

$$\mathrm{Map}_{diff} = \frac{\mathrm{Map}_{bc} - \mathrm{Map}_{ac}}{\mathrm{Map}_{bc}}. \tag{9.5}$$

The dashed line shows the scan direction. Some features visible on the maps are due to the fact that no correction is made to the data apart the atmospheric correction, as well as the fact that we use only one direction of scan to build these maps. On the difference map, we can see that the correction of the time constants on the data causes a difference in the signal less than 6%. This effect is not noticeable on the calculation of PSF but it will be important in the context of polarization maps. Note that this step has not yet been implemented in the data processing pipeline. The maps shown in the following sections are therefore not corrected for time constants. This will be one of the major steps to be implemented soon to improve the polarization maps.

9.2.2 Deglitching

Glitches present in the timelines must be removed before the data are supplied to the map making algorithms because they can appear as false sources in the maps. In order to detect the glitches, we used the method described in section 3.4.1. A glitch mask was defined from this method and the data affected by glitches are flagged as undefined value in the timelines. The holes left in the timelines are filled by a method of gap filling that replace the undefined values with white noise consistant with the rest of the scan.

9.2.3 Atmospheric subtraction

Part of the signal measured by PILOT is due to emission by the residual atmosphere, which creates a common mode of signal variations. The atmo-

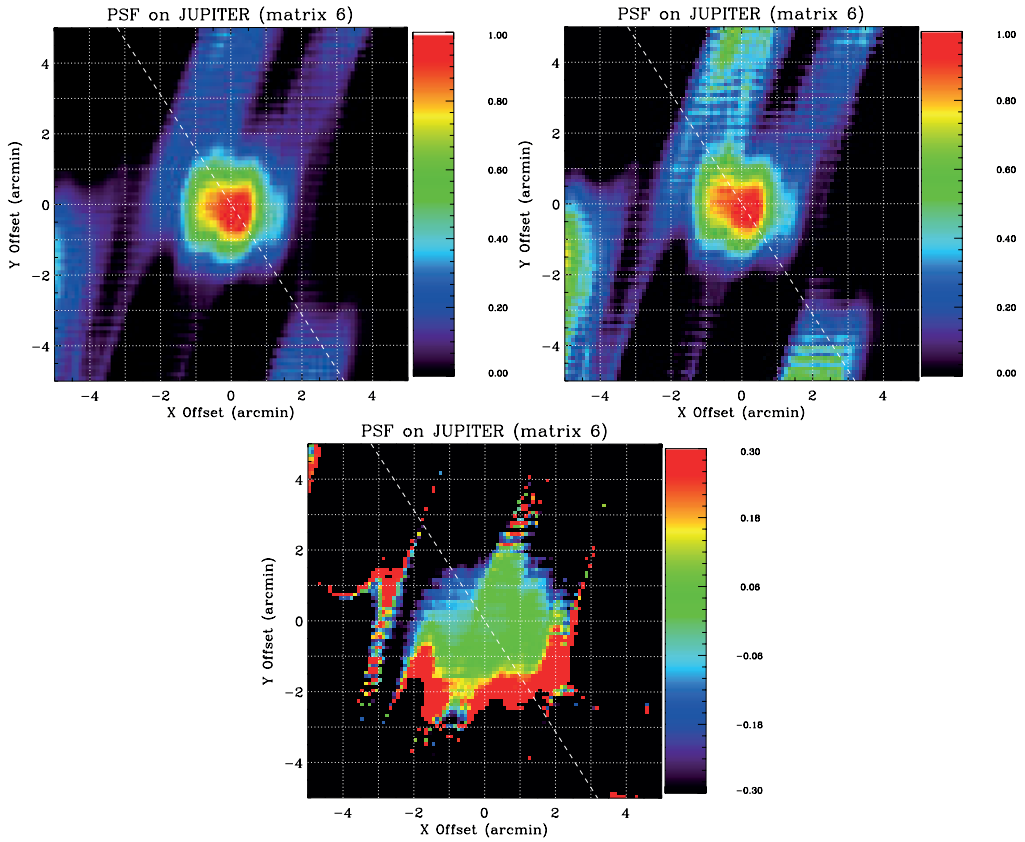

Figure 9.3: Normalized maps of Jupiter constructed by combining data of array 6 from one observation including only scans performed in the same direction. Top left: Data not corrected from the effects of the time constant. Top right: Data corrected from the effects of the time constant. Bottom: Difference between the map on the left and the map on the right defined by equation 9.5. The dashed line shows the scan direction.

spheric response is defined as the slope of the correlation of the atmospheric signal with elevation. We measure it by using sky-deep sequences but also scans over the whole flight in the case of Flight#2. This signal is removed from the data by subtracting the best correlation to the data. The accuracy of the response map is improved at 1% level or better when using the scans over the whole flight thanks to the increased statistics with respect of having only the sky-deep observations. This confirms the advantage of having a scanning strategy with varying elevation as implemented for the Flight#2. Figure 9.4 show timelines from the same scene before and after decorrelation of the atmosphere, respectively. We can see that the signal that was previously strongly modulated by the atmosphere is flattened after decorrelation.

9.2.4 Responses correction

Timelines have been corrected for temporal and spatial variations of the detector response which are described in section 6.2). For each scene, the response R_{xy} is defined as the average of the atmospheric response of each pixel on the whole flight R_{xy}^{ref} divided by the mean ICS response $S_{ICS}(x, y)$ for the whole flight and multiplied by the mean ICS response on this scene $S'_{ICS}(x, y, t)$:

$$R_{xy} = \frac{R_{xy}^{ref}}{S_{ICS}(x, y)} * S'_{ICS}(x, y, t) \tag{9.6}$$

S_{ICS} is defined in chapter 6 by the equation 6.3. The accuracy of this response correction applied to the timelines can be verified by measuring the residual polarization on unpolarized sources such as planets. We generate I,Q,U maps from two observations of Jupiter for each array and we compute the flux of the planet by subtracting the image median value in a background region and summing values inside the source region. The source region is defined as pixels within 7 arcminutes of the source position and the background region is defined as an annulus from 12' to 17' from the source position (see figure 9.5). Results are visible in figure 9.6 which shows the distribution of fluxes for all arrays after response correction for all JUPITER observations. The vertical lines for each sequence show the average flux over all arrays and the $\pm 2\%$ range. The squares represent the different arrays. The correction generally flattens the flux and therefore corrects for the evolution of the response. Variations remain at the level of 2-4%. We measured the residual polarization on Jupiter using maps provided by ROMA. The residual polarization intensity is of the order of 3%. Figure 9.7 shows the Q (red curve) and U (black curve) residuals as a function of the integration radius. We

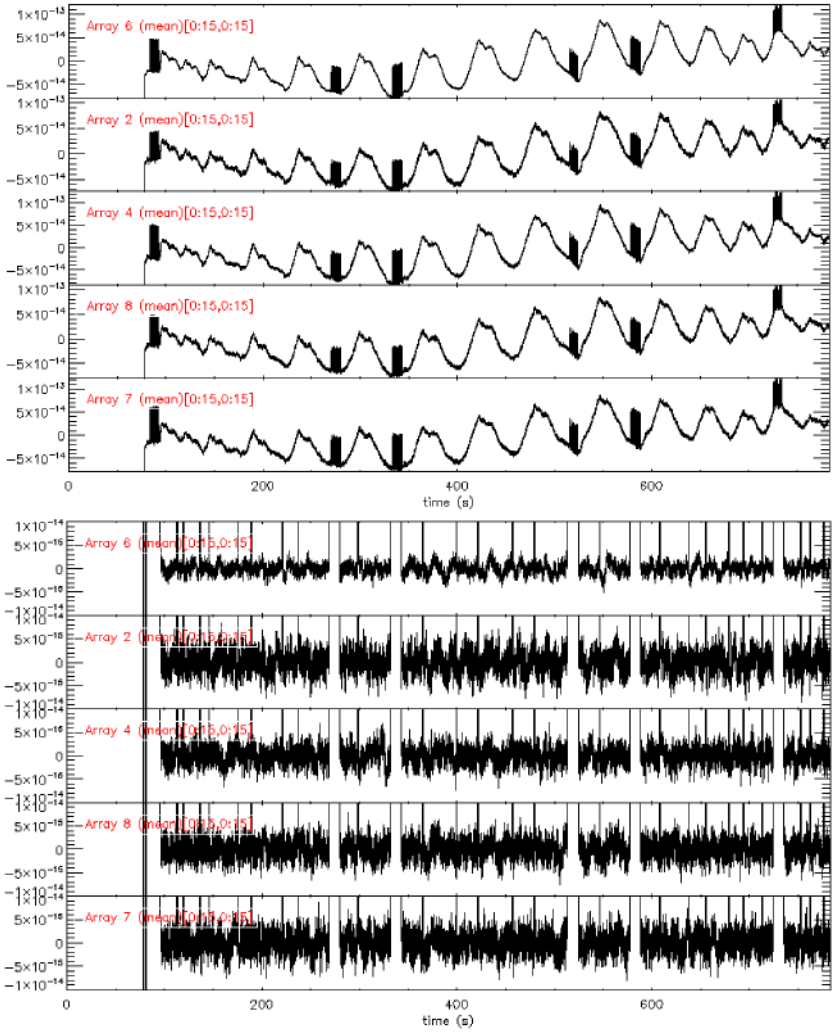

Figure 9.4: Top: Array averaged signal measured during a scene of the second flight on the Large Magellanic Cloud uncorrected for the effects induced by the atmosphere. Bottom: Same as previous, but corrected for the effects induced by the atmosphere.

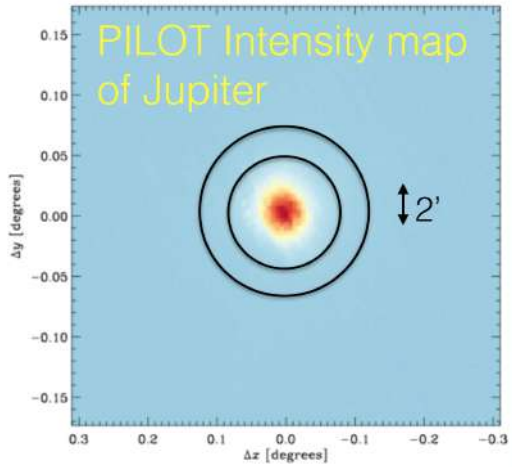

Figure 9.5: Intensity map of Jupiter obtained with PILOT measurements.

can see that the residuals are dominated by the Q residuals. The reason of this is under investigation. We used here the v0 version of pointing, for which we know that the focal plane geometry is slightly off, which may be producing some of the differences observed between arrays. In addition, the scenes of Jupiter were made after the recycling of the fridge, which impacts the response of the detectors. Finally, time constants have not been taken into account in this estimate, which could similarly have an impact on these results. A significant improvement is expected from the ongoing analysis.

9.3 Simulations

To test the various map-making tools, we developped the simulations of the PILOT data using the Planck sky maps extrapolated to the PILOT frequency using a single grey body. The simulations use the coordinates as described in chapter 4. For Planck, the convention used to define Stokes parameters is the GALACTIC-COSMO convention. In PILOT, we use the EQUATORIAL-IAU convention (see 9.8) . The main difference is that the local x-axis points North and the local z-axis points inwards to the observer for a right-handed system for the IAU system and in the polarization convention used historically in the CMB community, the local x-axis points South and the local z-axis points outwards from the observer for a right-handed system. For both systems, the local y-axis points East (see figure 9.8). Switching from the COSMO convention to the IAU convention therefore reverses the sign of

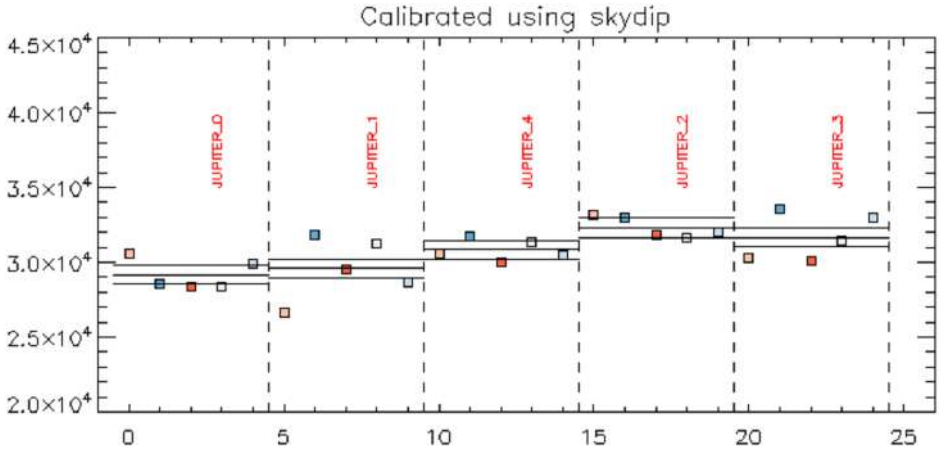

Figure 9.6: Distribution of fluxes for all arrays after response correction for all JUPITER observations.The vertical lines for each sequence show the average flux over all arrays and the ±2% range. The squares represent the different arrays.

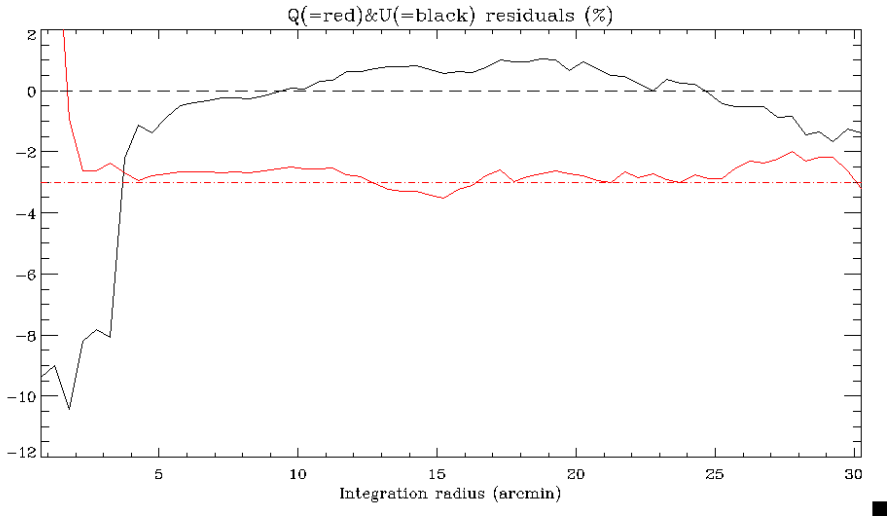

Figure 9.7: Q (red curve) and U (black curve) residuals in percent as a function of the integration radius

the parameter U. We must therefore transform the parameters Q and U to switch from one convention to the other. We first pass the parameters of the galactic to equatorial coordinates by the following equation:

$$\begin{pmatrix} Q \\ U \end{pmatrix}_{equ} = \begin{pmatrix} \cos 2\theta & \sin 2\theta \\ -\sin 2\theta & \cos 2\theta \end{pmatrix} \begin{pmatrix} Q \\ U \end{pmatrix}_{gal}, \tag{9.7}$$

with θ, the angle between the galactic and the equatorial north at a given sky position. The value of the polarization direction is taken from the flight data. The bolometer signals are computed from the sky maps and the bolometer sky coordinates are provided by the stellar sensor. Since the Planck sky maps are created using Healpix format (Gorski et al. 2005), the intensity values are derived via the Healpix library and a nearest neighbor interpolation. The simulated signal can be calculated in MJy/sr, Watts or ADU. In these simulations we can take into account:

- The bolometer time responses by convolving the signal with a function $\exp^{-\frac{t}{\tau}}$ where τ is the time constant of a given bolometer,
- The noise power spectrum including white noise and $1/f$ noise. The power spectrum is used to generate a noise timeline for each bolometer of the transmission and reflection arrays, assuming a random phase for each bolometer,
- Glitches. We can add glitches with a given number of events per minute,
- ICS signal. The ICS signal calculation is based on the ICS current intensity and the ICS impedance. The spatial distribution of the ICS illumination on the focal planes is taken into account. The ICS noise is assumed to have a power spectrum similar to that of bolometers and the noise TOI is computed in a similar way as for the bolometers.

The data generated by the simulations are recorded and read in the same way as the PILOT data. An example of a simulated timeline is visible in figure 9.9.

9.4 Preliminary results

9.4.1 I,Q,U maps

Figure 9.10 shows the preliminary PILOT Intensity maps of different regions of the sky observed during Flight#2: L0, Rho-Ophiuchi, L30 and Orion,

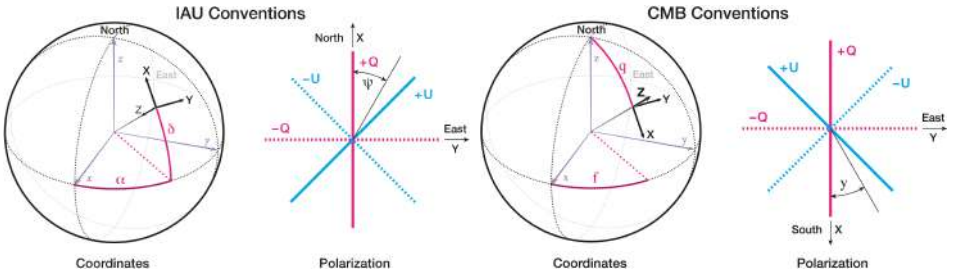

Figure 9.8: Left: schematic representation of the IAU convention. Right: shematic representation of the COSMO convention. Figures from lambda.gsfc.nasa.gov

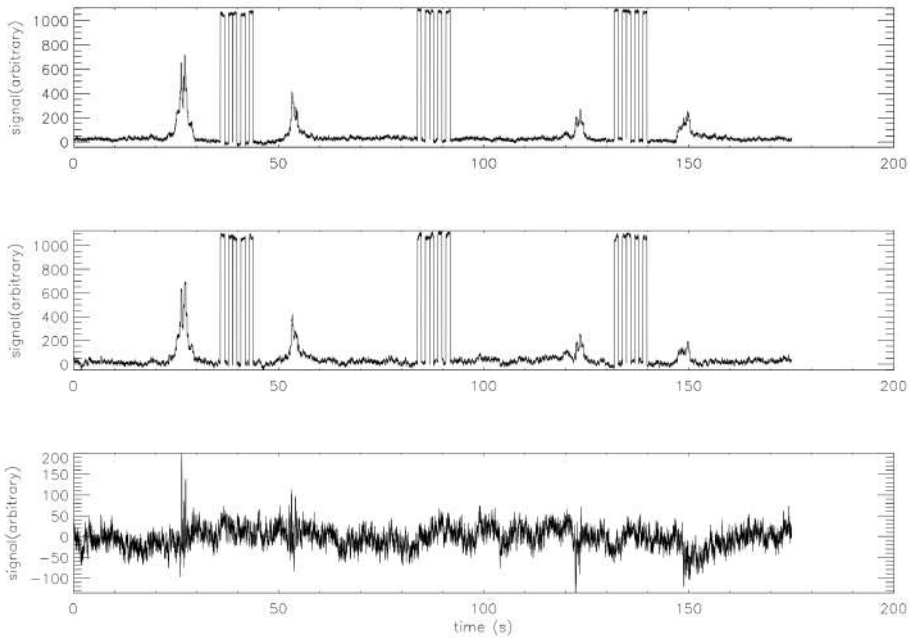

Figure 9.9: Example of a simulated time-line in the 240 µm channel for the average of all PILOT arrays for one observation of the Orion region. The plots show four consecutive scans, separated by calibrations on the ICS, which is visible in the time-lines as a strongly modulated signal. The upper and middle panels show time-lines for the TRANS and REFLEX arrays respectively. The large bumps in the data correspond to strong thermal dust emission in the Orion molecular cloud. The lower panel shows the difference between the two focal planes. The variations of the difference signal are due to the polarization of the simulated astrophysical emission.

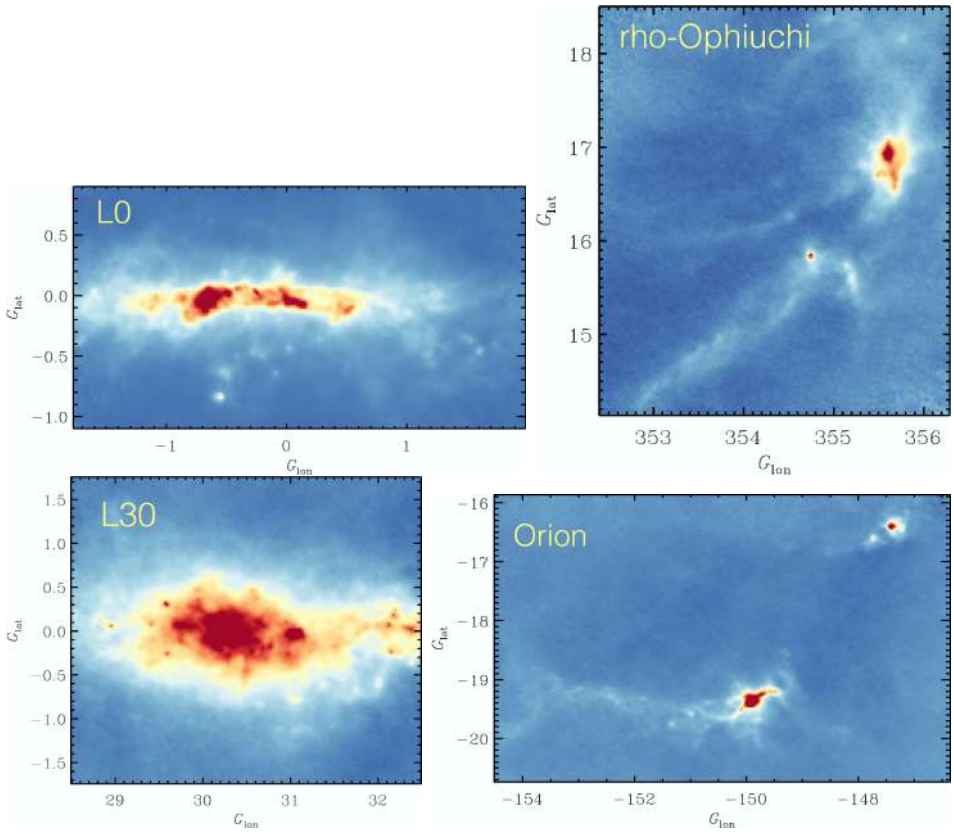

Figure 9.10: Preliminary PILOT Intensity maps obtained with ROMA. From top left to bottom right: L0, Rho-Ophiuchi, L30 and Orion.

clockwise in the figure. They were constructed after applying the different step of preprocessing using the ROMA map-making algorithm. The map of the L0 region is obtained by combining data from four scenes for a total of 30 minutes of observations. We chose the Galactic center (L0) to verify the calibration, the intercalibration between the pixels and the response corrections of the detectors because it is very bright and weakly polarized (around 2%).

Figures 9.11 and 9.12 show respectively the I,Q,U PILOT maps and the I,Q,U maps obtained with the same processing applied on Planck simulations. For both the ROMA algorithm has been used . the intensity maps show that measurements made with PILOT are consistent with simulations performed on the Planck data. The Q and U maps, which are preliminary maps, show common structures with the simulations. Note that these are preliminary maps and that there is still a a large margin for improvement in

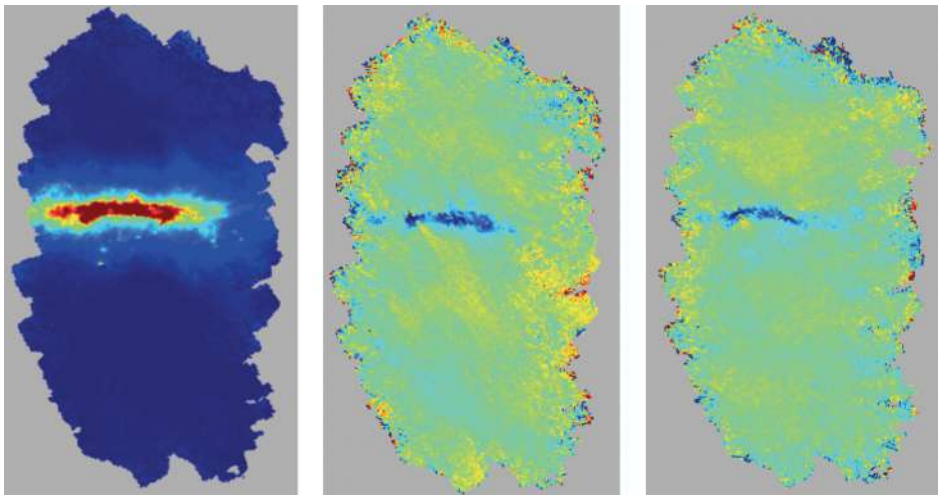

Figure 9.11: PILOT maps of the Stokes parameters I,Q,U of the Galactic center L0 obtained with ROMA map-making. From left to right: Total intensity, polarization parameter Q and polarization parameter U. Maps are shown in the EQU-IAU convention at an angular resolution of 2'.

the processing of PILOT data. Moreover, the simulations are created taking as basis the Planck data that suffer from bandpass mismatch in bright regions like the Galactic center which causes leakage from I to Q or U (Planck intermediate results XLVI et al. 2016).

9.4.2 Polarisation angles

We derive the polarisation angles using the equation 8.10. Figure 9.13 shows the intensity map of the Galactic center L0, with the superposition of the polarisation angles measurements. The red lines correspond to the polarization angle measured with PILOT, the black lines correspond to the polarization angle measured with Planck at 850μm. It appears that the agreement between PILOT and Planck is good, especially in the regions of the Galactic center. The PILOT and Planck polarization angles are consistant with a magnetic field parallel to the Galactic plane. In order to quantify the agreement between the PILOT and Planck measurments, we compute the histogram of the polar angles shown in figure 9.14. The histogram of the polarization angles measured with PILOT is shown in brown, Planck at 850 µm in black, Planck at 1.3 mm in red and Planck at 2 mm in blue. The agreement with Planck is of the same order as the dispersion between Planck frequencies. The remaining differences can have multiple origins. The systematic

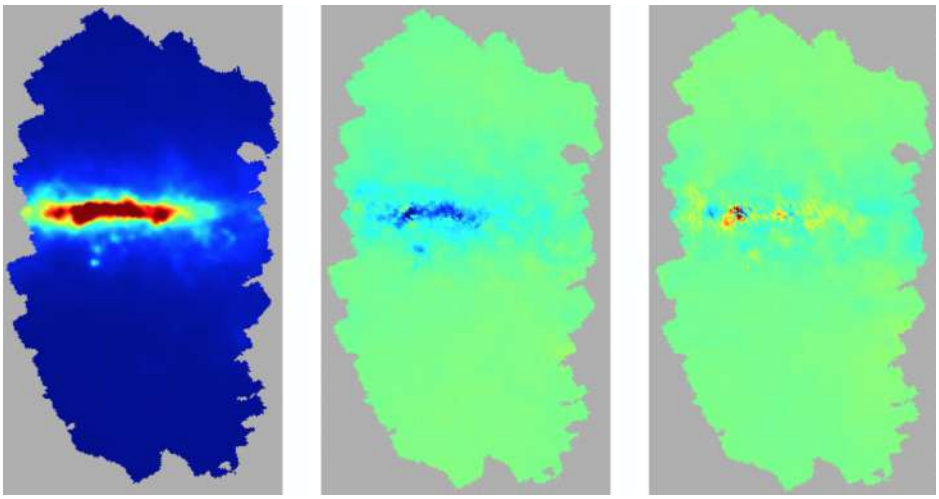

Figure 9.12: ROMA Maps of Stokes parameters obtained with data from simulations made from the Planck map extrapolated to the PILOT frequency of the Galactic center L0. From left to right: Total intensity, polarization parameter Q and polarization parameter U. Maps are shown in the EQU-IAU convention at an angular resolution of 2'.

residuals for PILOT are still under investigation. At this stage of the data processing, the analysis of the PILOT data on the Galactic center confirms a good control of gain inter-calibration and we finds an average orientation of the magnetic field along the galactic plane which is in agreement with expectations as we can see on figure 9.15 which shows the intensity map of dust emission measured by PILOT draped with a pattern indicating the direction of the magnetic field lines projected on the plane of the sky, orthogonal to the observed polarization.

9.5 Work in progress.

At the moment we have two polarization map making pipelines: ROMA and scanamorphos. The ROMA map making used so far for the polarisation results. An improved version providing the residuals and polarization errors has been implemented and it is currently under test. The Scanamorphos interface with the PILOT pipeline has been validated. Validation on simulations and data are currently in progress. Some preprocessing steps have not been included at this stage in the pipeline. The next steps of improvement of data processing will be the inclusion of the time constant correction routines

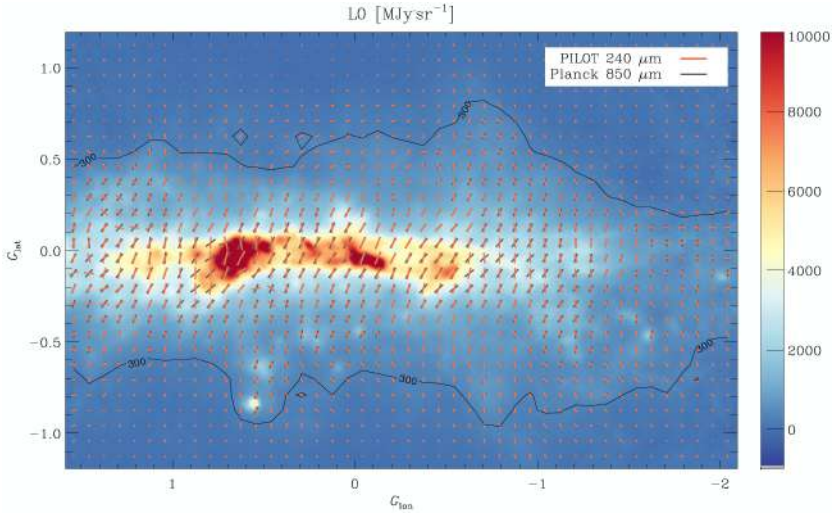

Figure 9.13: Intensity map of the Galactic center with the superposition of the polarisation angles measurements. The red lines correspond to the polarization angle measured with PILOT,the black lines shows the polarization angle measured by Planck at 850μm.

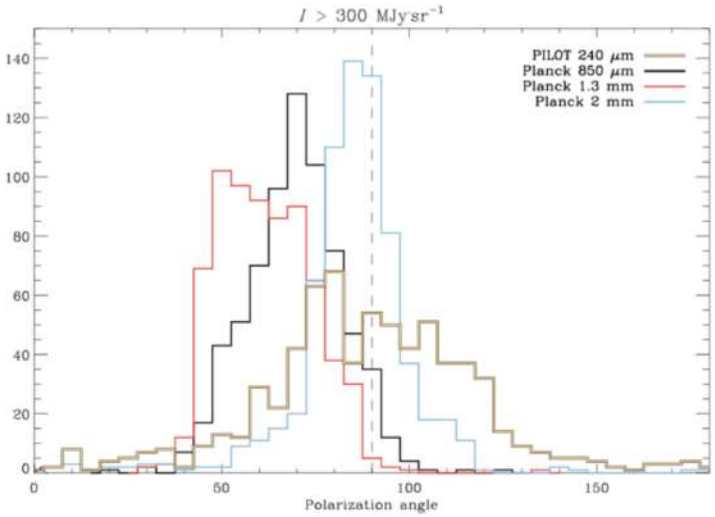

Figure 9.14: Histogram of the polarization angles measured with PILOT (brown), Planck at 850 µm (black), Planck at 1.3 mm (red) and Planck at 2 mm (blue)

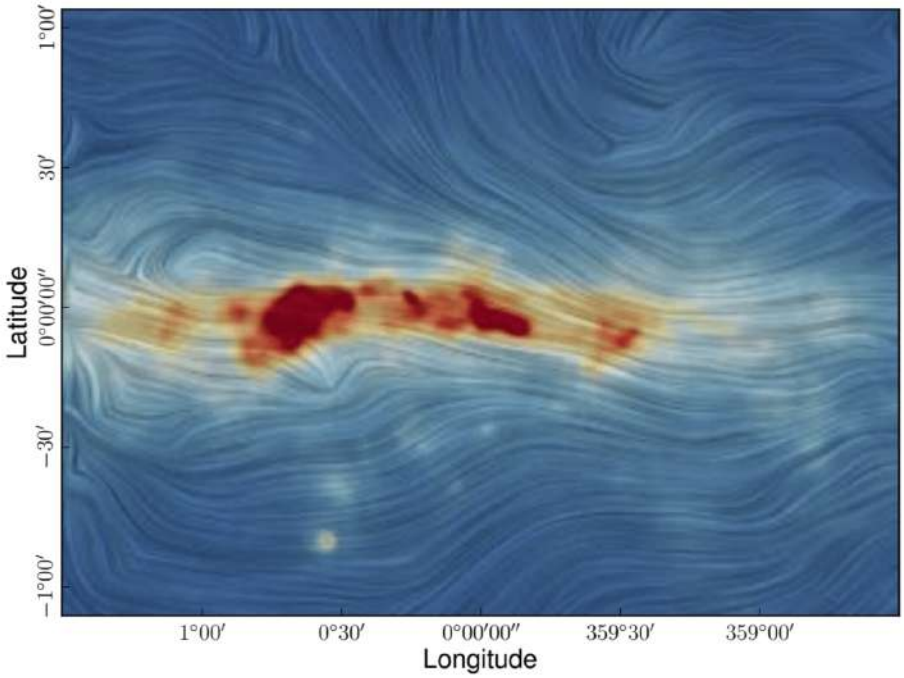

Figure 9.15: View of the magnetic field and total intensity of dust emission measured by PILOT in the galactic center. The colours represent intensity. The "drapery" pattern, produced using the line integral convolution (LIC, Cabral and Leedom 1993) indicates the orientation of the magnetic field projected on the plane of the sky, orthogonal to the observed polarization

and the improvement of the pointing accuracy using the maps provided by Scanamorphos as a basis for the correlation with Herschel.
Others systematics effects that have not been discussed in this thesis also remain to be corrected. For example, we noticed the presence of a "ghost" around strong sources like Jupiter. This is due to the response time of the readout electronics. A fraction of a source seen by a pixel is added to the signal of the next pixel (by the readout chain). That involves a gap in the map corrected in a first order by the focal plane geometry.
For the ROMA pipeline, we are not using the full noise covariance information. We assume that the noise covariance matrice is block-diagonal. The next step in improving the ROMA pipeline will be to provide the algorithm with a non-diagonal matrix that takes into account the noise self and cross-correlation among the bolometers in both focal planes.
The two map-making algorithms are complementary and tests will be made to provide ROMAXpol timelines preliminarily destriped by Scanamorphos instead of raw data in order to further improve the map-making (De Gasperis et al. 2016).

Conclusions et perspectives (English version)

This thesis focuses on the inflight performance of the PILOT experiment. PILOT observes the polarized emission of dust from the interstellar medium. The results obtained during the two scientific flights of the instrument show that the inflight performances are in adequacy with the design requirements. Early polarization results indicate that the PILOT experiment should provide valuable scientific information on polarized dust emission.
During this thesis I actively participated to the two PILOT flights in Canada (Timmins, september 2015) and Australia (Alice Springs, april 2017), during which I helped to set up the tools for processing and analyzing the PILOT data in real time. In particular, I participated in the development of the tools for real-time computation of the PILOT coordinates and of the tools allowing for the rapid construction of intensity maps of the observed regions of the sky.
I worked on the data analysis, in particular on the determination of the bolometers time constants, the correction of the pointing variations related to the thermal deformations of the instrument and the characterization of the optical performances. I also helped interfacing the PILOT data pipeline with the two map-making algorithm that were not originally designed to work with PILOT data.
This work certainly contributed to the success of the two PILOT flights and it was only possible thanks to the work and the advice of the entire PILOT team.
Below I summarize the main results obtained and make some remarks about the future prospects.
In Chapter 3, I presented the study I did on the bolometer time constants. The reading time delay of the bolometer lines within the different arrays has been taken into account in order to refine the measurement. Since the internal calibration source itself has a time constant, it was necessary to take into account its effects on the measurement. However we have seen that the

value of this time constant was not known. The analysis of the time constant on glitches was therefore crucial for the measurement of the bolometer time constants.
Chapter 4 describes the pointing variations linked to the shift between the line of sight of the telescope and the line of sight of the stellar sensor. I explained the different methods that enabled us to control these variations throughout the flight. We have seen that it is possible to create a model of these pointing variations taking into account the thermal deformations and the gravitational deformations due to the elevation change of the instrument. This model will evolve thanks to the improved quality of the maps that will be provided by Scanamorphos. Indeed these data will allow us to access lower intensity sources present on the maps and thus refine the measurement of the offsets with the maps provided by the Herschel telescope. Although not yet implemented, this pointing model will be essential for the reconstruction of pointing in regions without strong sources such as the BICEP2 region or the regions not observed by Herschel.
The temporal and spatial variations of the noise measured on PILOT were presented in Chapter 5. The spectra and noise levels are in agreement with those measured during the ground tests. However, signal variations were observed in some observations. These variations are probably due to the temperature fluctuations of the screen at 300 mK. They are common to the detectors of the same array and are currently corrected in the data.
We studied the background and the detector response variations in Chapter 6. We found that during both flights, the background level measured was twice that measured in the ground tests. The inflight measurements also allowed us to confirm that the background was polarized with a polarization fraction between 4 and 10%. As concerning the detector response, we found that Array 6 has the best response, being 25% more responsive than Arrays 2 and 8. The variations in the array-averaged response over time are between 10% for all arrays. The response dependency on the background has also been constrained. We estimated that a variation of 1pW of the value of the background causes a variation of the response between 12 and 25 %.
In chapter 7, I studied the optical quality of the instrument. The full width at half maximum of the PSF was 10% higher than that expected by the ground measurements. However, this measurement proved to be consistent with simulations taking into account an optical PSF having a FWHM of 1.4 arcmin convolved by the size of a bolometer on the sky. In this chapter I also studied the effects of the time constant of the detectors on the measurement. This effect is small, but not insignificant on the PSF.
Finally, chapters 8 and 9 describe the pipeline set up for the data processing and the map-making. Chapter 9 present the first preliminary PILOT

polarisation maps of the Galactic center observed during Flight#2, in intense but weakly polarized region. These results show a good control of gain inter-calibration. These maps show a good agreement between measurements made with PILOT and those made with the Planck satellite. We expect a significant improvement from the on-going and future data processing. The data will be the subject of several iterations in order to improve the determination of the pointing variations and the measurement of the noise spectra. Time constants will also have to be taken into account in the process, which has not been the case at the moment. Similarly, in the case of ROMA, the full noise covariance between the detectors has not been taken into account. The two map-making algorithms, Scanamorphos and ROMA, working in different and complementary ways, we plan to inject is input to ROMA input the cleaned timelines provided by Scanamorphos, in order to reach optimality to further improve the map quality.

Conclusions et perspectives (version française)

Cette thèse traite des performances en vol de l'expérience PILOT. PILOT observe l'émission polarisée des poussières du milieu interstellaire.
Les résultats obtenus lors des deux vols scientifiques de l'instrument montrent que les performances en vole sont en adéquation avec les exigences de conception. Les premiers résultats en polarisation indiquent que l'expérience PILOT devrait fournir des informations scientifiques précieuses sur l'émission polarisée de la poussière.
Au cours de ce travail de thèse j'ai participé activement aux deux vols de l'expérience au cours desquels j'ai aidé à la mise en place d'outils de traitement et d'analyse en temps réel des données de l'instrument. J'ai notamment participé à la mise ne place d'outils de calculs en temps réel des coordonnées observées avec par les détecteurs de PILOT et à l'élaboration d'outils permettant la construction rapide de carte d'intensité des régions du ciel observées.
A la suite de ces vols, j'ai également travaillé sur l'analyse des données, notamment sur la détermination des constantes de temps des bolomètres, la correction des variations de pointage liés aux déformations thermiques de l'instrument et à la caractérisation des performances optiques. J'ai également aidé à l'interfaçage des données avec différents algorithms de "map-making" qui n'étaient pas initialement conçus pour fonctionner avec PILOT.
Ce travail a certainement contribué au succès de ces vols et n'a été possible que grâce au travail et aux conseils de l'ensemble de l'équipe PILOT.
Ci-dessous je résume les principaux résultats obtenus et formule quelques remarques sur les perspectives d'avenir.
Dans le chapitre 3, j'ai présenté l'étude que j'ai faite sur les constantes de temps des bolomètres. Le décalage du temps de lecture des lignes de bolomètres au sein des différentes matrices a été pris en compte afin d'affiner la mesure. La source interne de calibration disposant elle-même d'une constante de temps, il a été nécessaire de prendre en compte ses effets sur la mesure. Cependant que la valeur de cette constante de temps n'était pas

connue. L'analyse de la constante de temps sur les glitchs a donc été cruciale pour la mesure des constantes de temps des bolomètres.
Dans le chapitre 4 concernant les variations de pointage lié au décalage entre la ligne de visée du télescope et la ligne de visée du senseur stellaire, j'ai exposé les différentes méthodes qui nous ont permis de contrôler ces variations tout au long du vol. Nous avons vu qu'il était possible de créer un modèle de ces variations de pointage en prenant en compte les déformations thermiques et les déformations gravitationnelles dues au changement d'élévation de l'instrument. Ce modèle est amené à évoluer grâce aux cartes qui nous seront fournies par Scanamorphos. En effet ces données vont nous permettre d'accéder à des sources plus faibles en intensité présentes sur les cartes et donc d'affiner la mesure des offsets avec les cartes fournies par le télescope Herschel. Bien que n'ayant pas encore été implémenté, ce modèle de pointage s'avèrera indispensable pour la reconstruction du pointage dans des régions ne disposant pas de sources fortes telle que la région BICEP2 ou les régions n'ayant pas été observée avec Herschel.
Les variations temporelles et spatiales du bruit mesuré sur PILOT ont été présentés au cours du chapitre 5. Les spectres et les niveaux de bruit sont conformes à ceux mesurés lors des tests au sol. Cependant, des variations de signal ont été observées lors de certaines scènes. Ces variations sont probablement dues aux fluctuations de température de l'écran à 300 mK. Elles sont communes aux détecteurs d'une même matrice et sont corrigés des donnés.
Nous avons étudié les variations de background et de réponse au cours du chapitre 6. Nous avons pu constater qu'au cours des vols de l'instrument, le niveau de background mesuré était deux fois supérieur à celui mesuré lors des tests au sol. Les mesures en vol nous ont aussi permises de confirmer que le background était polarisé avec une fraction de polarisation comprise entre 4 et 10%. Les mesures de variations de réponses ont montré que la réponse de la matrice 6 était meilleure d'environ 25%. Les réponses moyennes de chaque matrice varient d'environ 10%. La dépendance au background à elle aussi été contrainte. Ainsi nous avons pu voir qu'une variation de 1pW de la valeur du background entraine une variation de réponse comprise entre 12 et 25%.
Dans le chapitre 7 je me suis intéressé à la qualité optique de l'instrument. La largeur à mi-hauteur de la PSF mesurée était supérieure de 10% à celle attendue par les mesures au sol. Cependant, cette mesure s'est avéré consistante avec des simulations prenant en compte une PSF optique ayant une largeur à mi-hauteur de 1.4 arcmin convoluée par la taille d'un bolomètre sur le ciel. Ce chapitre a été de même l'occasion d'étudier les effets de la constante de temps des détecteurs sur la mesure. Cet effet est faible, mais non négligeable sur la mesure.

Enfin les chapitres 8 et 9 ont été l'occasion de présenter le pipeline mis en place pour le traitement des données et les algorithmes de "map-making". Dans le chapitre 9 j présente les premières cartes en polarisation du centre Galactic, qui a été observé durant le second vol. C'est une région intense mais faiblement polariée. Les résultats montrent un bon contrôle de l'intercalibration du gain. Ces cartes montrent un bon accord entre les mesures effectuées avec PILOT et celles effectuées avec le satellite Planck. Nous esperons une amélioration significative de ces cartes grâce au traitement des données toujours en cours. Les données feront l'objet d'un certain nombre d'itérations afin d'améliorer la détermination des variations de pointage et la mesure des spectres de bruit. Les constantes de temps devront elle aussi être prises en compte dans le processus, ce qui n'a pas été le cas pour le moment. De même, dans le cas de ROMA, la covariance du bruit entre les détecteurs n'a pour l'instant pas été prise en compte. Les deux algorithmes de map-making, Scanamorphos et ROMA, fonctionnant de manière différentes et étant complémentaires, nous essaierons d'injecter en entrée de ROMA les données fournies par Scanamorphos dans le but d'améliorer la qualité des cartes.

Appendix A

Experimental Astronomy paper

PILOT balloon-borne experiment in-flight performance

Noname manuscript No.
(will be inserted by the editor)

PILOT balloon-borne experiment in-flight performance

G. Foënard, A. Mangilli, J. Aumont, A. Hughes, B. Mot, J-Ph. Bernard, A. Lacourt, I. Ristorcelli, L. Montier, Y. Longval, P. Ade, Y. André, L. Bautista, P. deBernardis, O. Boulade, F. Bousqet, M. Bouzit, N. Bray, V. Buttice, M. Charra, M. Chaigneau, B. Crane, E. Doumayrou, J.P. Dubois, X. Dupac, C. Engel, P. Etcheto, Ph. Gelot, M. Griffin, S. Grabarnik, P. Hargrave, Y. Lepennec, R. Laureijs, B. Leriche, S. Maestre, B. Maffei, J. Martignac, C. Marty, W. Marty, S. Masi, F. Mirc, R. Misawa, J.M. Nicot, J. Montel, J. Narbonne, F. Pajot, E. Pérot, G. Parot, J. Pimentao, G. Pisano, N. Ponthieu, L. Rodriguez, G. Roudil, H. Roussel, M. Salatino, G. Savini, O. Simonella, M. Saccoccio, S. Stever, P. Tapie, J. Tauber, C. Tibbs, C. Tucker

Received: date / Accepted: date

Abstract The Polarized Instrument for Long-wavelength Observation of the Tenuous interstellar medium (*PILOT*) is a balloon-borne experiment aiming at measuring the polarized emission of thermal dust at a wavelength of 240 μm (1.2 THz). A first *PILOT* flight (flight#1) of the experiment took place from Timmins, Ontario, Canada, in September 2015 and a second flight (flight#2) took place from Alice Springs, Australia in april 2017. In this paper, we present the inflight performance of the instrument during these two flights. We concentrate on performances during flight#2, but allude to flight#1 performances if significantly different. We first present a short description of the instrument and the flights. We determine the time constants of our detectors combining in-flight information from the signal decay following high energy particle impacts (glitches) and of our internal calibration source. We use these time constants to deconvolve the data timelines and analyse the optical quality of the instrument as measured on planets. We then analyse the structure and polarization of the instrumental background. We measure the detector response flat field and its time variations using the signal from the residual atmosphere and of our internal calibration source. Finally, we analyze the detector noise spectral and temporal properties. The in-flight performances are found to be satisfactory and globally in line with

G. Foënard, A. Mangilli, J. Aumont, J-Ph. Bernard, A. Hughes, A. Lacourt, C. Marty, W. Marty, R. Misawa , B. Mot, L. Montier, J. Narbonne, F. Pajot, I. Ristorcelli, G. Roudil, L. Bautista
Institut de Recherche en Astrophysique et Planetologie (IRAP), Université Paul Sabatier, 9 Av du Colonel Roche, BP 4346, 31028 Toulouse cedex 4;
E-mail: gabriel.foenard@gmail.com

C. Engel
LAM 38 rue F. Joliot-Curie 13388 Marseille CEDEX 13, France;

M. Bouzit, V. Buttice, M. Charra, B. Crane, J.P. Dubois, B. Leriche, Y. Longval, B. Maffei, S. Stever, M. Chaigneau
Institut d'Astrophysique Spatiale (IAS), Bât 121, Université Paris XI, Orsay, France;

P. Ade, M. Griffin, P. Hargrave, G. Pisano, G. Savini, C. Tucker
Department of Physics and Astrophysics, PO BOX 913, Cardiff University, 5 the Parade, Cardiff, UK;

Y. André, F. Bousqet, S. Maestre, J. Montel,O. Simonella, M. Saccoccio, P. Gelot, J.M. Nicot, P. Tapie,F. Mirc,N. Bray, P. Etcheto, G. Parot
Centre National des Etudes Spatiales, DCT/BL/NB, 18 Av. E. Belin, 31401 Toulouse, France;

P. deBernardis, S. Masi, M. Salatino, J. Pimentao
Universita degli studi di Roma "La Sapienza", Dipartimento di Fisica, P.le A. Moro, 2, 00185, Roma, Italia;

O. Boulade, E. Doumayrou, L. Rodriguez, Y. Lepennec, J. Martignac
CEA/Saclay, 91191 Gif-sur-Yvette Cedex, France;

S. Grabarnik, R. Laureijs, J. Tauber, C. Tibbs, X. Dupac
Scientific Support Office, SRE-S, ESTEC, PO Box 299,2200AG Noordwijk, The Netherlands;

N. Ponthieu
Grenoble University, Grenoble, France;

E. Pérot
Thales Services, Toulouse, France;

G. Savini
Department of Physics & Astronomy, University College London, Gower Place, London WC1E 6BT, United Kingdom;

H. Roussel
Institut d'Astrophysique de Paris 98 bis boulevard Arago, 75014 Paris, France;

expectations from ground calibrations. We conclude by assessing the expected in-flight sensitivity of the instrument in light of the above in-flight performances.

Keywords PILOT, inflight performances, Interstellar Dust, Polarization, Far Infrared, Point Spread Function, Straylight, Pointing, Background, Responses, Glitches

1 Introduction

Interstellar dust grains account for 1% of the mass of the interstellar medium (ISM). They are involved in different important processes such as photo-electric heating of the neutral interstellar gas, cooling in dense star-forming regions and the formation of molecules, including H_2 at their surface. Dust emission is used to trace the Interstellar Medium (ISM) structure of the Milky Way and in the local Universe (e.g., [1–3]). The thermal dust emission can be modelled using a modified blackbody spectrum in the infrared to submillimetre wavelenght range. ISM dust grains absorb starlight in the Visible and ultra-violet, which heats them to temperatures of $\simeq$17 K in the dffsue ISM in our Galaxy. Dust grains probably have an irregular shapes and as they rotate, align their minor axes on the local magnetic field (e.g., [4, 5]). This partial alignment causes a fraction of their thermal emission to be linearly polarized in a direction orthogonal to the magnetic field direction as projected on the sky. For the same reason, non-polarised starlight passing through aligned dust grains also becomes polarized: preferential absorption along the grains long axis leads to extinction that is polarized parallel to the magnetic field lines.

The balloon experiment Archeops ([6]) mapped the polarized dust emission at 353 GHz with $\sim 13'$ resolution over $\sim$ 20% of the sky. These measurements indicated high polarization levels (up to 15%) in the diffuse ISM. More recently, the Planck satellite has mapped the polarized dust emission in the wavelength range from 850 mm (353 GHz) to 1.0 cm (30 GHz) over the entire sky ([7]). The planck satellite data allowed us to confirme the existence of highly polarized regions at high galactic latitudes with polarization fractions up to 20%. As a consequence, polarized dust thermal emission is a dominant foreground contaminant to the observation of the Cosmic Microwave Background (CMB) polarization (see, [8]). The goal of the *PILOT* observations is to improve our understanding of the thermal dust polarization signal, by measuring it at higher frequencies in the far-infrared.

Following a brief introduction in Sect. 1, the *PILOT* instrument and the flights and observations are briefely described in Sect. 2.1 and 3 respectively. The use of glitches and our internal calibration source to measure detector time constants is developped in Sect. 4 and 4.3. The in-flight optical quality is discussed in Sect. 5. The instrumental background observed in-flight is described in Sect. 6. Detector response as measured on the residual atmospheric signal and detector noise properties are given in Sect. 7.1 and Sect. 8 respectively. Section 9 summarizes the instrument sensitivity expected given the in-flight performances. Section 10 is devoted to conclusions.

2 The *PILOT* instrument

2.1 Instrument description

A complete description of the *PILOT* instrument is available in [9]. In this section, we only give a brief description of the instrument, for completeness. Table 1 summarizes the main characteristics of the instrument.
The optics of the instrument is composed of an off-axis paraboloid primary mirror (M1) of 0.83m diameter and an off-axis ellipsoid secondary mirror (M2). The combination respects the Mizugushi-Dragone condition to minimize depolarization effects (see [9] and [10]). All optics following M1, including M2, is cooled at cryogenic temperature of 2 K.

The Gregorian telescope is followed by a re-imager and a polarimeter through a flat mirror (M3). Two lenses (L1 and L2) are used to re-image the focus of the telescope onto the detectors. A Lyot-stop is placed between the lenses at a pupil plane that is conjugate of the primary mirror. A rotating Half-Wave Plate (HWP), made of Sapphire, is located next to the Lyot-stop. The birefringent material of the HWP introduces a phase delay between the two orthogonal components of the incident light. A polarization analyzer, which consists of parallel metallic wires, is placed at a 45^o angle in front of the detectors, in order to transmit one polarisation to the transmission (TRANS) focal plane and reflect the other polarisation to the reflection (REFLEX) focal plane. Observations at, at least two, different HWP angles allow us to reconstruct the stokes parameters I, Q and U. Each of the (TRANS and REFLEX focal planes include 2048 bolometers (8 arrays of 16 X 16 pixels). They are cooled to 300 mK by a closed cycle ^{3}He fridge. The detectors were developed by CEA/LETI for the PACS instrument on board the Herschel satellite.

In order to reconstruct the pointing of the instrument, we use the Estadius stellar sensor developed by CNES for stratospheric applications and described in [11]. This system provides an angular resolution of a few arcseconds, needed to optimally combine observations of the same part of the sky obtained with various polarization analysis angles. Estadius also remains accurate for scanning at speeds up to a 1^o/s. An internal calibration source (ICS) is used in-flight to calibrate time variations of the detector responses. This device is described in [12] and [13]. The source is located behind mirror M3 and illuminates all detectors simultaneously. It is driven using a square modulated current and the

Table 1: Main optical characteristics of the *PILOT* instrument.

Telescope Type	Gregorian	
Equivalent focal length [mm]	1790	
Numerical aperture	$F/2.5$	
FOV [°]	1.0×0.8	
Ceiling altitude	$\sim$3 hPa	
Pointing reconstruction	translation= $1''$, rotation= $6''$, 1σ	
Gondola Mass	$\sim$1100 kg	
Primary mirror type	Off-axis parabolic	
Primary mirror dimension [mm]	930 x 830	
M1 used surface projeted diameter [mm]	730	
Focal length [mm]	750	
Detector type	Multiplexed bolometer arrays	
Number of Detectors	2048	
Detector temperature [mK]	300	
Sampling rate [Hz]	40	
Photometric channels	SW Band	LW Band
λ_0 [μm]	240	550
ν_0 [GHz]	1250	545
$\Delta\nu/\nu$	0.27	0.31
beam FWHM [$'$]	1.9	3.3
Minimum Strehl Ratio	0.95	0.98

current and voltages of the source are measured permanently during flight to monitor the power dissipated in the source.

2.2 Polarisation measurements

Assuming a perfect HWP, the *PILOT* measurements m are related to the input Stokes parameters I, Q, U of partially linarly polarized light through

$$m = R_{xy}T_{xy} \times [I \pm Q_{inst}\cos 4\omega \pm U_{inst}\sin 4\omega] + O_{xy}, \quad (1)$$

where R_{xy} and T_{xy} are the system response and optical transmission respectively and O_{xy} is an arbitrary electronics offset. For the configuration of the HWP and polarizer in place in the instrument, ω is the angle between the HWP fast axis direction and the horizontal direction measured counterclockwise as seen from the instrument and the $\pm$ sign is $+$ and $-$ for the REFLEX and TRANS arrays respectively (see [9]). Note that with the above conventions Q_{inst} and U_{inst} are defined with respect to instrument coordinates in the IAU convention, with Q_{inst}=0 for vertical polarization. When refering to skylight polarization Q_{sky} and U_{sky}, Equ. 1 becomes

$$m = R_{xy}T_{xy} \times [I \pm Q_{sky}\cos(2\theta) \pm U_{sky}\sin(2\theta)] + O_{xy}, \quad (2)$$

where $\theta = 2 \times \omega + \phi$ is the analysis angle, ϕ is the time varying paralactic angle measured counterclockwise from Celestrial North to Zenith for the time and direction of the current observation, and Q and U are in the IAU convention with respect to equatorial coordinates. In practice, maps of Q and U are derived from observing the same patch of sky with at least 2 values of the analysis angle taken at different times in general. Inversion to derive sky maps of I, Q and U can be done through polarization map-making algorithms (see for instance [14]). The light polarization fraction p and polarization direction ψ are then defined as:

$$p = \frac{\sqrt{Q^2+U^2}}{I} \quad (3)$$

and

$$\psi = 0.5 \times \arctan(U, Q). \quad (4)$$

3 The Pilot flights and observations

PILOT is carried to the stratosphere by a generic gondola suspended under an open stratospheric balloon operated by the French National Space Agency (CNES). *PILOT* uses 803Z class balloons, with a Helium gas volume of $\sim$ 800 000 m^3 at ceiling altitude. The instrument can be pointed to a given direction using the gondola motion around the flight chain and motion around an elevation axis (see [9]). Scientific observations are organized in individual observation tiles (also called observations for short) where a given rectangular region of the sky is scanned by combining the azimuth and elevation axis of the instrument.

The flight plan is built taking into account the various observational constraints such as the visibility of astronomical sources, the minimum angular distance between the instrument optical axis and bright sources such as the sun or the moon, elevation limits due to the presence of the Earth

at low elevations and the balloon at high elevations. The expected performance of the instrument are taken into account when establishing the flight plan in order to distribute the observing time according to the science objectives requirements, and to evenly distribute polarization analysis directions (angle θ in Eq. 2), as well as sky scanning direction angles for any given astronomical target.

3.1 flight#1

The first flight of the *PILOT* experiment took place from the launch-base facility at the airport of Timmins, Ontario, Canada on September 21, 2015 at 9:00 PM local time. The launch was part of a campaign led by CNES and the Canadian Space Agency (CSA), during which six stratospheric balloon experiments were successfully operated.

The ascent to the stratosphere took 2.5 hr. At ceiling, the altitude of the experiment remained relatively stable between 38 km and 39 km over a time period of 18 hr. The total duration of the flight was 24 hr allowing us to obtain about 15 hr of science data. Approximately 4 hr were spent optimizing the detector readout chain settings, recycling of the ^{3}He fridge and slewing between individual observing regions. The focal plane temperature remained stable during the whole ceiling period at temperature of $\simeq 321\,mK$ and $\simeq 325\,mK$ for the TRANS and REFLEX focal planes respectively. Out of the 8 bolometer arrays, array #1 (TRANS) and array #3 (REFLEX) were not operational during flight#1 due to a failure in the time-domain multiplexing clock signal, a problem which was already experienced during ground calibrations (see [15]).

The scientific observations performed during flight#1 are summarized in Tab. 2. During this flight, scientific observations were performed scanning the telescope at constant elevation, in order to minimize residual atmospheric emission. We collected a total of 5.5 hr of science data on star forming regions, 2.4 hr on cold cores, 1.4 hr on external galaxies, and 4.6 hr on a relatively empty region of the sky. Calibration data were obtained on planets Uranus and Saturn. We also obtained 'skydip' measurements during which we explored the whole range of allowed elevations, in order to characterize the residual atmospheric emission (see Sect. 7.1).

The experiment succesfully landed under parachute and was recovered about 350 km East of Timmins in a dry forest area. The instrument had suffer some damages, essentially on electrical harness and optical baffle, due to collision with trees and branches. The mechanical structure of the gondola has well protected the payload. Inspection of the instrument and analysis of a video recorded during the flight showed that the front baffle of the instrument deteriorated during the day part of the flight. This was caused by a defect in the thermal insulation of the baffle. It produced additional straylight which, despite subtantial subtraction during data processing, limited the quality of the science data obtained during this flight. Deteriorations of the instrument were fixed during the preparation for its second flight (see Sect. 3.2).

3.2 Improvements between flights

Following flight#1, a series of modifications were made to the instrument. In particular, the cryostat was tested in the laboratory for operations with stronger pumping on the ^{4}He bath, which allowed reaching lower detector temperatures and increased the cryogenic lifetime of the cryostat from > 27 hr to > 33.5 hr. We also increased the size of the optical field-stop located in the cryostat, which was producing parasitic reflections affecting the polarization curves for pixels at the edges of the focal planes. We modified the thermal insulation of the optical front baffle to avoid deformation under sunlight exposure. We also decided to implement the possibility of scanning the sky at an arbitrary angle with respect to the horizon. This leaves residual atmospheric emission signal in the data that would need to be removed but can be used to calibrate the instrument response (see Sect. 7.1). It also allows us to obtain observations at different scan angles on the sky, which is important for optimal removal of low frequency noise through destriping, without waiting for the sky to rotate. The new scanning mode was obtained by subordinating the elevation scan speed to the cross-elevation scan speed to obtain the desired scan angle. It was tested on the ground with the actual gondola, in order to check that this did not excite oscillation modes of the flight chain. We also modified the on-board computer sofware to allow scanning only the rectangular region around the target defined by the observer, and implemented a more flexible calibration sequence scheduler, in order to reduce overhead times. All of these changes were successfully implemented for flight#2.

3.3 flight#2

The second flight was conducted from the USA-operated launch base of Alice Springs, Australia. The launch was carried out as part of a launch campaign led by CNES, which enabled successful flights of 3 stratospheric gondolas.

The flight lasted approximately 33 hr, during which 24 hr of scientific observations were obtained. The launch took place at 6:30 AM local time. The experiment reached ceiling altitude about 2 hr after take-off. The instrument reached an altitude of 39 km slowly decreasing to 36 km during the first day of the flight. The altitude decreased down to 31-34 km during the night due to the lower ascensional force of the balloon and despite getting rid of a fraction of the available balast. During the second day, the altitude rose again to reach 38-40 km. The focal planes temperatures evolved slightly with altitude during the ceiling period and remained

Fig. 1: The *PILOT* experiment on the tarmac before launch for flight#1 from Timmins, Ontario, Canada on September 21 2015.

Table 2: Summary of the observations obtained during flight#1.

Source	Observation Time [mn]	Map size [deg x deg]	Total depth [deg^2/h]
Taurus	117	12 x 8	55
Orion	145.3	10 x 10	47.8
Aquila Rift	46	8 x 8	94
Cygnus OB7	21	7 x 7	166.5
L1642	44	2 x 2	9.5
G93	61	2 x 2	6.3
L183	41	2 x 2	9.5
M31	84	3 x 3	6.1
Polaris	160	5 x 5	12.3
Cosmo field	116	16 x 16	160
Uranus	31	3 x 2	19
Saturn	12	2 x 2	34
SkyDip	10	n/a	n/a

in the range $\simeq 304-307$ mK and $\simeq 308-312$ mK for the TRANS and REFLEX focal planes respectively. Out of the 8 bolometer arrays, array #1 (TRANS), array #3 (REFLEX) and array #5 (TRANS) were not operational during flight#2 for similar reasons as during flight#1.

The scientific observations obtained during flight#2 are summarized in Tab. 3. Appart for the Orion molecular cloud and planets, all targets observed are specific to southern hemisphere. We mapped two regions along the inner Galactic plane near the Galactic center (L0) and near $l = 30^o$ (L30). We also obtained maps of several known molecular clouds. A large integration time was allocated to map a fraction of the Large Magellanic Cloud (LMC). We also obtained long measurements of the empty field observed by the *BICEP2* ground experiment ([16]) in order to attempt constraining the polarization properties of dust in a typical region of low galactic foreground to the CMB.

The flight trajectory was Eastward during most of the flight. We succesfully used the two telemetry antennas located in AliceSprings and in Longreach. The gondola was recovered about 850 km East of the launch site, in a desertic area and brought back to the Alice Springs base using an helicopter and a truck. The gondola and the instrument suffered no major damage from landing or recovery, which was later confirmed by a thorough inspection following the return of the instrument to France.

Table 3: Observations obtained during flight#2.

Source	Observation Time [mn]	Map size [deg x deg]	Total depth [deg^2/h]
L30	72	5 x 5	21
L0	32	2 x 5	18.8
Orion	140.8	5 x 10	21.3
Rho-oph	268.8	9 x 4	8.0
Musca	185.6	2 x 3	1.9
LMCridge	134.4	3.5 x 1	1.6
LMCridgeBIG	232.5	4.0 x 2	2.0
BICEP	290.1	30 x 12	74.5
Jupiter	27.7	3 x 2	13.0
Saturn	23.5	5 x 3.4	43.0
Skydip	21.3	n/a	n/a

4 Glitches and time constants

The *PILOT* data are affected by 'glitches', which are characterized by an abrupt deviation in the signal timeline of a bolometer followed by an exponential decay. These features can be positive or negative, and they are caused by energetic particles striking the detector absorber or the walls of the integration cavity surrounding the detectors (see [17]). Removal of glitches from the *PILOT* timelines is important since they do not follow the same Gaussian distribution as the detector noise, and hence produce a bias in statistical descriptions of the data, e.g. the signal mean. They are also a significant source of artifacts for steps in the *PILOT* data processing that are performed in Fourier space. Finally, the decay following glitches can be used to constrain the time constant of individual bolometers. In this section, we give a brief description of our method for identifying glitches, a preliminary analysis of the glitch properties and the use of glitch decay to constrain detector time constants.

4.1 Glitch identification

We emphasize that our goal at this stage is to identify and suppress the most significant anomalous features in the signal timelines (i.e. those that noticeably affect the accuracy of our detector noise estimation) in an efficient, automated fashion across the entire flight, and to identify strong glitches that can be used to measure the detector time constants (Sect. 4.3). More sophisticated methods for glitch identification and signal reconstruction will be tested and applied to the *PILOT* data in future works that present the *PILOT* science data.

We identify glitches in the *PILOT* timelines using the following procedure. First, we construct an estimate of the high frequency (HF, 40 Hz$\sim$ 1sample) noise by shifting the timeline for each bolometer by 1 sample, and subtracting this shifted timeline from the original timeline. We refer to the resulting timeline as the 'shifted data timeline'. We then replace the value of each sample in the shifted data timeline with a local estimate of the median absolute deviation, which is calculated using adjacent samples within a rolling window of 5 seconds. We refer to the resulting timeline as the 'local HF noise timeline'. Next, we divide the shifted data timeline by the local HF noise timeline. Large (positive or negative) values in this glitch signal-to-noise (S/N) timeline provide a preliminary list of glitch candidates. Since glitches are characterized by a sharp change followed by an exponential decay, we expect positive glitches to appear in the shifted data and glitch S/N timelines as a large positive value, followed immediately by a (lower amplitude) negative value (and vice versa for negative glitches). In practice, however, this idealized characteristic signature is complicated by the presence of detector noise (for weaker glitches), very strong glitches (that saturate the detector for longer than one sample) and glitches that fall exactly between two samples. We reduce our list of preliminary glitch candidates by rejecting candidates with S/N < 5. We further impose a criterion that a positive value in the S/N timeline should be followed by a negative value of comparable amplitude. We define 'comparable amplitude' using an exponential softening function ($|thresh| = -0.75\exp(-1 + S/N/5)$ that depends on the S/N of the glitch candidate, such that it rejects moderate significance glitch candidates ($5 < S/N < 8$) if they do not exhibit the characteristic positive-negative (or negative-positive) signature. For glitch candidates with high S/N ($S/N \geq 10$), the range of allowed values for the next sample becomes sufficiently relaxed that essentially all such candidates are retained.

4.2 Glitch statistics

The glitch intensity histogram averaged over the whole focal plane for both positive and negative glitches during flight#2 is shown in Fig. 2. The statistics for glitches below $\simeq 150$ ADU is affected by noise excursions also detected by the detection method. Both positive and negative glitches are detected, with a ratio of 86.8% for positive glitches (13.2% for negative glitches) above an absolute glitch intensity of

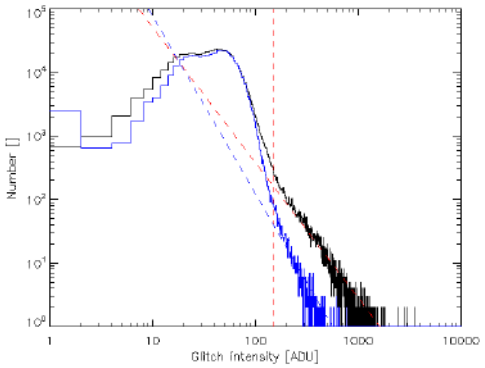

Fig. 2: Histogram of glitch intensities as measured during flight#2. The black and blue curves are for positive and negative glitches respectively. The dashed lines show fits of the distributions constrained above 150 ADU. The vertical line shows the approximate limit of 150 ADU above which true glitches dominate over noise.

150 ADU. This ratio is similar to what has been observed for glicthes on the PACS/Herschel detectors as reported by [17]. For glitches above 150 ADU, the glitch rate observed during flight#2 is about 0.68 gli/pix/hr. This figure goes up to 2.24 gli/pix/hr for positive glitches with intensity above 100 ADU. These values are comparable to those obtained for the PACS instrument on board Herschel by [17]. The glitch rate is observed to be roughly constant during flight#2 and the distribution across the focal plane is mostly homogeneous. Figure 3 shows the average profile of the signal decay following positive glitches for the various arrays, obtained by stacking signal around glitch locations, for glitches with intensity above 150 ADU. Above the threshold, individual pixels receive about 10 such glitches during flight#2, which allows to constrain bolometer time constants, as described in Sect. 4.3. As can be seen on the figure, most arrays show similar decay profiles, except for array #6 which shows significantly longer time constants.

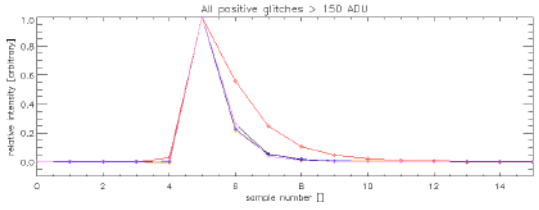

Fig. 3: Array-average of the signal following positive glitches with intensity larger than 150 ADU. The data has been co-added with the glitch position at sample number 5 and the average profiles have been normalized to their peak value. The various colors (red, orange, black, blue, violet) correspond to the various arrays (arrays #6, 2, 4, 7 and 8 respectively).

	TRANS			REFLEX				ALL
Array	2	6	Avg	7	4	8	Avg	Avg
τ_{gli}	0.61	1.51	1.06	0.69	0.74	0.68	0.70	0.85
τ_{det}	0.61	0.89	0.75	0.58	0.63	0.58	0.60	0.66

Table 4: Array-averaged values of the detector time-constants as measured using glitches and using ICS downard decay assuming an intrinsic ICS time constant of τ_{ics}=11 ms (see text).

4.3 Detectors time constants

During the calibration sequences with the ICS, the bolometric signal following each extinction of the source gradually decreases with a characteristic time τ_{cal}. This progressive decay results from the convolution of the square pulse controlled by the current injected into the ICS with the transfer function of the ICS and that of the bolometers. A similar decrease follows the absorbtion of high energy particles (glitches) by the detectors, which can also be used to determine the response of individual detectors.

In the following, we assume that the transfer functions of the ICS and the bolometers can be described by an exponential decay of the form $e^{-t/\tau}$, where τ is the time constant. We call τ_{ics} the time constants of the ICS and τ_{det} that of the individual bolometers.

Because the glicth rate is low, determining τ_{det} from glitch transients alone would lead to a noisy determination. Instead, we use a combination of the glitch and ICS transients described below. The array-averaged values determined for each array are summarized in Tab. 4.

In a first step, we measure a first estimate of the detectors time constant using glitches, which we call τ_{gli}. We averaged the measurements over 15 samples following positive glitches with intensity larger than 200 ADU. The average values derived for each array are given in Tab. 4 and the focal plane distribution of τ_{gli} is shown on Fig. 4. The time constant derived using glitches are arround 0.7 samples (17.5 ms) for most arrays, except for array #6 for which it is around 1.5 samples (37.5 ms).

In a second step, we measure the time constant of the ICS using calibration sequences. We stack all decays of the signal following the extinction of the ICS and compute the corresponding average ICS downward profile viewed by each pixel. We then deconvolve this profile in Fourier space, using the transfer function $e^{(-t/\tau_{gli})}$. We then average this profiles over pixels and fit the average profile with an exponential funtion and derive a value of τ_{ics} of 0.41 samples (10.25 ms). This can be compared to the value of 9.23 ms measure by [12] for a device similar to our source and operated under similar conditions.

In the last step, we determine the final values of τ_{det}. We proceed in the same way as for the measurement of τ_{ics}, except that we use here the above value of τ_{ics} as parameter for the deconvolution kernel and fit the downard profile

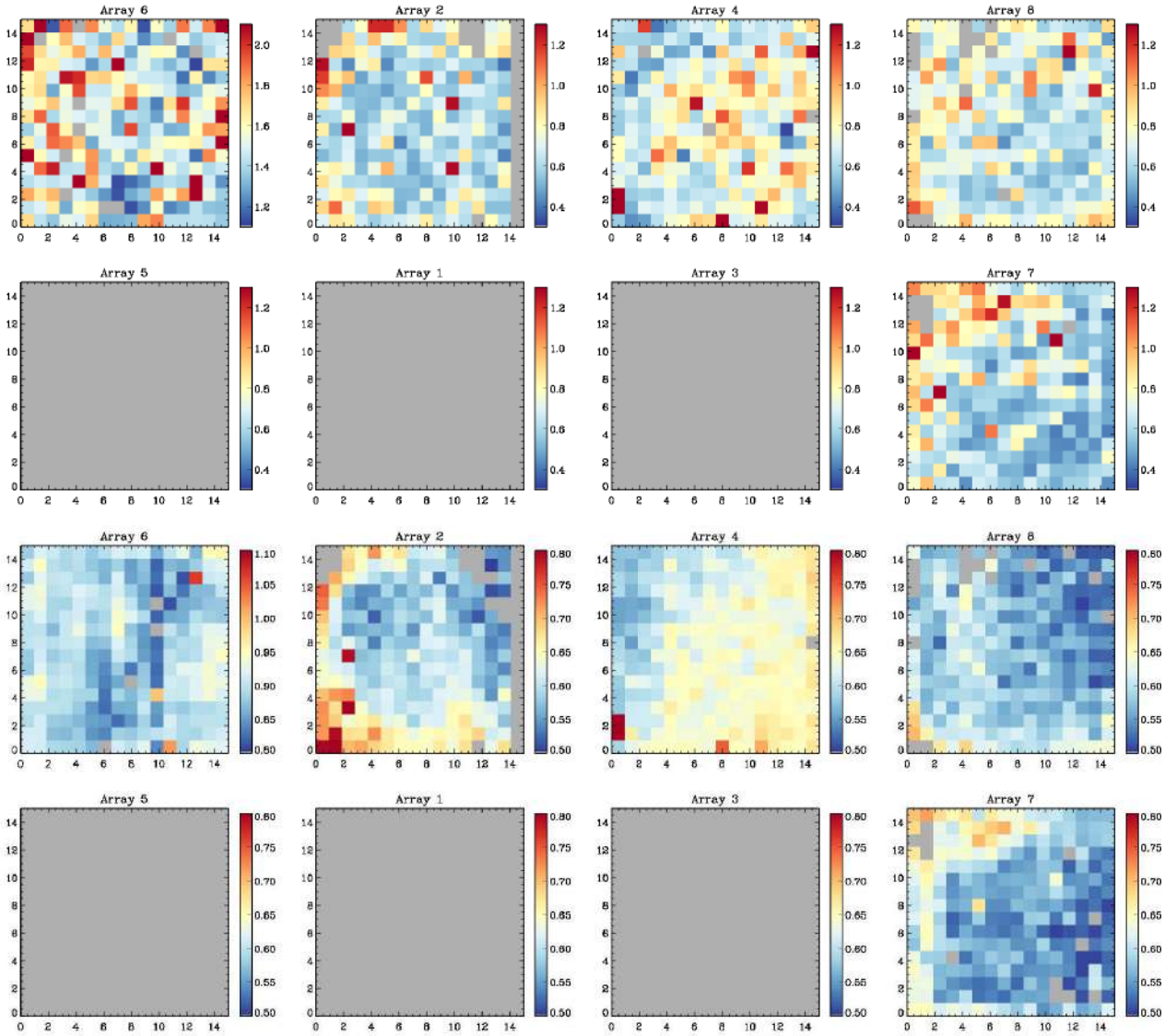

Fig. 4: Top: Focal plane distribution of the bolometer time constants as measured from glitches τ_{gli}. Bottom: Focal plane distribution of the bolometers time constants τ_{det} as measured using the ICS downward transitions. The four arrays shown on the left (resp. right) belong to the TRANS (resp. REFLEX) focal planes, such that arrays #6 and #4 (or arraus #2 and #8) are optical conjugates. In this representation, elevation increases towards the top-left and cross-elevation increases towards the top-right corner of each focal plane. The same convention and array numbering is used for all figures of the paper.

of each pixel in order to derive the values of τ_{det} for each pixel. The array-averaged values of τ_{det} are given in Tab. 4 and are of the order of 0.60 samples (15.00 ms). On average, array #6 is slower than other arrays, with an average τ_{det} of 0.89 samples (22.25 ms). The focal plane distribution of τ_{det} is shown on Fig. 4.

5 Point Spread Function

Most of the optical elements in the *PILOT* instrument, except the primary mirror M1, are cooled below 3K inside a cryostat (the photometer). The overall optical quality of the system is therefore sensitive to the positioning of the primary mirror with respect to the cryostat. External conditions can modify the relative positioning of the optics in-flight, in particular thermo-elastic and bending under gravity effects in the mechanical structure holding the primary mirror. To minimize thermal effects, the pre-flight optical alignment

was based on the flight thermal modeling and thermo-elastic analysis of the instrument and in-flight temperature predictions [18]. Checking the optical quality using in-flight measurements is therefore of particular importance.

During each flight of the instrument, we observed planets which can be assimilated to point sources at the resolution of *PILOT* and can therefore be used to assess the optical quality through a measurement of the instrument Point Spread Function (PSF). Planet maps were constructed with a pixel size of $0.1'$ for each detector array and for each scan through the planet (referred to as planet crossings). All the data have been corrected for the responses calculated on the skydips, as described in Sect. 7.1 and corrected for the effects of the time constant of the detectors through deconvolution of the time constants as measured in Sect. 4.3.

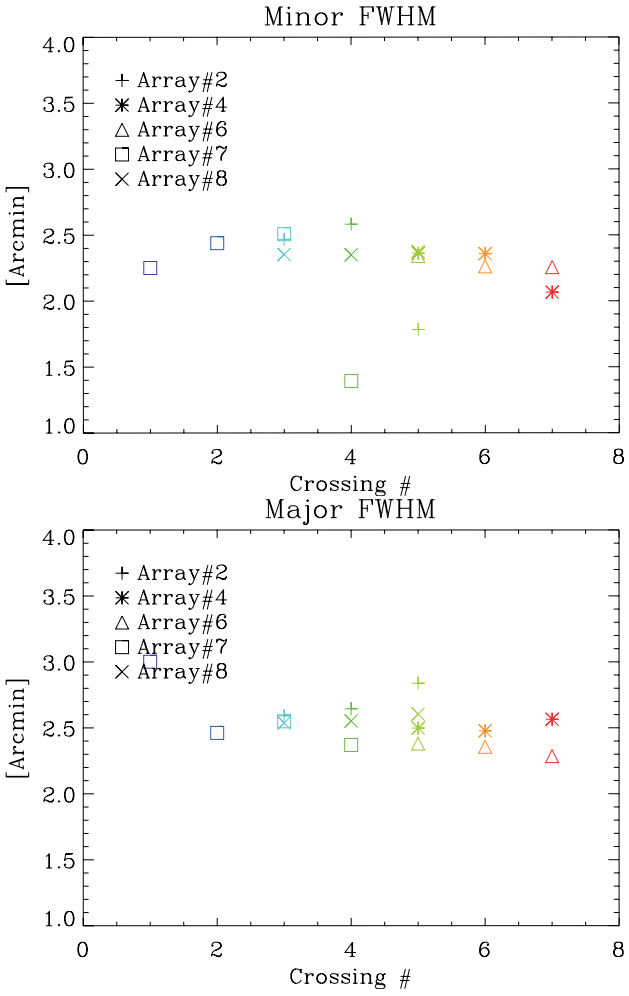

Fig. 5: Characteristics of the PSF obtained on Jupiter crossings during flight#2. The top and bottom pannels show the evolution of the minor and major axis respectively as a function of the crossing number. The different colors correspond to the different crossings of the focal plane

The parameters of the PSF were deduced using an elliptical Gaussian fit applied to the individual crossing images. Figure 5 shows the values obtained for the major and minor axis dimensions of the PSF obtained on Jupiter. We obtain an average full-width half maximum (FWHM) size of $2.25' \pm 0.15'$, taking into account the apparent size of the planet ($44.2''$). The uncertainties were derived from the statistics between the planet crossings.

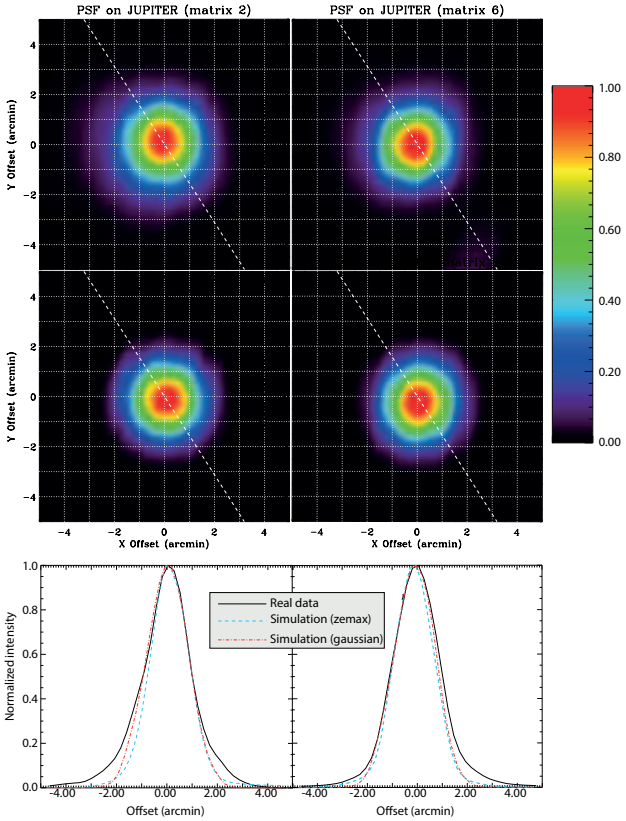

Fig. 6: Top: Images of Jupiter obtained with array #2 (left) and 6 (right) during one of the observing sequence of the planet. Middle: Map obtained on array #2 (left) and #6 (right) from signal simulated using the actual pointing (see text). The scan direction is shown by the dashed white line. Bottom: Circular average profile of the PSF measured on array #2 (left) and array #6 (right). The solid black curve corresponds to measurements from the observations on Jupiter during flight#2. The dashed blue curve is obtained from a simulation (see text) using an input PSF from the modelling of the optical system with zemax [19]. The red dash-dotted curve is obtained from the sme simulation using a PSF approximated with a Gaussian function. Each PSF has been normalized by its maximum value.

Figure 6 shows the normalized average total intensity image over all crossings of Jupiter obtained with array #2 and array #6 during one observation of flight#2. The PSF shows no particular elongation along the scan direction, indicating accurate accounting for the detectors time constant. However, we can see that the PSF images are boxy, which

likely reflects that they result from the convolution of the optical PSF with a square pixel.

To understand the origin of the ”box effect” which may be induced by the convolution of the PSF and the size of the bolometers pixels, we simulated timelines calculated as the integral of the flux received by a square detector with a pixel size matching that of *PILOT* (1.4′) observing a Gaussian diffraction-limited optical PSF with the expected size for *PILOT* (≈ 1.4′) centered at the predicted position of the planet. The resulting map is compared to the observed PSF in Fig. 6. The simulated PSF also shows the observed ”box effect”. This confirms the hypothesis that they result from the convolution of the optical PSF with a square pixel. By applying to this simulation the same analysis as to the data, we measure a FWHM of $2.31' \pm 0.07$. The value obtained in the simulation is therefore consistent with the value measured in-flight.

Figure 6 also shows the circular average profile of the PSF measured on array #2 and array #6 and the comparison with the simulations. The profiles are quite similar, except for the presence of more intense PSF wings in the measurements, an effect that was also observed during ground tests.

6 Instrumental Background

We estimated the background level in-flight using a combination of calibration measurements obtained at ceiling altitude and during ground tests. These calibration measurements involve, firstly, a short sequence of data recorded with difference detector settings, from which we obtain an empirical conversion between the signal measured in ADU and its equivalent in Volts. This procedure is relatively quick, and was repeated during ground tests and at the beginning of both *PILOT* flights. A second – much longer – ground calibration measurement procedure is required to establish the relation between the output voltage of each bolometer and the intensity of the background incident on the detectors. These measurements were performed during tests in front of a controlled black body at cryogenic temperature at the CEA in 2012 and 2016.

6.1 Background Level

Figure 7 shows examples of the background image obtained during flight#1 and flight#2 using the technique described above.

The typical background value measured during flight#1 and flight#2 were in the range 13-16 pW per pixel towards the center of the focal plane. These absolute values are quite uncertain due to the limited sampling of the calibration measurements, which could only be conducted for a finite set of detector settings and incident background levels and the difficulties in interpolating for the in-flight settings. As seen in the top row of Fig. 7, this is evident from the unphysical offsets between the array-averaged background levels that we infer (i.e. the average background on arrays #2 and #4 is lower than on the other arrays). Nevertheless, it seems likely that the background during both *PILOT* flights was somewhat higher than the values predicted using our instrument photometric model of 8 pW per pixel at the center of the focal plane. Variations in the background level were monitored throughout each flight, and were found to be relatively stable except for variations related to residual atmospheric emission and HWP position, due to the background polarization (see Sect. 6.2). The background distribution in the focal plane is shown in the bottom row of Fig. 7, where we have normalised the pixel values by the average background level measured on each array. The shape of the background follows a similar distribution as observed during ground calibrations, with values raising by about a factor of two from the center to the corners of the focal plane, a distribution that is explained by the absorption in the lens located just in front of the focal plane.

6.2 Background polarization

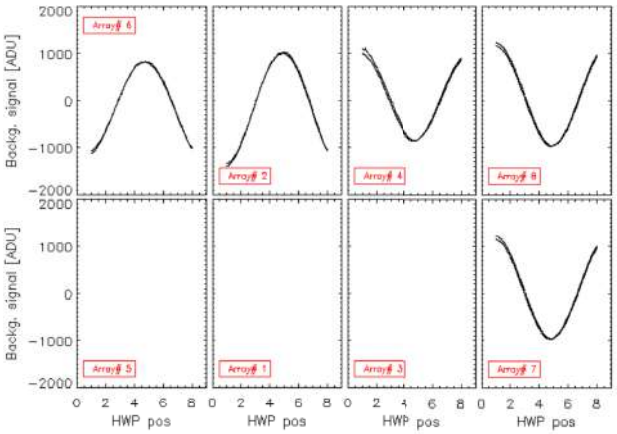

Fig. 8: Variation of the background signal as a function of the HWP for all arrays during one observation of flight#2. The sine curve with opposite phase on the TRANS and REFLEX arrays is due to the polarization of the instrumental background emission.

Figure 8 shows the variations of the signal observed on each array as a function of HWP positions as measured during flight#2. During this observation, the half wave plate was moved successively from position 1 to position 8 and then back to position 1. The signal adopts a sinusoidal shape in phase opposition between the arrays in transmission and the

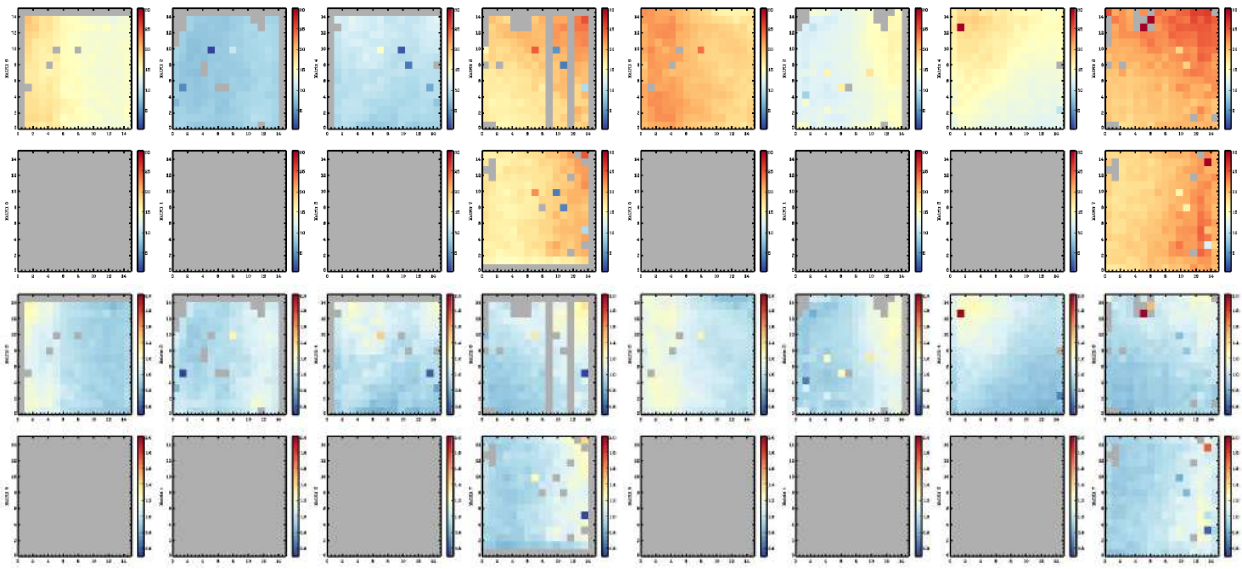

Fig. 7: Example focal plane images of the background derived during flight#1 (left) and flight#2 (right), each from ~ 30 seconds of observation. The top row shows an estimate for the absolute background level, the bottom row shows the background level normalized by the average on each array. In each panel, the four arrays on the left (resp. right) belong to the TRANS (resp. REFLEX) focal planes, such that arrays #6 and v4 (or arrays #2 and #8) are optical conjugates.

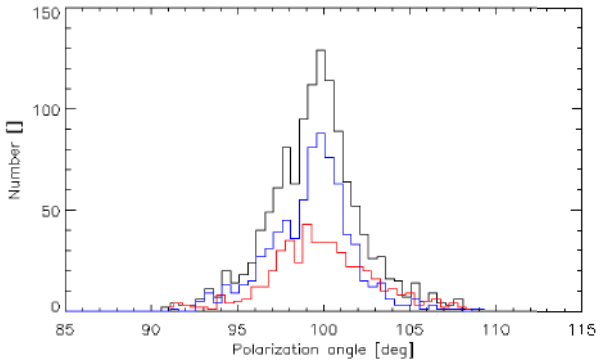

Fig. 9: Histogram of the polarization angle ψ. The black, red and blue lines show the curves for all pixels and the TRANS and REFLEX pixels respectively.

TRANS and REFLEX arrays. We used this data to derive the polarization properties of the background. The signal amplitude varies by about 2.10^3 ADU, which corresponds to 0.5 pW, corresponding to 2.5% of the measured background level. The maximum signal on the TRANS array (or minimum signal on the REFLEX arrays), is at around HWP position 5, which corresponds to the fast axis of the HWP being roughly vertical in the instrument restframe. Given the orientation of the polarizer in the instrument, this implies a polarization direction roughly horizontal. Figure 9 shows the histogram of the polarization angle in the instrument restframe, deduced using a fit of the data using Eq. 1, with ω being the HWP angle in the instrument reference frame, increasing counterclockwise when looking at the sky. The polarization angle values are well peaked around 100^o, indicating that the polarization direction is roughly horizontal and constant over the focal plane. Very similar polarization angles and fractions were observed during flight#1.

Note that a similar polarization of the background was observed during ground calibrations as reported in [15]. Within the large uncertainties on the absolute value of the background level, the polarization fraction on the ground was similar to that observed in flight. However, the polarization angle is markedely different, with horizontal polarization in-flight and at around $\psi = -45^o$ during ground calibration. We currently attribute this rotation to a different origin of the background in the two situations. While the in-flight background is mostly due to the instrument, the background measured during ground calibrations is dominated by the room atmosphere in the few first centimeters in front of the entrance window of the cryostat. The fact that the angles are strongly rotated indicates that polarization probably arises from propagation of the unpolarized background through the instrument, with a differentail rotation depending on where in the instrument the background is originating.

7 Detector response

The response of bolometers, which measures their ability to convert flux variation into an electrical signal variations, varies with their temperature and with the optical background

they receive. It is important to accuractely quantify these variations in order to calibrate the data, in particular for polarization measurements, which, for the *PILOT* instrument, rely on combining data taken by different detectors at different times and with different HWP positions. We use our Internal Calibration Source (ICS) to precisely measure the time variations of the response, and we use the variations of the residual atmospheric signal in order to measure the spatial variations of the responses (or response flat-field) in the focal plane.

7.1 Response time variations

The ICS source is turned on at regular intervals during flights, at the end of individual mapping scans and occasionally during instrument manoeuvers. Calibration sequences typically accounts for $\simeq 5$ ON-OFF cycles. The source is driven with a square modulated current with a period of $\simeq$1 sec, and the current (I) and voltage (V) are recorded continuously. The ground calibration tests have shown that the ICS optical flux measured by the detectors is proportional to the electrical power $P = V \times I$ dissipated in the source (see [**?**]).

In practice, in order to correct for amplitude drifts unrelated to the ICS signal, we subtract drifts due to the residual atmospheric emission in each timeline, using a correlation with pointing elevation and apply a low-pass filter to the bolometer signal timelines. In order to mitigate the effects associated with the time constants of the bolometers, a few data samples at the beginning and end of each ICS sequence are discarded. We only consider ICS sequences when the HWP is not moving and discard truncated ICS sequences with less than 4 ON-OFF cycles. We then compute the response of each bolometer to the ICS signal for a given calibration sequence as

$$\rho_{ICS} = \frac{\Delta^{ICS}_{\rm on-off}}{\langle R_{\rm ICS}(\langle I_{\rm ON}\rangle^2 - \langle I_{\rm OFF}\rangle^2)\rangle} R_{\rm ref} I^2_{\rm ref}, \quad (5)$$

where $\Delta^{ICS}_{\rm on-off}$ is the observed average signal difference in ADU between the ON and OFF states of the source, $R_{\rm ICS}$ is the source impedance and $\langle I_{\rm ON}\rangle$ and $\langle I_{\rm OFF}\rangle$ are the time-average currents during the ON and OFF periods of the calibration sequence respectively. $R_{\rm ref} = 300\Omega$ and $I_{\rm ref} = 1.8$ mA are the reference impedance and current values used for normalization. $R_{\rm ICS}$ is measured as the time-average of $V_{\rm ICS}/I_{\rm ICS}$ over the ON periods.

Figure 10 shows the time variations of the array-averaged detector response to the ICS signal for individual arrays during flight#2. In general, array #6 has the best response and is $\simeq$ 25% more responsive than arrays #2 and #8. The variations in the array-averaged response with time are about 10% for all arrays. Step-like variations are clearly seen in both the TRANS and REFLEX focal plane arrays. These variations are mostly caused by variations of the background level on the various detectors between individual observations. Some of these variations are due to observation elevation, which changes the intensity of the residual atmospheric emission and therefore the optical background in the same way on both focal planes. Some variations are caused by observing with different HWP angles, which, due to the polarized instrumental background (see Sec. 6.2), changes the optical background in opposition on the two focal planes, causing reversed variations of the detector responses.

Template	correlation coefficeints (α_i)
$cos(4\times\omega)$	-0.604594
$sin(4\times\omega)$	0.481638
90°-elevation	-0.395260
altitude	0.240485
T_{300}	-0.224808
$T_{\rm win}$	-0.260774
$T_{\rm win}$	-0.332954
T_{77}	0.145752

Table 5: Coefficients α_i for the various house-keeping templates included in the ICS array-averaged response model for array #6 shown in Fig. 11 and defined in Sec. 7.1

To better characterize the origin of the response time variations, we performed a linear regression of ρ_{ICS} with house-keeping information for 9 parameters impacting the optical background or focal plane temperature. In particular, we included in the fit $cos(4\omega)$ and $sin(4\omega)$ describing changes of the background with HWP angles due to the background polarization, the observation elevation and the altitude of the experiment which impact the residual atmosperic contribution to the background. We also included the temperatures of several optical elements such as the primary miror, the cryostat entrance window and the cryostat cold shield at 77 K and the measured temperature of the focal plane. The array averaged ICS response model is defined as:

$$\rho^{model}_{ICS} = \sum_{i=1}^{9} \alpha_i \frac{xp_i}{\langle xp_i\rangle} + c, \quad (6)$$

where xp_i is the template of a given house-keeping parameter averaged over the calibration sequence, $\langle\rangle$ designates averaging over all sequences and c is an arbitrary constant.

Figure 11 compares the prediction of the above model with the time evolution of the average response to the ICS signal for array #6. The uncertainties shown on the figure were computed from the statistics of the individual ON-OFF measurements in each calibration sequence. In general, the model describes the data with good accuracy over the whole flight for all the arrays. The median difference between the model and the data is around 2%. A few exceptions for which the model does not match very well the data are visible in Fig. 11 which are associated to a larger uncertainty in the response estimate. These observations are located (around the

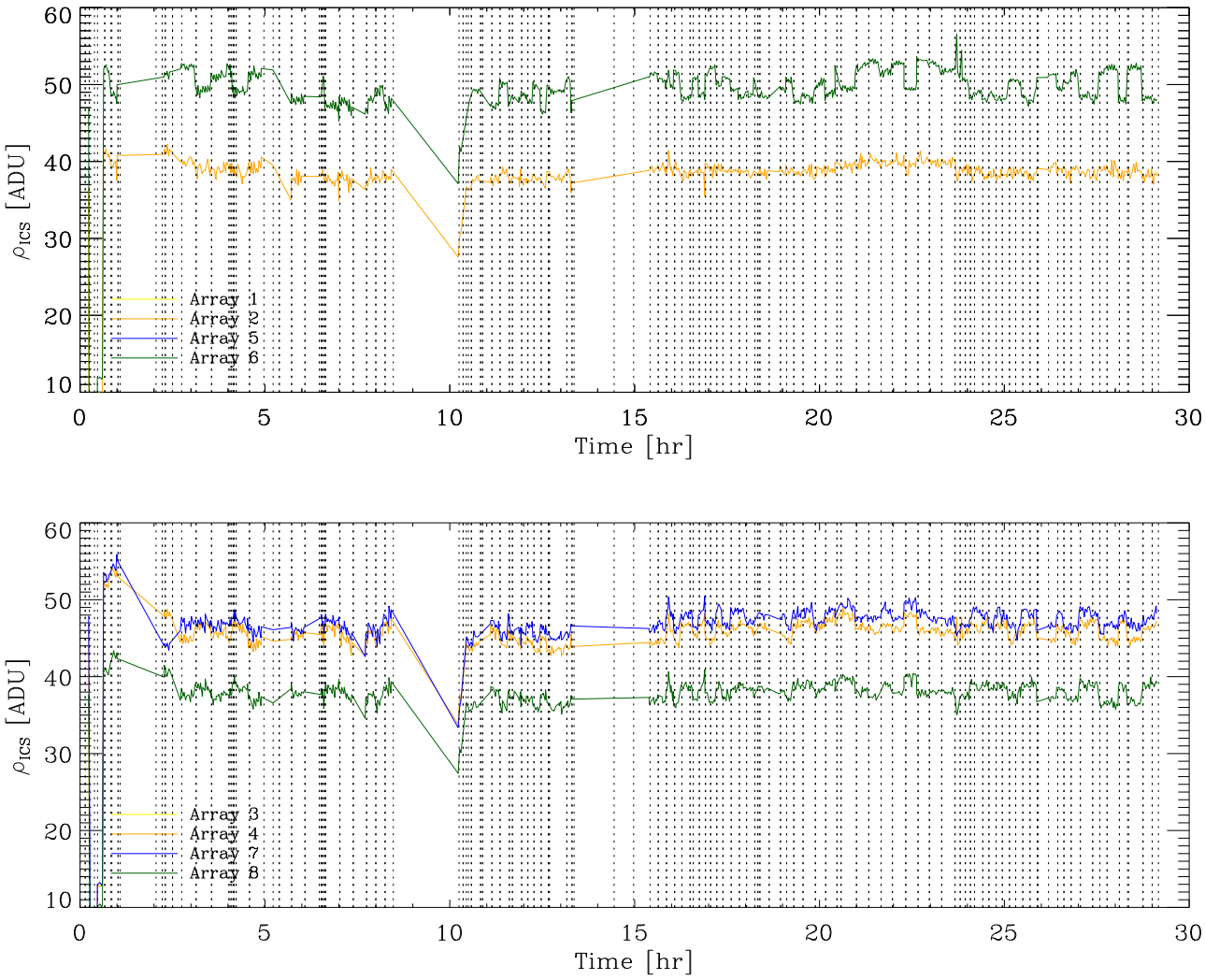

Fig. 10: Top: Time variations of the array-averaged detector response to the ICS for arrays on the TRANS focal plane (arrays #6 and #2) during flight#2. Bottom: Same for the REFLEX focal plane (arrays #4, #7 and #8). The vertical dashed lines show the boundaries between different observations.

calibration sequence 200 in the Figure) just after the recycling of the ^{3}He fridge which caused very large fluctuations of the 300 mK stage.

The α_i coefficients are given in Tab. 5 in order of decreasing magnitude. The main correlations are with the HWP angle, indicating a strong dependance to the background level through its polarisation. Atmopsheric parameters come second also showing a significant impact of the residual atmopsheric emission to the response. temperatures of the instrument explain the low frequency variations observed in Fig. 11.

7.2 Response spatial variations

The thermal emission from the residual atmosphere is clearly detected even at high altitude in the stratosphere. This strong signal is in principle extended and can therefore be used to measure the response flat-field of the detectors. In addition, since this signal is in principle unpolarized, it can be use to intercalibrate detectors of the TRANS and REFLEX focal planes.

We measure the detector response using the residual atmospheric emission as the slope of the correlation between the bolometer signal and the pointing elevation. This was done both for dedicated 'skydip' measurements where the pointing elevation is changed continuously and during normal science observations obtained at variable elevation angles during flight#2. Figures 12 and 13 show the focal plane

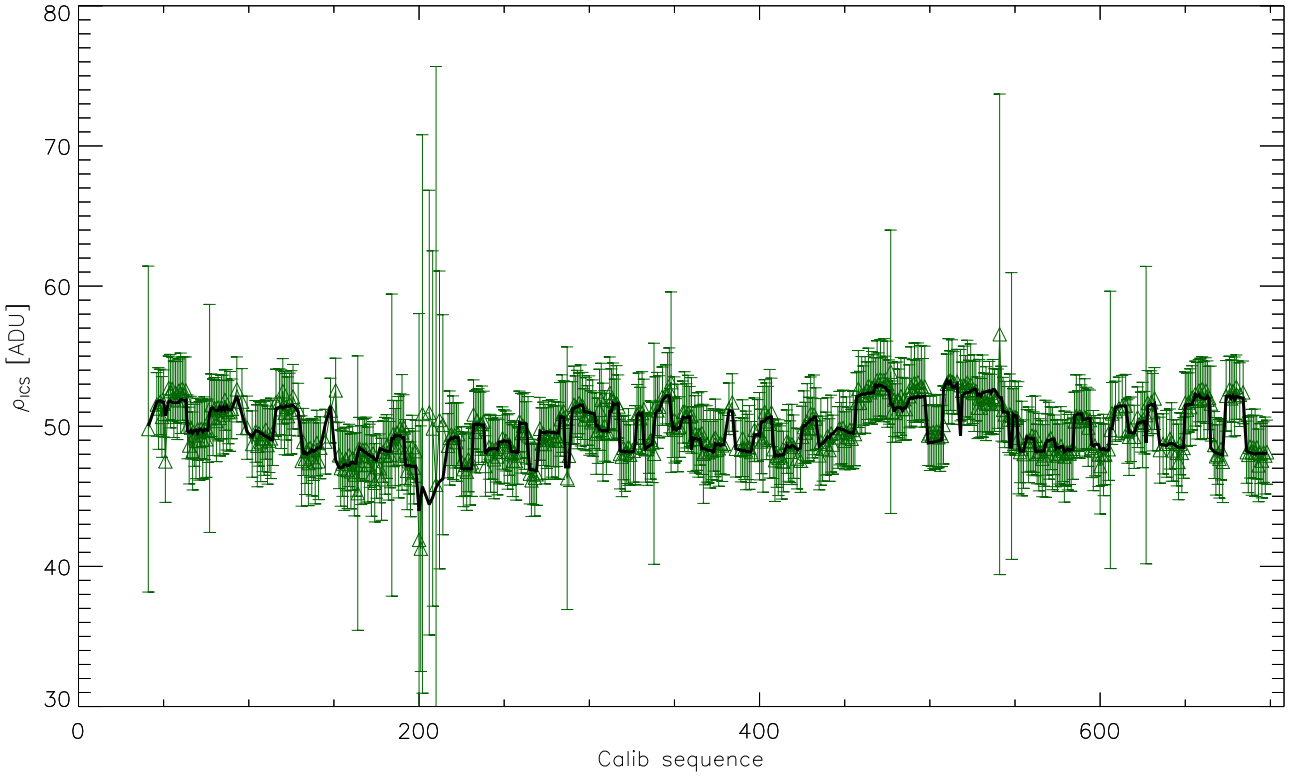

Fig. 11: Array-averaged ICS response for array #6 as a function of the calibration sequence number (green) compared to the predictions of the parametric model described in Sec. 7.1 (black).

map of the mean response computed on the atmospheric signal during the skydips and all the observations during flight#2, respectively. Both maps present similar patterns. This pattern is also similar to that observed during ground test where the focal planes were operated in front of an extended black-body, indicating that the structures observed are intrinsic pixel-to-pixel variations of the response across the focal planes. The accuracy of the response map is improved at the 1% level or better when using all observations, due to the increased statistics with respect to skydip observations alone. This confirms the advantage of using a scanning strategy with varying elevation as implemented for flight#2.

8 Detector noise

We present in this section the instrumental noise properties for flight#2. The noise properties during flight#1 were similar to those of flight#2 in terms of spectral shape, noise levels and stability.

8.1 Flight-averaged noise power spectra

We compute the noise power spectra during flight#2 for each detector and during each observation scan. For this purpose, the raw data are first corrected for the response time variations derived in Sect. 7.1 and converted to watts using the detector-averaged ground calibration value of $2.116\,10^{10}$ V/W derived from ground calibrations of the detectors alone in front of an absolute black body. The calibrated timelines are corrected for the atmospheric signal to first order, by removing their linear correlation with observation elevation as calculated over each observation, taking into account only scan data (ie, excluding time samples associated to the calibrations, slews, etc...). Given the noise levels, we can assume that, after the atmospheric signal removal, the individual detector timelines are dominated by instrumental noise.

We compute the mean timeline among valid pixels of each array and scale it by the square root of the number of valid detectors in each array to keep a single-detector normalization. The array-averaged power spectra $P_{m,s}(\nu)$ are computed for each detector array m and each scan s from these array-averaged timelines, in $\mathrm{W}/\sqrt{\mathrm{Hz}}$, in the range of frequencies $\nu \in [0.02,20]$ Hz. Finally, we take the median value of $P_{m,s}(\nu)$ among the scans s as the flight-averaged noise power spectra.

Similarly, we compute the half-pixel difference (HPD) noise power spectra by removing a common mode to all the detector timelines. For this purpose, we split each detector array in two subsets with the same number of pixels, cho-

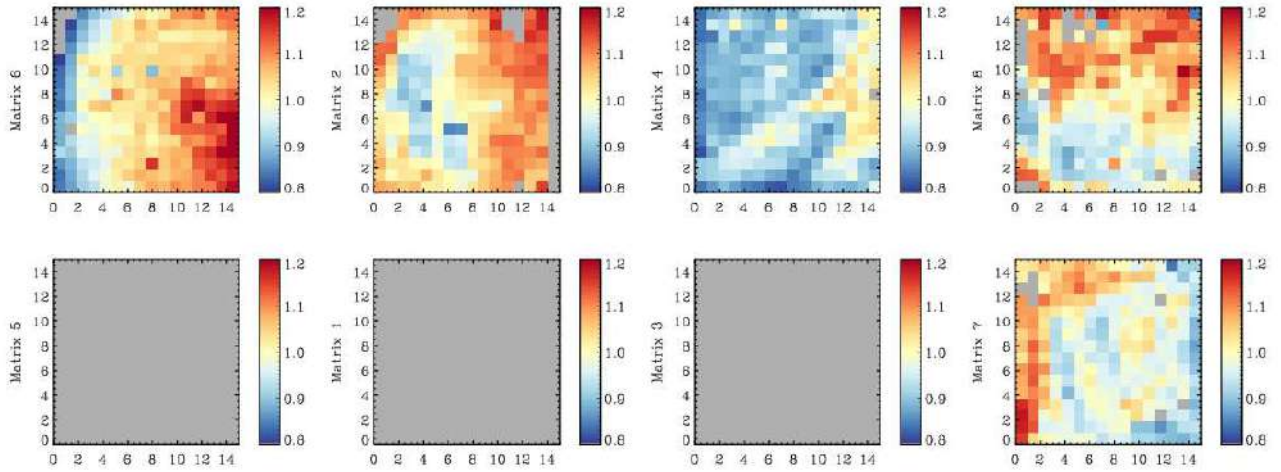

Fig. 12: Focal plane map of the mean response computed on the residual atmospheric signal during skydip observations of flight#2. The response map has been divided by its average over valid detectors so that it has a mean equal to unity. The relative dispersion between these values and the one computed during the rest of the flight (see Fig. 13) is 0.9 %.

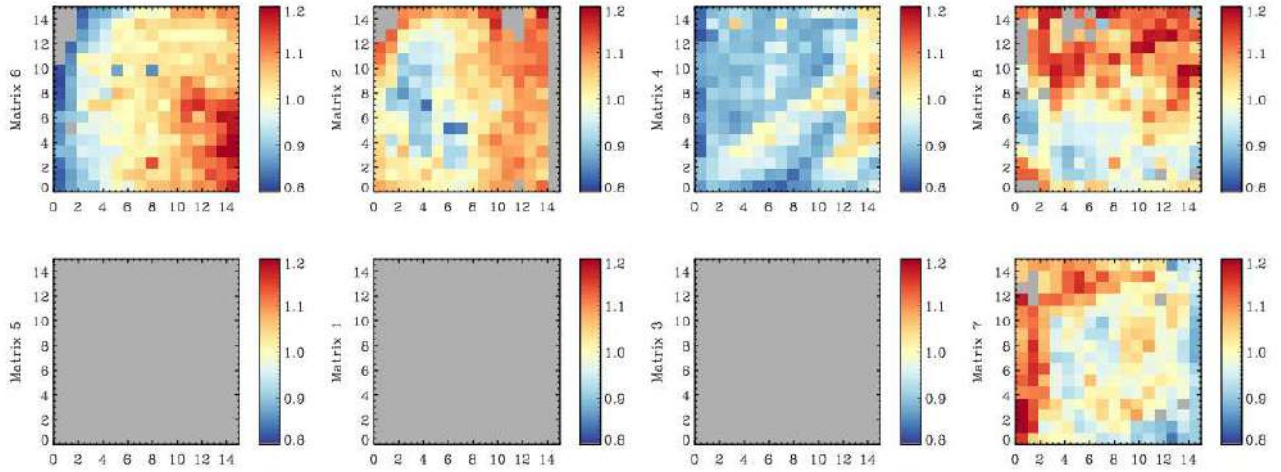

Fig. 13: Focal plane map of the mean response computed on the residual atmospheric signal during all scientific observations of flight#2. The response map has been divided by its average over valid detectors so that it has a mean equal to unity.

sen randomly, and compute the half-difference of the two detector-averaged timelines. From these HPD timelines, for each detector array and each scan, we compute the HPD power spectra $P_{m,s}^{\mathrm{HPD}}(\nu)$, which do not contain the common mode.

The flight-averaged noise power spectra are shown in Fig. 14 for array #6. The spectra are qualitatively similar for other detector arrays. For both the array-averaged spectrum $P_{m,s}(\nu)$ and the HPD spectrum $P_{m,s}^{\mathrm{HPD}}(\nu)$, two regimes can be identified. At high frequency, a flat spectrum component is observed, corresponding to white noise, presumably caused by photon noise. At low frequency, a $1/\nu$ and $1/\sqrt{\nu}$ components are observed for $P_{m,s}(\nu)$ and $P_{m,s}^{\mathrm{HPD}}(\nu)$, respectively. The former contains residuals from atmospheric emission and possibly variations of the focal plane temperature that contribute to the low-frequency rise of the spectrum. In the HPD case, we can consider that all atmospheric and temperature variations are removed with the per-array common mode.

8.2 Noise stability

In order to study the noise stability during flight#2, we build time-frequency diagrams for $P_{m,s}(\nu)$ and $P_{m,s}^{\mathrm{HPD}}(\nu)$, shown

for array #6 in Fig. 15. These diagrams are qualitatively similar for the other arrays.

In the array-averaged time-frequency diagram, some observations can be identified, having a larger low-frequency component. This is due to the simple atmospheric emission removal we have implemented here, that sometimes fails to properly subtract the low-frequency contribution. At higher frequency, a good stability of the white noise is observed outside these observations. In the HPD case, where the common mode for all the detectors belonging to the same array has been removed, the stability is remarkable for both low and high frequencies, during the whole duration of flight#2.

8.3 High-frequency noise levels

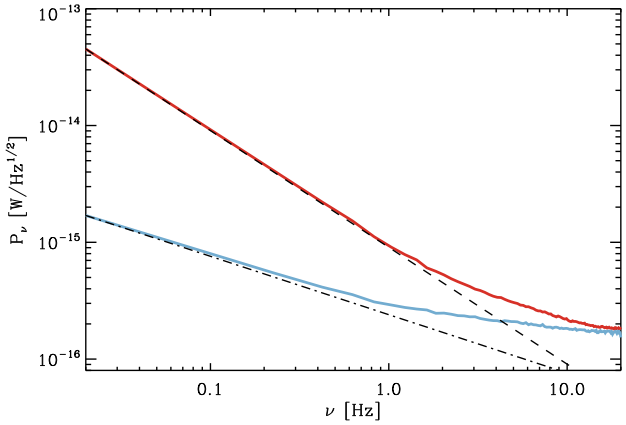

Fig. 14: Array #6 array-flight-averaged power spectrum $P_{6,s}(\nu)$ (red) and HPD flight-average $P^{\rm HPD}_{6,s}(\nu)$ (blue) in W/$\sqrt{\rm Hz}$, during flight#2. $1/\nu$ and $1/\sqrt{\nu}$ curves are overplotted to guide the eye as dashed- and dashed-dotted-lines, respectively.

To assess the high-frequency noise level statistics during flight#2, we repeat the initial steps presented in Sect. 8.1. However, instead of averaging the signal among the detectors for each array, we compute the noise power spectra $P_{i,s}(\nu)$ for each detector i and each scan s. For each detector, we compute the flight-averaged spectrum $P_i(\nu)$ as the median over all the scans. The high frequency noise levels are then taken to be the mean value of $P_i(\nu)$ in the range $\nu \in$[0.02,20] Hz.

The statistics of these high-frequency noise levels are presented in Tab. 6. The focal plane median high-frequency noise level is $4.6\,10^{-16}$ W/$\sqrt{\rm Hz}$. Array #6 is the most sensitive with a median sensitivity corresponding to a high-frequency noise level of $1.9\,10^{-16}$ W/$\sqrt{\rm Hz}$. Arrays #2, #4, #7 and #8 have similar sensitivities (ranging from 4.5 to $6\,10^{-16}$ W/$\sqrt{\rm Hz}$).

9 Expected sensitivities

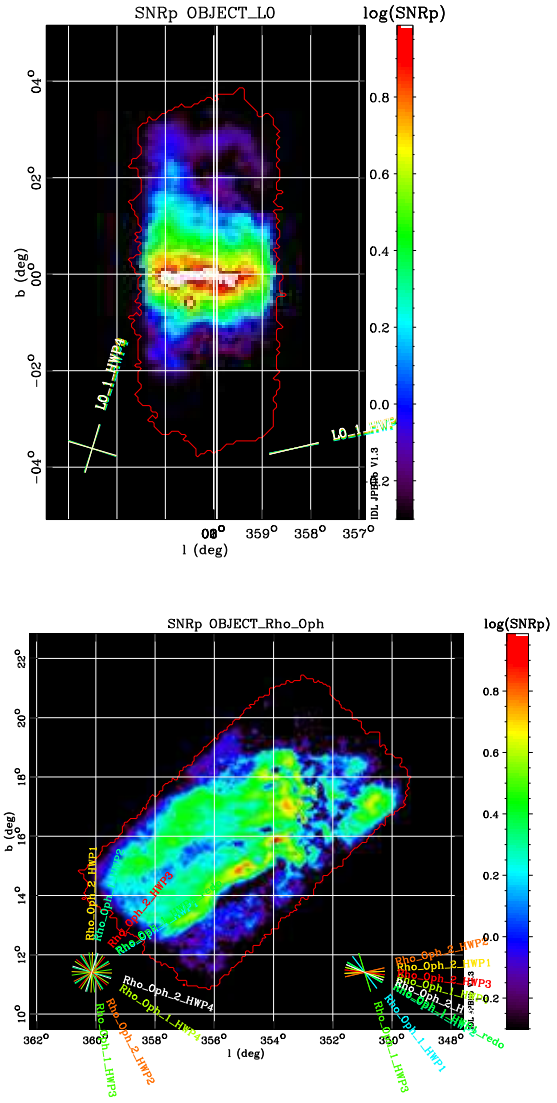

Fig. 16: Maps of the expected SNR ratio on the polarization fraction p for the Galactic center region at 2′ resolution (left) and the Rho-Ophiuchi region (right) at 5′ resolution.

We present the signal to noise ratio predictions for the polarization fraction p (SNR_p), based on the simulations that are done with the flight#2 observing strategy and parameters. The expected sensitivities are calculated as described in [9], based on simulations where the Stokes parameters I, Q, U are taken from the Planck polarization maps at 353 GHz [7], and extrapolated to the *PILOT* frequency using a modified black body spectrum with a dust emissivity index and dust temperatures also determined from analysis of the Planck data ([20]). We use the median value of the high fre-

Appendix B

SPIE conference paper

Misawa et al., 2014, PILOT: a balloon-borne experiment to measure the polarized FIR emission of dust grains in the interstellar medium, *Millimeter, Submillimeter, and Far-Infrared Detectors and Instrumentation for Astronomy VII*, 9153,

Noname manuscript No.
(will be inserted by the editor)

PILOT: a balloon-borne experiment to measure the polarized FIR emission of dust grains in the interstellar medium

J-Ph. Bernard, P. Ade, Y. André, J. Aumont, L. Bautista, N. Bray, P. deBernardis, O. Boulade, F. Bousquet, M. Bouzit, V. Buttice, A. Caillat, M. Charra, M. Chaigneau, B. Crane, J.-P. Crussaire, F. Douchin, E. Doumayrou, J.-P. Dubois, C. Engel, P. Etcheto, P. Gélot, M. Griffin, G. Foenard, S. Grabarnik, P. Hargrave, A. Hughes, R. Laureijs, Y. Lepennec, B. Leriche, Y. Longval, S. Maestre, B. Maffei, J. Martignac, C. Marty, W. Marty, S. Masi, F. Mirc, R. Misawa, J. Montel, L. Montier, B. Mot, J. Narbonne, J-M. Nicot, F. Pajot, G. Parot, E. Pérot, J. Pimentao, G. Pisano, N. Ponthieu, I. Ristorcelli, L. Rodriguez, G. Roudil, M. Salatino, G. Savini, O. Simonella, M. Saccoccio, P. Tapie, J. Tauber, J.-P. Torre, C. Tucker

Received: date / Accepted: date

Abstract Future cosmology space missions will concentrate on measuring the polarization of the Cosmic Microwave Background, which potentially carries invaluable information about the earliest phases of the evolution of our universe. Such ambitious projects will ultimately be limited by the sensitivity of the instrument and by the accuracy at which polarized foreground emission from our own Galaxy can be subtracted out. We present the *PILOT* balloon project, which aims at characterizing one of these foreground sources, the polarized continuum emission by dust in the diffuse interstellar medium. The *PILOT* experiment will also constitute a testbed for using multiplexed bolometer arrays for polarization measurements. This paper presents the instrument and its expected performances.

Keywords Astrophysics · Interstellar Medium · Instrumentation · Polarization

1 Introduction

The cold interstellar medium (ISM) in galaxies consists of tenuous gas (mostly neutral hydrogen, with a tiny fraction of more complex molecules) and dust. In the diffuse ISM,

J-Ph. Bernard, C. Engel, G. Foenard, A. Hughes, C. Marty, W. Marty, R. Misawa, L. Montier, B. Mot, J. Narbonne, I. Ristorcelli, G. Roudil
Institut de Recherche en Astrophysique et Planetologie (IRAP), Université Paul Sabatier, 9 Av du Colonel Roche, BP 4346, 31028 Toulouse cedex 4;
E-mail: Jean-Philippe.Bernard@irap.omp.eu

J. Aumont, M. Bouzit, V. Buttice, A. Caillat, M. Chaigneau, M. Charra, B. Crane, J.-P. Crussaire, J.-P. Dubois, B. Leriche, Y. Longval, B. Maffei, F. Pajot, J.-P. Torre
Institut d'Astrophysique Spatiale, CNRS, Univ. Paris-Sud, Université Paris-Saclay, Bât. 121, 91405 Orsay cedex, France

P. Ade, M. Griffin, P. Hargrave, G. Pisano, G. Savini, C. Tucker
Department of Physics and Astrophysics, PO BOX 913, Cardiff University, 5 the Parade, Cardiff, UK;

Y. André, F. Bousquet, N. Bray, F. Douchin, P. Etcheto, P. Gélot, S. Maestre, F. Mirc, J. Montel, J-M. Nicot, G. Parot, O. Simonella, M. Saccoccio, P. Tapie
Centre National des Etudes Spatiales, DCT/BL/NB, 18 Av. E. Belin, 31401 Toulouse, France;

P. deBernardis, S. Masi, M. Salatino, J. Pimentao
Universita degli studi di Roma "La Sapienza", Dipartimento di Fisica, P.le A. Moro, 2, 00185, Roma, Italia;

O. Boulade, E. Doumayrou, Y. Lepennec, J. Martignac, L. Rodriguez
CEA/Saclay, 91191 Gif-sur-Yvette Cedex, France;

S. Grabarnik, R. Laureijs, J. Tauber
Scientific Support Office, SRE-S, ESTEC, PO Box 299,2200AG Noordwijk, The Netherlands;

N. Ponthieu
Grenoble University, Grenoble, France;

E. Pérot
Thales Services, Toulouse, France;

L. Bautista
COMAT, Toulouse, France;

G. Savini
Department of Physics & Astronomy, University College London, Gower Place, London WC1E 6BT, United Kingdom;

dust grains absorb starlight in the ultra-violet (UV) to visible regime, which heats them to temperatures of 15 to 30 K. They re-radiate this absorbed energy as continuum emission across the far-infrared (FIR) to sub-millimeter (submm) wavelength range, where they dominate the total emission of galaxies. Critically for polarization studies, dust grains are elongated rather than spherical, and as the grains rotate, their minor axis becomes aligned with the local magnetic field. While the details of this dust alignment process remain unclear ([1, 2]), there is consensus that the angular momentum of a grain spun up by photon-grain interactions ([3–7]) becomes aligned with the grain's shortest axis, and then with the magnetic field via precession (e.g., [8, 9]). This partial alignment causes preferential extinction of starlight along the major axis of the grains, so that the transmitted starlight is slightly polarized along the magnetic field direction as projected on the plane of the sky (see e.g. [10]). Likewise, the partial alignment of dust grains causes a fraction of their thermal emission to be linearly polarized in a direction orthogonal to the magnetic field direction as projected on the sky ([11]).

To date, measurements of dust polarization have suffered several important biases. In extinction, ground-based observations at visible wavelengths have measured the polarization toward stars (e.g. [12, 13]), but these measurements are restricted to regions of the sky with bright stars and moderate extinction. Large ground-based telescope also have measured the polarization of thermal dust emission (e.g. [14, 15]), but only towards the brightest regions of the sky, which are typically in the immediate vicinity of star-forming regions. The polarization properties of these extreme environments are not necessarily representative of the diffuse ISM.

The balloon experiment *Archeops* ([16]) mapped the polarized dust emission at 353 GHz with $\sim$ 13 arcminute resolution over $\sim$ 20% of the sky ([17]). Several regions of the Galactic plane, including regions corresponding to individual molecular clouds, were found to have a strong polarization signal, with polarization fractions between 5 and 20%. These polarization fractions were higher than predictions based on the earlier observations of bright star-forming regions. While *Archeops* lacked the sensitivity to map the polarization directly at higher galactic latitudes, it predicted that polarized emission from ISM dust would be the dominant foreground contaminant for future CMB polarization experiments.

The *Planck* satellite has recently mapped the polarized dust emission at multiple frequencies in the submm regime over the entire sky (see for an overview [18]). A tight correlation between polarization in visible (VIS) extinction towards selected stars and the polarized submm emission at 353 GHz along the same sightlines confirms that the same dust grains are responsible for the polarization in emission and extinction ([19]). Like *Archeops*, *Planck* identified regions with polarization fractions at 353 GHz up to $\sim$ 20%, including extensive regions of diffuse ISM at high galactic latitudes ([18]). The existence of these highly polarized regions confirms that dust in diffuse regions can be efficiently aligned and intrinsically polarized to much higher fractions than previously expected. The *Planck* data also showed that regions with high column density systematically exhibit low polarization fractions ([18]), and that the direction of the apparent dust emission polarization is homogeneous in regions with high polarization fraction, but rotates abruptly in regions with low polarization fraction. Taken together, these results suggest that the 3D geometry of the magnetic field along the line of sight is a key parameter that determines the apparent dust polarization fraction (see [20] for a comparison between the *Planck* results and numerical simulations).

In this paper, we present the *PILOT* balloon-borne experiment, which will precisely measure the polarized emission from dust grains in the diffuse ISM. The *PILOT* project has two major scientific objectives. First, *PILOT* observations will constrain the large scale geometry of the magnetic field in our Galaxy in the diffuse and dense phases of the ISM. With such data, we aim to study how the magnetic field shapes the neutral interstellar gas on $\sim$ 100 pc scales, and the role it plays in the gravitational collapse leading to star formation. In this domain, the *PILOT* data will be complementary with *Planck* measurements at longer wavelengths. *PILOT* will bring information at a higher angular resolution than *Planck*, which is critical for studying the field geometry in crowded regions such as the Galactic plane. Second, the *PILOT* observations will measure the polarized dust emission towards the most diffuse regions of the sky with good sensitivity. This is critical for current and future cosmology experiments that aim to measure the B-mode polarization of the cosmic microwave background (CMB). The CMB B-modes are due to the interaction between CMB photons at the last scattering surface and quadrupole anisotropies induced by primordial gravitational waves; their detection would provide direct experimental evidence for the theory of inflation. The B-mode polarization signal is expected to be extremely weak, however, so the success of future CMB polarization measurements will hinge on their ability to characterize and remove unrelated sources of polarized emission, of which dust in the Milky Way's ISM is the dominant component.

The rest of this paper is organized as follows. We present an overview of the *PILOT* project in Section 2. A detailed description of the *PILOT* instrument is presented in Section 3. In Section 4, we describe the strategy for polariza-

tion observations, and develop a photometric model of the instrument. In Section 5 we calculate the expected sensitivity. In Section 6, we describe data simulations which were used to set some of the requirements on subsystems. In Section 7, we describe the pre-flight ground calibration tests that we conducted, and present the results. We conclude in Section 8 with a summary of *PILOT*'s status and anticipated performance.

2 The *PILOT* Instrument

PILOT (Polarized Instrument for the Long-wavelength Observation of the Tenuous ISM) [1] is a balloon-borne astronomy experiment to measure the polarization of dust emission at far-infrared (FIR) wavelengths. *PILOT* is designed to fly at a ceiling altitude of ~ 40 km (4 hPa pressure) in the stratosphere, to reduce contamination of the astronomical signal by the Earth's atmosphere. A schematic view of the instrument is shown in Fig. 1.

The *PILOT* instrument is designed to allow observations in two photometric channels at wavelengths of $240\,\mu$m (1.2 THz) and $550\,\mu$m (545 GHz), with an angular resolution of a few arcminutes. It uses large format bolometer arrays, which were originally developed for the *PACS* instrument on the *Herschel* satellite ([21,22]). With 1024 detectors per photometric channel, and photometric bands placed near the peak of the thermal dust emission SED, *PILOT* is optimized for sensitive observations of polarized dust emission. The proposed method to measure polarization using filled arrays has been validated by end-to-end simulations. *PILOT*'s sensitivity will surpass that of *Archeops* and even that of *Planck* (see Sect. 5) for a given column density of interstellar matter. The *PILOT* experiment is unique in its ability to measure the polarization properties of dust FIR emission over large regions of the sky, since none of the instruments on the Herschel satellite were sensitive to polarization and the *BLAST-Pol* balloon experiment [23] is optimized for mapping small sky regions at higher angular resolution.

3 *PILOT* Instrument Description

This section gives a full description of the *PILOT* instrument in its nominal configuration, which includes two photometric channels at short (SW) and long (LW) wavelengths. Table 1 gives the main characteristics of the instrument in this configuration. Note however that, in the configuration used for the ground tests performed so far and for the first flight of the experiment, the whole focal plane was equipped with detectors optimized for the $240\,\mu$m channel only. In particular, expected sensitivities reported in Tab. 1 will therefore have to be scaled according to the actual number of detectors of the in-flight configuration.

[1] http://pilot.irap.omp.eu

Table 1 Key characteristics and performance of the *PILOT* instrument in its nominal configuration. The last lines gives the expected 3σ performance in the two extreme observing modes corresponding to deep ($5^{\square}$/hour) and large ($150^{\square}$/hour) surveys respectively. Our estimated polarization sensitivity assumes a dust polarization fraction of 10%.

Primary mirror diameter [mm]	700	
Equivalent focal length [mm]	1800	
Numerical aperture	$F/2.5$	
Detector temperature [mK]	300	
Mapping speed [$^{\square}$/h]	[5-150]	
FOV [^{o}]	1.0×0.8	
	SW Band	LW Band
λ_0 [μm]	240	550
ν_0 [GHz]	1250	545
$\Delta\nu/\nu$	0.27	0.31
Tr(dust)	0.025	0.136
beam FWHM [']	1.9	3.29
Number of Detectors	1024	1024
background [pW/pix]	5.7	4.0
NEP$_{Det}$ [$W/\sqrt{Hz}$]	$2.0\,10^{-16}$	$2.0\,10^{-16}$
NEP$_{Phot}$ [$W/\sqrt{Hz}$]	$9.8\,10^{-17}$	$6.0\,10^{-17}$
NEP$_{Tot}$ [$W/\sqrt{Hz}$]	$2.2\,10^{-16}$	$2.1\,10^{-16}$
Sensitivity (3σ in 3.5')		
Intensity [MJy/sr]	[0.98-6.28]	[0.33-2.13]
Av [mag]	[0.05-0.30]	[0.12-0.75]
Av polar [mag]	[0.47-2.99]	[1.17-7.48]

3.1 Gondola

The *PILOT* experiment will be carried by a generic CNES stabilized gondola with altazimuthal coarse pointing control, as shown in Fig. 1. Mapping of the sky will be accomplished by rotating the gondola over a large azimuth range ($\pm 30^{o}$) at constant elevation, in order to reduce the residual atmospheric contribution. The elevation of the pointed payload is controlled by a electric jack and can vary between 20^{o} to 60^{o}. The fine attitude of the instrument and the effective pointing direction will be constructed a-posteriori, using the signal from a fast, large format CCD stellar sensor (see Sect. 3.10), co-aligned with the sub-mm optical axis of the instrument. The maximum allowed rotation speed for azimuthal scanning (1.2^{o}/s) is a compromise between the need to map large areas and to reduce instrumental drifts, and the need to distinguish point sources from parasitic "spikes" and to respect the response times of the detectors and the stellar sensor. The total gondola weight will be ~ 1100 kg.

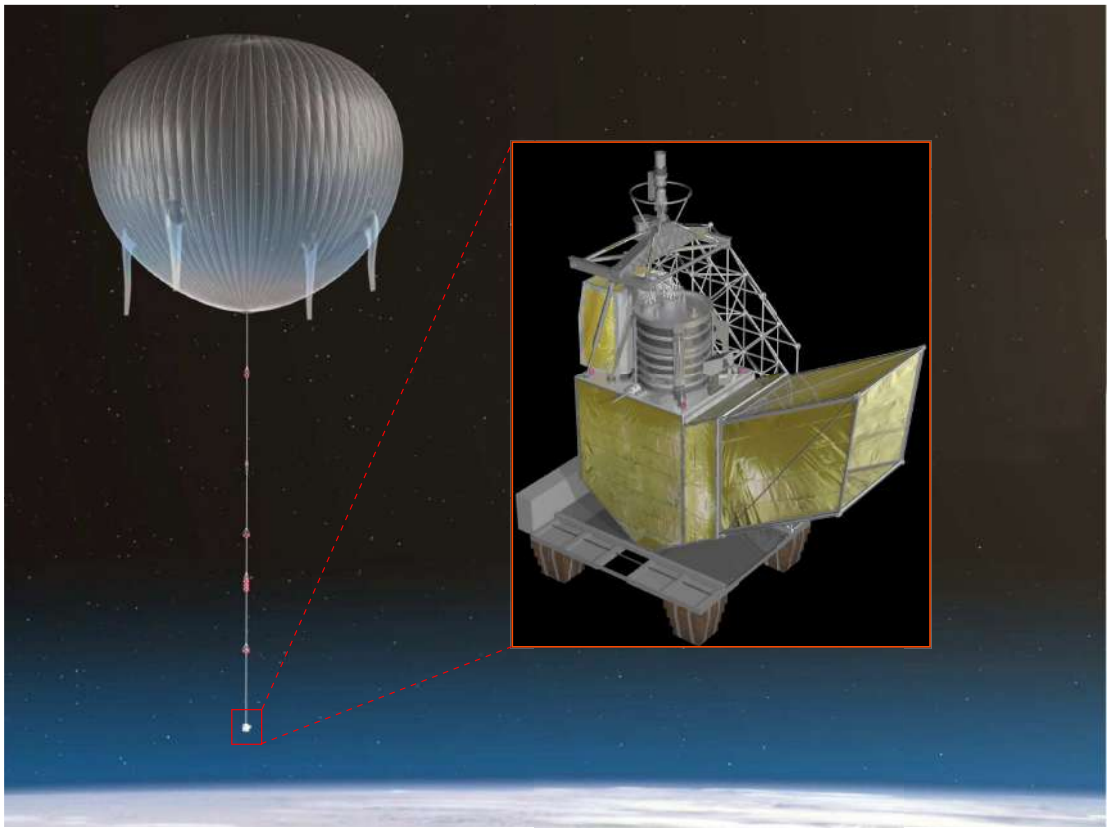

Fig. 1 Schematic view of the *PILOT* experiment. Left: Artist's view of the instrument gondola below the stratospheric balloon. Right: CAD model of the *PILOT* gondola. The cryostat (cylinder on top) and the primary mirror are attached to the pointed load, which can rotate around its elevation axis in order to change the elevation of the submillimetre optical axis. Motion around the flight chain is provided by the azimuth swivel. Not all optical baffles and thermal protection screens surrounding the experiment are shown.

3.2 Optics

The optics of *PILOT* is designed to provide an instantaneous field-of-view (FOV) of $1^o \times 0.76^o$, with an equivalent focal distance of 1790 mm and an F/2.6 numerical aperture. The angular resolution of the instrument ($< 3.5'$) is a compromise between our aim to map large regions of sky with a resolution comparable to the *IRAS* satellite, and the maximum telescope size that conforms to weight constraints.

The optics consists of an off-axis Gregorian telescope with a diameter of $\simeq 800$ mm and a reimaging refractive objective (see Fig. 2). The telescope is composed of an off-axis paraboloid primary mirror (M1) and a off-axis ellipsoid secondary mirror (M2), both made of aluminium. The combination respects the Mizuguchi-Dragone condition (minimizing instrumental polarization) and is equivalent to an on-axis parabolic system. The characterization and performance of the M1 mirror has been presented by [24].

The re-imaging refractive objective consists of two lenses acting as a telecentric objective, re-imaging the focus of the telescope onto the detectors. A Lyot-stop is located between the lenses at a pupil plane that is a conjugate of the primary mirror. The polarization will be measured using a rotating Half Wave Plate (HWP) (see Sect. 3.4) located next to the Lyot-stop and a fixed polarizer in front of the detectors. The fixed polarizer is tilted to 45^o in order to reflect one polarization component onto one bolometer housing (the reflection focal plane) and to transmit the other polarization component onto a second bolometer housing (the transmission focal plane). This optical configuration is optimized to have good optical performance and to minimize straylight inside and outside the cryostat.

M1 is the only optical component at room temperature. The rest of the optics is inside the cryostat (see Sect. 3.6) at cryogenic temperature of $\simeq 2\,K$. Optical simulations indicate that the accuracy requirement on the distance between M1 and M2 is $\pm 300\,\mu$m in order to obtain diffraction-limited performance. This rigidity is ensured by an aluminium hexapod system that connects the instrument plate holding the cryostat and the M1 mirror support.

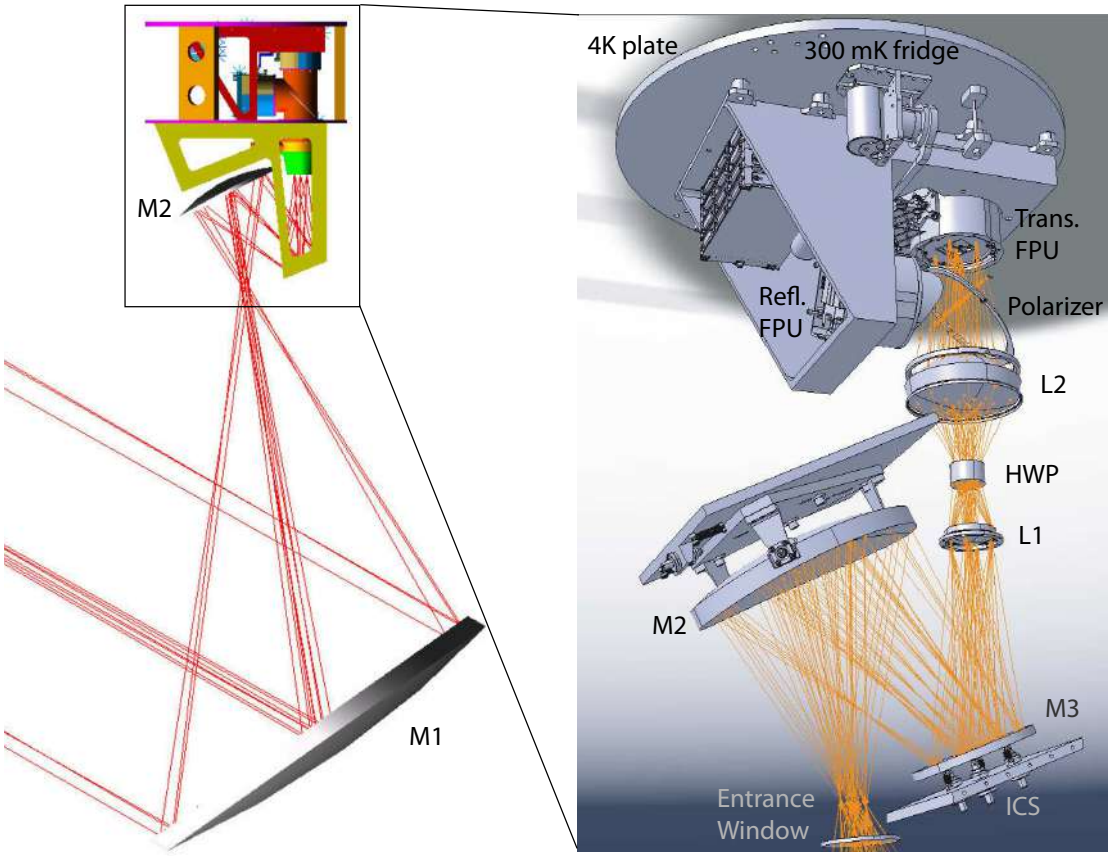

Fig. 2 CAD model of the *PILOT* optical system showing the propagation of optical rays (red lines). Left: Full view showing the off-axis primary mirror (M1) and the cold optics inside the cryostat. The incoming beam is focussed by M1 near the entrance window of the cryostat. Right: Zoomed-in view of the cold optics inside the cryostat. The location of the mirrors (M2, M3), the lenses (L1, L2), the Half Wave Plate (HWP) and tilted polarizer are shown. The two orthogonal polarization components are split towards the transmission (top) and reflection (left) focal plane units (FPU). The drawing also shows the location of the ^{3}He fridge and the 4 K cold plate of the cryostat.

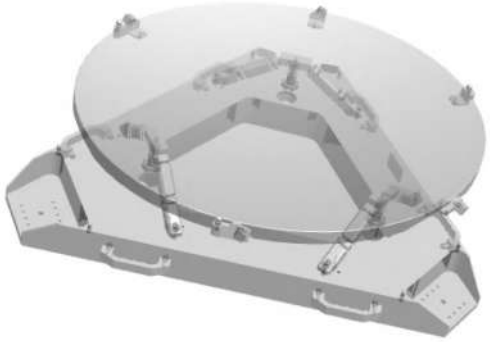

Fig. 3 CAD model of the *PILOT* primary mirror (M1). The mirror is attached to an interface plate.

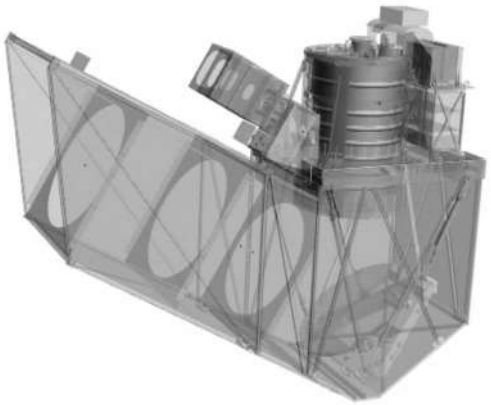

Fig. 4 CAD model of the *PILOT* pointed load. The figure shows the various subsystems, including the baffles, the primary mirror, the cryostat and the Estadius stellar sensor.

3.3 Baffles

The scientific payload is protected by baffles to prevent sunlight heating the instrument and to minimize external straylight.

To develop a suitable baffle design, we modelled the irradiance of straylight on the detector plane. The main sources

of straylight are the surface of the Earth and the envelope of the balloon. The balloon straylight was computed assuming that the telescope only sees emission coming from the bottom half of the balloon, which is conical shaped by the load of the *PILOT* experiment. The balloon straylight consists of two components: Lambertian thermal emission and emission from the Earth that is reflected by the balloon. We assume that the Earth's surface emits as a blackbody at 273 K, with *PILOT* situated at an operational altitude of 35 km.

The main scattering surfaces due to dust contamination in the optical path are the primary mirror and the cryostat window, which are both in direct contact with the ambient surroundings. We assumed Lambertian scattering and adopted a total integrated scattering (TIS) of 0.1% for the surface of the primary mirror and a TIS of 0.01% for the cryostat window at the operating wavelength of 240 μm.

We investigated several baffle designs. For each design, we computed the irradiance on the detectors at different elevations using the ASAP^{TM} software package. In the simplest cases, we cross-checked the ASAP^{TM} results with Zemax^{TM} non-sequential ray-tracing calculations, or with analytical calculation. In the model, we included the *PILOT* optical design down to the detector plane. We first computed a baffle design with Lambertian surfaces with a TIS of 100% and compared the results assuming a similar mechanical design with specular reflecting baffle surfaces. It was found that the specular surfaces caused a significantly lower straylight irradiance of the detector plane.

The design of the baffle was constrained by the mass and ease of assembly of the baffle structure. The final baffle design has the following characteristics: first, the main tube should be rectangular, to facilitate mechanical construction; second, the inner surfaces of the baffle should be reflecting; and third, we included vanes with circular apertures which enable additional straylight suppression.

The straylight contributions of the Earth and balloon are roughly comparable, but components are strong functions of the elevation angle of the telescope. At high elevations of the pointed load, up to 53^o, the balloon dominates by a factor of ~ 4, but at low elevations (30^o) the Earth straylight dominates by a factor of ~ 20. For an initial design of a rectangular specular tube, the balloon straylight contribution increases by a factor $\simeq 17$ between 30^o and 53^o, while the Earth straylight decreases by a factor of ~ 6 over the same range in elevation. We found that the balloon straylight suppression was only marginally imporoved by varying the length of the tube. Depending on the elevation angle, a factor of ~ 2 to 5 suppression of the straylight could be achieved by inserting five specular vanes, while a factor of ~ 2 to 4 suppression could be achieved with three vanes. More vanes resulted in poorer performance. Changing the distances between the vanes inside the tube yielded improvements of 20 to 40%, but only at some elevation angles. This information was used to fine-tune the baffle design. For the three-vaned model that we adopted for *PILOT*, we predict straylight irradiances on the detector plane of 3×10^{-8} Wm^{-2} at 30^o elevation and 9×10^{-9} Wm^{-2} at 53^o elevation. Figure 4 shows a schematic view of the baffles, as built for the first *PILOT* flight. The baffles are made of styrofoam covered with reflective aluminized mylar. The three vanes are made of aluminium. The results of our straylight modelling will be presented in more detail in [25].

3.4 Half Wave Plate

PILOT measures linear polarization via a rotating Half Wave Plate (HWP) followed by a fixed polarizer. The HWP, composed of an optically birefringent material, introduces a phase delay between the two orthogonal components of the incoming radiation. The polarizer, composed of parallel metallic wires, reflects the component parallel to the wires towards one focal plane and transmits the orthogonal component towards the other focal plane. With such a configuration, at least two analysis directions are necessary to measure polarization. Different analysis directions are obtained by rotating the HWP. In order to reduce systematic instrumental effects, the *PILOT* observing strategy is to observe the sky at a fixed position of the HWP, and to rotate the HWP only between consecutive scans or maps of the sky. In order to reduce instrumental polarized emission modulated at the same frequency as the astrophysical signal [26], the HWP and its rotating mechanism are located in the cryostat at cryogenic temperatures next to a pupil plane of the optics. The requirement on cross-polarization due to the HWP is $< 5\%$. The HWP exploits the birefringence of sapphire to create the phase delay. Ideally, the phase shift should be equal to 180^o across the two photometric channels. In practice this can be obtained only over a narrow frequency range due to the wavelength dependence of the refraction index. To obtain good performance for both *PILOT* channels, the *PILOT* HWP exploits five plates of sapphire with 500 μm thickness and with optical axes rotated at suitable angles with respect to each other [27], resulting in an achromatic HWP [28]. To reduce reflection losses and standing waves between optical components, the HWP is coated with a dielectric anti-reflection coating based on artificial dielectric metamaterials, as described in [29].

The rotation of the *PILOT* HWP is achieved using a dedicated cryogenic mechanism (HWPM, for Half Wave Plate Mechanism) which allows the HWP to rotate between eight discrete angular positions. A view of the HWPM is shown in Fig. 5. The system is composed of a worm drive, rotated by a step motor at room temperature that is located outside the cryostat. The rotation is transmitted through magnetic coupling to a fiberglass shaft and a flexible spring acting as a 90^o gearing. The HWP can be positioned at eight discrete

positions separated by 11.25°, evenly sampling angular positions between 0° and 78°.

To minimize its contribution to the polarization error budget and avoid the generation of spurious signal, the HWP position angle must be known with an accuracy better than 0.1° [30,31]. The eight positions are registered through an optical encoder using three pairs of optical fibers, which codes positions using a 3-bit coded mask. With this system, the HWP position is determined with a relative accuracy better than 0.03°. In practice, the system can also be driven using the step motor to reach any angular position. The angular speed of the HWP rotation is $\simeq 1^{o}/s$. The rotation system dissipates less than 10 mW [31]. A description of a preliminary version of the *PILOT* HWPM is given in [32].

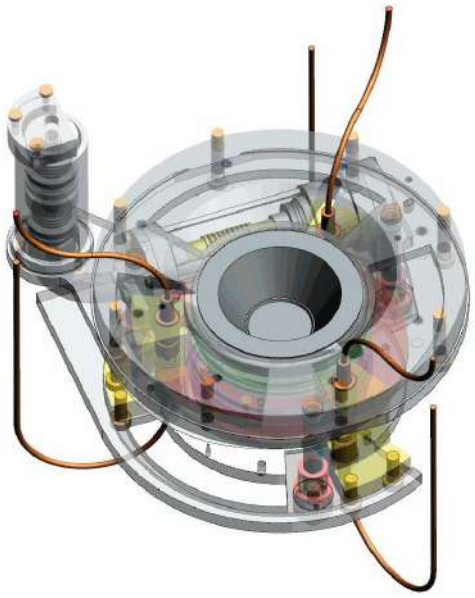

Fig. 5 Schematic view of the Half Wave Plate rotation mechanism. The HWP is located at the center and is rotated through a worm drive mechanism. The three optical fibers used to read the HWP position are also shown.

3.5 Filters

The spectral filtering of the instrument is based on a series of quasi-optical mesh filters [33]. Following a 1 mm thick polypropylene window on the optical entrance of the cryostat, thermal and frequency Low Pass Edge (LPE) filters are located on each of the thermal stages (150, 80, 40 and 2.5 K). The purpose of these filters is to reduce the radiative thermal loading on cryostat and the detectors, and to reduce the out-of-band high frequency spectral leakage.

The final spectral band is achieved through a combination of one High Pass Edge (HPE) filter and two LPE filters located at the entrance of the 300 mK box encasing the detector arrays. The filter scheme is designed to provide good performance for both *PILOT* photometric channels. Thus the filter performance represents a compromise between the peak in-band transmission of both bands. Nevertheless the final average in-band transmission for each of the thermal and LPE filters is above 95%. The average in-band transmission for the HPE filters – each servicing only one spectral band – is better than 85%.

During the end-to-end optical tests on the ground, an extra filter (neutral density) has been included on the 2.5 K stage in order to set the instrument to in-flight-like conditions in terms of optical load on the detectors. Most of the atmosphere being absent at 40 km altitude, its emission, creating an extra signal, has to be taken into account on the ground.

For the end-to-end tests optical tests on the ground (see Sect. 7, we also included an attenuator filter on the 3 K stage of the cryostat, which reduces the total background to the level anticipated in flight. The band-averaged transmission of that filter is 0.04 and was computed based on the *PILOT* photometric model described in Sect. 4.2.

3.6 Cryostat

Fig. 6 Schematic view of the cryostat. The right panel shows the inner structure of the helium tank (upper part), the cold optics compartment (lower part) and the various thermal screens.

In order to reduce the background level on the bolometers, all optical elements except the primary mirror are located inside a cryostat, which is illustrated in Fig. 6. The cryostat is 1180 mm in height and 370 mm in diameter. It is cooled to 2 K using a pumped helium bath. The detectors are further cooled to 0.3 K using a ^{3}He closed cycle fridge, mounted on the 2 K plate. The cryostat also enables the thermalization of the $\sim$ 480 electrical connections carrying scientific and house-keeping signals on the different cryogenic stages. A set of optical filters are mounted next to

the entrance window of the cryostat to reduce mid-infrared radiation entering the crystostat. Another set of filters located close to each detector housing is used to defined the bandpass of each photometric channel, such that half of the detectors at each focal plane can operate at 240 μm and the remaining half can operate at 550 μm. A more complete description of the *PILOT* cryostat will be given in [34].

3.7 Detectors

PILOT uses filled bolometer arrays that were developed by CEA/LETI for the *PACS* instrument on board the *Herschel* satellite (see Fig. 7). Their technology is described in [22]. The detectors incorporate fully multiplexed readout at 300 mK. They are produced as filled arrays of 16×18 detectors, of which 16×16 pixels are active. The readout is multiplexed in time so that 16 pixels are read by the same amplifier. The arrays are assembled into a mechanical housing (FPU, for Focal Plane Unit), which includes the multiplexing and amplification circuits. Kevlar wires are used to suspend the 300 mK stage inside the 2 K stucture to reduce the conduction heat load. The 300 mK stage is linked to the cold tip of a 300 mK cryocooler located on the 2 K cold plate of the cryostat, through a rigid strap going through each FPU mechanical housings.

We use two FPUs, one on each side of the polarization analyser (45^o polarizer), to measure the transmitted (Trans FPU) and the reflected (Refl FPU) light respectively. Each FPU contains four bolometer arrays, each with 256 bolometers. In the nominal configuration of the instrument, two arrays per FPU are equipped with filters for the SW channel and two are equipped for the LW channel, so that each photometric channel uses 1024 bolometers. The FPUs are oriented such that they scan the sky with an angle of 45^o between the edge of the array and the scan direction, in order to avoid large gaps from missing columns and to mitigate the effects of possible inter-pixel response variations.

The Noise Equivalent Power (NEP) of each bolometer is a few $10^{-16}\ W/\sqrt{Hz}$, including noise from the readout electronics. The readout speed of this type of detector is much slower than for individual bolometers (such as those used by the *Archeops* and *Planck* experiments). The detectors are read at a frequency of 40 Hz. The readout electronics unit is located behind the cryostat at room temperature and is a spare of the BOLC electronics on *PACS*.

3.8 Internal Calibration Source

Since the polarization measurements are derived from differences between bolometer signals (see Sect. 4.1) – either simultaneously received on different detectors, or received by the same detector at different times – accurate inter-calibration of the bolometer signal across all timescales is mandatory. This is achieved though the use of an Internal Calibration Source (ICS). We use the spare model of the PCAL internal calibration source developed for the *SPIRE* instrument on board *Herschel* ([35,36]). The ICS is shown on Fig. 8, and its main characteristics and performance are presented in [37,36]. This source shines light through a hole of the flat mirror (M3) within the cryostat and the lenses (see Fig. 7) so as to fully illuminate both arrays with a highly reproducible illumination pattern. The ICS will be used between sky scans to calibrate the variations of the response flat-field of the detectors. The ICS is driven in current with a square modulation and maximum current up to $2\,mA$. The voltage and current are measured continuously, allowing use to monitor variations of the electrical power dissipated in the source, independently of possible temperature-dependent variations in its impedance.

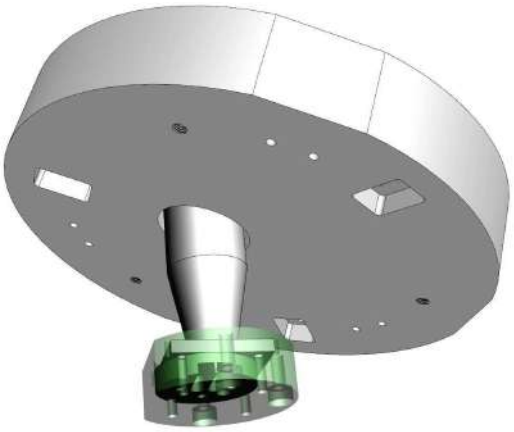

Fig. 8 Schematic view of the *PILOT* Internal Calibration Source (ICS) as implemented behind the M3 flat miror.

3.9 House-Keeping Electronics

A dedicated electronics (UGTI, for "Unité de gestion des données Techniques de lInstrument") is used for a variety of house-keeping tasks. In particular, the UGTI monitors cryogenic temperatures in the range 2-77 K inside the cryostat, and ambient temperatures for the rest of the instrument. The UGTI is also used to regulate the intensity of the current inside the ICS calibration source, to operate cryogenic valves that open and close the cryostat helium tank, and to operate heaters on the outer shell of the cryostat and in the helium tank.

3.10 Stellar Sensor

To combine observations of the same part of the sky obtained with various polarization analysis angles, the accu-

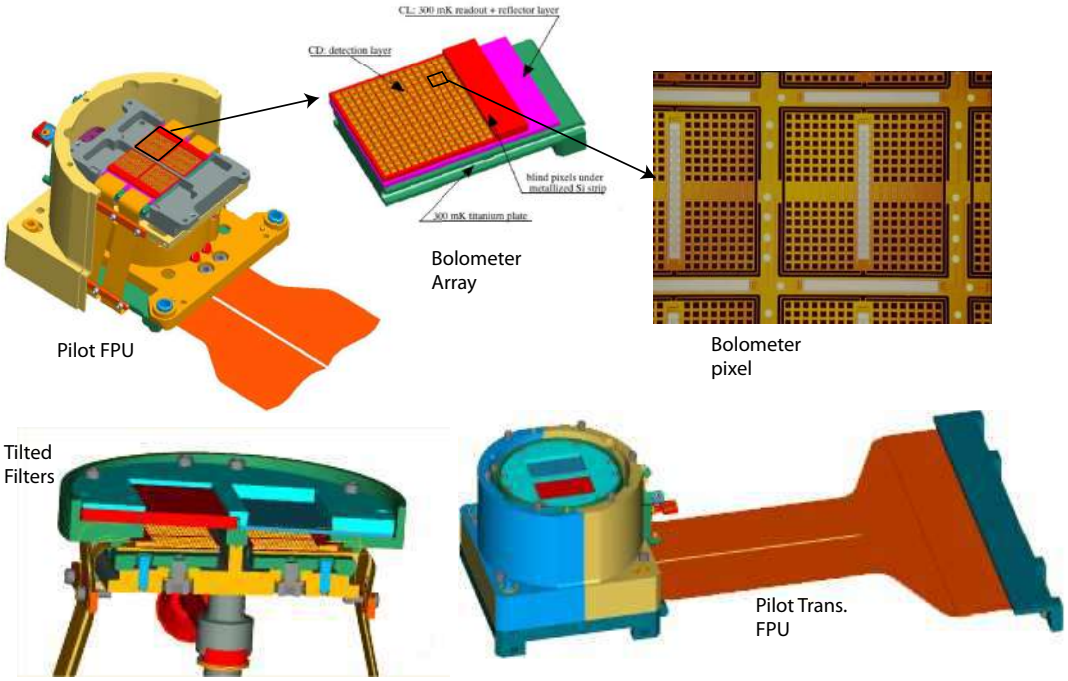

Fig. 7 Schematic view of the *PILOT* detectors. The top row shows an open view of the transmission focal plane unit (FPU), the structure of an individual 16×16 bolometer array, and a picture of one of the pixels. The bottom row shows the implementation of the bandpass filters in front of the detectors (left) and a global view of the transmission FPU with connectors.

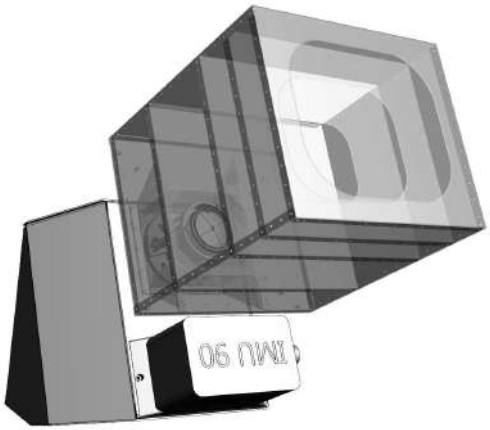

Fig. 9 Schematic view of the Estadius stellar sensor.

racy of the *a posteriori* pointing reconstruction must be better than a few arcseconds over a few minutes of time, under both night and day conditions. Since the *PILOT* observation strategy involves fast wide-field scanning, the pointing system must also remain accurate for angular scan speeds up to a few degrees per second. Only a system based on a daytime star sensor coupled to an accurate gyrometer is able to fulfil both these requirements. Estadius is an accurate, robust daytime attitude estimation system that has been designed and developed by CNES for stratospheric applications, and for the *PILOT* experiment in particular. A schematic view of Estadius is shown in Figure 9. A more detailed description of Estadius is presented in [38].

The key components of Estadius are an accurate optical fiber gyrometer (FOG) and an autonomous, wide-field stellar sensor. The star sensor is composed of a 16 Megapixel visible-CCD camera and a large aperture camera lens with a focal length of 135 mm, an aperture of f/1.8 and a FOV of $10^o \times 15^o$. The system provides very accurate star position measurements due to the small angular size of each pixel, and is able to detect stars against a bright sky background. The gyrometer is a optical fiber gyroscope (FOG) with a drift of $\simeq 0.01^o/h$. The system is adapted to work down to an altitude of $\simeq 25$ km, even under highly unstable flight conditions. The system provides highly accurate pointing reconstruction (1 arcsec in translation, 6 arcsec in rotation at 1σ), and demonstrates good autonomy through the use of automatic constellation recognition. It remains accurate at fast scanning speeds (i.e. angular speeds up to a few degrees per second), and is robust against straylight due to a high performance baffle. The Estadius system has been tested on four successful qualification stratospheric balloon flights: from Kiruna (Sweden) in 2010 and 2011, and from Timmins (Canada) in 2013 and 2014. As Estadius is a very flexible system, it is foreseen that it will be used regularly in future balloon missions with stringent pointing reconstruction requirements.

3.11 On-Board Computer

The On-Board Computer (OBC) controls the *PILOT* instrument. It is composed of PC/104 stackable modules, a GPS card and a Solid State Drive and a removable redundant flash storage. The (OBC commands the HWP rotation mechanism (HWPM), the house-keeping (HK) readout electronics (UGTI) and the gondola pointing. Those commands are either uploaded from the ground in the telemetry commands (TC), or generated automatically by the OBC. In particular, the execution of the scientific observing sequences are generated by the OBC, based on a pre-loaded scientific flight-plan. Each observing sequence is defined by several parameters, such as the coordinates of the center of the region to be observed, the number of constant elevation scans to be executed and their lengths, the separation between scans in the cross-elevation direction, the HWP positions to be used, the characteristics of the ICS sequences to be executed at the end of each scan, and a description of the HK parameters to be acquired during observations and calibrations. From parameters uploaded from the ground, the OBC computes in real time the azimuth and elevation pointing coordinates needed to complete the observing sequence and sends them to the gondola for execution.

The OBC also receives data from the bolometer readout electronics (BOLC), the UGTI, a GPS and the Estadius stellar sensor. Communication with BOLC is achieved through the Spacewire protocol. All data collected are time-tagged, saved on a flash disk on board and downloaded to the ground through the telemetry system. The telemetry provided by the CNES through the NOSYCA system is continuous and operate at a rate of $\simeq 1.4$ Mbits/s, which is sufficient to download all data in real-time. This not only reduces the risk of data losses, but also permits real-time monitoring of data quality and real-time modification of the flight plan, adapted to the actual observing conditions and instrument performance.

4 Polarization measurement

PILOT measures polarization using a combination of a rotating half-wave plate and a fixed analyzer grid positioned in front of the detector housings. This is a classical design in which the polarized part of the incident light is phase-shifted by the wave-plate and selectively transmitted by the analyzer. Such systems are often used with HWP rotation frequencies of a few Hertz followed by in-phase analysis of the bolometer signal. This produces a modulation of the polarized signal at twice the rotation frequency of the plate. Using the system in this way for observing astrophysical signals has one key disadvantage: the instrumental background is typically $\sim 10^5$ times higher than astrophysical emission, so any fluctuation of the background introduced by the rotating plate, such as anisotropies of the plate transmission, will produce a strong signal that completely dominates the astrophysical emission. For mapping experiments where scanning of the sky is obtained by constant drifting, the polarization modulation ends up being at a frequency close to that corresponding to the sky structures to be measured. Although well-adapted to fast readout single bolometers, this technique is not the optimal strategy for slower bolometer arrays.

For *PILOT*, we plan to use a stepping wave-plate, changing the angular position of the wave-plate at the end of each scan on the sky. Each sky region must be observed with at least two HWP angles. Our measurement method is therefore more similar to the approach used Polarization Sensitive Bolometers (PSBs) or Orto-Mode Transducers (OMT) pairs. The *StokesI* and *StokesQ* Stokes parameters are measured at a given time t through a differential measurement, and the *StokesI* and *StokesU* parameters are measured at a later time t'. For *PILOT*, the time difference between the two measurements is the time separation between successive scans. This is equivalent to modulating the polarized signal at a very low frequency, well below the frequencies associated with the spatial structure of astrophysical sources. We therefore expect that the background signal should be vary slightly for different HWP positions, but this will contribute a constant offset between individual scans, which can be removed during data processing and will not affect the structures observed along the scan. A second advantage of our measurement strategy is that individual scans will be obtained with a constant orientation of the analyzer, so redundancy in the scans can be used to intercalibrate the response of individual bolometers (response flat-field) at any time. This will be used to monitor variations of the response flat-field between successive ICS sequences. However, such low frequency modulation does not necessarily suppress the low frequency drifts of the bolometer noise (so called $1/f$ noise) or fluctuations of the residual atmospheric signal with sufficient accuracy. Results of numerical simulations for these contributions indicate that this will not affect our ability to recover the polarization intensity, in part because the $1/f$ noise of the *PILOT* bolometers is low.

4.1 Photometric equations

The Stokes parameters I, Q, U are related to the polarization fraction p and polarization direction ψ as

$$p = \frac{\sqrt{Q^2+U^2}}{I} \tag{1}$$

and

$$\psi = 0.5 \times \arctan(U,Q), \tag{2}$$

which invert into

$$Q = pI\cos(2\psi) \quad (3)$$

$$U = pI\sin(2\psi). \quad (4)$$

The Jones matrix of the HWP can be written

$$J_H = \begin{pmatrix} T_1 & 0 \\ 0 & T_2 e^{i\phi} \end{pmatrix} \quad (5)$$

where T_1 and T_2 are the transmission of the HWP along its fast and slow axis respectively and ϕ is the phase shift induced by birefringence in the HWP. The corresponding normalized Mueller matrix can be written as

$$M_H = \begin{pmatrix} 1 & \beta\cos 2\omega & \beta\sin 2\omega \\ \beta\cos 2\omega & \cos^2 2\omega + 2\gamma\sin^2 2\omega & (1-2\gamma)\cos 2\omega\sin 2\omega \\ \beta\sin 2\omega & (1-2\gamma)\cos 2\omega\sin 2\omega & \sin^2 2\omega + 2\gamma\cos^2 2\omega \end{pmatrix} \quad (6)$$

where $\beta = (T_1^2 - T_2^2)/(T_1^2 + T_2^2)$ and $\gamma = T_1 T_2 \cos\phi/(T_1^2 + T_2^2)$. β is the differential transmission between the fast and slow axis of the HWP. γ reflects the phase shift induced by the HWP. If the HWP is perfect, $\beta = 0$ and $\gamma = -0.5$ The Mueller matrix of the polarizer is given by

$$M_A = \begin{pmatrix} 1 & \pm p & 0 \\ \pm p & 1 & 0 \\ 0 & 0 & \sqrt{1-p^2} \end{pmatrix}, \quad (7)$$

where the $\pm$ is $+$ and $-$ for TRANS and REFLEX arrays respectively.

The Stokes vector of radiation falling on each detector is given by $S = M_H M_A S_0$ where $S_0 = (I, Q, U)$ is the Stokes vector of the incident radiation. As a result, the power m measured by detectors in the TRANS and REFLEX focal planes is given by

$$\begin{aligned} m = R_{xy}T_{xy}I \times [1 \pm \frac{1+2\gamma}{2} p\cos 2\psi + (p\beta\cos 2\psi + \beta)\cos 2\omega \\ + p\beta\sin 2\psi\sin 2\omega \pm \frac{1-2\gamma}{2} p\cos 2\psi\cos 4\omega \\ \pm \frac{1-2\gamma}{2} p\sin 2\psi\sin 4\omega] + O_{xy} \end{aligned} \quad (8)$$

where I is the total intensity, R_{xy} is the detector response, T_{xy} is the optics transmission. The additional term O_{xy} is to account for a an arbitrary electrical offset.

For a perfect HWP, $\beta = 0$ and $\gamma = -0.5$, and there is no term in 2ω in Equ. 8 which simplifies in

$$m = R_{xy}T_{xy}I \times [1 \pm p\cos 2\psi\cos 4\omega \pm p\sin 2\psi\sin 4\omega] + O_{xy}. \quad (9)$$

In terms of the Stokes parameters as defined in the instrument reference frame, this equations writes

$$m = R_{xy}T_{xy} \times [I \pm Q\cos 4\omega \pm U\sin 4\omega] + O_{xy}, \quad (10)$$

where the $\pm$ is $+$ and $-$ for TRANS and REFLEX arrays respectively.

4.2 Photometric Model

It is important to be able to estimate the optical power falling on individual stages of the instrument during the instrument definition. This is critical for the focal plane, since bolometers are optimized for a given background level and their response degrades for inappropriate background values. The total power falling on one pixel must therefore be predicted accurately, not only for in-flight conditions, but also under ground conditions so that useful data can be obtained during ground tests.

We developed a photometric model for the *PILOT* instrument that allows us to compute the total background power P_{tot} as light propagates through the instrument. In the far-infrared, the background during flight is dominated by the instrument emission and, on the ground, by atmospheric emission. We use the *PILOT* photometric model to adjust the background level during flight to a level acceptable for the bolometer arrays, which is $\simeq 4\,pW$ per pixel. The model was also used to determine the transmission of a density filter which was added to one of the cold screens of the cryostat during ground measurements. The model also predicts the spectral transmission between any optical elements in the system. We have used the photometric model to predict the total transmission, and also to adjust the level of the ICS source so that its contribution remains well below the instrumental background.

The background power P_{tot} is computed using:

$$P_{tot} = \sum_{i=1}^{N} P_i \quad (11)$$

$$P_i = S_{pix}\Omega_i \int_0^\infty Tr_{i+1}(\nu)\varepsilon_i(\nu)B_\nu(T_i,\nu)F_\tau(\nu)d\nu, \quad (12)$$

$$(13)$$

where optical element numbers (from 1 to N) increase along the light-path through the instrument. $Tr_{i+1}(\nu)$ is the total optical transmission at frequency ν from optical element $i+1$ to the bolometer and is given by

$$Tr_{i+1}(\nu) = \prod_{j=i+1}^{N} Tr_j(\nu). \quad (14)$$

Table 2 gives the list of these elements as well as their temperatures for the two *PILOT* photometric channels. $Tr_i(\nu)$ is the total optical transmission of optical element i, $\varepsilon_i(\nu)$ is the emissivity of optical element i, $B_\nu(T_i,\nu)$ is the Planck function at frequency ν for temperature T_i of the optical element i, S_{pix} is the bolometer matrix pixel surface and Ω_i is the solid angle under which photometric element number i is shinning on individual pixels. For the two photometric channels of *PILOT* and elements after the Lyot-stop, $S_{pix}\Omega_i = 7.19\,10^{-8}\,\mathrm{m^2/sr}$. The term $F_\tau(\nu)$ represents the effective transmission of filter i over its own emission and is

computed as

$$F_\tau(\nu) = \frac{1-e^{-\tau_i(\nu)}}{\tau_i(\nu)}, \quad (15)$$

$$\tau_i(\nu) = -log(Tr_i(\nu)). \quad (16)$$

We assume a fixed emissivity for each element, which we generally inferred from the literature for the material composing the element. For the residual atmosphere, we computed the transmission curve using the MODTRAN model at 38 km altitude and an elevation angle of 45°. We estimated the atmosphere emissivity in the *PILOT* bands assuming the transmission to be fully due to absorption ($\varepsilon = 1. - Tr$). We estimated the emissivity of the entrance window from FTS measurements of the transmission of bulk polyethylene, assuming no reflection ($\varepsilon = 1. - Tr$), scaled to the thickness of the flight window (200 μm). For the primary mirror M1, we adopted an emissivity of 0.01. This corresponds to the specifications for the newly constructed mirror, and is likely to increase as the mirror ages.

The transmission of lenses L1 and L2 were computed using FTS measurements of the transmission of bulk polyethylene to derive the absorption coefficient. The average length of optical rays through each lens was computed using the Zemax^{TM} software for a position at the center of the focal plane. The spectral transmission curves of other optical elements are taken from FTS subsystem measurements. The resulting total transmission of the instrument is shown in Fig. 10. For the detectors, the transmission value listed corresponds to the detector efficiency. The derived optical background power contribution of each optical element is given in Table 2.

The total background in the two channels is given in Tab. 2. In flight configuration, the background is computed to be about 5.7 and 4.0 in the 240 μm and 550 μm channels respectively. Note that this is the background absorbed by the detector, i.e. the value includes the detector absorptivity. This value is compatible with the background level acceptable for the detectors in the 240 μm channel, and the value at 550 μm was used to specify the fabrication of detectors for this channel. The photometric model was also used to estimate the expected background level during calibration on the ground. For a 300 K background with $\varepsilon = 1$, we derived background values of 83.7 pW/pix and 46.8 pW/pix for the 240 μm and 550 μm channels respectively. Based on this prediction, an optical attenuator with transmission $Tr \simeq 0.04$ in both bands was mounted on the coldest screen to reduce the optical background to suitable levels during ground tests.

5 Expected Sensitivity

The signal-to-noise of measurements *SNR* is related to the sensitivity *S*, total integration time t_{int} and system noise equivalent power (NEP_{tot}) through

$$SNR = \frac{S \times \sqrt{2t_{int}}}{NEP_{tot}}. \quad (17)$$

The total NEP is obtained from the quadratic sum of the detector and photon noise NEP, ie, $NEP^2_{tot} = NEP^2_{det} + NEP^2_{phot}$. The factor of two on integration time comes from the fact that the instrument bandwith used for the NEP corresponds to half a second integration time.

The sensitivity to extended sources in one pixel of the final map with the size of a physical pixel of the array is therefore given by

$$\frac{S_{pix}}{MJy/sr} = \frac{10^{20}}{\sqrt{2}} \times \frac{SNR}{Tr} \frac{NEP_{tot}}{W/\sqrt{Hz}} \left(\frac{t_{int}}{sec}\right)^{-1/2} \left(\frac{S\Omega_{pix}}{m^2/sr}\right)^{-1} \left(\frac{\Delta_\nu}{Hz}\right)^{-1} \quad (18)$$

where t_{int} is the integration per pixel of the final map, $S\Omega_{pix}$ is the solid angle subtended by one bolometer, Δ_ν is the optical bandwidth and Tr is the transmission of the optics. Note that Tr and Δ_ν must be defined in a consistent way, such that their product, multiplied by the input signal at frequency ν_0, equals the in-band integral of the detected signal. The value of Tr corresponding to the FWHM of the bandpass Δ_ν for a dust spectrum with spectral index $\beta = 1.6$ and dust temperature $T_D = 17$ K is given in Tab. 1. Note also that Tr must incorporate the transmission of the polarization splitter.

If the integration time t_{int} is evenly distributed over the mapped area, we have

$$\frac{t_{int}}{sec} = 60^2 \left(\frac{\mathrm{M}}{\square/hr}\right)^{-1} \frac{2 \times S_{array}}{\square}, \quad (19)$$

where M is the mapping speed and S_{array} is the projected surface of one photometric channel (Reflection or Transmission) on the sky. For the nominal configuration of *PILOT*, each photometric band has 512 detectors (2 arrays of 16×16) in the Reflection or Transmission focal planes, so

$$S_{array} = 512 \times S_{bolo}, \quad (20)$$

where S_{bolo} is the bolometer surface.

The NEP was calculated from the nominal NEP of the individual bolometers for Herschel *PACS* ($2.0\,10^{-16}\,\mathrm{W}/\sqrt{\mathrm{Hz}}$) and using the photon noise NEP derived from the photometric model of the instrument (see Sect. 4.2), corresponding to $9.8\,10^{-17}\,\mathrm{W}/\sqrt{\mathrm{Hz}}$ and $6.0\,10^{-17}\,\mathrm{W}/\sqrt{\mathrm{Hz}}$ at 240 μm and 550 μm respectively. These values are comparable to or lower than the NEP of the readout electronics at 240 μm.

The *PILOT* sensitivity computed using Eq. 18 and 20 are plotted as a function of mapping speed for $SNR = 1$ and $SNR = 3$ in Fig. 11, both expressed as sky brightness (I_ν) and equivalent dust extinction at visible wavelength ($\mathrm{A_V}$). The sensitivity at 1° resolution is also shown. The sensitivities for the two extreme mapping speeds of $5^{\square}/hr$ and

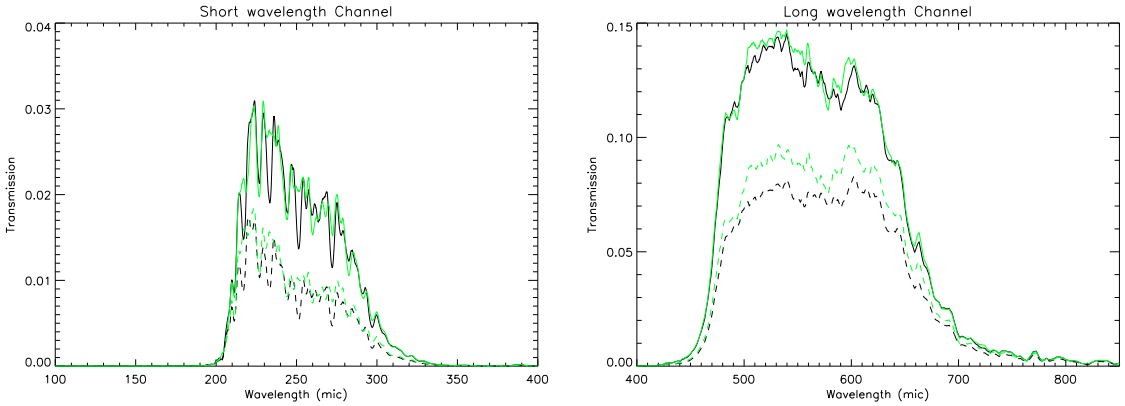

Fig. 10 Instrumental transmission in the 240 μm and 550 μm channel as predicted using the photometric model, for HWP positions of 0^o (black curve) and 45^o (green curve), on the transmission and reflection arrays respectively. The transmission values shown include polarizer transmission and detector absorption.

Table 2 Contribution to the background of the various optical elements, as predicted by the photometric model in the flight configuration. The elements are ordered from the outside of the cryostat to the detector. Type is the element type (R=Reflector, T=transmitor). ε is the assumed emissivity of each element. $< Tr >$ is the band-averaged transmission of each element. $< T_c >$ is the band averaged cumulative transmission from the given element to the detector. P is the contribution of each element to the absorbed background. For the 240 μm and 550 μm channels, P is expressed in pW/pixel and percentage of the total background.

Element	Type	T [K]	ε	240 μm $< T_c >$	$< Tr >$	P [pW/pix]	P [%]	550 μm $< T_c >$	$< Tr >$	P [pW/pix]	P [%]
ATMOSPHERE	T	253.0	0.010	0.022	0.990	$6.518\,10^{-1}$	11.37	0.125	0.990	$3.683\,10^{-1}$	11.39
M1	R	300.0	0.020	0.023	0.980	1.608	28.05	0.127	0.980	$8.988\,10^{-1}$	27.79
WINDOW	T	300.0	0.020	0.024	0.939	1.651	28.80	0.130	0.979	$9.105\,10^{-1}$	28.15
THERM1	T	300.0	0.010	0.024	0.993	$8.511\,10^{-1}$	14.85	0.131	0.996	$4.622\,10^{-1}$	14.29
THERM2	T	140.0	0.010	0.024	0.993	$3.550\,10^{-1}$	6.19	0.131	0.996	$2.057\,10^{-1}$	6.36
W1360	T	80.0	0.030	0.028	0.867	$5.507\,10^{-1}$	9.61	0.138	0.952	$3.379\,10^{-1}$	10.45
THERM3	T	40.0	0.010	0.030	0.943	$6.508\,10^{-2}$	1.14	0.141	0.978	$4.900\,10^{-2}$	1.52
W1359	T	2.5	0.030	0.033	0.920	$2.105\,10^{-10}$	0.00	0.144	0.981	$5.302\,10^{-6}$	0.00
W1337	T	2.5	0.030	0.036	0.899	$2.279\,10^{-10}$	0.00	0.168	0.855	$5.762\,10^{-6}$	0.00
M2	R	2.5	0.020	0.037	0.980	$1.614\,10^{-10}$	0.00	0.172	0.980	$4.213\,10^{-6}$	0.00
M3	R	2.5	0.020	0.038	0.980	$1.647\,10^{-10}$	0.00	0.175	0.980	$4.299\,10^{-6}$	0.00
L1	T	2.5	0.030	0.058	0.653	$3.080\,10^{-10}$	0.00	0.198	0.885	$6.860\,10^{-6}$	0.00
HWP	T	2.5	0.030	0.080	0.722	$4.358\,10^{-10}$	0.00	0.212	0.933	$7.646\,10^{-6}$	0.00
L2	T	2.5	0.030	0.274	0.293	$9.830\,10^{-10}$	0.00	0.296	0.717	$9.516\,10^{-6}$	0.00
POLARIZER	-	2.5	0.030	0.547	0.500	$3.414\,10^{-9}$	0.00	0.592	0.500	$2.237\,10^{-5}$	0.00
W1506	T	0.3	0.030	0.783	0.704	$6.446\,10^{-26}$	0.00	0.698	0.849	$1.206\,10^{-26}$	0.00
W875	T	0.3	0.030	0.875	0.895	$1.078\,10^{-25}$	0.00	0.754	0.926	$1.507\,10^{-26}$	0.00
W1371	T	0.3	0.030	0.922	0.949	$1.246\,10^{-25}$	0.00	0.800	0.942	$1.947\,10^{-26}$	0.00
Detector	-	0.3	0.030	1.000	0.922	$1.387\,10^{-25}$	0.00	1.000	0.800	$2.517\,10^{-26}$	0.00
Total						5.7				4.0	

$150^{\square}/hr$ are given in Tab. 1. The correspondence between sky brightness and dust extinction was computed using

$$A_V = \frac{\tau_{250}\,(A_V/N_H)}{p_D\,(\tau/N_H)_{250}}, \quad (21)$$

$$\tau_{250} = \tau_{\nu 0}\left(\frac{240}{250}\right)^{\beta}, \quad (22)$$

$$\tau_\nu = \frac{I_\nu}{B_\nu(T_D)} \quad (23)$$

where τ_ν is the dust optical depth, $B_\nu(T_D)$ is the Planck function for dust temperature T_D, N_H denotes the gas column density and p_D is the dust polarization fraction. We used the standard A_V to N_H conversion ratio $(A_V/N_H) = 5\,10^{-22}\,cm^2$ from [39], the dust emissivity at 250 μm $(\tau/N_H))_{250} = 10^{-25}\,cm^2$ from [40] a dust temperature of $T_D = 17.5$ K and a dust spectral index β=1.65. The sensitivities were computed assuming dust polarization of 10% ($p_D = 0.1$).

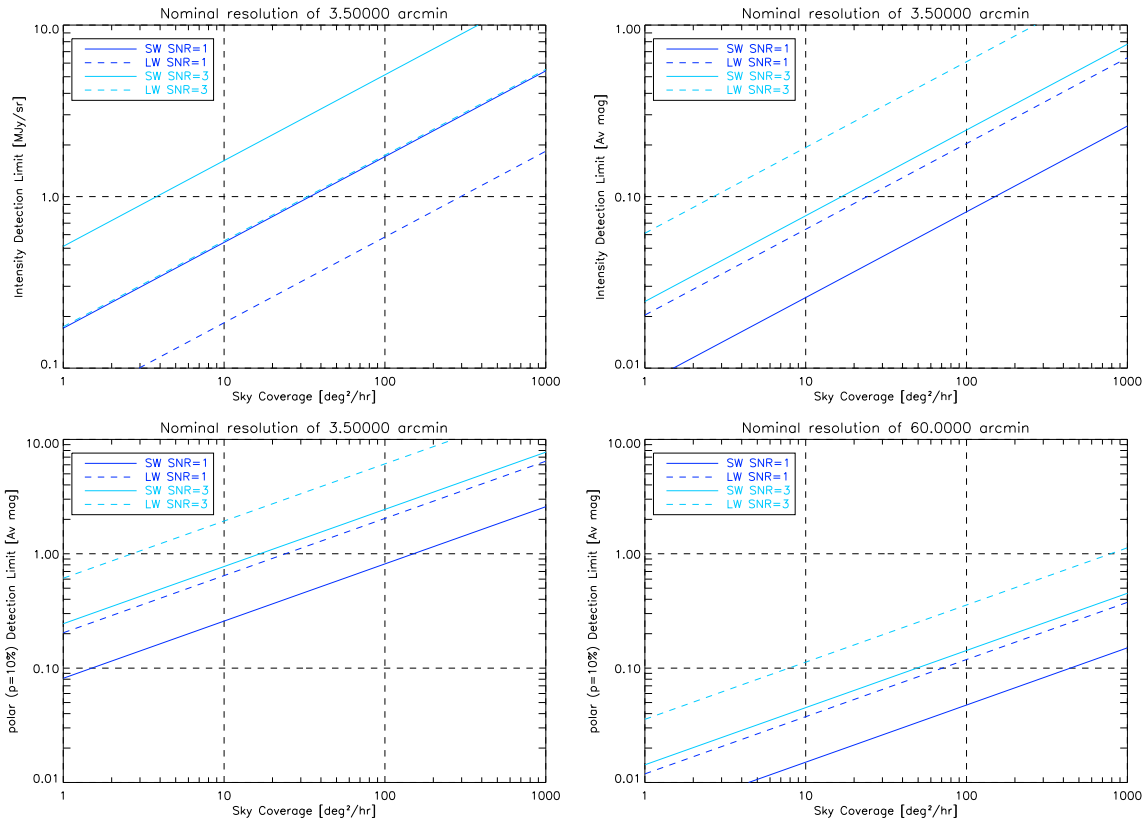

Fig. 11 The expected sensitivity of *PILOT* as a function of mapping speed. The upper pannel shows sensitivity to total intensity in MJy/sr and visual dust extinction, derived using standard dust parameters (see text). The lower plots show *PILOT* sensitivity to polarization at the nominal *PILOT* angular resolution, and at 1^o resolution.

The *PILOT* sensitivity is compared to the average emission spectrum of the ISM in Fig. 12 for the two extreme modes of observation with *PILOT*.

In the 240 μm channel, observations in "Deep Survey" mode will detect a cirrus cloud in intensity with a column density equivalent to $A_V = 0.05$ mag with $SNR = 3$. In polarization, the same observing strategy will detect a cloud with A_V=0.5 mag and a dust polarization fraction of 10% with $SNR = 3$.

6 Simulations

We performed a suite of simulations in order to validate the instrumental concept, to determine requirements for various sub-systems and to optimize the scientific flight plans. We simulate observations in which the center of the focal plane scans a region of sky at constant elevation with constant speed. The simulations use the OBC software that is used to command the gondola motion and instrument pointing. This allows us to test the different observing modes that we anticipate using during flight. Signal time series are produced at the BOLC sampling rate of 40 Hz for each bolometer. From Equ. 10, the detector measurements on the TRANS (m_T) and

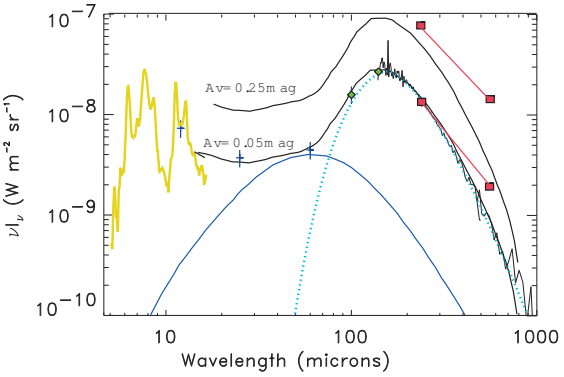

Fig. 12 Average emission spectrum of the ISM from the mid-IR to the submm, as observed by ISO (yellow curve, PAH emission), IRAS (blue crosses), DIRBE (green diamonds) and FIRAS (black curve above 140 μm). The spectra are normalized to a visual extinction of $A_v = 0.05$ mag ($N_H = 10^{20}$ H/cm^2) and $A_v = 0.25$ mag ($N_H = 5\,10^{20}$ H/cm^2). The red squares show the *PILOT* sensitivity at full resolution to total intensity (3σ) in the two extreme observing modes, i.e. "Large Survey" and "Deep Survey" (lower curve).

REFLEX (m_R) focal planes are computed using

$$m_T(t) = T_{xy}R_{xy}\left[I_{sky} + \cos(\omega')Q_{sky} + \sin(\omega')U_{sky}\right] \quad (24)$$

$$m_R(t) = T_{xy}R_{xy}\left[I_{sky} - \cos(\omega')Q_{sky} - \sin(\omega')U_{sky}\right]. \quad (25)$$

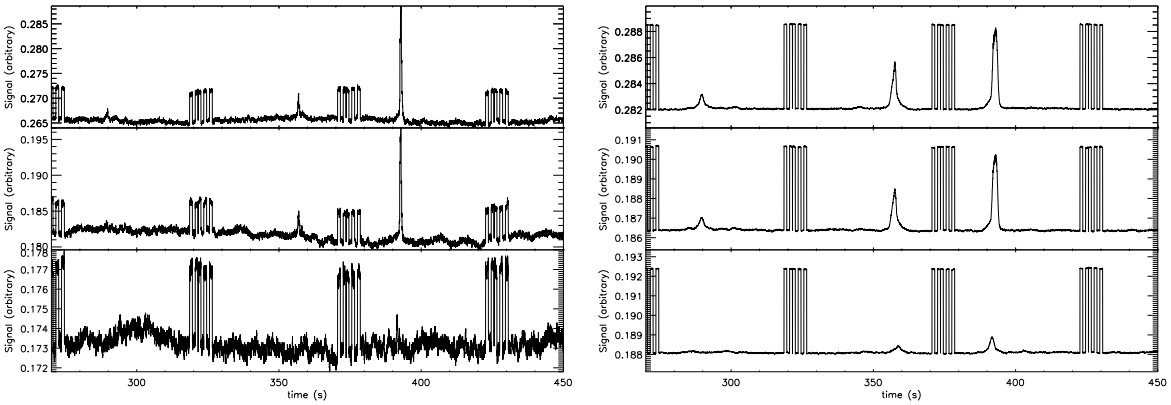

Fig. 13 Example of simulated time-lines in the 240 μm channel, for individual pixels (left) and for the average across one of the *PILOT* arrays (right). The plots show three consecutive scans, separated by calibration on the ICS, which is visible in the time-lines as a strongly modulated signal. The upper and middle panels show time-lines for the TRANS and REFLEX arrays respectively. The large bumps in the data correspond to strong thermal dust emission in the Orion molecular cloud. The lower panel shows the difference between the two focal planes. The variations of the difference signal reflect polarization of the simulated astrophysical emission.

The Stokes parameters I_{sky}, Q_{sky} and Q_{sky} at the current sky position are taken from the *Planck* polarization maps at 353 GHz presented in [18], and extrapolated to the *PILOT* frequency channels using a modified black body spectrum with a dust emissivity index and dust temperatures also determined from analysis of the *Planck* data [41]. The Stokes parameters Q_{sky} and U_{sky} are defined with respect to equatorial north according to IAU convention. The angle ω' then reads

$$\omega' = 4\omega + 2\varphi - 2\theta, \tag{26}$$

where ω is the angle of the slow axis of the HWP with respect to the horizontal scan axis direction, φ is the angular distance between the celestial north and the elevation axis which varies with time, and θ is the polarization rotation angle, which potentially varies with location in the focal plane. The instrument transmission T_{xy} was assumed constant over the focal plane and taken from the prediction of the photometric model described in Sect. 4.2. The detector response R_{xy} was taken from calibration measurements on the *PILOT* detectors obtained in front of an extended blackbody source.

We added detector and photon noise to the simulated time-lines. The detector and electronics noise were estimated from long (more than three hours) time-lines recorded during the calibration of *PACS*-like bolometer arrays under a low background. We isolated from these measurements the noise component that is uncorrelated between detectors and used the corresponding noise power spectrum to generate independent detector noise for each bolometer in the simulation. The noise level of this component is about $2\,10^{-16}\ W/\sqrt{Hz}$ at a few Hz and increases towards low frequency roughly as $\nu^{-1/2}$. We also added a noise component with a flat power spectrum, corresponding to the photon noise, which was calculated using the prediction of the photometric model described in Sect. 4.2. The noise level of this component is produced by thermal emission from the instrument as summarized in Tab. 1. An example of a noisy, simulated time-line obtained when scanning across the Orion star-forming region is shown on Fig. 13.

Several sources of systematic instrumental effects are included in our simulations. In particular, we introduced pointing errors with an amplitude of the errors set to 10" on the three axes, corresponding to the required reconstruction accuracy of the stellar sensor. Other uncertainties, such as the error on the positioning of the rotating HWP or imperfect optics of the HWP (see Sect. 4.1) were also included, in order to investigate their effect on the reconstruction of the polarized signal. In Fig. 14, we show the effect of the error on the wave-plate angle (ω in Eq. 26) as an example. Simulations such as these have been used to set requirements on various sub-systems.

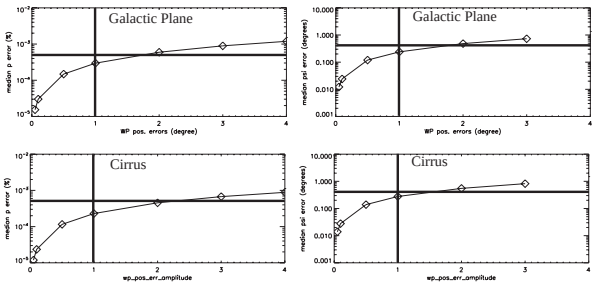

Fig. 14 Error on the polarization degree (left) and polarization angle (right) as a function of the angular positional error of the HWP for a standard observation of the Galactic plane (upper panel) and of a diffuse cirrus cloud (lower panel). The criterion used to set the requirement on this parameter is indicated by the thick horizontal line.

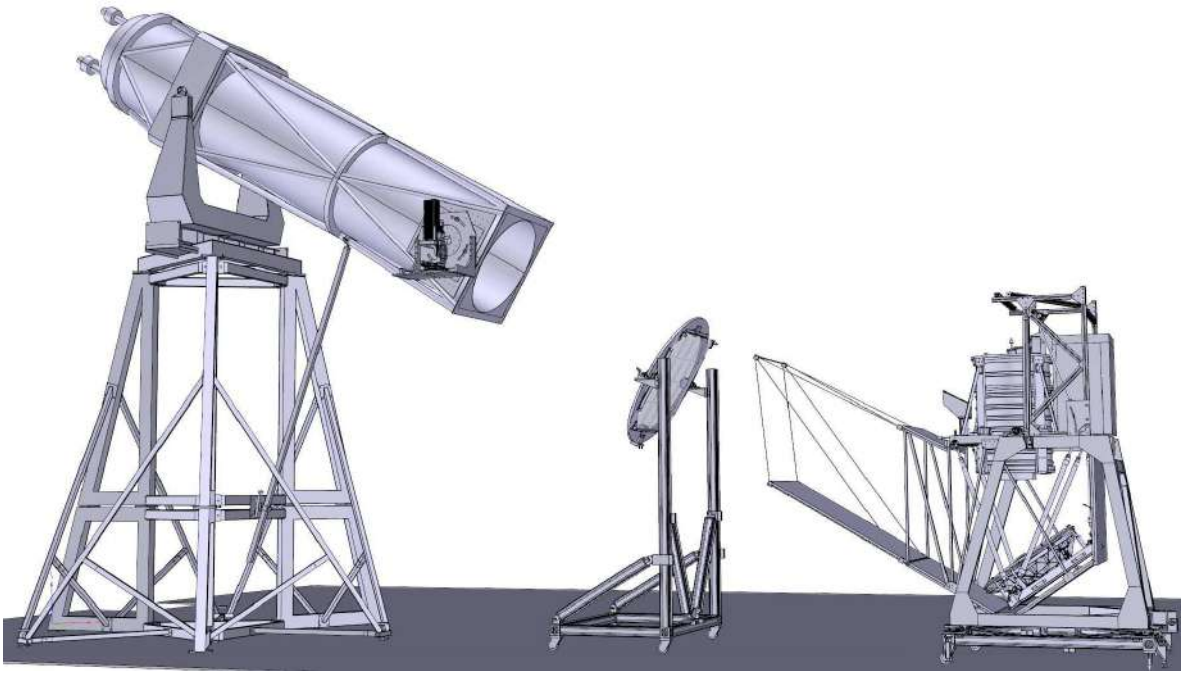

Fig. 15 Optical bench used to characterize polarization properties of the instrument.From right to left, the *PILOT* pointed load, the large format *Archeops* polarizer and the IRAP $\phi = 1\,\mathrm{m}$ collimator.

7 Ground Tests

A series of ground tests of the *PILOT* instrument has been performed. These include the characterization of the primary mirror reported in [24], tests of the photometer alone, measurements of the spectral response in polarization using a FTS in Martin-Pupplet mode, and end-to-end tests of the instrument reported in [42].

Our assessment of the overall optical quality indicates that the alignment between the primary mirror and the photometer must be accurate to $\sim 300\,\mu$m. This implies a precise characterisation of the mechanical and optical properties of the primary mirror and an efficient procedure to align the two subsystems, both in the laboratory and at the launch site. The primary mirror is mounted on an aluminium hexapod, which was adjusted during alignment tests at IRAP using the collimated beam from a 1 m diameter collimator that replicates a distant point-source. The relative position of the two subsystems is registered with respect to a series of optical reference cubes and reference balls, so that the setting can be reproduced at the launch site using a laser tracker. Before launch, the optical system is actually positioned such that it will move into the correct focus for the expected temperature at ceiling, based on a thermoelastic model of the instrument and meteorological predictions for conditions in the stratosphere.

Optical calculations show that the direction of an incident linear polarization is slightly rotated through the optics from the primary mirror to the detector. This rotation angle varies accross the focal-plane, and can reach a few degrees away from the optical axis. This rotation matrix must be measured precisely and taken into account during data processing. We measured this rotation during ground tests, using the experimental configuration shown in Fig. 15. A large format ($1 \times 1\,\mathrm{m}$) polarizer, originally developed for the *Archeops* experiment, was inserted into the beam of the IRAP collimator, in order to produce a highly polarized beam of known polarization direction. A similar set-up was used to attempt measurement of the Q and U beams and their possible spatial variations on the array. The results of these end-to-end optical tests will be presented in [43].

8 Conclusion

In this paper, we have presented the *PILOT* balloon-borne experiment, which takes advantage of large format multiplexed bolometer arrays to obtain sensitive maps of polarized thermal dust emission at far-infrared wavelengths. *PILOT* measurements will allow us to map the direction and intensity of the magnetic field in diffuse regions of our Galaxy at unprecedented angular resolution and to study the magnetic properties of interstellar dust grains. *PILOT* will be used to measure polarization towards very diffuse regions at high galactic latitude. This type of observation will be very important when devising methods to subtract the contribution of polarized foreground emission for future cosmology

missions that aim to measure the B-mode polarization signal of the cosmic microwave background.

The *PILOT* project is supported and funded by the French Space agency (CNES). The first flight of the *PILOT* took place from Timmins, Ontario Canada in September 2015. The second flight is scheduled to take place from Alice Springs, Australia in early 2017.

Acknowledgements *PILOT* is an international project that involves several European institutes. The institutes that have contributed to hardware developments for *PILOT* are IRAP and CNES in Toulouse (France), IAS in Orsay (France), CEA in Saclay (France), Rome University in Rome (Italy) and Cardiff University (UK).

This work was supported by the CNES. It is based on instrumentation work preparatory to the *PILOT* mission, which has been flown under a balloon operated by CNES, under the agreement between CNES and CNRS /INSU, during the Timmins 2015 campaign.

References

1. A. Lazarian, J. Quant. Spec. Radiat. Transf.**79**, 881 (2003). DOI 10.1016/S0022-4073(02)00326-6
2. A. Lazarian, J. Quant. Spec. Radiat. Transf.**106**, 225 (2007). DOI 10.1016/j.jqsrt.2007.01.038
3. A.Z. Dolginov, I.G. Mitrofanov, Ap&SS**43**, 291 (1976). DOI 10.1007/BF00640010
4. B.T. Draine, J.C. Weingartner, ApJ**470**, 551 (1996). DOI 10.1086/177887
5. B.T. Draine, J.C. Weingartner, ApJ**480**, 633 (1997). DOI 10.1086/304008
6. A. Lazarian, T. Hoang, MNRAS**378**, 910 (2007). DOI 10.1111/j.1365-2966.2007.11817.x
7. T. Hoang, A. Lazarian, MNRAS**388**, 117 (2008). DOI 10.1111/j.1365-2966.2008.13249.x
8. L. Davis, Jr., J.L. Greenstein, ApJ**114**, 206 (1951). DOI 10.1086/145464
9. P.G. Martin, MNRAS**153**, 279 (1971). DOI 10.1093/mnras/153.3.279
10. P.G. Martin, in *EAS Publications Series*, *EAS Publications Series*, vol. 23, ed. by M.A. Miville-Deschênes, F. Boulanger (2007), *EAS Publications Series*, vol. 23, pp. 165–188. DOI 10.1051/eas:2007011
11. W. Stein, ApJ**144**, 318 (1966). DOI 10.1086/148606
12. C. Heiles, AJ**119**, 923 (2000). DOI 10.1086/301236
13. D.C.B. Whittet, J.H. Hough, A. Lazarian, T. Hoang, ApJ**674**, 304 (2008). DOI 10.1086/525040
14. D. Ward-Thompson, J.M. Kirk, R.M. Crutcher, J.S. Greaves, W.S. Holland, P. André, ApJ**537**, L135 (2000). DOI 10.1086/312764
15. B.C. Matthews, C.D. Wilson, ApJ**531**, 868 (2000). DOI 10.1086/308523
16. A. Benoît, Archeops Collaboration, Advances in Space Research **33**, 1790 (2004). DOI 10.1016/j.asr.2003.05.021
17. A. Benoît, P. Ade, A. Amblard, R. Ansari, É. Aubourg, et al., A&A**424**, 571 (2004). DOI 10.1051/0004-6361:20040042
18. Planck Collaboration Int. XIX, A&A, submitted, [arXiv:astro-ph/1405.xxxx] (2014)
19. Planck Collaboration Int. XXI, A&A, submitted, [arXiv:astro-ph/1405.xxxx] (2014)
20. Planck Collaboration Int. XX, A&A, submitted, [arXiv:astro-ph/1405.xxxx] (2014)
21. P. Agnese, C. Cigna, J.L. Pornin, R. Accomo, C. Bonnin, N. Colombel, M. Delcourt, E. Doumayrou, J. Lepennec, J. Martignac, V. Reveret, L. Rodriguez, L.G. Vigroux, in *Millimeter and Submillimeter Detectors for Astronomy*, *Proc. SPIE*, vol. 4855, ed. by T.G. Phillips, J. Zmuidzinas (2003), *Proc. SPIE*, vol. 4855, pp. 108–114. DOI 10.1117/12.459191
22. F. Simoens, P. Agnese, A. Béguin, J. Carcey, J.C. Cigna, J.L. Pornin, P. Rey, A. Vandeneynde, L. Rodriguez, O. Boulade, J. Lepennec, J. Martignac, E. Doumayrou, V. Reveret, L. Vigroux, in *Z-Spec: a broadband millimeter-wave grating spectrometer: design, construction, and first cryogenic measurements*, *Proc. SPIE*, vol. 5498, ed. by C.M. Bradford, P.A.R. Ade, J.E. Aguirre, J.J. Bock, M. Dragovan, L. Duband, L. Earle, J. Glenn, H. Matsuhara, B.J. Naylor, H.T. Nguyen, M. Yun, J. Zmuidzinas (2004), *Proc. SPIE*, vol. 5498, pp. 177–186. DOI 10.1117/12.551299
23. L.M. Fissel, P.A.R. Ade, F.E. Angilè, S.J. Benton, E.L. Chapin, M.J. Devlin, N.N. Gandilo, J.O. Gundersen, P.C. Hargrave, D.H. Hughes, J. Klein, A.L. Korotkov, G. Marsden, T.G. Matthews, L. Moncelsi, T.K. Mroczkowski, C.B. Netterfield, G. Novak, L. Olmi, E. Pascale, G. Savini, D. Scott, J.A. Shariff, J.D. Soler, N.E. Thomas, M.D.P. Truch, C.E. Tucker, G.S. Tucker, D. Ward-Thompson, D.V. Wiebe, in *Millimeter, Submillimeter, and Far-Infrared Detectors and Instrumentation for Astronomy V*, *Proc. SPIE*, vol. 7741 (2010), *Proc. SPIE*, vol. 7741, pp. 77,410E–77,410E–14. DOI 10.1117/12.857601
24. C. Engel, I. Ristorcelli, J.P. Bernard, Y. Longval, C. Marty, B. Mot, G. Otrio, G. Roudil, Experimental Astronomy **36**, 21 (2013). DOI 10.1007/s10686-013-9332-7
25. S.e.a. Grabarnik, Experimental Astronomy pp. ?–? (2016)
26. M. Salatino, P. de Bernardis, ArXiv e-prints (2010)
27. G. Savini, G. Pisano, P.A.R. Ade, Appl. Opt.**45**, 8907 (2006). DOI 10.1364/AO.45.008907
28. G. Pisano, G. Savini, P.A.R. Ade, V. Haynes, W.K. Gear, Appl. Opt.**45**, 6982 (2006). DOI 10.1364/AO.45.006982
29. J. Zhang, P.A.R. Ade, P. Mauskopf, L. Moncelsi, G. Savini, N. Whitehouse, Appl. Opt.**48**, 6635 (2009). DOI 10.1364/AO.48.006635
30. C.J. MacTavish, P.A.R. Ade, E.S. Battistelli, S. Benton, R. Bihary, J.J. Bock, J.R. Bond, J. Brevik, S. Bryan, C.R. Contaldi, B.P. Crill, O. Doré, L. Fissel, S.R. Golwala, M. Halpern, G. Hilton, W. Holmes, V.V. Hristov, K. Irwin, W.C. Jones, C.L. Kuo, A.E. Lange, C. Lawrie, T.G. Martin, P. Mason, T.E. Montroy, C.B. Netterfield, D. Riley, J.E. Ruhl, M. Runyan, A. Trangsrud, C. Tucker, A. Turner, M. Viero, D. Wiebe, ApJ**689**, 655 (2008). DOI 10.1086/592732
31. M. Salatino, P. de Bernardis, S. Masi, A&A**528**, A138 (2011). DOI 10.1051/0004-6361/201015288
32. M. Salatino, P. de Bernardis, A. Iacoangeli, S. Masi, J. Pimentão, J.P. Bernard, Mem. Soc. Astron. Italiana**79**, 905 (2008)
33. P.A.R. Ade, G. Pisano, C. Tucker, S. Weaver, in *Society of Photo-Optical Instrumentation Engineers (SPIE) Conference Series*, *Proc. SPIE*, vol. 6275 (2006), *Proc. SPIE*, vol. 6275, p. 62750U. DOI 10.1117/12.673162
34. M. Salatino, the PILOT team, *Exp. Astronomy*
35. G. Pisano, P. Hargrave, M. Griffin, P. Collins, J. Beeman, R. Hermoso, Appl. Opt.**44**, 3208 (2005). DOI 10.1364/AO.44.003208
36. P. Hargrave, T. Waskett, T. Lim, B. Swinyard, in *Society of Photo-Optical Instrumentation Engineers (SPIE) Conference Series*, *Proc. SPIE*, vol. 6275 (2006), *Proc. SPIE*, vol. 6275, p. 627514. DOI 10.1117/12.673197
37. P.C. Hargrave, J.W. Beeman, P.A. Collins, I. Didschuns, M.J. Griffin, B. Kiernan, G. Pisano, in *IR Space Telescopes and Instruments*, *Society of Photo-Optical Instrumentation Engineers (SPIE) Conference Series*, vol. 4850, ed. by J.C. Mather (2003), *Society of Photo-Optical Instrumentation Engineers (SPIE) Conference Series*, vol. 4850, pp. 638–649
38. J. Montel, CNES. 22nd ESA PAC Symposium, Norway, 2015 (2015)
39. R.C. Bohlin, B.D. Savage, J.F. Drake, ApJ**224**, 132 (1978). DOI 10.1086/156357

List of Figures

List of Tables

Bibliography

P. A. R. Ade, G. Pisano, C. Tucker, and S. Weaver. A review of metal mesh filters. In *Society of Photo-Optical Instrumentation Engineers (SPIE) Conference Series*, volume 6275 of Proc. SPIE, page 62750U, June 2006. doi: 10.1117/12.673162.

Peter AR Ade, N Aghanim, Z Ahmed, RW Aikin, Kate Denham Alexander, M Arnaud, J Aumont, C Baccigalupi, Anthony J Banday, D Barkats, et al. Joint analysis of bicep2/keck array and planck data. *Physical review letters*, 114(10):101301, 2015.

C. L. Bennett, D. Larson, J. L. Weiland, N. Jarosik, G. Hinshaw, N. Odegard, K. M. Smith, R. S. Hill, B. Gold, M. Halpern, E. Komatsu, M. R. Nolta, L. Page, D. N. Spergel, E. Wollack, J. Dunkley, A. Kogut, M. Limon, S. S. Meyer, G. S. Tucker, and E. L. Wright. Nine-year Wilkinson Microwave Anisotropy Probe (WMAP) Observations: Final Maps and Results. ApJS, 208:20, October 2013. doi: 10.1088/0067-0049/208/2/20.

Alain Benoit, P Ade, A Amblard, R Ansari, É Aubourg, S Bargot, JG Bartlett, J-Ph Bernard, RS Bhatia, A Blanchard, et al. First detection of polarization of the submillimetre diffuse galactic dust emission by archeops. *Astronomy & Astrophysics*, 424(2):571–582, 2004.

J. P. Bernard, A. Abergel, I. Ristorcelli, F. Pajot, J. P. Torre, F. Boulanger, M. Giard, G. Lagache, G. Serra, J. M. Lamarre, J. L. Puget, F. Lepeintre, and L. Cambrésy. PRONAOS observations of MCLD 123.5 + 24.9: cold dust in the Polaris cirrus cloud. A&A, 347:640–649, July 1999.

J.-P. Bernard, P. Ade, P. De Bernardis, M. Giard, M. Griffin, P. Hargrave, A. Laurens, B. Leriche, C. Leroy, Y. Longval, C. Marty, S. Madden, B. Maffei, S. Masi, C. Meny, M.-A. Miville-Deschênes, J. Narbonne, L. Nati, F. Pajot, G. Pisano, E. Pointecouteau, N. Ponthieu, I. Ristorcelli, L. Rodriguez, G. Roudil, M. Salatino, and G. Savini. PILOT: Measuring polarization in the Interstellar Medium. In M.-A. Miville-Deschênes

and F. Boulanger, editors, *EAS Publications Series*, volume 23 of *EAS Publications Series*, pages 189–203, 2007. doi: 10.1051/eas:2007012.

J.-Ph. Bernard et al. Pilot: a balloon-borne experiment to measure the polarized fir emission of dust grains in the interstellar medium. submitted, 2016.

BICEP2 Collaboration, P. A. R. Ade, R. W. Aikin, D. Barkats, S. J. Benton, C. A. Bischoff, J. J. Bock, J. A. Brevik, I. Buder, E. Bullock, C. D. Dowell, L. Duband, J. P. Filippini, S. Fliescher, S. R. Golwala, M. Halpern, M. Hasselfield, S. R. Hildebrandt, G. C. Hilton, V. V. Hristov, K. D. Irwin, K. S. Karkare, J. P. Kaufman, B. G. Keating, S. A. Kernasovskiy, J. M. Kovac, C. L. Kuo, E. M. Leitch, M. Lueker, P. Mason, C. B. Netterfield, H. T. Nguyen, R. O'Brient, R. W. Ogburn, A. Orlando, C. Pryke, C. D. Reintsema, S. Richter, R. Schwarz, C. D. Sheehy, Z. K. Staniszewski, R. V. Sudiwala, G. P. Teply, J. E. Tolan, A. D. Turner, A. G. Vieregg, C. L. Wong, and K. W. Yoon. Detection of B-Mode Polarization at Degree Angular Scales by BICEP2. *Physical Review Letters*, 112(24):241101, June 2014. doi: 10.1103/PhysRevLett.112.241101.

Nicolas Billot. *Etalonnage d'un nouveau type de détecteur bolométrique pour l'instrument PACS de l'Observatoire Spatial Herschel*. Theses, Université Paris Sud - Paris XI, December 2007. URL `https://tel.archives-ouvertes.fr/tel-00292030`.

M. Bottema, W. Plummer, and J. Strong. Water Vapor in the Atmosphere of Venus. ApJ, 139:1021–1022, April 1964. doi: 10.1086/147841.

Brian Cabral and Leith Casey Leedom. Imaging vector fields using line integral convolution. In *Proceedings of the 20th annual conference on Computer graphics and interactive techniques*, pages 263–270. ACM, 1993.

Che-Yu Chen, Patrick K King, and Zhi-Yun Li. Change of magnetic field-gas alignment at the gravity-driven alfvénic transition in molecular clouds: Implications for dust polarization observations. *The Astrophysical Journal*, 829(2):84, 2016.

L. Davis, Jr. and J. L. Greenstein. The Polarization of Starlight by Aligned Dust Grains. ApJ, 114:206, September 1951. doi: 10.1086/145464.

Giancarlo De Gasperis, Amedeo Balbi, Paolo Cabella, Paolo Natoli, and Nicola Vittorio. Roma: A map-making algorithm for polarised cmb data sets. *Astronomy & Astrophysics*, 436(3):1159–1165, 2005.

Giancarlo De Gasperis, Alessandro Buzzelli, Paolo Cabella, Paolo de Bernardis and Nicola Vittorio. Optimal cosmic microwave background map-making in the presence of cross-correlated noise *Astronomy & Astrophysics*, 593, A15, 2016.

Bruce T Draine. Interstellar dust grains. *Annual Review of Astronomy and Astrophysics*, 41(1):241–289, 2003.

C. Engel. *Optimisation des performances du système optique et estimation de la polarisation instrumentale de l'expérience embarquée sous ballon stratosphérique PILOT*. PhD thesis, Institut de Recherche en Astrophysique et Planétologie (IRAP), Université Paul Sabatier, 6 2012.

C. Engel, I. Ristorcelli, J.-P. Bernard, Y. Longval, C. Marty, B. Mot, G. Otrio, and G. Roudil. Characterization and performances of the primary mirror of the PILOT balloon-borne experiment. *Experimental Astronomy*, 36:21–57, August 2013. doi: 10.1007/s10686-013-9332-7.

Edward L Fitzpatrick. Correcting for the effects of interstellar extinction. *Publications of the Astronomical Society of the Pacific*, 111(755):63, 1999.

Martin Giard. *Mesure de l'emission diffuse galactique dans la raie a 3, 3 micrometre avec l'experience ballon arome*. PhD thesis, Toulouse 3, 1988.

T. Gold. The alignment of galactic dust. MNRAS, 112:215, 1952. doi: 10.1093/mnras/112.2.215.

Krzysztof M Gorski, Eric Hivon, AJ Banday, Benjamin D Wandelt, Frode K Hansen, Mstvos Reinecke, and Matthia Bartelmann. Healpix: a framework for high-resolution discretization and fast analysis of data distributed on the sphere. *The Astrophysical Journal*, 622(2):759, 2005.

J. S. Hall. Observations of the Polarized Light from Stars. *Science*, 109: 166–167, February 1949. doi: 10.1126/science.109.2825.166.

P. Hargrave, T. Waskett, T. Lim, and B. Swinyard. Performance of flight-model on-board calibration sources on Herschel-SPIRE. In *Society of Photo-Optical Instrumentation Engineers (SPIE) Conference Series*, volume 6275 of *Society of Photo-Optical Instrumentation Engineers (SPIE) Conference Series*, page 14, June 2006. doi: 10.1117/12.673197.

Peter C Hargrave, Jeffrey W Beeman, Patrick A Collins, Iris Didschuns, Matthew J Griffin, Brian Kiernan, Giampaolo Pisano, and R Hermoso. In-flight calibration sources for herschel-spire. In *Proceedings of SPIE*, volume 4850, pages 638–649, 2003.

Michael G Hauser and Eli Dwek. The cosmic infrared background: measurements and implications. *Annual Review of Astronomy and Astrophysics*, 39(1):249–307, 2001.

Patrick Hennebelle. On the origin of non-self-gravitating filaments in the ism. *Astronomy & Astrophysics*, 556:A153, 2013.

W. A. Hiltner. On the Presence of Polarization in the Continuous Radiation of Stars. II. ApJ, 109:471, May 1949. doi: 10.1086/145151.

W. F. Hoffmann and C. L. Frederick. Far-Infrared Observation of the Galactic-Center Region at 100 Microns. ApJ, 155:L9, January 1969. doi: 10.1086/180293.

Pointing Accuracy Improvement, Micha Schmidt, and Dave Salt. Herschel pointing accuracy improvement. 2012.

R. V. Jones and L. Spitzer, Jr. Magnetic Alignment of Interstellar Grains. ApJ, 147:943, March 1967. doi: 10.1086/149086.

MF Kessler, JA Steinz, ME Anderegg, J Clavel, G Drechsel, P Estaria, J Faelker, JR Riedinger, A Robson, BG Taylor, et al. The infrared space observatory (iso) mission. *Astronomy and Astrophysics*, 315:L27–L31, 1996.

L. M. Krauss, S. Dodelson, and S. Meyer. Primordial Gravitational Waves and Cosmology. *Science*, 328:989–, May 2010. doi: 10.1126/science.1179541.

J. M. Lamarre. Photon noise in photometric instruments at far-infrared and submillimeter wavelengths. *Appl. Opt.*, 25(6):870–876, Mar 1986. doi: 10.1364/AO.25.000870. URL `http://ao.osa.org/abstract.cfm?URI=ao-25-6-870`.

A. Lazarian. Tracing magnetic fields with aligned grains. J. Quant. Spec. Radiat. Transf., 106:225–256, July 2007. doi: 10.1016/j.jqsrt.2007.01.038.

S Masi, P De Bernardis, G De Troia, M Giacometti, A Iacoangeli, F Piacentini, G Polenta, PAR Ade, PD Mauskopf, JJ Bock, et al. The boomerang experiment and the curvature of the universe. *Progress in Particle and Nuclear Physics*, 48(1):243–261, 2002.

John C Mather. Bolometer noise: nonequilibrium theory. *Applied Optics*, 21 (6):1125–1129, 1982.

R. Misawa. *Observation and Analysis of the dust polarization in the Interstellar Medium with the PILOT experiment*. PhD thesis, Institut de Recherche en Astrophysique et Planétologie (IRAP), Université Paul Sabatier, 7 2016.

R. Misawa, J.-P. Bernard, P. Ade, Y. André, P. de Bernardis, M. Bouzit, M. Charra, B. Crane, J. P. Dubois, C. Engel, M. Griffin, P. Hargrave, B. Leriche, Y. Longval, S. Maes, C. Marty, W. Marty, S. Masi, B. Mot, J. Narbonne, F. Pajot, G. Pisano, N. Ponthieu, I. Ristorcelli, L. Rodriguez, G. Roudil, M. Salatino, G. Savini, and C. Tucker. PILOT: a balloon-borne experiment to measure the polarized FIR emission of dust grains in the interstellar medium. In *Millimeter, Submillimeter, and Far-Infrared Detectors and Instrumentation for Astronomy VII*, volume 9153 of Proc. SPIE, page 91531H, July 2014. doi: 10.1117/12.2055506.

R. Misawa, J.-P. Bernard, P. Ade, Y. Andre, P. de Bernardis, L. Bautista, O. Boulade, F. Bousquet, M. Bouzit, N. Bray, C. Brysbaert, V. Buttice, A. Caillat, M. Chaigneau, M. Charra, B. Crane, F. Douchin, E. Doumayrou, J. P. Dubois, C. Engel, P. Etcheto, J. Evrard, P. Gelot, A. Gomes, S. Grabarnik, M. Griffin, P. Hargrave, A. Jonathan, R. Laureijs, A. Laurens, Y. Lepennec, B. Leriche, Y. Longval, J. Martignac, C. Marty, W. Marty, S. Maestre, S. Masi, F. Mirc, J. Montel, L. Motier, B. Mot, J. Narbonne, J. M. Nicot, G. Otrio, F. Pajot, E. Perot, G. Pisano, N. Ponthieu, I. Ristorcelli, L. Rodriquez, G. Roudil, M. Saccoccio, M. Salatino, G. Savini, O. Simonella, J. Tauber, P. Tapie, C. Tucker, and G. Versepuech. Pilot End-to-End Calibration Results. In L. Ouwehand, editor, *22nd ESA Symposium on European Rocket and Balloon Programmes and Related Research*, volume 730 of *ESA Special Publication*, page 575, September 2015.

R. Misawa, J.-P. Bernard, Y. Longval, and I. Ristorcelli. The optical performance of the pilot instrument from ground end-to-end tests. submitted, 2016.

J. Montel. ESTADIUS: a high motion "one arcsec" daytime attitude estimation system for stratospheric applications. *CNES. 22nd ESA PAC Symposium, Norway, 2015*, January 2015.

G. Neugebauer and R. B. Leighton. *Two-micron sky survey. A preliminary catalogue*. NASA SP. NASA, Washington, 1969.

G. Neugebauer, H. J. Habing, R. van Duinen, H. H. Aumann, B. Baud, C. A. Beichman, D. A. Beintema, N. Boggess, P. E. Clegg, T. de Jong, J. P. Emerson, T. N. Gautier, F. C. Gillett, S. Harris, M. G. Hauser, J. R. Houck, R. E. Jennings, F. J. Low, P. L. Marsden, G. Miley, F. M. Olnon,

S. R. Pottasch, E. Raimond, M. Rowan-Robinson, B. T. Soifer, R. G. Walker, P. R. Wesselius, and E. Young. The Infrared Astronomical Satellite (IRAS) mission. ApJ, 278:L1–L6, March 1984. doi: 10.1086/184209.

Nils Olsen, Lars Toffner Clausen, Terence J. Sabaka, Peter Brauer, Jose M.G. Merayo, John L. Jorgensen, J. M. Leger, Otto V. Nielsen, Fritz Primdahl, and Torben Risbo. Calibration of the orsted vector magnetometer. *Earth, Planets and Space*, 55(1):11–18, 2003. doi: 10.1186/BF03352458.

Arno A Penzias and Robert Woodrow Wilson. A measurement of excess antenna temperature at 4080 mc/s. *The Astrophysical Journal*, 142:419–421, 1965.

G. L. Pilbratt, J. R. Riedinger, T. Passvogel, G. Crone, D. Doyle, U. Gageur, A. M. Heras, C. Jewell, L. Metcalfe, S. Ott, and M. Schmidt. Herschel Space Observatory. An ESA facility for far-infrared and submillimetre astronomy. A&A, 518:L1, July 2010. doi: 10.1051/0004-6361/201014759.

Peter AR Planck Collaboration Int. XX., Ade, Nabila Aghanim, D Alina, MIR Alves, G Aniano, C Armitage-Caplan, M Arnaud, D Arzoumanian, M Ashdown, F Atrio-Barandela, et al. Planck intermediate results. xx. comparison of polarized thermal emission from galactic dust with simulations of mhd turbulence. *Astronomy & Astrophysics*, 576:A105, 2015.

R Planck Collaboration Int. XXX, Adam, Peter AR Ade, Nabila Aghanim, M Arnaud, J Aumont, C Baccigalupi, Anthony J Banday, RB Barreiro, JG Bartlett, N Bartolo, et al. Planck intermediate results-xxx. the angular power spectrum of polarized dust emission at intermediate and high galactic latitudes. *Astronomy & Astrophysics*, 586:A133, 2016.

Ade Planck Collaboration. XI., Abergel, Peter AR Ade, N Aghanim, MIR Alves, G Aniano, C Armitage-Caplan, M Arnaud, M Ashdown, F Atrio-Barandela, J Aumont, et al. Planck 2013 results. xi. all-sky model of thermal dust emission. *Astronomy & Astrophysics*, 571:A11, 2014.

Peter AR Planck Collaboration. XV., Ade, N Aghanim, C Armitage-Caplan, M Arnaud, M Ashdown, F Atrio-Barandela, J Aumont, C Baccigalupi, Anthony J Banday, RB Barreiro, et al. Planck 2013 results. xv. cmb power spectra and likelihood. *Astronomy & Astrophysics*, 571:A15, 2014.

Nabila Planck intermediate results XLVI, Aghanim, M Ashdown, J Aumont, C Baccigalupi, M Ballardini, AJ Banday, RB Barreiro, N Bartolo, Suman

Basak, R Battye, et al. Planck intermediate results-xlvi. reduction of large-scale systematic effects in hfi polarization maps and estimation of the reionization optical depth. *Astronomy & Astrophysics*, 596:A107, 2016.

B. Reichborn-Kjennerud, A. M. Aboobaker, P. Ade, F. Aubin, C. Baccigalupi, C. Bao, J. Borrill, C. Cantalupo, D. Chapman, J. Didier, M. Dobbs, J. Grain, W. Grainger, S. Hanany, S. Hillbrand, J. Hubmayr, A. Jaffe, B. Johnson, T. Jones, T. Kisner, J. Klein, A. Korotkov, S. Leach, A. Lee, L. Levinson, M. Limon, K. Macdermid, T. Matsumura, X. Meng, A. J. Miller, M. Milligan, E. Pascale, D. Polsgrove, N. Ponthieu, K. Raach, I. Sagiv, G. Smecher, F. Stivoli, Radek Stompor, H. Tran, M. Tristram, G. S. Tucker, Y. Vinokurov, A. Yadav, M. Zaldarriaga, and K. Zilic. EBEX: a balloon-borne CMB polarization experiment. In *Millimeter, Submillimeter, and Far-Infrared Detectors and Instrumentation for Astronomy V*, volume 7741, page 77411C, San Diego, United States, June 2010. Prism Business Media. doi: 10.1117/12.857138. URL `http://hal.in2p3.fr/in2p3-00517912`.

Isabelle Ristorcelli. *Contribution a l'etude de la matiere interstellaire et au developpement d'instrumentation spatiale infrarouge et submillimetrique.* PhD thesis, Toulouse 3, 1995.

H. Roussel. Scanamorphos: A Map-making Software for Herschel and Similar Scanning Bolometer Arrays. PASP, 125:1126–1163, September 2013. doi: 10.1086/673310.

Francois Simoens, Patrick Agnese, Alain Beguin, Jacques Carcey, Jean-Charles Cigna, Jean-Louis Pornin, Patrice Rey, Aurelie Vandeneynde, Louis Rodriguez, Olivier Boulade, Jean Lepennec, Jerome Martignac, Eric Doumayrou, Vincent Reveret, and Laurent Vigroux. Submillimeter bolometers arrays for the pacs/herschel spectro-photometer, 2004. URL `http://dx.doi.org/10.1117/12.551299`.

Juan Diego Soler, P Hennebelle, PG Martin, M-A Miville-Deschênes, C Barth Netterfield, and LM Fissel. An imprint of molecular cloud magnetization in the morphology of the dust polarized emission. *The Astrophysical Journal*, 774(2):128, 2013.

B Stepnik, A Abergel, J-P Bernard, F Boulanger, L Cambrésy, M Giard, AP Jones, G Lagache, J-M Lamarre, C Meny, et al. Evolution of dust properties in an interstellar filament. *Astronomy & Astrophysics*, 398(2): 551–563, 2003.

J. A. Tauber, N. Mandolesi, J.-L. Puget, T. Banos, M. Bersanelli, F. R. Bouchet, R. C. Butler, J. Charra, G. Crone, J. Dodsworth, and et al. Planck pre-launch status: The Planck mission. A&A, 520:A1, September 2010. doi: 10.1051/0004-6361/200912983.

J. P. Torre and G. Chanin. Miniature liquid [U+2010] 3he refrigerator. *Review of Scientific Instruments*, 56(2):318–320, February 1985. doi: http://dx.doi.org/10.1063/1.1138350. URL http://scitation.aip.org/content/aip/journal/rsi/56/2/10.1063/1.1138350.

J. E. Vaillancourt, C. D. Dowell, R. H. Hildebrand, L. Kirby, M. M. Krejny, H.-b. Li, G. Novak, M. Houde, H. Shinnaga, and M. Attard. New Results on the Submillimeter Polarization Spectrum of the Orion Molecular Cloud. ApJ, 679:L25–L28, May 2008. doi: 10.1086/589152.

N. J. Woolf, M. Schwarzschild, and W. K. Rose. Infrared Spectra of Red-Giant Stars. ApJ, 140:833, October 1964. doi: 10.1086/147989.